Iridium(III) Photosensitisers for Photoredox Catalysed Carboxylation Reactions of Ketimines

Tara Davids

Department of Chemistry

University of Cape Town

January 2024

Iridium(III) Photosensitisers for Photoredox Catalysed Carboxylation Reactions of Ketimines

A dissertation submitted to the University of Cape Town in
fulfilment of the requirements for the degree of

Master of Science

by

Tara Davids

Supervisor: Professor Gregory Smith

Department of Chemistry
University of Cape Town
Rondebosch
7701

January 2024

Plagiarism Declaration

I know the meaning of plagiarism and declare that all of the work in the document, "**Iridium(III) Photosensitisers for Photoredox Catalysed Carboxylation Reactions of Ketimines** " is my own work and to the best of my knowledge has not been previously submitted for examination for any degree, at any university. All sources of information are cited and fully referenced at the end of each chapter.

Signed by candidate

Signature: ____________________________

Date: 4 January 2024

Acknowledgements

Above all, I am overwhelmingly thankful for the goodness and faithfulness of God. He blessed me with a spirit of perseverance and strength that enabled me to pursue and complete this Master's degree. He has been my source of steadfast peace during the ups and downs I've faced during the past two years.

To my supervisor, Professor Gregory Smith. I am deeply appreciative of his guidance, valuable input and support throughout my academic career, from Honours to Masters. I'm thankful for the travel opportunities he has afforded me, where I could present my research and learn from prominent researchers in their field.

To all the members of the GS Organometallic Research Group, thank you for your constructive discussions and encouragement during our group meetings. Thank you to Ms Taryn Golding for proofreading a chapter of my MSc work and for being part of my academic journey since Honours. A special thank you to Dr Reinner Omondi for taking the time to measure the quantum fluorescence yields as well as the triplet excited state lifetimes of my photosensitisers, during his research stint at Rhodes University. To Dr Marwaan Rylands, thank you for recording my 2D NMR spectra. I'd also like to extend my outmost gratitude to Dr Wade Petersen for his sincerity and support, insightful discussions and advice about science as well as life in general.

We gratefully acknowledge the National Research Foundation and the University of Cape Town for funding this Masters project.

To my phenomenal "behind the scenes" support structure. My friends Jess, Kirsten, Holly and Sandisiwe. You all have been so supportive of me, encouraging me at every step and reminded me that there is always something to smile or laugh about. To my parents and Hannah, I am deeply appreciative of the unconditional love you have always shown me, for always believing in me and reminding me of my worth. Finally, to Justin. You have been a source of love and light this year. Thank you for making me feel seen and keeping me calm. Thank you all for bringing me so much joy.

Conference Contributions

Oral Presentation: Tara K. Davids and Gregory S. Smith. *Iridium(III) Photosensitisers for Photoredox Catalysed Carboxylation Reactions of Ketimines.* Presented at CATSA 2023-33rd Annual Conference, in Mossel Bay, November 2023.

Oral Presentation: Tara K. Davids and Gregory S. Smith. *Polymetallic Ir(III) and Ru(II) Photosensitisers for Photoredox Catalysed Organic Transformation Reactions.* Presented at The 31st International Conference on Photochemistry in Sapporo, Japan, July 2023.

Awards

Runner up for best student presentation in the oral category at CATSA conference in 2023.

Abstract

The increasing need for catalytic systems driven by sustainable energy sources continues to motivate the development of processes that utilise photochemical energy to initiate chemical reactions. Photoredox catalysis has piqued great interest in this regard, creating a means for a milder energy source (visible light) to drive chemical reactions and thus revolutionising the field of synthetic radical chemistry and photochemistry. Recently, photoredox catalysis has paved a way for the direct incorporation of CO_2 into organic molecules, as a strategy to mitigate CO_2 accumulation. Pertinent to this study, is the photoredox catalysed fixation of CO_2 to afford unnatural α-amino acids, which have important applications in the pharmaceutical industry.

Following on from the above, polymetallic transition metal complexes have been promulgated as photocatalysts in processes such as CO_2 reduction. These polymetallic photocatalysts were reported to exhibit higher reactivity due to multiple active sites, improved photostability and increased durability in comparison to their mononuclear congeners. We have also demonstrated enhanced photocatalytic abilities of trinuclear heteroleptic ruthenium(II) polypyridyl photocatalysts in the context of the visible light mediated regioselective hydrothiolation reaction of alkenes. The higher yields obtained for the hydrothiolation reaction was attributed to there being a greater driving force for electron transfer processes with the trinuclear complexes.

In this study, a series of 2,2'-pyridyl substituted benzimidazole ligands (**L1-L3**) were synthesised *via* standard N-alkylation reactions. Subsequently, two mononuclear cationic bis-cyclometalated iridium(III) complexes (**C1**, **C2**) and a new trinuclear iridium(III) complex (**C3**) were synthesised. The complexes (**C1-C3**) were obtained as racemic mixtures (Λ, Δ isomers) which is an attribute of the helical chirality, inherent to these types of tris-bidentate octahedral complexes. Characterisation of the synthesised ligands and complexes was achieved by ^{1}H NMR, $^{13}C\{^{1}H\}$ NMR spectroscopy, infrared spectroscopy and high-resolution mass spectrometry. A crystal structure was also obtained for the new iridium(III) complex (**C2**), and confirms its molecular structure.

Furthermore, the photophysical properties (absorption and emission studies), electrochemical properties, as well as the photostability of the synthesised iridium(III) complexes have been ascertained, where the effects of ligand modifications on these properties have been observed and described. Finally, the catalytic activity of complexes (**C1-C3**) was evaluated in the visible light mediated photoredox catalysed carboxylation reaction of ketimines using CO_2, affording unnatural amino acids. This known reaction was selected as an ideal proof-of-concept reaction, due to the green nature of the reaction (with respect to Green Chemistry principles) and the utility of the α-amino acid product. The desired amino acid salt product and/or an additional product was obtained in the photocatalytic reactions with complexes (**C1**-**C3**) as the photoredox catalysts. The structure of this additional product was elucidated *via* spectroscopic analysis. Differences in the photocatalytic activity exhibited by the synthesised iridium complexes (**C1**-**C3**) and the model photoredox catalyst, $[Ir(ppy)_2(dtbbpy)]PF_6$ is discussed herein. The results obtained from the photocatalysis highlight the importance of judicious ligand design when developing efficient and versatile photosensitisers, and reveal that the benzimidazole scaffold may not be the most well-suited *N^N* ligand for this application.

Abbreviations and Symbols

°	Degree
Å	Angstrom (10^{-10} m)
δ	Chemical Shift
v	Wavenumber
Φ_{Em}	Emission quantum yield
ΔG_{ES}	Gibbs free energy change for the excited state
λ_{abs}	Absorption wavelength
λ_{em}	Emission wavelength
λ_{ex}	Excitation wavelength
Ar-H	Aromatic proton
ATR-IR	Attenuated total reflectance infrared spectroscopy
bpy	2,2’-Bipyridine
^{13}C NMR	Carbon 13- nuclear magnetic resonance
CCS	CO_2 capture and storage
CCU	CO_2 capture and utilisation
cm^{-1}	Reciprocal centimetres
COSY	Homonuclear correlation spectroscopy
Cy_2Me	*N,N*-dicyclohexylmethylamine
DCM	Dichloromethane

dd	Doublet of doublets
DIPEA	*N,N*-diisopropylethylamine
DMF	Dimethylformide
dtbbpy	4,4'-Di-*tert*-butyl-2,2'-bipyridine
ESI-MS	Electrospray ionisation mass spectrometry
EtOAc	Ethyl acetate
eq.	Equivalents
eV	Electron volt(s)
FMO	Frontier molecular orbital
g	Gram(s)
Gt	Giga ton(s)
h	Hours
HAT	Hydrogen atom transfer
^{1}H NMR	Proton nuclear magnetic resonance
HOMO	Highest occupied molecular orbital
HSQC	Heteronuclear single quantum correlation
Hz	Hertz
ISC	Intersystem crossing
J	Coupling constant

LC	Ligand-centred transition
LECs	Light emitting electrochemical devices
LED	Light emitting diode
LLCT	Ligand-to-ligand charge transfer
LUMO	Lowest unoccupied molecular orbital
m	Multiplet (NMR); medium (IR)
MC	Metal centred transition
MeCN	Acetonitrile
MeOH	Methanol
MHz	Megahertz
mL	Millilitre
MLCT	Metal to ligand charge transfer
mol	Mole(s)
mmol	Millimole(s)
mV	Millivolt(s)
mV/s	Millivolt(s) per second
nm	Nanometre(s)
NHE	Normal Hydrogen Electrode
PC	Photocatalyst
PDT	Photodynamic therapy

Pet. ether	Petroleum ether
PPA	Polyphosphoric acid
ppm	Parts per million
ppy	2-phenylpyridine
PT	Proton transfer
rt	Room temperature
s	Singlet (NMR); strong (IR)
SET	Single electron transfer
SOC	Spin-orbit coupling
t	Triplet (NMR)
TLC	Thin layer chromatography
TMS	Tetramethylsilane
TTIP	Titanium isoproproxide
UV	Ultraviolet
V	Volt(s)
XRD	X-ray diffraction

Table of Contents

Chapter 1: Literature Overview

1.1 Introduction to Green Chemistry and transition metal catalysis

The term 'Green Chemistry' can be concisely defined as: "Green Chemistry efficiently utilises (preferably renewable) resources, eliminates waste and avoids the use of toxic and/or hazardous reagents and solvents in the manufacture and application of chemical products."[1] This term was first introduced in the early 1990s by Anastas and colleagues at the US Environmental Protection Agency. Anastas also devised the 12 principles of Green Chemistry (Figure 1.1), which encapsulates his 'benign by design' concept.[2] In this 'benign by design' concept, the focus of Green Chemistry is to design chemical reaction schemes in such a way as to eliminate any possible waste at the start, rather than having to get rid of excess waste produced at the end. Essentially, Green Chemistry is a way in which to achieve the goal of chemical and environmental sustainability.[1]

The 'Environmental factor' (E- factor) and 'Atom Economy' are two important concepts to note in the field of Green Chemistry. These two terms broadly provide a means to assess the overall "greenness" and environmental impact of the proposed reaction.[1] For the majority of the time in the synthesis and manufacturing of organic compounds, stoichiometric amounts of reagents are used which results in excess waste and high E-factors. This is obviously unfavourable and a way to circumvent this issue is to utilise catalysts in these synthetic processes.[1, 2]

Transition metal-based catalysis plays a crucial role in science due to it offering a greener alternative for the manufacture of chemicals and materials.[3] That is, compared to reactions that use stoichiometric amounts of reagent, catalysts lower the activation energy of a reaction and improve the overall energy efficiency of a reaction and in so doing, result in less waste being produced.[4] Transition metal catalysts have made a myriad of organic transformation reactions possible, which were previously unachievable without the addition of a catalyst. A few noteworthy reactions include the hydroformylation reaction, the palladium catalysed cross-coupling reaction and C-H functionalisation reactions.[5-7] Due to these favourable outcomes, transition metal catalysis is employed in both the fine and bulk chemical industries.[4]

However, it is important to note that although the catalytic strategies discussed above provide a step closer in achieving the goals of Green Chemistry, these strategies also possess a downfall. These catalytic strategies usually require elevated temperatures and pressures to trigger the reaction.[8] Alternative forms of energy such as photochemical energy have thus been investigated as a means to improve these reaction conditions. An attractive strategy that utilises photochemical energy to drive reactions, which has received great attention in recent years, is the field of photoredox catalysis.

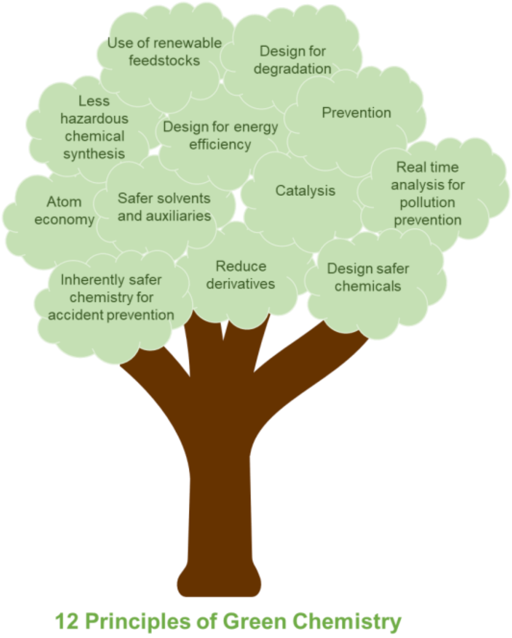

Figure 1.1. Diagram representing the 12 Principles of Green Chemistry.

1.2 Introduction to photoredox catalysis

1.2.1 Overview of photoredox catalysis

In recent years, photoredox catalysis has revolutionised the field of synthetic radical chemistry and photochemistry in that it has created a means for a greener energy source, visible light, to drive reactions.[8,9] Typically, photoredox catalysts consist of transition metal complexes, such as complexes of ruthenium(II) and iridium(III), or organic dyes.[8] Upon excitation by visible light irradiation, photoredox catalysts initiate single electron transfer events (SET) to/from a stable substrate and in so doing, results in the formation of a highly reactive excited-state species that can be involved in reaction pathways that were previously not possible under thermal control.[8, 10]

The versatility of photoredox catalysis has made it applicable in a wide variety of processes including natural product synthesis,[11] carbon dioxide reduction[12] and water splitting reactions.[13] In the scope of Green Chemistry, photoredox catalysis is an invaluable resource as it provides a means to generate cleaner, safer and less toxic synthetic routes to generate highly reactive radicals.[9] That is, photoredox catalysis harnesses visible light as the reaction driving force, which means that reactions can generally be performed at mild or ambient temperatures, and it replaces the need for temperature unstable radical initiators or alternative metalloid reagents that were once required for radical propagation.[8, 9] Thus, photoredox catalysis fulfils the following Green Chemistry principles:

1. Catalysts: by employing a catalytic amount (instead of a stoichiometric quantity) of transition metal complex or organic photosensitiser to convert light energy into chemical energy. In turn, the chemical energy can initiate the electron transfer step between reacting substrates.[9]
2. Design for energy efficiency: visible light (a milder and renewable energy source) is used to initiate the photocatalytic reaction. Reactions are typically performed at milder temperatures as well.
3. Inherently safer chemistry for accident prevention: It avoids the use of toxic or hazardous radical initiators.

4. Less hazardous chemical synthesis: Ties in with the reason described in point 3 above.

Thus the versatility and the synthetic advantages provided by photoredox catalysis provides a means for achieving the goal of chemical sustainability as outlined in the scope of Green Chemistry.[1]

1.2.2 Important properties of photocatalysts

The following points are important considerations when choosing or designing an appropriate photocatalyst for a photocatalysed reaction:

1. Photocatalysts must possess a good absorption spectrum, preferably at a distinctive wavelength, where the other reacting species cannot absorb as well. A wider absorption wavelength range also enhances the versatility of the photocatalyst.[14]
2. The photo-excited state of the photocatalyst must be sufficiently long-lived in order to undergo the required reaction with the reacting substrate, and then efficiently be able to regenerate itself to maintain its viability as part of the catalytic cycle.[14]
3. A photoredox catalyst specifically, should preferably exhibit reversible electrochemistry, as it needs to be adequately stable in its oxidised or reduced form to maintain its viability over multiple catalytic turnovers for a given reaction.[14]
4. Finally, tunability and synthetic accessibility are important when modifying the excited state reactivity of the photocatalyst, for a specific reaction.[14]

1.2.3 Transition metal complexes as photoredox catalysts

Photoredox catalysts can be in the form of transition metal complexes,[8] organic dyes,[8] inorganic semiconductors[15-17] or sometimes even in a combination of these forms.[18]

The extensive use of *d*-block transition metal complexes as photoredox catalysts suggests that there is a dependence on the nature of the metal and ligand identity upon photoexcitation of these complexes. An advantage of transition metal complexes is that the metal centre and/or the ligand can be readily modified.[18] $[Ru(bpy)_3]^{2+}$ was the first transition metal-based complex that was used as a photocatalyst in the context of organic chemistry, in which Nobel Laureate, David W.C. MacMillan and coworkers utilised this complex in their photoredox catalysed reaction involving the asymmetric alkylation of aldehydes.[19] Simultaneously, Yoon *et al.* utilised $[Ru(bpy)_3]^{2+}$ as a photoredox catalyst for [2+2] enone cycloaddition reactions and following from the success of these groups, coordination compounds have been explored in a range of organic transformation reactions.[20, 21]

Due to their high earth abundance and low cost, first row transition metals have been investigated as potential photoredox catalysts as well.[22] However, first row transition metals experience weaker ligand fields compared to second and third row transition metals, where the lowest unoccupied orbitals of $3d^6$ complexes become metal-based.[23] As a result, bipyridyl catalysts with these transition metals tend to exhibit non-luminescent and very short-lived excited states (picosecond-nanosecond range), due to ultrafast deactivation by the metal centred (MC) states.[22, 23] Thus, the most utilised photoredox catalysts are the ubiquitous d^6 polypyridyl complexes of ruthenium(II) and iridium(III), as represented in Figure 1.2. These complexes are particularly advantages in that they:

1. Strongly absorb light in the visible region, which makes it simpler to selectively excite them, relative to the reacting organic substrate. Organic substrates are usually transparent and generally don't absorb visible light (unless they are highly conjugated systems).[14, 18]
2. Possess relatively long-lived photoexcited states (ns-µs range) that can react with an organic substrate.[18] These excited states are also formed with 100% efficiency.[24]
3. In their excited states, they are powerful single electron transfer reagents.[18]
4. They exhibit appropriate reversible electrochemical behaviour and photostability such that there is little degradation of the photoexcited oxidised/reduced species.[18]

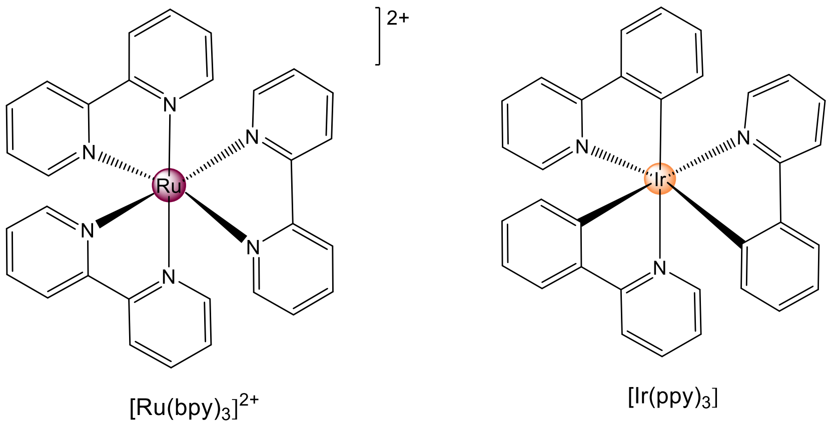

Figure 1.2. Structures of the prototypical ruthenium(II) and iridium(III) polypyridyl photoredox catalysts, $[Ru(bpy)_3]^{2+}$ and $[Ir(ppy)_3]$.

The photophysical processes that occur to a transition metal complex upon the absorption of visible light is demonstrated by the Jablonski diagram in Figure 1.3.[25] Firstly, it is important to note that the spin multiplicity of a specified electronic state can consist of an electron pair (singlet state) or unpaired electrons (triplet state). Typically, the ground electronic state is a singlet state, which is designated by S_0 in Figure 1.3, and the excited states are either singlet (S_1, S_2) or triplet states (T_1). Upon the absorption of visible light, an electron is promoted from the t_2g orbital that is centred on the metal, to the π^* orbital centred on the ligand, in a metal to ligand charge transfer (MLCT) process. The selection rules for electronic states specifies that the spin state of the electron should be maintained upon excitation, and thus the photoexcited electron is promoted to a singlet excited state (S_1/^{1}MLCT). Once in the ^{1}MLCT state, a host of non-radiative and radiative pathways can be followed, upon returning to the ground state.

Non-radiative pathways include vibrational relaxation and internal conversion. Vibrational relaxation occurs when the photoexcited molecule relaxes very rapidly (within 10^{-14}-10^{-12} s) to the lowest vibrational level of the excited electronic state.[26] This generally occurs prior to luminescence processes. Internal conversion occurs when there is relaxation between electronic states of the same spin multiplicity, such as going from $S_2 \rightarrow S_1$ in Figure 1.3. This happens on a time-scale of about of 10^{-12} s.[26]

However, non-radiative processes are not strictly limited to electronic states that possess the same spin multiplicity. Intersystem crossing (ISC) can occur between excited states of different spin multiplicity. Due to the change in conservation of spin multiplicities, ISC is generally a less probable process than internal conversion, and thus occurs at a slower rate of approximately 10^{-8} s.[26] A notable attribute of particularly the high atomic number and heavier *d*^{6} transition metals such as iridium(III), osmium(II) and ruthenium(II) is that they exhibit strong spin orbit coupling (SOC, $\zeta = 3903$, 3381, 1042 cm^{-1} respectively)[27] which facilitates a change in spin of the electrons, and thus there is almost unitary ISC to the lower-energy ^{3}MLCT/ T_1 state for these metals.[26, 28] Hence, these transition metal complexes can undergo luminescent radiative pathways upon the absorption of visible light.

Radiative decay pathways involve fluorescence and phosphorescence. Fluorescence involves the emission of light, which is associated with a spin allowed radiative electronic transition ($S_1 \rightarrow S_0$). Fluorescence is a rapid process, where the average excited-state lifetimes are $<10^{-6}$ s.[26] Less probable than florescence, is the emission of light *via* phosphorescence, which involves a spin-forbidden transition ($^3\text{MLCT} \rightarrow S_0$). The spin-forbidden nature of phosphorescence results in slower transitions and thus longer-lived excited states (from 10^{-6} s to several seconds), which can be susceptible to other non-radiative processes as mentioned above, or electrochemical quenching with an appropriate quencher molecule.[26, 29] That is, specifically in a photoredox catalysis context, the ^{3}MLCT excited state photocatalyst can be quenched by an organic substrate, whereby electrochemical quenching with an electron donor constitutes the reductive quenching cycle, and quenching with an electron accepting substrate constitutes the oxidative quenching cycle.[9]

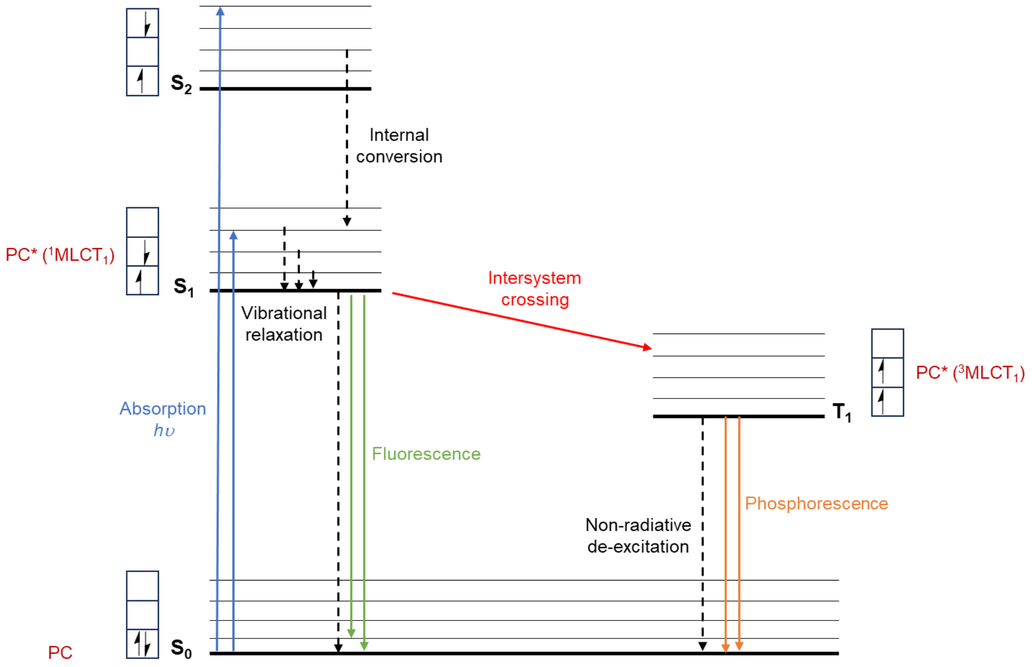

Figure 1.3. Jablonski diagram depicting the photophysical processes that occur in a transition metal photocatalyst upon excitation by light irradiation. Radiative and non-radiative processes are respectively represented by solid and dashed arrows. Modified from Omary *et al.*[26]

1.2.4 Mechanism of photoredox catalysis

Photoredox catalysis relies on the property that excited states are more easily oxidised or reduced than their analogous ground state forms, and thus the photocatalyst can act as an electron donor or acceptor to be regenerated during the course of the photocatalytic cycle. The general mechanism of a photoredox catalysed reaction is depicted in Figure 1.4. The mechanism of the photoredox catalytic cycle can be explained in the following manner: in the case of oxidative quenching, the photoexcited photocatalyst (Pcat*) can donate an electron to a reacting substrate to afford a strong oxidant (PCat^{*+}). Thereafter, PCat^{*+} is reduced by reacting with an electron donating species (D), which returns the oxidation state of PCat^{*+} to that of the starting photocatalyst (PCat).

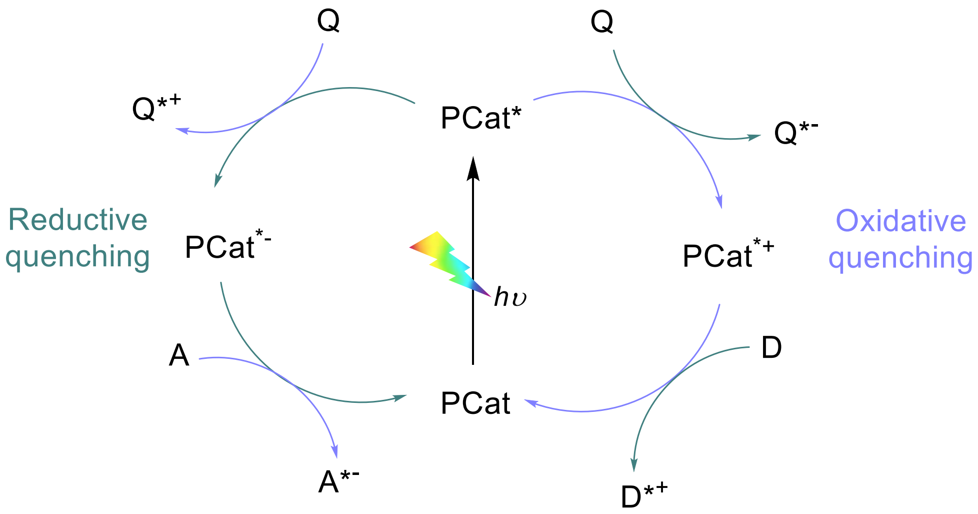

Figure 1.4. General mechanism of the oxidative (purple) and reductive (green) pathways of photoredox catalysis. PCat=Photocatalyst, A=Acceptor, D=Donor and Q=Quencher.[30]

In reductive quenching, the excited photocatalyst can accept an electron from a substrate to afford a strong reductant ($PCat^{*-}$). $PCat^{*-}$ is subsequently oxidised by donating an electron to an electron deficient acceptor species (A), returning the oxidation state of $PCat^{*-}$ to that of the starting photocatalyst (PCat).[30] Additionally, this process can also occur *via* the reaction of Pcat* with the respective substrate first, which is subsequently returned to PCat by interaction of Pcat* with the sacrificial electron donor/acceptor.

1.3 Cyclometalated iridium(III) complexes as photosensitisers

1.3.1 Characteristic attributes of cyclometalated iridium(III) complexes

The extensive use of $[Ru(bpy)_3]^{2+}$ in photoredox catalysed organic reactions may make it seem as if this complex is a “one size fits all” photocatalyst. However, the most suitable photocatalyst for a given reaction depends on the kinetics and thermodynamics of the reaction.[14] A need for stronger catalytic oxidants and reductants arose as the popularity of ruthenium(II) photoredox catalysts increased in organic reactions.

Following on from this, charge neutral and cationic iridium(III) complexes, such as those represented in Figure 1.5 were evaluated as photoredox catalysts. From the redox potentials, excited state lifetimes and photophysical properties exhibited by these iridium(III) complexes, it was evident that these complexes are capable of photoredox catalysis similar to [Ru(bpy)$_3$]$^{2+}$.[9]

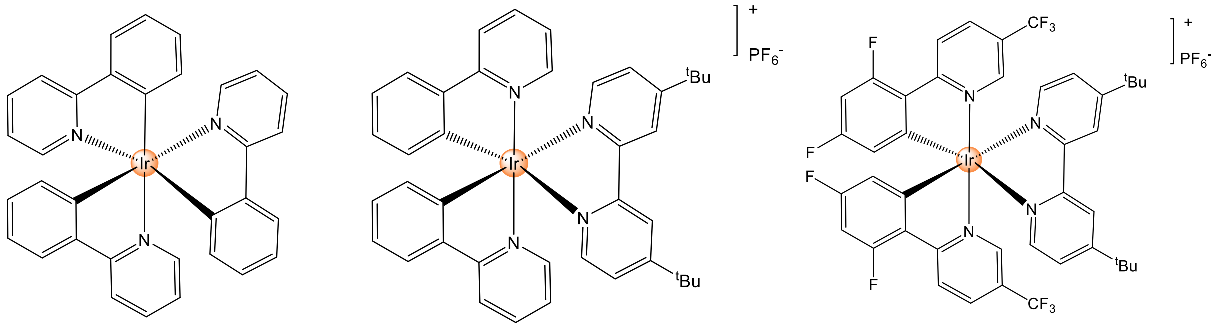

[Ir(ppy)$_3$]

[Ir(ppy)$_2$(dtbbpy)]PF$_6$

[Ir(dF(CF$_3$)ppy)$_2$(dtbbpy)]PF$_6$

Figure 1.5. Selected examples of charge neutral and cationic archetypal iridium(III) complexes evaluated as photoredox catalysts. [31, 32]

Iridium(III) complexes play a significant role in photoredox catalysis because the nature of the iridium(III) centre and its surrounding ligands provide a unique photochemical environment. Iridium coordination chemistry is highly versatile, where it can undergo either the standard N^N coordination or N^C cyclometalation with ligands such as bipyridine (bpy). The free ring rotation around the 2,2'-bpy bond means that under certain synthetic conditions, the bpy ligand can coordinate to the iridium(III) centre *via* the classic N^N or less common N^C binding motif, as is the case for the complex [Ir(bpy)$_3$]$^{3+}$. [33-35] This is a renowned and exclusive property of iridium(III). Iridium(III) complexes also have the ability to be mono-, bis-, or tris-cyclometalated, which further increases the diversity of the available iridium(III) complexes.[36]

Photoexcitation of the iridium(III) ion results in a multitude of photophysical steps, due to the strong electronic interactions of the iridium(III) centre with its surrounding chelated ligands, favouring delocalisation of the frontier molecular orbitals over the entire cyclometalated iridium(III) complex, as is the case for the prototypical photoredox catalyst, [Ir(ppy)$_3$].[37]

The highest occupied molecular orbital (HOMO) is delocalised over the t_{2g} orbital of the iridium(III) centre and the π orbitals of the 2-phenylpyridine ligands, whereas the lowest unoccupied molecular orbital (LUMO), is delocalised over the π^* orbital of 2-phenylpyridine only. Following on from this, photoexcitation promotes at least two electronic transitions, which are from the iridium(III) centre → ligand (metal to ligand charge transfer, MLCT) and from the ligands' $\pi \rightarrow \pi^*$ orbitals (ligand centred, LC) as well.[37] In addition to these transitions, the iridium(III) core exhibits strong spin orbit coupling which facilitates ISC to the triplet MLCT and LC transitions. This results in four possible electronic states: ^{1}MLCT, ^{3}MLCT or ^{1}LC, ^{3}LC states, with the energy order of these states being ^{1}LC>^{1}MLCT>^{3}MLCT>^{3}LC.[37] Figure 1.6 shows a simplified molecular orbital diagram of [Ir(ppy)]$_3$ photochemistry.

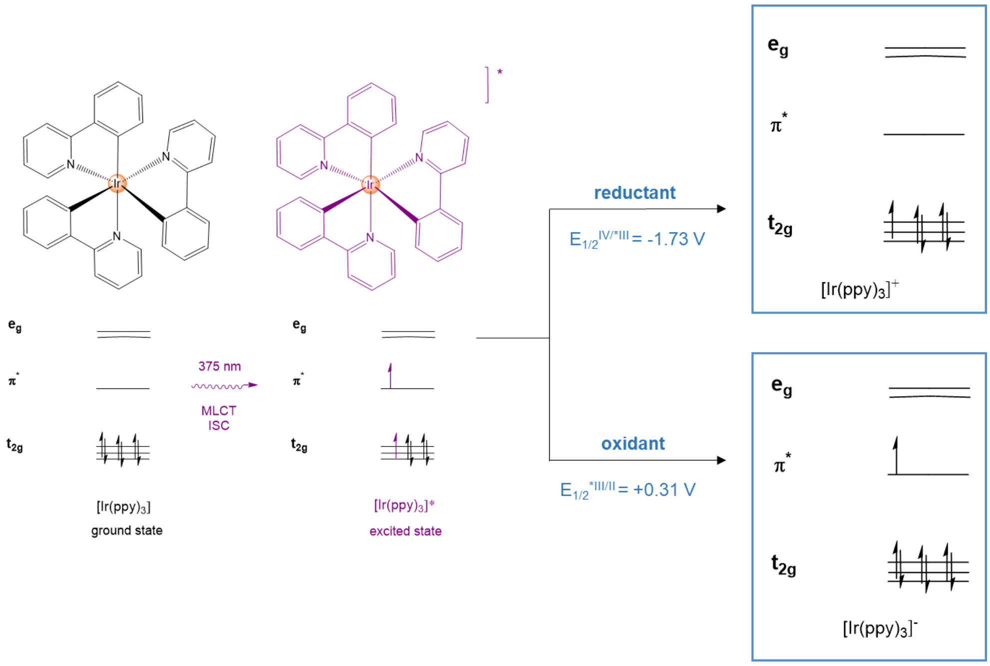

Figure 1.6. Simplified molecular orbital diagram of [Ir(ppy)$_3$] and its excited state. Adapted from Shaw *et al.*[38]

Additionally, tuning the ligands by modifying their electron-donating or -withdrawing properties can significantly affect the frontier orbital energies and in so doing, control the energy of the triplet state.[37] Thus, the iridium(III) centre provides the perfect environment to design an array of ligands with specifically modified electronic properties which could aid in improving the efficiency of these complexes as photoredox catalysts.[36]

Finally, iridium(III) complexes exhibit extensive splitting of their *d* orbitals (large Δ_{oct}) wider than analogous d^6 complexes ruthenium(II) and iron(II).[36] This is because iridium(III) has a greater ionic charge, larger *d* orbitals and an inherently strong field exerted by its cyclometalated, *C^N* ligands, for cyclometalated complexes specifically.[36] As a result, the pseudo-e_g antibonding orbitals that are centred on the chelating ligands, are raised in energy above the π* orbitals of ligands (Figure 1.6). Transition metal complexes that possess the above described electronic structure can exhibit emissive and redox-active MLCT states, with limited absorption features attributed to metal centred (MC) electronic transitions in the UV spectrum.[23, 36] The restricted accessibility to the MC states, which are renowned to be non-emissive/undergo photodissociation is a significant attribute of iridium(III) complexes when compared to iron(II), where iron(II) is penalised for its luminescence output or stability due to deactivation of these MC states.[36]

1.3.2 Cyclometalated iridium(III) complexes with an *N^N* chelated benzimidazole ancillary ligand

The benzimidazole moiety (Figure 1.7) is a heterocyclic aromatic ring which is comprised of a benzene ring that has been fused onto the 4- and 5- positions of an imidazole ring. Modifications at the 2- and 5- positions of the benzimidazole scaffold have afforded an array of biologically active compounds.[39] Accordingly, the benzimidazole scaffold is a well-known pharmacophore that has a diverse range of applications in antimicrobial, antiviral and anticancer treatments.[40] The reactive N-H bond on the imidazole portion of the benzimidazole scaffold also allows for facile functionalisation with a variety of functional groups. Additionally, many benzimidazole-based ligands are commercially available or quite easily synthesised, which affords a great deal of structural and chemical diversity. The significance of ease of modification of the benzimidazole ligand is particularly important in the context of photosensitiser design, as this allows one to easily modify the photophysical, electrochemical and photocatalytic properties of the photosensitiser.[41]

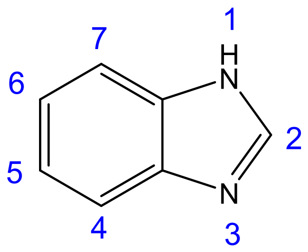

Figure 1.7. Structure of 1*H*-benzimidazole.

Iridium(III) complexes bearing particularly the 2,2'-pyridyl-substituted benzimidazole as an *N^N* chelated ancillary ligand have applications in an array of photochemistry related fields including light emitting electrochemical devices (LECs),[42, 43] photodynamic therapy (PDT)[44] and pertinent to this work, photocatalysis.[41] The latter application involved the photocatalytic dehydrogenation of N-heterocycles, whereby the iridium(III) photosensitisers exhibited highly efficient and selective photocatalytic activity to afford a host of N-heteroarene products such as indoles, quinolines, acridines and quinoxalines.[41] These photosensitisers also exhibited good photostability, sufficiently long-lived excited-state lifetimes and versatile redox behaviour.[41] The structure of these photosensitisers is represented in Figure 1.8.

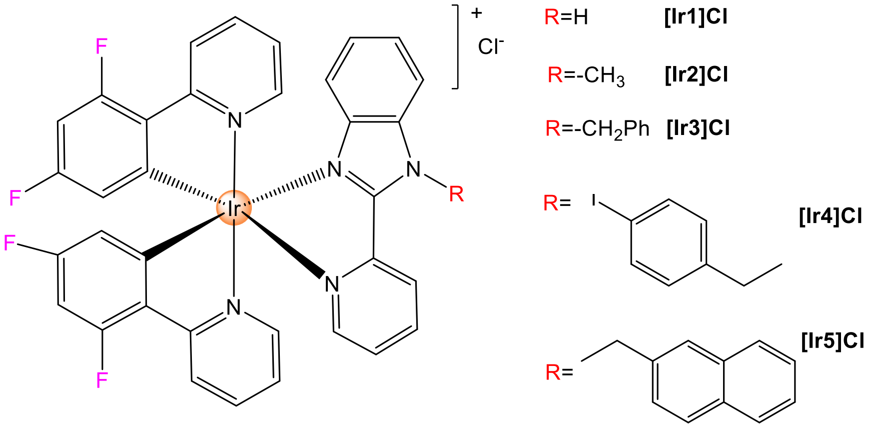

Figure 1.8. Iridium(III) photosensitisers evaluated in the photocatalytic dehydrogenation reaction of N-heterocycles, by Echevarría *et al.*[41]

Additionally, LECs with the appropriately functionalised 2,2'-pyridyl-substituted benzimidazole scaffold have reported to exhibit high luminescence efficiency, photostability as well as long lifetimes, with short turn on times.[42, 43] As PDT agents, these kinds of complexes have again been described to possess good photostability, high quantum phosphorescent yields and the ability to generate singlet oxygen.[44] Thus, the benzimidazole scaffold grafted onto the iridium(III) centre affords a diverse range of photosensitisers that possess optical, bioactive or photocatalytic properties.

1.4 Polymetallic photocatalysts in photoredox catalysed reactions

As previously discussed, photocatalysis has proved to be a revolutionary technique in the field of synthetic organic chemistry because it has enabled the transformations of challenging reactions that were previously not possible without it. However, the majority of photocatalysts studied have all been mononuclear complexes that unfortunately can exhibit poor durability and have limited active sites which hinders reactivity enhancement.[45] Polymetallic complexes have thus been promulgated as potential photocatalysts, and have shown to exhibit higher reactivity due to multiple active sites, improved stability and increased durability when compared to mononuclear complexes.[45, 46]

Polymetallic complexes act as photoredox catalysts in electron transfer processes such as CO_2 reduction[12, 47, 48] and water oxidation reactions.[13] In the context of CO_2 reduction, CO_2 requires high reduction potentials (-1.9 V *vs* NHE) for its electrochemical activation of one electron reductions due to the molecule's inherent stability.[49] This issue is resolved by introducing multi-electron transfer systems in the reduction process of CO_2, which lowers the reduction potential of these reactions.[49] This enhanced catalytic activity exhibited by polymetallic photocatalysts was demonstrated by Reithmeier *et al.* in their photocatalytic reduction of CO_2 by trinuclear iridium(III) photocatalysts. Here, they noted that there was a two-fold increase in the turnover number for their trimetallic iridium(III) complex, when compared to its mononuclear analogue.[12]

Similar trends were observed in the case of Zhang *et al*. in their photocatalytic oxidation of water by trinuclear ruthenium(II) complexes,[13] and in the case of Cancelliere *et al*. where they used a trinuclear ruthenium(II)-rhenium(I) supramolecular photocatalyst for CO_2 reduction.[47] Selected structures of these polymetallic complexes are illustrated in Figure 1.9. The increased catalytic activity exhibited by these polymetallic photocatalysts is due to enhanced redox properties, that is attributed to the polynuclear nature of the photocatalyst, where all of the active metal centres are contained within a single macromolecule.[50]

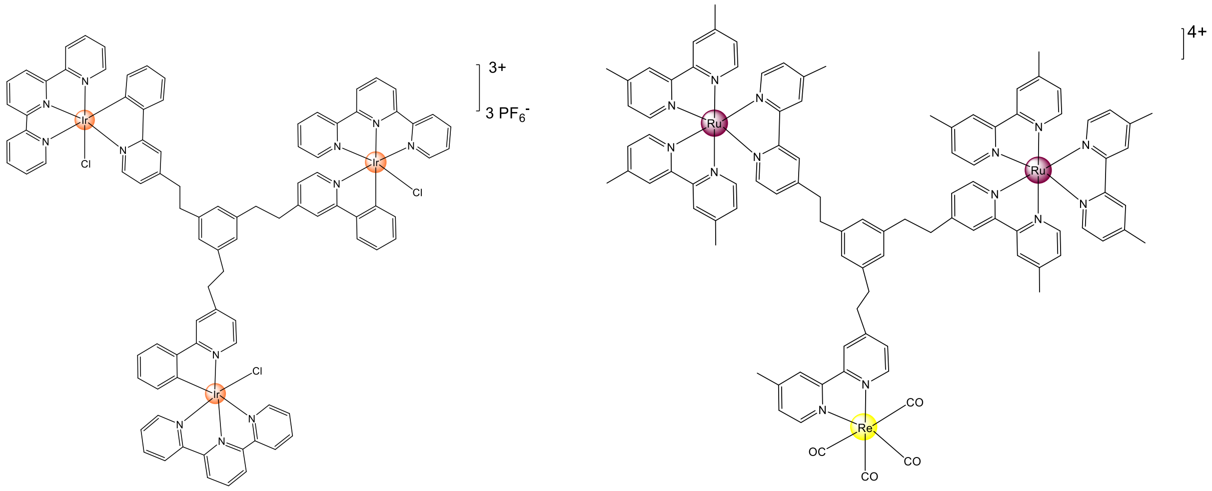

Figure 1.9. Polymetallic photoredox catalysts used for CO_2 reduction. (i) Synthesised by Reithmeier *et al.*[12] and (ii) synthesised by Cancelliere *et al.*[47]

Furthermore, in recent work performed in our research group, we have also demonstrated the enhanced catalytic abilities of polymetallic photocatalysts in the context of the visible light mediated regioselective hydrothiolation reaction of alkenes.[51] N. Motimani *et al*. reported that improved reaction yields were obtained with their new trinuclear heteroleptic imine- and amine- functionalised ruthenium(II) photoredox catalysts (Figure 1.10) in comparison to the respective mononuclear congeners.[51] Motimani *et al*. postulated that the trinuclear ruthenium(II) complexes exhibit a greater driving force for the electron transfer processes, which contribute to the observed higher yields for the hydrothiolation reactions.[51]

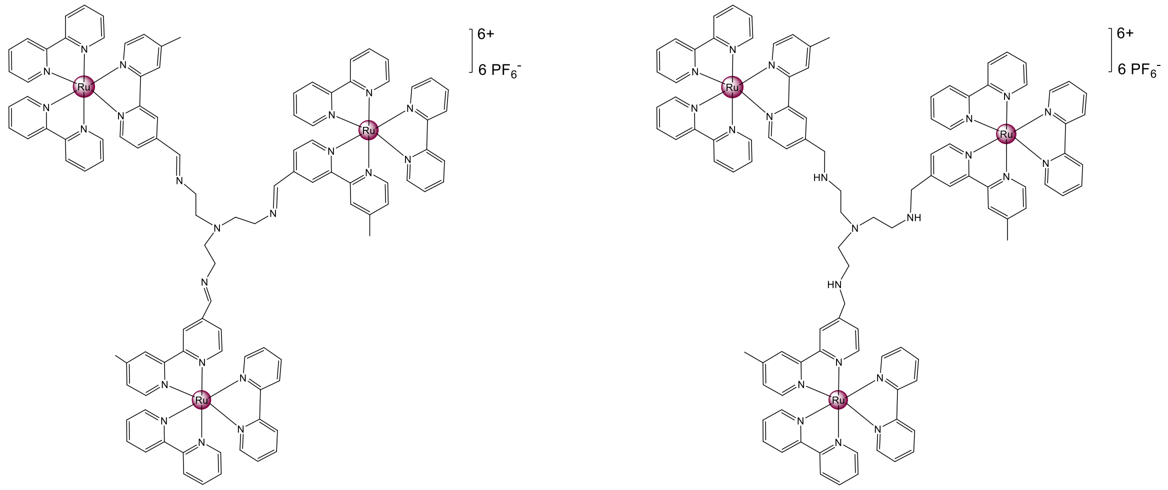

Figure 1.10. Structures of the heteroleptic trinuclear ruthenium(II) photoredox catalysts, synthesised by Motimani *et al.*, which were evaluated in the regioselective hydrothiolation reaction of alkenes.[51]

1.5 CO_2 emission and utilisation strategies

In 2021 CO_2 emission in the atmosphere reached an alarming level of 34.9 Gt.[52] While there are natural sources that contribute to CO_2 emissions in the atmosphere, human activities such as the burning of fossil fuels are the primary contributors in causing the increase of atmospheric CO_2, since the industrial revolution.[53] This excess of CO_2 in the atmosphere contributes to the greenhouse effect which in turn exacerbates the effects of global warming and climate change. Climate change threatens the balance of natural ecosystems as well as endangering the lives of many species and humans.[54] In light of these environmental issues and with the 12 principles of Green Chemistry in mind, it is thus of utter importance and urgency that CO_2 capture, storage and conversion strategies are developed to reduce atmospheric CO_2 concentrations.

There has been significant developments in CO_2 chemistry and industry in the last few decades; these developments being carbon dioxide capture and storage (CCS) and carbon dioxide capture and utilisation (CCU).[54] The process of CCS involves the removal of CO_2 from fossil-fuel based powerplants and chemical plants *via* the aid of industrial processes and once captured, the CO_2 is transported for permanent underground storage.[55]

Although CCS provides an effective strategy for reducing CO_2 levels, CCU presents an even better alternative because CO_2 is a non-toxic molecule, available in high natural abundance, which can be converted into value added products.[56] That is, CO_2 can be used as a feedstock to synthesise fuels and synthetic products *via* the formation of an array of chemical bonds such as C-N, C-C, C-H and C-O bonds.[56, 57] Typical CO_2 synthetic product transformations are shown in Figure 1.11.

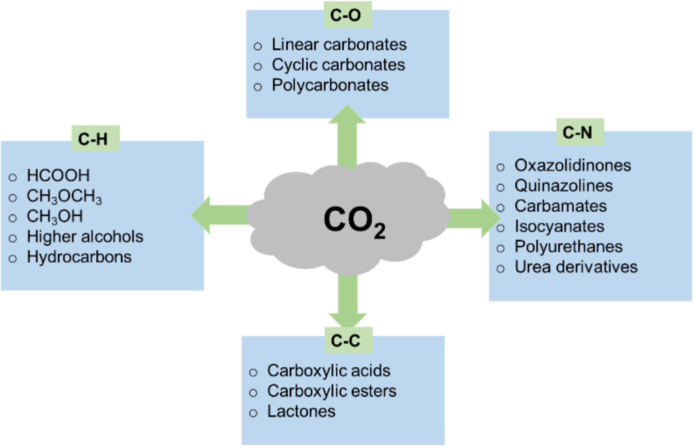

Figure 1.11. Typical CO_2 synthetic transformations. Modified from He *et al.*[56]

Despite CCS and CCU processes being promising strategies, the inherently inert nature of CO_2 makes the application of these processes difficult. CO_2 is the most oxidised form of carbon, is thermodynamically stable and kinetically inert and thus large energy input is required for the transformation of CO_2.[57] In the context of organic CO_2 transformation reactions, very reactive reagents are required in order for the direct incorporation of CO_2 into organic substrates.[58] Additionally, CO_2 fixation methods have been restrictive in that these methods required stoichiometric amounts of organometallic reductants or harsh reaction conditions.[59] An array of techniques have been explored in an attempt to overcome this issue which include, thermal, catalytic, electrochemical, photoelectrical, photochemical and biochemical technologies.[58,59] At the forefront, photocatalytic techniques have piqued the greatest interest due to the simplicity, generality, scalability (*via* continuous flow techniques), and the mild nature of these reactions.[59]

1.6 Photoredox catalysis as a strategy for CO_2 utilisation in organic synthesis

The emergence of photoredox catalysis in recent years, has paved a way for direct CO_2 incorporation into organic molecules.[60] Photoredox catalysis has applications in carboxylation reactions and other variations of CO_2 fixation techniques into organic moieties, to afford several valuable synthetic building blocks such as amino acids, carboxylic acids, esters and heterocycles (Figure 1.12).[59] This is because photoredox catalysis involves the creation of reactive intermediates (*via* SET events) where these reactive intermediates can readily react with CO_2, which is not as easily achieved with other catalytic systems.[59] In the process of photochemical CO_2 integration into organic substrates, two mechanisms are mainly encountered (Figure 1.12). The first mechanism involves CO_2 being inserted as an electrophile and the second mechanism involves the single electron reduction of CO_2, to form the radical anion species, $[CO_2]^{\bullet -}$ and here CO_2 acts as a nucleophile.[59] The reduction potential of CO_2 is quite high and in order to surpass this barrier, suitable photoredox catalysts with high reduction potentials are required for CO_2 integration under mild conditions.[59]

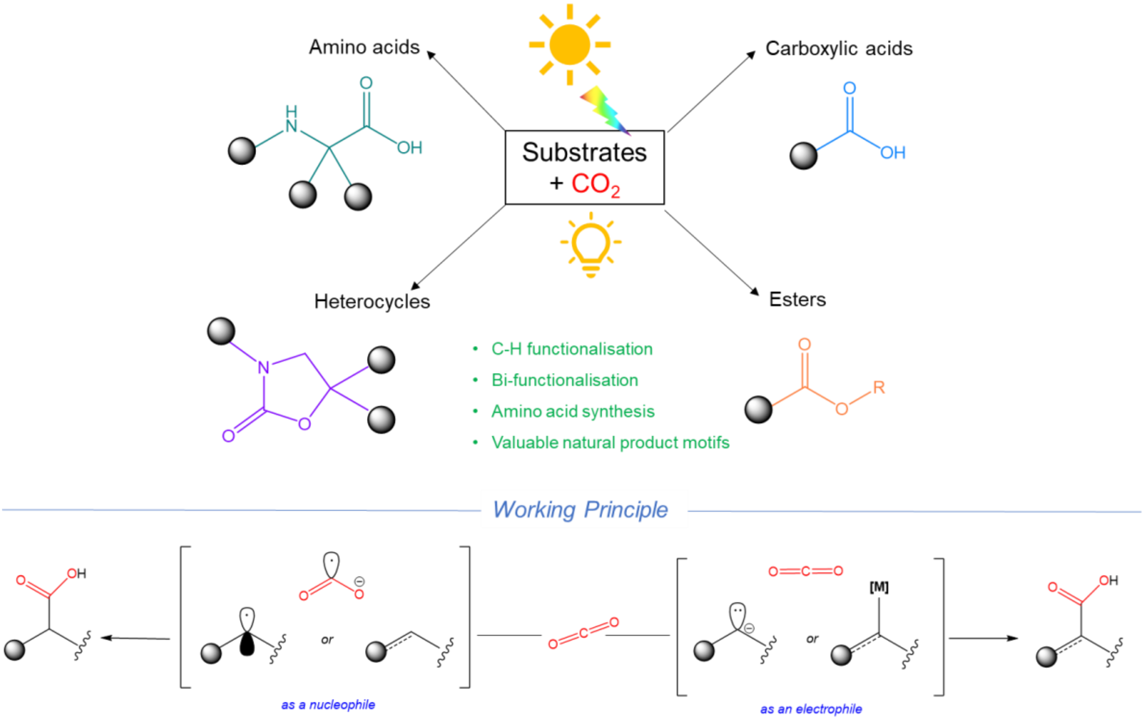

Figure 1.12. Overview of photoredox catalysed carboxylative processes and the working principle behind the mechanism of these processes. Adapted from Pradhan *et al.*[59]

Considering photoredox catalysis with CO_2 frequently involves electron reduction processes, olefins are the common radical acceptors in this chemistry. Olefins are also a cost-effective and readily available feedstock and so CO_2 carboxylation reactions with these substrates have been a topical field of research.[59] Photoredox catalysis mediated hydrocarboxylation reactions of olefins have been studied by the Jamison and Iwasawa groups to respectively afford linear[61] and branched[62] carboxylic acid products. König *et al*. reported on a visible light photoredox/nickel catalysed reaction involving the ligand-controlled Markovnikov and anti-Markovnikov hyrdocarboxylation reaction of styrenes with atmospheric CO_2 at room temperature.[63] Additionally, difunctionalisation of olefins with CO_2 and photoredox catalysis have been reported by Yu *et al*. (thiocarboxylation reactions)[64] and Martin *et al.* (carbocarboxylation reactions).[65]

Alternative carboxylation reactions with CO_2 have been investigated with molecules containing different functional groups, such as CO_2 incorporation into alkynes. Wu *et al.* were the first group to report on the visible light driven hydrocarboxylation and carbocarboxylation of alkynes with CO_2 and an iridium/cobalt dual catalyst.[66] Following from this, Chen *et al.* described a visible light promoted metal-free approach for carboxylative cyclisation reactions of propargylic amines with CO_2 and iodine to yield *exo*-iodomethylene 2-oxazolidinones.[67] Furthermore, aryls and alkyl halides have also been reported to react with CO_2 under visible light photoredox catalysis in combination with transition metal catalysis. This was reported by Martin and Iwasawa and coworkers in their visible light driven carboxylation of aryl bromides and chlorides with CO_2 utilising a combination of $Pd(OAc)_2$ as the carboxylation catalyst and $[Ir(ppy)_2(dtbpy)]PF_6$ as a photoredox catalyst.[68]

Thus, the incorporation of CO_2 into organic moieties under the influence of visible light photoredox catalysts has proven to be an effective and versatile strategy for CO_2 utilisation. Moreover, this technique has paved a way for more sustainable organic synthetic chemistry methods and is a step closer to achieving the Green Chemistry principles.

1.6.1 Carboxylation reactions of imines to afford amino acids

As discussed in subsection 1.6 above, photoredox catalysed carboxylation reactions have shown to be a promising and diverse field in the context of CO_2 utilisation in organic synthesis. Closely following on from this, is the photoredox catalysed fixation of CO_2 to afford unnatural α-amino acids.[69-74] Unnatural amino acids play an important role in medicinal chemistry, where they act as key building blocks for complex molecules, fundamental components of peptidomimetic drugs and potential drugs on their own.[70, 75]

Recently, α,α-diaryl α-amino acids have shown to be a good source of amino acids for transamination reactions for the synthesis of bioactive nitrogen-containing compounds,[76] and these α,α-diaryl α-amino acids can be used to prepare the clinical anticonvulsant drug, phenytoin and its derivatives.[77] Furthermore, an array of other biologically active compounds can be synthesised *via* α,α-disubstituted amino acids. These include the BACE1 inhibitor which is used for treatment of Alzheimer's disease,[78] the ELA2 inhibitor which is used for obesity treatment,[79, 80] and α_{1A} receptor antagonists that are used for the treatment of hypertension and high cholesterol, are synthesised from α,α-disubstituted amino acids.[81] Figure 1.13 portrays the discussed bioactive molecules that are synthesised from α,α-disubstituted amino acids.

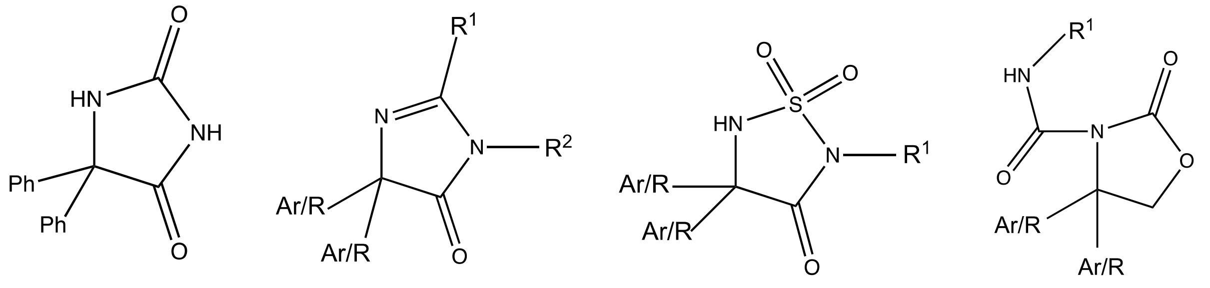

Phenytoin BACE1 inhibitor ELA2 inhibitor α_{1A} receptor antagonists

Figure 1.13. Selected bioactive molecules that are synthesised from α,α-disubstituted amino acids.

Jamison *et al*. were pioneers in the field of α-amino acid synthesis *via* CO_2 fixation, with their direct coupling of tertiary amines with CO_2 to afford α-amino acids in a continuous flow synthesis, which was mediated by >280 nm light using p-terphenyl as the organic photoredox catalyst.[82] Thereafter Yu *et al*. reported on the first selective photoredox catalysed reactions involving the hydrocarboxylation of imines and enamides with CO_2 to afford valuable α,α-disubstituted α-amino acids.[83] Here, the mechanistic rationale was that the enamide was converted to the corresponding imine (in equilibrium), which was organo-photochemically reduced by utilising the tertiary amine, DIPEA (*N,N*-diisopropylethylamine), as a sacrificial reductant to generate an α-amino carbanion, which was subsequently engaged in CO_2 trapping.[83] Shortly after these reports and pertinent to this study, is the work by Walsh and coworkers. Walsh and coworkers implemented an iridium(III) based photocatalyst that was involved in visible light/sunlight photoredox-catalysed reductive hyrdocarboxylation reactions of imines with CO_2 to afford α,α-disubstituted α-amino acids.[60] The authors proposed that the sacrificial electron donor, Cy_2Me (*N,N*-dicyclohexylmethylamine) gets oxidised to form an amine radical cation upon the reductive quenching step of the iridium(III) excited state, and this radical cation exerts a crucial role in activating imines towards single-electron reduction by the reduced iridium(II) species. The developments of all the above discussed carboxylation reactions are depicted in Figure 1.14.

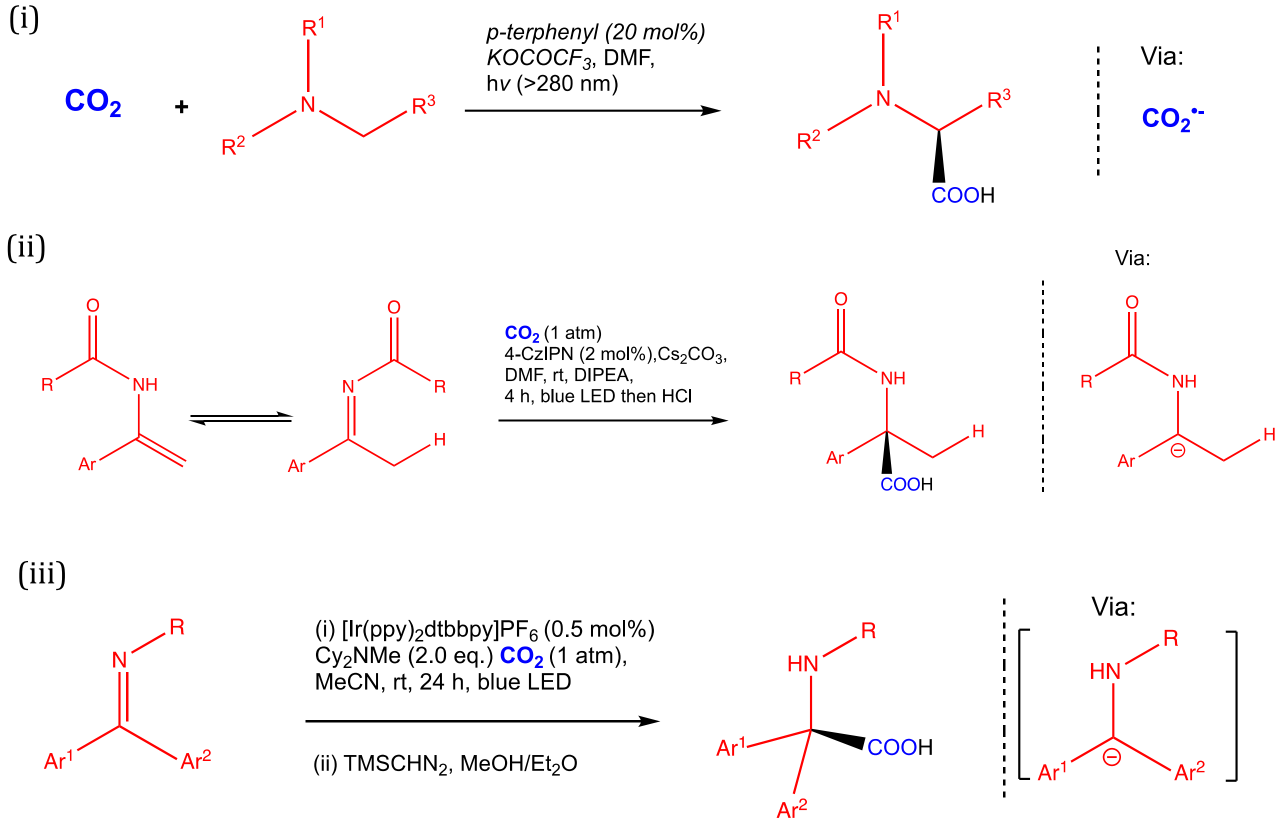

Figure 1.14. Developments of selected carboxylation reactions involved in α-amino acids synthesis. (i) Coupling of tertiary amines with CO_2 by Jamison *et al.*[82] (ii) Organo-photoredox catalysed hydrocarboxylation of imines and enamines with CO_2 by Yu *et al.*[83] (iii) Visible light photoredox catalysed hydrocarboxylation of imines, using an iridium(III) photocatalyst and CO_2 by Walsh and coworkers.[60]

An interesting observation from Figure 1.14 (ii) and (iii) is the surprisingly nucleophilic carbonyl carbon intermediates. This is due to umpolung reactivity of the imine exhibited under visible light photoredox catalysed conditions. Umpolung refers to reversal of the 'natural' polarisation of a group i.e., electrophilic sites are reversed to become nucleophilic and vice versa.[84] Figure 1.15 shows a visual representation of this phenomenon. Umpolung activity is particularly important in the development of synthetic strategies of biologically active molecules because the action of these molecules depends on the precise spatial arrangement of their atoms with biological targets.[84]

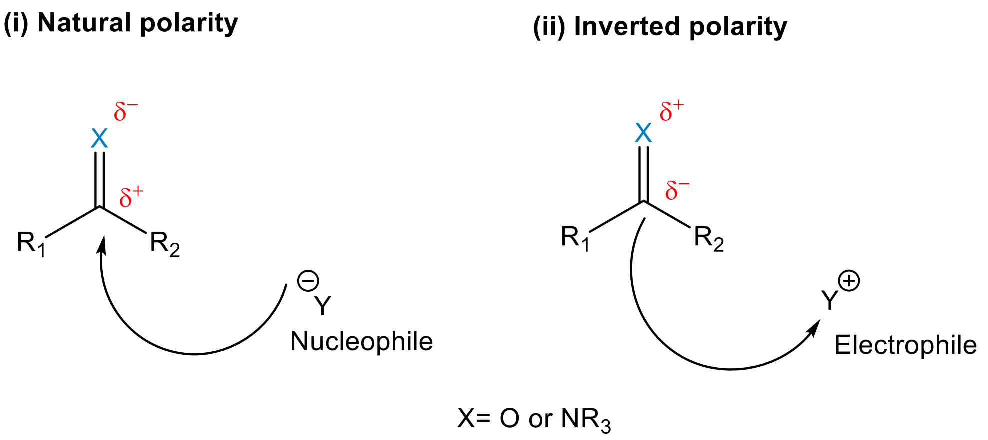

Figure 1.15. Umpolung activity exhibited by ketones and imines. Adapted from F. Romanov-Michailidis and T. Rovis.[84]

1.7 Research rationale for this study

Photoredox catalysis is an invaluable resource in the scope of Green Chemistry. It is a low-cost chemical synthetic strategy that provides a means to generate safer and more environmentally friendly synthetic routes, which can be applied to a wide range of organic transformation reactions. Polypyridyl iridium(III) complexes are renowned photosensitisers in the scope of photoredox catalysis owing to their favourable photophysical and electrochemical properties. Additionally, the photophysical and electrochemical properties of iridium(III) photosensitisers can be easily modified *via* judicious tuning of the organic ligand chelated to the iridium(III) centre. This can afford versatile iridium(III) photosensitisers with long-lived triplet photoexcited states which play an important role in an array of photochemical applications (such as photoredox catalysis).

With this in mind, in this study, a series of (*N^N* chelated) 2,2'-pyridyl-substituted benzimidazole cyclometalated iridium(III) complexes were synthesised. The rudimentary benzimidazole ligand, 2-(pyrdin-2-yl)-1*H*-benzo[*d*]imidazole was selected as the imidazole N-H allows for facile functionalisation with a variety of functional groups, which assists in tuning the photophysical properties of the iridium(III) photosensitiser.

Furthermore, this ligand framework was extended to a trinuclear iridium(III) complex as polymetallic photocatalysts have reported to exhibit enhanced photocatalytic activity in CO_2 reduction reactions, compared to their mononuclear analogues. This improved photocatalytic activity was also observed in previous work conducted in our research group, in the regioselective hydrothiolation reaction of alkenes. Thus, in this work we sought out to investigate the influence of the N^N ancillary benzimidazole ligand, as well as the effect of increasing the number of photoactive metal centres on the photocatalytic activity in a model photoredox catalysed reaction.

The proof-of-concept reaction was the visible light mediated photoredox catalysed carboxylation of ketimines utilising CO_2 to afford unnatural α-amino acids. This reaction was selected due to its green nature, employing a sustainable synthetic technology (photoredox catalysis) and utilising a high abundant waste product, CO_2. Despite the advantages offered by polymetallic complexes and the relevance of α-amino acids in the pharmaceutical industry, there are no studies (to date) that have utilised polymetallic complexes in the scope of photoredox catalysed synthesis of these important bioactive molecules. Thus, the rationale behind this study was to develop efficient and versatile iridium(III) photosensitisers and in doing so, evaluate the potential of cyclometalated benzimidazole iridium(III) complexes as photoredox catalysts. Finally, this research also aligns with the United Nations Sustainable Development goals, goal 13 (Climate Action, Figure 1.16).[85]

Figure 1.16 United Nations seventeen Sustainable Development Goals.[85]

1.8 Overall aim and specific objectives

1.8.1 Overall aim

The overall aim of this study was to synthesise and fully characterise iridium(III) polypyridyl photosensitisers containing a *N^N*-benzimidazole ancillary ligand. These photosensitisers were evaluated in the context of the visible light mediated photoredox catalysed carboxylation reaction of ketimines using CO_2.

1.8.2 Specific objectives

(a) To synthesise the basis benzimidazole ligand, **L1.**

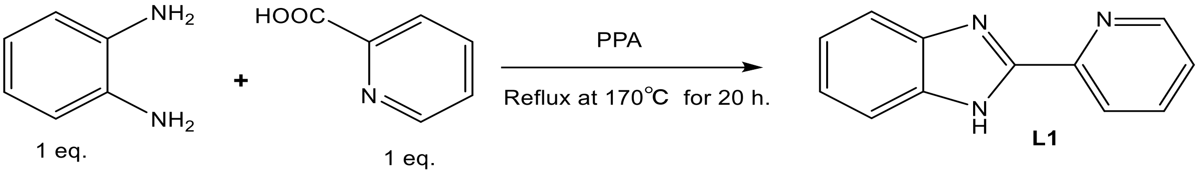

Scheme 1.1. Outline for the synthesis of the benzimidazole ligand, **L1** (2-(pyridin-2-yl)-1*H*-benzo[*d*]imidazole).

(b) To synthesise the monomeric benzimidazole functionalised ligand, **L2.**

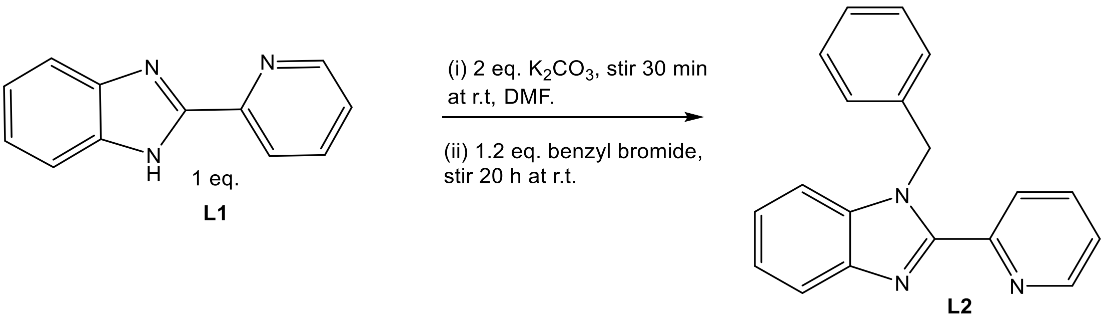

Scheme 1.2. Outline for the synthesis of the monomeric functionalised benzimidazole ligand, **L2** (1-benzyl-2-(pyridin-2-yl)-1*H*-benzo[*d*]imidazole).

(c) To synthesise the trimeric benzimidazole functionalised ligand, **L3**.

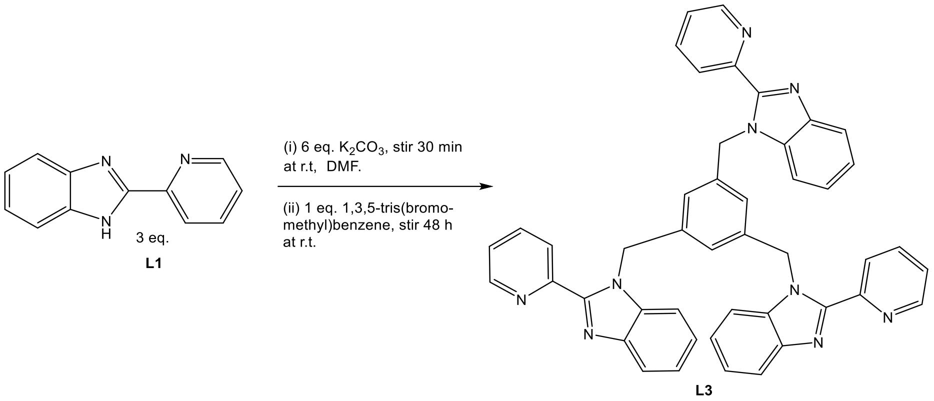

Scheme 1.3. Outline for the synthesis of the trimeric functionalised benzimidazole ligand, **L3** (1,3,5-tris((2-(pyridin-2-yl)-1*H*-benzo[*d*]imidazol-1-yl)methyl)-benzene).

(d) To synthesise the chloro-bridged iridium dimer, $[Ir(ppy)_2(\mu\text{-}Cl)]_2$.

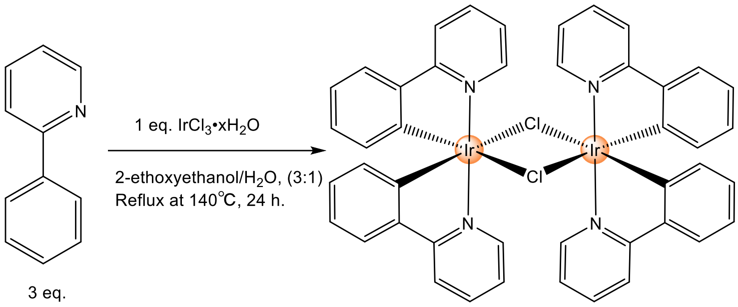

Scheme 1.4. Outline for the synthesis of the iridium dimer, $[Ir(ppy)_2(\mu\text{-}Cl)]_2$.

(e) To synthesise the mononuclear iridium(III) complex, **C1**.

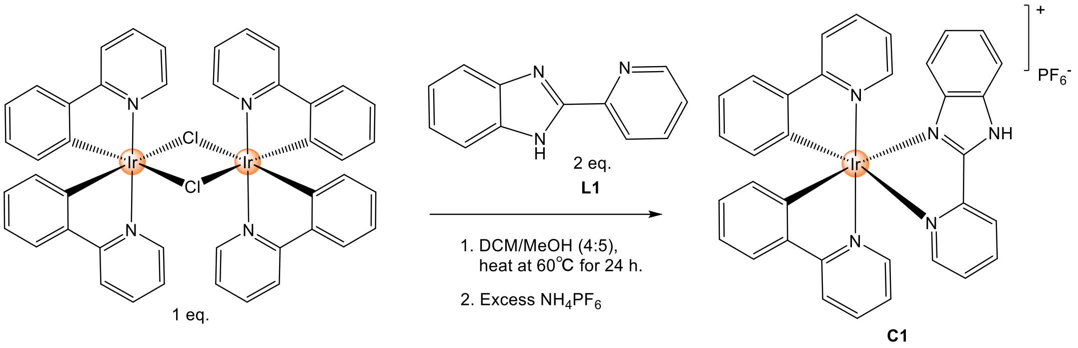

Scheme 1.5. Outline for the synthesis of the cationic iridium(III) 2-(pyridin-2-yl)-1*H*-benzo[*d*]imidazole complex, **C1.**

(f) To synthesise the new benzyl-functionalised iridium(III) complex, **C2**.

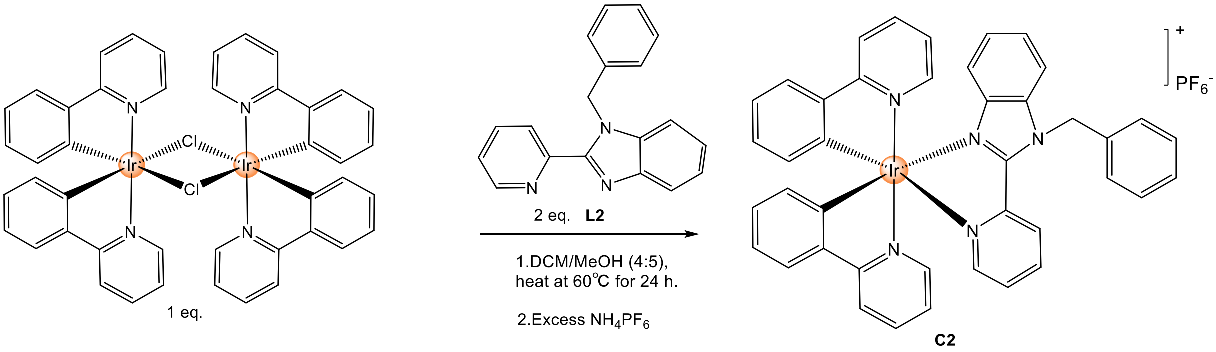

Scheme 1.6. Outline for the synthesis of the cationic iridium(III) 1-benzyl-2-(pyridin-2-yl)-1*H*-benzo[*d*]imidazole complex, **C2.**

(g) To synthesise the new trinuclear iridium(III) complex, **C3**.

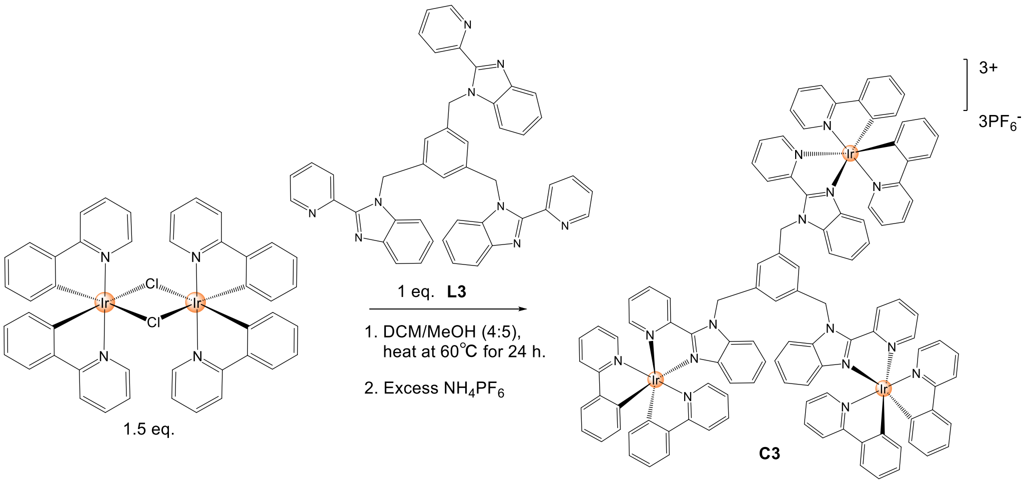

Scheme 1.7. Outline for the synthesis of the cationic trinuclear iridium(III) 1,3,5-tris((2-(pyridin-2-yl)-1*H*-benzo[*d*]imidazol-1-yl)methyl)benzene complex, **C3**.

(h) To characterise these synthesised ligands (**L1**-**L3**) and iridium(III) complexes (**C1**-**C3**) using an array of analytical and spectroscopic techniques including: ^{1}H and ^{13}C{^{1}H} Nuclear Magnetic Resonance (NMR) spectroscopy, Fourier-Transformed Infrared (FT-IR) spectroscopy, Electrospray Ionisation Mass Spectrometry (ESI-MS), Melting Point and Elemental Analysis (EA). Single crystal X-ray diffraction (XRD) analysis was also used to provide further insight to the structure of one of the synthesised compounds (**C2**).

(i) To evaluate the photophysical properties (UV-vis absorption and emission studies) of the on the iridium complexes (**C1**-**C3**) to see the effects of ligand-modified substituents on the photophysical properties of these complexes, as well as to determine a suitable excitation wavelength for the photoredox catalysis.

(j) To investigate the electrochemical properties of the iridium(III) complexes (**C1**-**C3**) by cyclic voltammetry and differential pulse voltammetry for complex (**C3**).

(k) To synthesise and characterise the ketimine precursors, **K1** and **K2**.

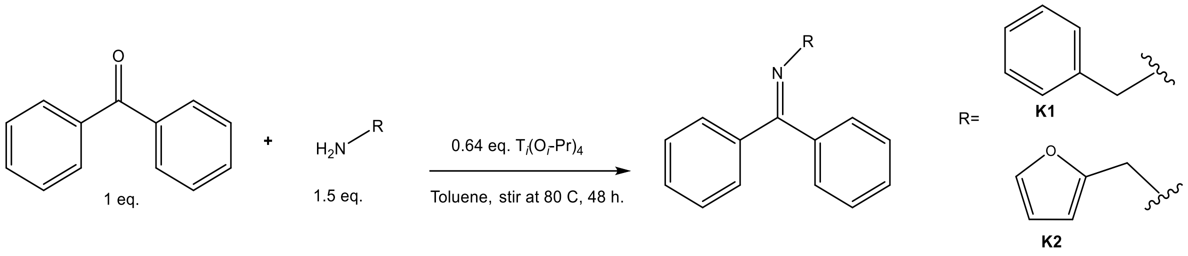

Scheme 1.8. Synthetic outline for the ketimine precursors, **K1** and **K2**.

(l) To evaluate the synthesised iridium(III) complexes (**C1-C3**) as photosensitisers for visible light mediated photoredox catalysed carboxylations of ketimines using CO_2, as a proof of concept reaction.

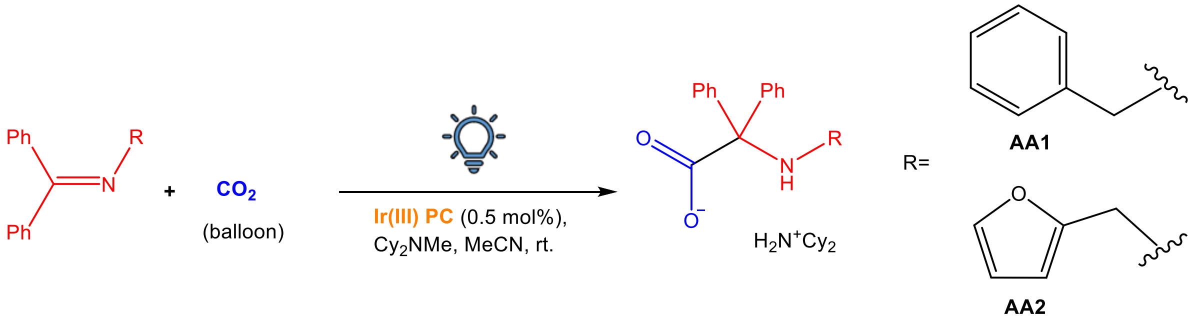

Scheme 1.9. Visible light mediated photoredox catalysed carboxylations of ketimines utilising CO_2.

1.9 References

1. R. A. Sheldon, I. ; Hanefeld, U., in *Green Chemistry and Catalysis*, 2007, pp. 1-47.
2. P. T. Anastas and J. C. Warner, *Green Chemistry: Theory and Practice*, Oxford University Press, 1998.
3. R. Noyori, *Nat. Chem.*, 2009, **1**, 5-6.
4. S. H. A. M. Leenders, R. Gramage-Doria, B. de Bruin and J. N. H. Reek, *Chem. Soc. Rev.*, 2015, **44**, 433-448.
5. C. C. Johansson Seechurn, M. O. Kitching, T. J. Colacot and V. Snieckus, *Angew. Chem. Int. Ed.*, 2012, **51**, 5062-5085.
6. L. C. Matsinha, S. Siangwata, G. S. Smith and B. C. E. Makhubela, *Catal. Rev.*, 2019, **61**, 111-133.
7. B. Zhao, R. Shang, G.-Z. Wang, S. Wang, H. Chen and Y. Fu, *ACS Catal.*, 2020, **10**, 1334-1343.
8. G. E. M. Crisenza and P. Melchiorre, *Nat. Commun.*, 2020, **11**, 803.
9. T. M. Monos and C. R. J. Stephenson, in *Iridium(III) in Optoelectronic and Photonics Applications*, John Wiley & Sons Inc., Chichester, West Sussex, 2017, pp. 541-581.
10. M. H. Shaw, J. Twilton and D. W. C. MacMillan, *J. Org. Chem.*, 2016, **81**, 6898-6926.
11. T. P. Nicholls, D. Leonori and A. C. Bissember, *Nat. Prod. Rep.*, 2016, **33**, 1248-1254.
12. R. O. Reithmeier, S. Meister, A. Siebel and B. Rieger, *Dalton Trans.*, 2015, **44**, 6466-6472.
13. L. L. Zhang, Y. Gao, Z. Liu, X. Ding, Z. Yu and L. C. Sun, *Dalton Trans.*, 2016, **45**, 3814-3819.
14. D. M. Arias-Rotondo and J. K. McCusker, in *Visible Light Photocatalysis in Organic Chemistry*, Wiley-VCH, 2018, pp. 1-24.
15. T. M. Suzuki, H. Tanaka, T. Morikawa, M. Iwaki, S. Sato, S. Saeki, M. Inoue, T. Kajino and T. Motohiro, *Chem. Commun.*, 2011, **47**, 8673-8675.
16. S. Sato, T. Arai, T. Morikawa, K. Uemura, T. M. Suzuki, H. Tanaka and T. Kajino, *J. Am. Chem. Soc.*, 2011, **133**, 15240-15243.
17. S. Sato, T. Morikawa, S. Saeki, T. Kajino and T. Motohiro, *Angew. Chem. Int. Ed.*, 2010, **49**, 5101-5105.
18. B. M. Hockin, C. Li, N. Robertson and E. Zysman-Colman, *Catal. Sci. Technol.* , 2019, **9**, 889-915.

19. D. A. Nicewicz and D. W. MacMillan, *Science*, 2008, **322**, 77-80.
20. M. A. Ischay, M. E. Anzovino, J. Du and T. P. Yoon, *J. Am. Chem. Soc.*, 2008, **130**, 12886-12887.
21. C. K. Prier, D. A. Rankic and D. W. C. MacMillan, *Chem. Rev.*, 2013, **113**, 5322-5363.
22. A. Gualandi, M. Marchini, L. Mengozzi, M. Natali, M. Lucarini, P. Ceroni and P. G. Cozzi, *ACS Catal.*, 2015, **5**, 5927-5931.
23. N. Sinha, C. Wegeberg, D. Häussinger, A. Prescimone and O. S. Wenger, *Nat. Chem.*, 2023.
24. N. Sutin and C. Creutz, *Pure Appl. Chem.*, 1980, **52**, 2717-2738.
25. V. Alvarez, J. Agramunt, M. Ball, M. Batallé, J. Bayarri, F. I. G. M. Borges, H. Bolink, H. Brine, S. Cárcel, J. Carmona, J. F. Castel, J. Catalá, S. Cebrián, A. Cervera, D. Chan, C. Conde, T. Dafni, T. Dias, J. Díaz and N. Yahlali, *J. Instrum.*, 2012, **7**, P02010.
26. M. Omary and H. H. Patterson, in *Luminescence Theory*, 2016, pp. 636-653.
27. M. Montalti, A. Credi, L. Prodi and M. T. Gandolfi, 2006.
28. L. Flamigni, A. Barbieri, C. Sabatini, B. Ventura and F. Barigelletti, in *Photochemistry and Photophysics of Coordination Compounds II*, eds. V., Springer Berlin, Heidelberg, 2007, pp. 143-203.
29. O. J. Stacey and S. J. A. Pope, *RSC Advances*, 2013, **3**, 25550-25564.
30. K. Zeitler, *Angew. Chem. Int. Ed.*, 2009, **48**, 9785-9789.
31. J. D. Slinker, A. A. Gorodetsky, M. S. Lowry, J. Wang, S. Parker, R. Rohl, S. Bernhard and G. G. Malliaras, *J. Am. Chem. Soc.*, 2004, **126**, 2763-2767.
32. M. S. Lowry, J. I. Goldsmith, J. D. Slinker, R. Rohl, R. A. Pascal, G. G. Malliaras and S. Bernhard, *Chem. Mater.*, 2005, **17**, 5712-5719.
33. S. Trofimenko, *ChemInform*, 1973, **4**.
34. I. N. Mills, J. A. Porras and S. Bernhard, *Acc. Chem. Res.*, 2018, **51**, 352-364.
35. S. Sprouse, K. A. King, P. J. Spellane and R. J. Watts, *J. Am. Chem. Soc.*, 1984, **106**, 6647-6653.
36. F. Monti, A. Baschieri, L. Sambri and N. Armaroli, *Acc. Chem. Res.*, 2021, **54**, 1492-1505.
37. Y. You and W. Nam, *Chem. Soc. Rev.*, 2012, **41**, 7061-7084.
38. M. H. Shaw, J. Twilton and D. W. C. MacMillan, *J. Org. Chem.*, 2016, **81**, 6898 - 6926.
39. K. Shah, S. Chhabra, S. K. Shrivastava and P. Mishra, *Med. Chem. Res.* , 2013, **22**, 5077-5104.

40. M. Gaba and C. Mohan, *Med. Chem. Res.* , 2016, **25**, 173-210.
41. I. Echevarría, M. Vaquero, B. R. Manzano, F. A. Jalón, R. Quesada and G. Espino, *Inorg. Chem.*, 2022, **61**, 6193-6208.
42. M. Martínez-Alonso, J. Cerdá, C. Momblona, A. Pertegás, J. M. Junquera-Hernández, A. Heras, A. M. Rodríguez, G. Espino, H. Bolink and E. Ortí, *Inorg. Chem.*, 2017, **56**, 10298-10310.
43. C. D. Sunesh, G. Mathai and Y. Choe, *ACS Appl. Mater. Interfaces*, 2014, **6**, 17416-17425.
44. E. Zafon, I. Echevarría, S. Barrabés, B. R. Manzano, F. A. Jalón, A. M. Rodríguez, A. Massaguer and G. Espino, *Dalton Trans.*, 2022, **51**, 111-128.
45. M. Sun, C. Wang, C.-Y. Sun, M. Zhang, X.-L. Wang and Z.-M. Su, *J. Catal.*, 2020, **385**, 70-75.
46. Y. Tamaki and O. Ishitani, *ACS Catal.*, 2017, **7**, 3394-3409.
47. A. M. Cancelliere, F. Puntoriero, S. Serroni, S. Campagna, Y. Tamaki, D. Saito and O. Ishitani, *Chem. Sci.*, 2020, **11**, 1556-1563.
48. Y. Tamaki, K. Watanabe, K. Koike, H. Inoue, T. Morimoto and O. Ishitani, *Faraday Discuss.*, 2012, **155**, 115-127.
49. H. Takeda, K. Koike, H. Inoue and O. Ishitani, *J. Am. Chem. Soc.*, 2008, **130**, 2023-2031.
50. C. He, S. Yu, S. Ma and F. Cheng, *Transit. Met. Chem.*, 2019, **44**, 515-524.
51. N. M. Motimani, S. Ngubane and G. S. Smith, *Polyhedron*, 2022, **212**, 115616.
52. Z. Liu, Z. Deng, S. J. Davis, C. Giron and P. Ciais, *Nat. Rev. Earth Environ.*, 2022, **3**, 217-219.
53. T. F. Stocker, D. Qin, G.-K. Plattner, M. Tignor, S. K. Allen, J. Boschung, A. Nauels, Y. Xia, V. Bex and P. M. Midgle, *Contribution of Working Group I to the Fifth Assessment Report of the Intergovernmental Panel on Climate Change.* Cambridge University Press, Cambridge, United Kingdom and New York, NY, USA.
54. D.-G. Yu and L.-N. He, *Green Chem.*, 2021, **23**, 3499-3501.
55. D. M. Reiner, *Nat. Energy*, 2016, **1**, 15011.
56. M. He, Y. Sun and B. Han, *Angew. Chem. Int. Ed.*, 2013, **52**, 9620-9633.
57. T. Sakakura, J.-C. Choi and H. Yasuda, *Chem. Rev.*, 2007, **107**, 2365-2387.
58. T. Baran, A. Dibenedetto, M. Aresta, K. KruczaBa and W. Macyk, *ChemPlusChem*, 2014, **79**, 708-715.

59. S. Pradhan, S. Roy, B. Sahoo and I. Chatterjee, *Chemistry*, 2021, **27**, 2254-2269.
60. X. Fan, X. Gong, M. Ma, R. Wang and P. J. Walsh, *Nat. Commun.*, 2018, **9**, 4936.
61. H. Seo, A. Liu and T. F. Jamison, *J. Am. Chem. Soc.*, 2017, **139**, 13969-13972.
62. K. Murata, N. Numasawa, K. Shimomaki, J. Takaya and N. Iwasawa, *Chem. Commun.*, 2017, **53**, 3098-3101.
63. Q.-Y. Meng, S. Wang, G. S. Huff and B. König, *J. Am. Chem. Soc.*, 2018, **140**, 3198-3201.
64. J. H. Ye, M. Miao, H. Huang, S. S. Yan, Z. B. Yin, W. J. Zhou and D. G. Yu, *Angew. Chem. Int. Ed.*, 2017, **56**, 15416-15420.
65. V. R. Yatham, Y. Shen and R. Martin, *Angew. Chem. Int. Ed.*, 2017, **56**, 10915-10919.
66. J. Hou, A. Ee, W. Feng, J.-H. Xu, Y. Zhao and J. Wu, *J. Am. Chem. Soc.*, 2018, **140**, 5257-5263.
67. X. He, X.-Y. Yao, K.-H. Chen and L.-N. He, *ChemSusChem*, 2019, **12**, 5081-5085.
68. K. Shimomaki, K. Murata, R. Martin and N. Iwasawa, *J. Am. Chem. Soc.*, 2017, **139**, 9467-9470.
69. L. Wang, A. Brock, B. Herberich and P. G. Schultz, *Science*, 2001, **292**, 498-500.
70. M. A. T. Blaskovich, *J. Med. Chem.*, 2016, **59**, 10807-10836.
71. X. Fan, Y. Ge, F. Lin, Y. Yang, G. Zhang, W. S. Ngai, Z. Lin, S. Zheng, J. Wang, J. Zhao, J. Li and P. R. Chen, *Angew. Chem. Int. Ed.*, 2016, **55**, 14046-14050.
72. Y. Ge, X. Fan and P. R. Chen, *Chem. Sci.*, 2016, **7**, 7055-7060.
73. D. F. Kreitler, D. E. Mortenson, K. T. Forest and S. H. Gellman, *J. Am. Chem. Soc.*, 2016, **138**, 6498-6505.
74. M. Jewginski, T. Granier, B. Langlois d'Estaintot, L. Fischer, C. D. Mackereth and I. Huc, *J. Am. Chem. Soc.*, 2017, **139**, 2928-2931.
75. T. Narancic, S. A. Almahboub and K. E. O'Connor, *World J. Microbiol. Biotechnol.*, 2019, **35**, 67.
76. Y. E. Liu, Z. Lu, B. Li, J. Tian, F. Liu, J. Zhao, C. Hou, Y. Li, L. Niu and B. Zhao, *J. Am. Chem. Soc.*, 2016, **138**, 10730-10733.
77. L. Konnert, B. Reneaud, R. M. de Figueiredo, J.-M. Campagne, F. Lamaty, J. Martinez and E. Colacino, *J. Org. Chem.*, 2014, **79**, 10132-10142.
78. https://patents.google.com/patent/US20080287460A1/en, (accessed 8 February 2022).

79. W. C. Groutas, R. Z. Kuang and R. Venkataraman, *Biochem. Biophys. Res. Commun.*, 1994, **198**, 341-349.
80. Z. Xiao and J. W. Timberlake, *J. Heterocycl. Chem.*, 2000, **37**, 773-777.
81. https://patents.google.com/patent/US6159990A/en, (acessed 8 February 2022).
82. H. Seo, M. H. Katcher and T. F. Jamison, *Nat. Chem.*, 2017, **9**, 453-456.
83. T. Ju, Q. Fu, J. H. Ye, Z. Zhang, L. L. Liao, S. S. Yan, X. Y. Tian, S. P. Luo, J. Li and D. G. Yu, *Angew. Chem. Int. Ed.*, 2018, **57**, 13897-13901.
84. F. Romanov-Michailidis and T. Rovis, *Nature*, 2015, **523**, 417-418.
85. https://sdgs.un.org/goals, (accessed 12 September, 2023).

Chapter 2: Synthesis and characterisation of the benzimidazole ligands and their corresponding iridium(III) photosensitisers

2.1 Introduction

Synthetic modification of the benzimidazole scaffold at the 2-position (Figure 2.1) with pyridine affords a bidentate ligand (2,2'-pyridyl motif) that can be *N^N* chelated to a metal centre. The focus of this study are cyclometalated iridium(III) complexes that possess the 2,2'-pyridylbenzimidazole motif as an *N^N* chelated ancillary ligand. These complexes have applications in an array of photochemistry related fields including light emitting electrochemical devices (LECs),[1,2] photodynamic therapy (PDT)[3] and notably, photocatalysis.[4] The reactive N-H bond on the imidazole portion of the benzimidazole scaffold allows for facile functionalisation with a variety of functional groups. Additionally, many benzimidazole-based ligands are commercially available or quite easily synthesised, which affords a great deal of structural and chemical diversity. The significance of ease of modification of the benzimidazole ligand is particularly important in the context of photosensitiser design, as this allows one to easily modify the photophysical, electrochemical and photocatalytic properties of the photosensitiser.[4]

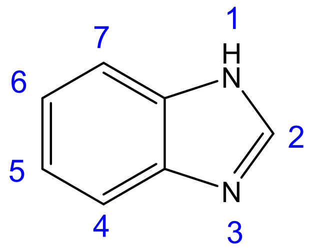

Figure 2.1. Structure of 1*H*-benzimidazole.

Following on from the above, heteroleptic cationic d^6 iridium(III) complexes possessing two *C^N* cyclometalated ligands and a *N^N* diimine ancillary ligand (Figure 2.2(i)) are prominent complexes in the scope of photochemical applications.

This is due to their modular synthesis and enhanced ligand field effects, which are a result of strong σ-donation from the cyclometalated carbon atoms. Strong spin-orbit coupling (SOC) of the iridium(III) centre results in almost unitary intersystem crossing (ISC) to the triplet state, which results in relatively long-lived triplet photoexcited states.[5-7] Furthermore, judicious tuning of the frontier molecular orbitals can be achieved by varying the functional groups on either the *C^N* or *N^N* ligands.[8] The HOMO is localised on the *d* orbitals of the iridium(III) centre and the cyclometalated ligands, whereas the LUMO is centred on the *N^N* chelated ancillary ligand.[6, 7, 9] Accordingly, introducing electron-withdrawing or electron-donating substituents on either the *C^N* or *N^N* ligands can respectively either stabilise or destabilise the corresponding molecular orbital energy levels (Figure 2.2(ii)).[10] Hence, heteroleptic cyclometalated iridium(III) complexes with a diimine ancillary ligand, provide the ideal environment to design an array of ligands with specifically modified electronic properties. This, in turn could aid in improving the efficiency of these complexes as photoredox catalysts.[6]

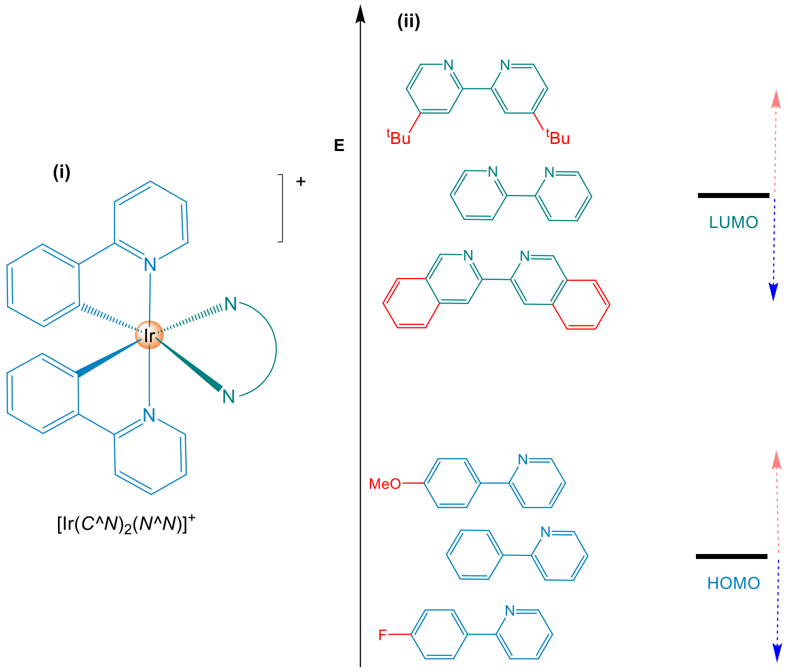

Figure 2.2. (i) Archetypical heteroleptic cationic iridium(III) complexes bearing *C^N* cyclometalated ligands and a *N^N* diimine ancillary ligand. (ii) Ligand modification allows independent tuning of the HOMO and LUMO energy levels. Dashed light-red arrows correspond to a raise in energy level and dashed blue arrows, a decrease in energy.[9, 11]

Thus, this chapter delves into the synthesis and spectroscopic characterisation of a series of benzimidazole ligands and their corresponding mononuclear and trinuclear iridium(III) complexes. A trinuclear iridium(III) benzimidazole complex was synthesised as polymetallic complexes have been reported to exhibit enhanced photocatalytic activity over their mononuclear congeners.[12-14] This is attributed to the enhanced photostability and redox properties observed for these polymetallic complexes.[12-14]

2.2 Synthesis and characterisation of 2-(pyridin-2-yl)-1*H*-benzo[*d*]imidazole (L1)

Scheme 2.1 depicts the synthetic outline for the basis benzimidazole ligand, 2-(pyridin-2-yl)-1*H*-benzo[*d*]imidazole (**L1**). **L1** was successfully synthesised by reacting *o*-phenylenediamine with 2-pyridinecarboxylic acid in the presence of polyphosphoric acid (PPA), which acted as an acid catalyst for the reaction.[15, 16] Ligand **L1** was obtained as a beige powder in a high yield of 95%. The proposed mechanism for the reaction is shown in Scheme 2.2.[17]

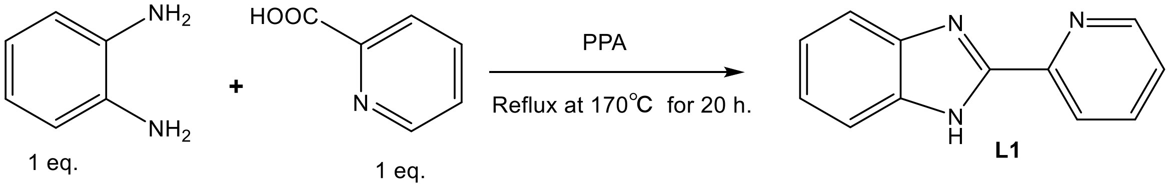

Scheme 2.1. Outline for the synthesis of the basis benzimidazole ligand, **L1**.

The reaction is initiated by a nucleophilic attack by one of the primary nitrogens of *o*-phenylenediamine at the electrophilic carbonyl centre of 2-pyridinecarboxylic acid. Here, PPA is postulated to be involved in protonating the carbonyl oxygen which increases the electrophilicity at the carbonyl centre, rendering the carbonyl carbon more susceptible to nucleophilic attack. A proton transfer (P.T.) occurs, whereby one of the adjacent hydroxyl groups accepts a proton from the positively charged $R_2N^+H_2$ group. This step is followed by the loss of the first water molecule to form an iminium species. An intramolecular nucleophilic attack then occurs, which is initiated by the lone electron pair of the other primary amine present in *o*-phenylenediamine.

A proton transfer occurs, whereby a proton is transferred from the newly formed $R_2N^+H_2$ moiety to the remaining hydroxyl group. Subsequently, the second molecule of water is lost to form the protonated benzimidazole species. The first step of the work-up procedure involves neutralising the reaction mixture with a 10% K_2CO_3 solution, which would quench the PPA as well as afford the final neutral benzimidazole product, ligand **L1**.

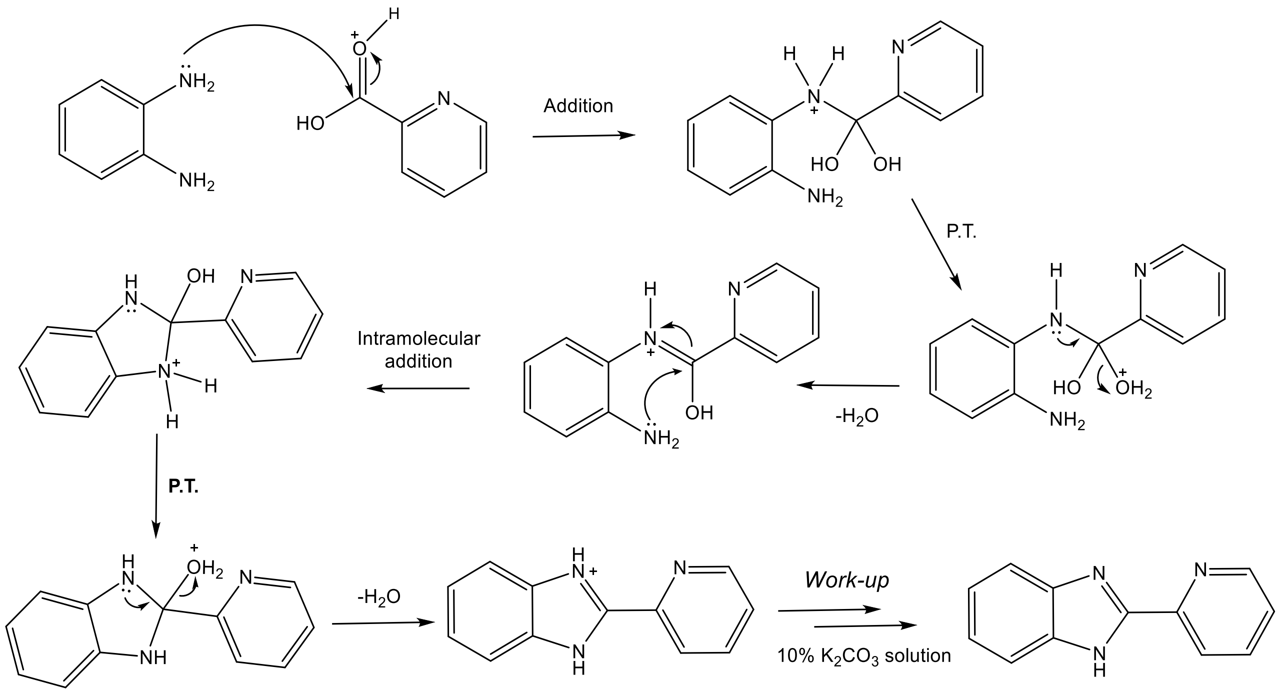

Scheme 2.2. Proposed mechanism for the cyclisation-condensation reaction for the formation of the basis benzimidazole ligand, **L1.**

Analysis of the ^{1}H NMR spectrum depicted in Figure 2.3 confirms the successful synthesis of the ligand, **L1**. The most downfield doublet at 8.73 ppm, is assigned to proton H_1, due to the carbon on which H_1 is attached being directly bonded to an electron-withdrawing nitrogen. Proton H_3, which is *para* to the pyridine nitrogen, occurs more downfield than proton H_2 (*meta* position) due to the nature of the pyridine ring. That is, pyridine is a π-deficient heteroaromatic system, where the lone pair of electrons on the nitrogen atom is orthogonal to the π-system (Figure 2.4).

Consequently, the lone pair cannot be delocalised into the ring, resulting in the *ortho* and *para* positions (relative to the nitrogen) in a pyridine ring being electron poor sites (Figure 2.4). Protons H_8 and H_{11} are assigned to the multiplet integrating for two protons, occurring more downfield than protons H_9 and H_{10}, due to H_8 and H_{11} being in a closer proximity to the two nitrogens of the imidazole ring. The appearance of the multiplet observed for protons H_8/H_{11} and the doublet of doublets corresponding to protons H_9/H_{10} is attributed to the unsymmetrical nature of the benzimidazole ligand, which is reflected in the splitting pattern. Furthermore, integration over the aromatic region of Figure 2.3 collectively integrates to the expected number of protons, and the ^{1}H NMR data is in agreement with what has been reported in literature.[15]

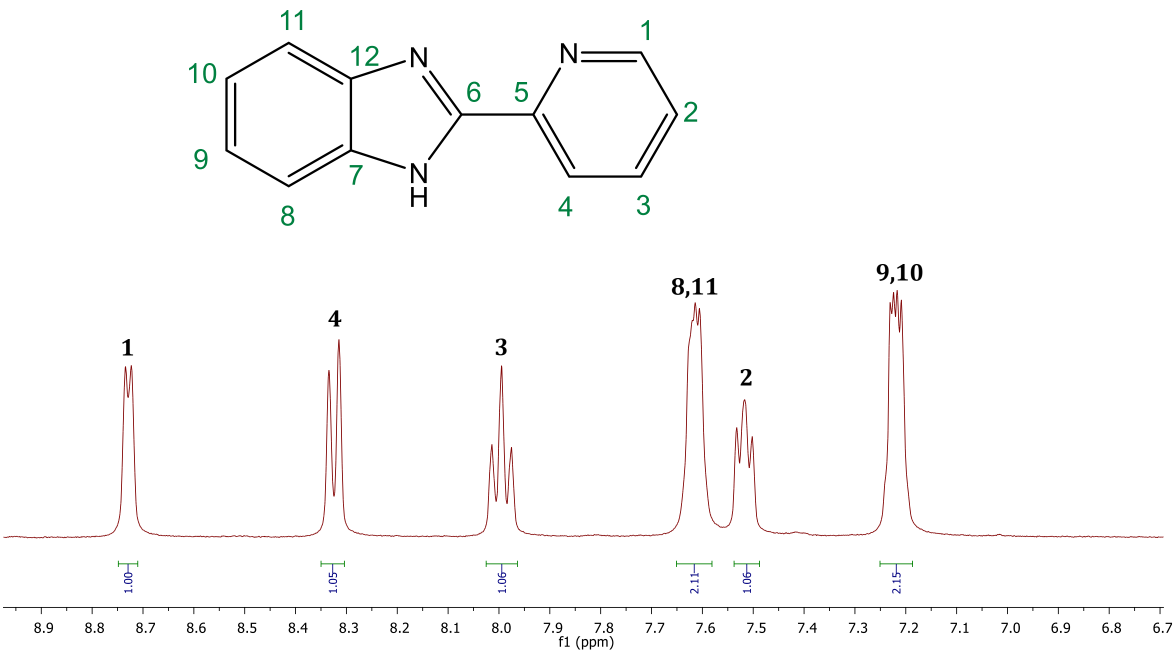

Figure 2.3. ^{1}H NMR spectrum over the aromatic region of ligand **L1**, in DMSO-d_6.

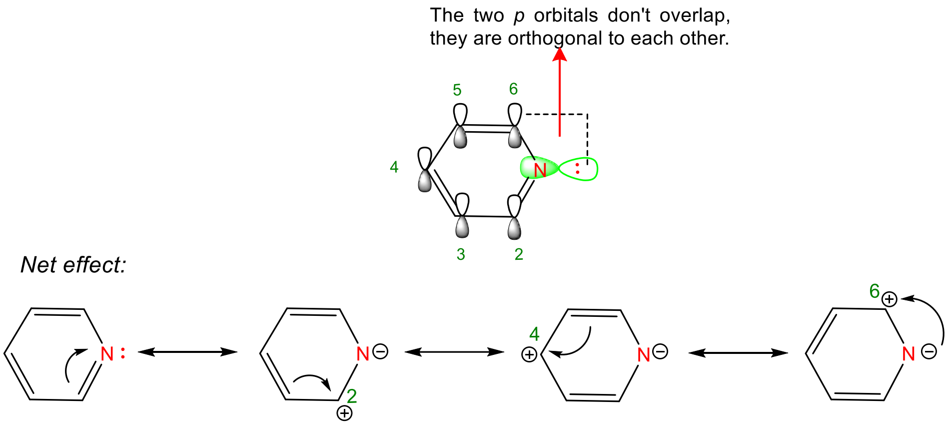

Figure 2.4. Resonance contributors for π-deficient heteroaromatic rings, such as pyridine. The *ortho* (2,6) and *para* (4) positions possess reduced electron density.

The infrared spectrum presented in Figure 2.5 further corroborates the successful synthesis of the ligand (**L1**). The characteristic N-H stretching frequency is observed at 3042 cm^{-1}, corresponding to the amine present in the imidazole ring of ligand **L1**. Additionally, C=N stretching occurs at 1590 cm^{-1} and 1444 cm^{-1}, which correspond to the imine and the 2-pyridyl moieties, respectively, in ligand **L1**. The infrared data is in agreement with literature.[15]

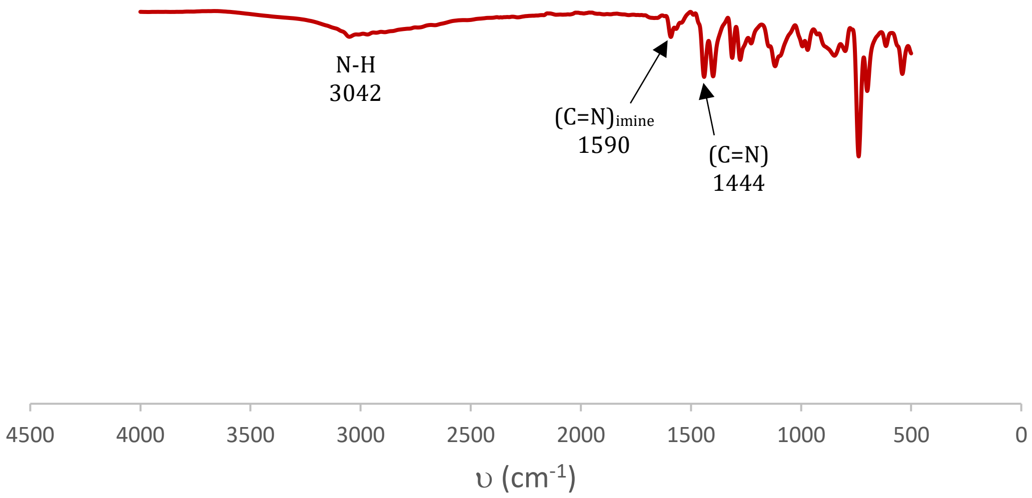

Figure 2.5. Infrared spectrum of ligand **L1**.

2.3 Synthesis and characterisation of 1-benzyl-2-(pyridin-2-yl)-1*H* benzo[*d*]imidazole (L2)

The monomeric functionalised benzimidazole ligand, 1-benzyl-2-(pyridin-2-yl)-1*H*-benzo[*d*]imidazole (**L2**) was synthesised in a one-pot, two-step N-alkylation reaction as presented in Scheme 2.3.[18] The first step involves the deprotonation of the amine nitrogen in the imidazole ring of 2-(pyridin-2-yl)-1*H*-benzo[*d*]imidazole using excess K_2CO_3. Following deprotonation, a proposed S_N2 reaction with benzyl bromide occurred which resulted in the formation of the appropriate benzyl-substituted benzimidazole ligand, **L2** as a reddish-brown solid in a good yield of 77%. Furthermore, excess K_2CO_3 was used as it has been reported to assist in the nucleophilic substitution reaction that takes place after the addition of benzyl bromide.[19]

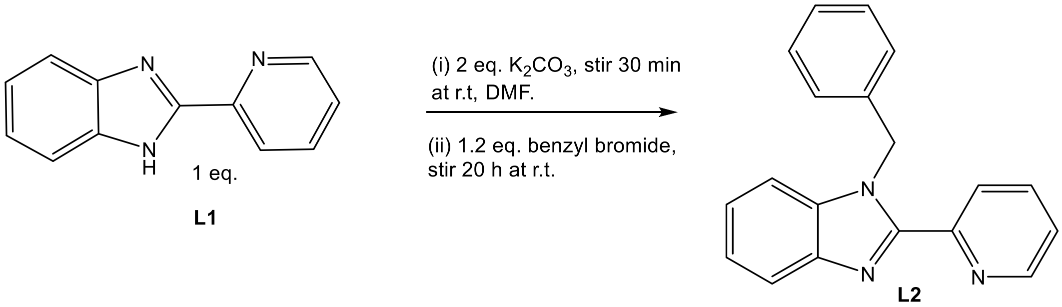

Scheme 2.3. Outline for the synthesis of the monomeric benzyl-functionalised benzimidazole ligand, **L2**.

The ^1H NMR spectrum presented in Figure 2.6(b) attests to the successful synthesis of ligand (**L2**). The diagnostic singlet (H_{13}) at 6.22 ppm, integrating for two protons is assigned to the methylene protons and thus confirms a successful N-alkylation reaction. The aromatic region was assigned using the appropriate multiplicities of each signal as well as taking the ^1H NMR spectrum of the precursor ligand, (**L1**) into account. Proton assignments were confirmed *via* 2D COSY NMR experiments (Figure A7). Furthermore, the aromatic region integrates for the expected 13 protons and the ^1H NMR data correlates with reported literature.[18]

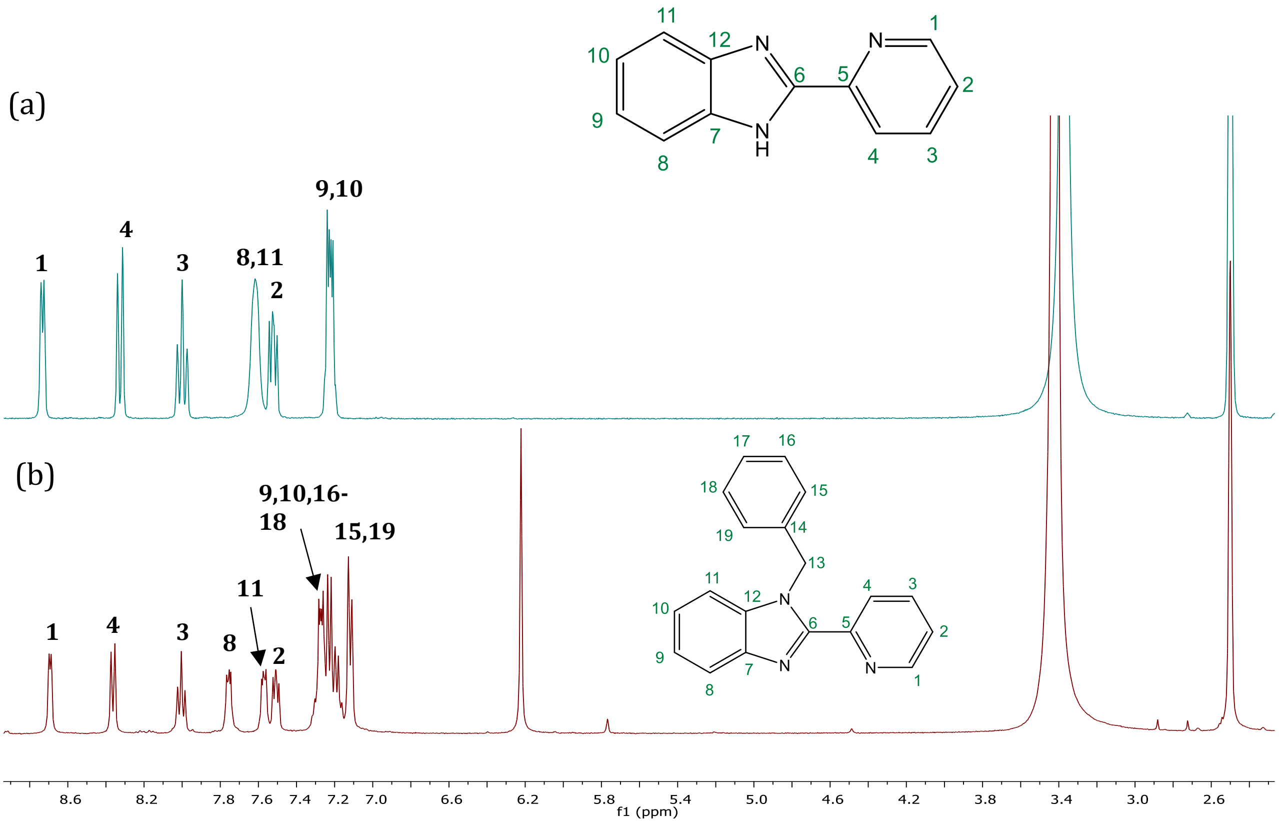

Figure 2.6. Stacked ^{1}H NMR spectra of (a) ligand **L1** and (b) ligand **L2**, in DMSO-d_6.

The stacked infrared spectra depicted in Figure 2.7 reveals the characteristic C=N bands for the imine and pyridyl moieties for ligand **L2**, at 1584 cm^{-1} and 1438 cm^{-1}, respectively. Moreover, Figure 2.7 provides additional evidence to support the successful N-alkylation. That is, the characteristic broad N-H stretching frequency observed for the precursor ligand (**L1**) at 3042 cm^{-1}, is no longer present in the infrared spectrum of ligand **L2**.

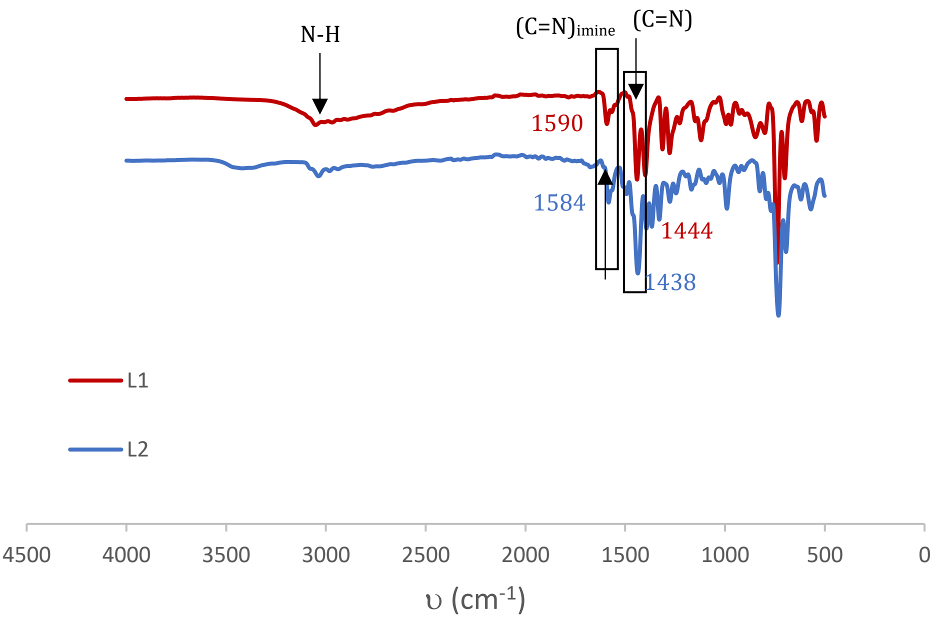

Figure 2.7. Stacked infrared spectra of compounds **L1** and **L2.**

2.4 Synthesis and characterisation of 1,3,5-tris((2-(pyridin-2-yl)-1*H*-benzo[*d*]imidazol-1-yl)methyl)benzene (L3)

The outline for the synthesis of the trimeric functionalised benzimidazole ligand, 1,3,5-tris((2-(pyridin-2-yl)-1*H*-benzo[*d*]imidazol-1-yl)methyl)benzene (**L3**) is illustrated in Scheme 2.4. This ligand was synthesised in an analogous manner to the monomeric ligand **L2**, but using 1,3,5-tris(bromomethyl)benzene as the alkyl halide in place of benzyl bromide. Ligand **L3** was obtained as white flakes, in a moderate yield of 59%, following a column chromatography purification step (eluent: 100% EtOAc).

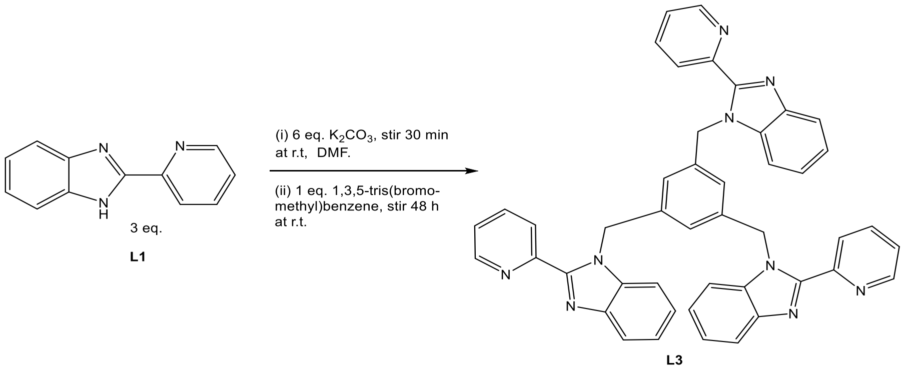

Scheme 2.4. Outline for the synthesis of the trimeric functionalised benzimidazole ligand, **L3.**

Analysis of the ^{1}H NMR spectrum depicted in Figure 2.8 supports the successful synthesis of ligand **L3**. The two diagnostic singlets occurring at 6.93 ppm (H_{15}) and 5.92 ppm (H_{13}), integrating for three and six protons respectively, confirms a successful N-alkylation with 1,3,5-tris(bromomethyl)benzene. The proton assignments for ligand **L3** as depicted in Figure 2.8, were made by comparing the respective proton signals to the previously synthesised benzimidazole ligands, **L1** and **L2**, as well as by looking at the appropriate multiplicities of each signal and are confirmed by COSY experiments (Figure A12). Additionally, integration of the spectrum correlates to the expected number of 33 protons which further attests to the successful synthesis of **L3**, and the ^{1}H NMR spectral data is in agreement with what has been reported in literature.[20]

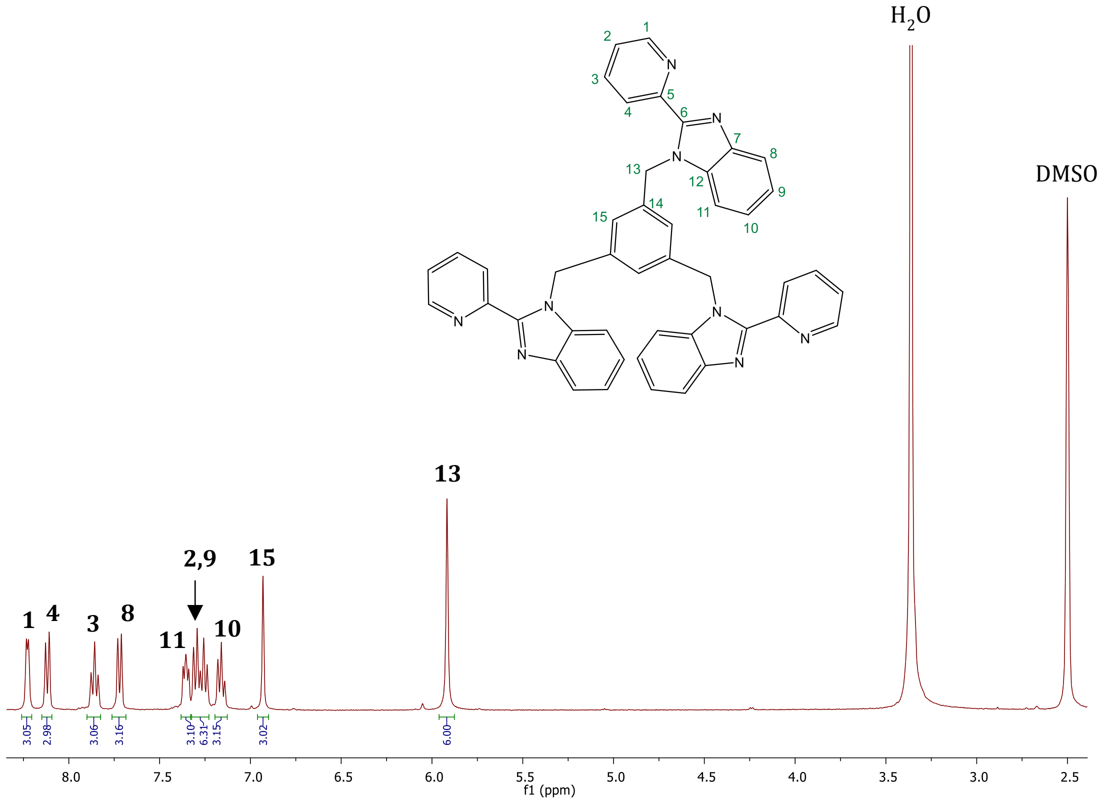

Figure 2.8. ^{1}H NMR spectrum of ligand **L3**, in DMSO-d_6.

High-resolution electrospray ionisation mass spectrometry (ESI-MS) was further used to substantiate the formation of compound **L3**. Figure 2.9 reveals a base peak corresponding to the protonated molecular ion $[M+H]^+$ with an experimentally determined value of m/z=700.2933. The calculated mass-to-charge value for this compound is m/z=700.2892 and thus the experimental and calculated values agree within an acceptable margin of error.

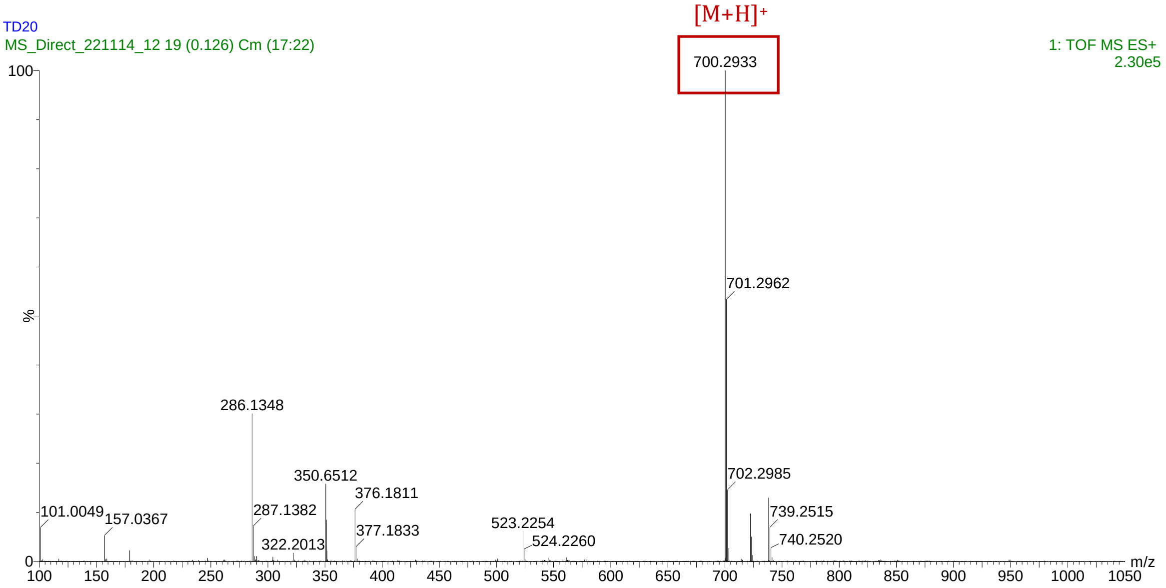

Figure 2.9. High-Resolution ESI Mass Spectrum of ligand **L3** recorded in the positive-ion mode.

2.5 Synthesis and characterisation of $[Ir(ppy)_2(\mu\text{-}Cl)]_2$

The iridium(III) dimer, dichlorotetrakis(2-(2-pyridinyl)phenyl)diiridium(III) was synthesised by a direct cyclometalation of iridium(III) chloride hydrate with 2-phenylpyridine, in a mixture of 2-ethoxyethanol/water, as outlined in Scheme 2.5.[21] $[Ir(ppy)_2(\mu\text{-}Cl)]_2$ was obtained as a bright yellow solid in a good yield of 78%.

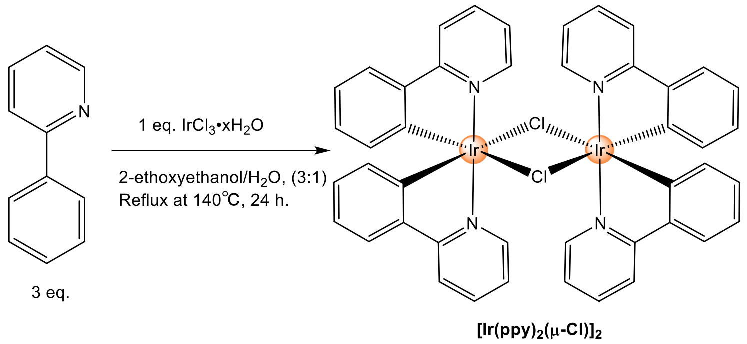

Scheme 2.5. Outline for the synthesis of the iridium dimer, $[Ir(ppy)_2(\mu\text{-}Cl)]_2$.

The proposed mechanism for the cyclometalation reaction shown in Scheme 2.5 is postulated to involve an electrophilic attack of the aromatic phenylpyridine moiety by the metal centre, to form the metal-carbon bond.[22, 23] The hydrogen that is originally bonded to the *ipso* carbon is proposed to be eliminated as HCl.[22] This step is postulated to be an intramolecular reaction involving the (phenyl)-hydrogen bond, which is *ortho* to the aromatic donor ligand (2,2'-pyridine moiety).[22]

Upon analysis of the stacked ^{1}H NMR spectra presented in Figure 2.10, the first observation that confirms the successful synthesis of $[Ir(ppy)_2(\mu\text{-}Cl)]_2$ is the loss of the proton signal corresponding to H_{1B} on the *ipso* carbon. This is the carbon that is involved in C-H activation upon coordination of 2-phenylpyridine to the iridium(III) centre. Additionally, proton H_{6B} which is *ortho* to the cyclometalated carbon, shows a dramatic upfield shift upon coordination of 2-phenylpyridine to the metal centre. This phenomenon is due to a well-known concept in organometallic chemistry known as the *synergistic effect*, which occurs upon ligand coordination to the metal centre. There is strong σ-donation from the filled π orbitals of the 2-phenylpyridyl ligands into the vacant *d*-orbitals of the metal centre, which increases the electron density at the metal centre. The metal responds to this increased electron density by back donating density from its filled *d*-orbitals into the empty π^* orbitals of 2-phenylpyridine. Thus, there is increased electron density near the coordination sites of the phenylpyridyl ligand, which results in an upfield shift for proton H_{6B}. Moreover, this shielding effect is consistent with what has been reported in literature for related *ortho*-metalated complexes, which also exhibit high-field resonances of protons that are *ortho* and *meta* to the cyclometalated carbon atom.[24, 25]

Additional evidence that supports successful cyclometalation is that the proton signals for protons H_{5A}-H_{5B} and H_{4A}-H_{4B} (Figure 2.10) become more distinct peaks. That is, these proton signals occur as a poorly resolved multiplet in the spectrum for 2-phenylpyridine (Figure 2.10 (a)) but in the case of the dimer (Figure 2.10 (b)), H_{4B} occurs as a more shielded triplet, distinct from H_{5A}-H_{5B}, and H_{4A} occurs as a well-defined triplet. This phenomenon occurs because the process of metalation "locks" the 2-phenylpyridine into place, restricting rotation about the bond linking the pyridyl and phenyl substituents together, and thus causes these protons to resonate in different and distinct environments.

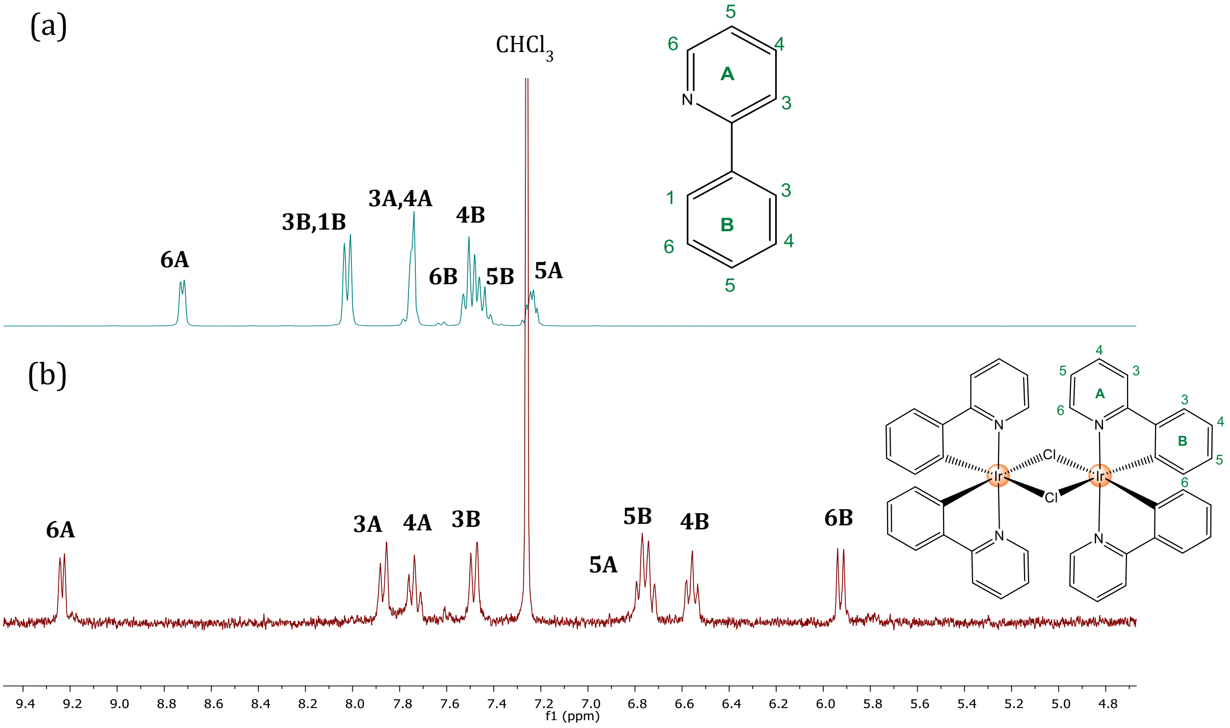

Figure 2.10. Stacked ^1H NMR spectra over the aromatic regions of (a) 2-phenylpyridine and (b) $[Ir(ppy)_2(\mu\text{–}Cl)]_2$, in $CDCl_3$.

Furthermore, this occurrence is observed in the $^{13}C\{^1H\}$ NMR data for $[Ir(ppy)_2(\mu\text{-}Cl)]_2$ as well, where the free 2-phenylpyridyl ligand gives rise to 9 carbon signals but upon cyclometalation, $[Ir(ppy)_2(\mu\text{-}Cl)]_2$ exhibits 11 carbon signals (Figure A16). The carbons that are *ortho* and *para* to the 2,2'-bond in 2-phenylpyridine are no longer symmetrical when cyclometalation occurs. The spectral data is in agreement with reported literature for $[Ir(ppy)_2(\mu\text{-}Cl)]_2$.[23]

Finally, X-ray crystal structures reported for structurally similar compounds to $[Ir(ppy)_2(\mu\text{-}Cl)]_2$ show that the Ir-C bonds exert a significant *trans* effect which favours the formation of the Ir-Cl bridge bonds *trans* to the Ir-C bonds.[23, 26, 27] Racemates of $[Ir(ppy)_2(\mu\text{-}Cl)]_2$ can potentially be formed in the synthesis of the chloro-bridged dimer but they can be indistinguishable in NMR experiments.

2.6 Synthesis and characterisation of the 2-(pyridin-2-yl)-1*H*-benzo[*d*]imidazole iridium(III) complex (C1)

The synthesis of the mononuclear, cationic iridium(III) 2-(pyridin-2-yl)-1*H*-benzo[*d*]imidazole complex (**C1**) was achieved *via* a two-step reaction, as is depicted in Scheme 2.6. In the first step, the iridium dimer $[Ir(ppy)_2(\mu\text{-}Cl)]_2$ underwent a facile bridge-splitting reaction with the *N^N* ancillary ligand (**L1**) to afford the chloride salt product. Secondly, an anion exchange reaction with ammonium hexafluorophosphate was carried out to afford complex (**C1**) as a yellow powder in a good yield of 77%.

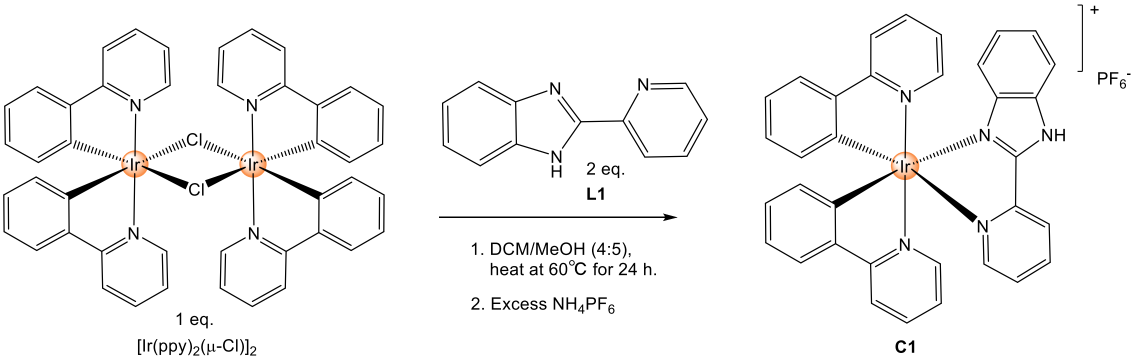

Scheme 2.6. Outline for the synthesis of the cationic iridium(III) 2-(pyridin-2-yl)-1*H*-benzo[*d*]imidazole complex, **C1**.

Analysis of the stacked ^{1}H NMR spectra (Figure 2.11) of the cationic *N^N* coordinated iridium(III) complex (**C1**) confirms the successful metalation reaction. Firstly, an upfield shift occurs for proton H_1 (relabelled as H_b in the structure of **C1**) of the precursor ligand (**L1**) upon complexation to the iridium(III) centre. This is due to proton H_1 being in an *ortho* position to the coordinated nitrogen and thus this proton would receive more electron density (compared to the free ligand) upon complexation due to the *synergistic effect*- a phenomenon that has been reported for structurally similar complexes in literature.[1, 4] The protons H_{12}-$H_{12'}$, which are *ortho* to the cyclometalated carbon donors of the 2-phenylpyridyl ligands also experience the *synergistic effect* to a large degree, and thus they appear as the second-last sets of most shielded doublets at 6.31 ppm and 6.25 ppm, respectively. A notable upfield shift is observed for proton H_{11} (relabelled as H_m in **C1**) from 7.64 –7.60 ppm in the free ligand, to the most shielded doublet occurring at 6.14 ppm in complex **C1**. The assignment of H_m correlates with literature and the significant shielding effect experienced by this proton is attributed to steric crowding around H_m, where the adjacent 2-phenylpyridyl ligand shields H_m from the cationic iridium(III) centre.[1, 28] Conversely, an overall downfield shift is observed for the majority of the other proton signals of complex **C1** when compared to the ancillary ligand, **L1**. This attests to the cationic nature of complex **C1**, which is a more electron-deficient system compared to the neutral ancillary ligand. Additionally, these protons are too far away from the sites of metal coordination, and thus they won't experience the shielding effects from the retro backdonation of the metal. Finally, integration over the aromatic region of complex **C1** correlates to the expected number of protons and the ^{1}H NMR data is in agreement with reported literature for this complex.[1]

Another interesting observation that can be made upon further examination of Figure 2.11(b), is that there is doubling up of the proton signals corresponding to the 2-phenylpyridyl ligands. This phenomenon is attributed to helical chirality innate to tris-bidentate *pseudo*-octahedral complexes (**C1**) and the asymmetric nature (C_1 symmetry) exhibited by complex **C1**. Rings B and B' of the two respective *C^N* donors are *trans* to different groups (benzimidazole *vs* pyridine, respectively), which results in the inequivalence of the two 2-phenylpyridyl ligands. This inequivalence of the two 2-phenylpyridyl ligands is also observed in the ^{13}C {^{1}H} NMR data obtained for complex **C1**, where each ligand gives rise to distinct set of peaks for the carbon signals (Figure A19).

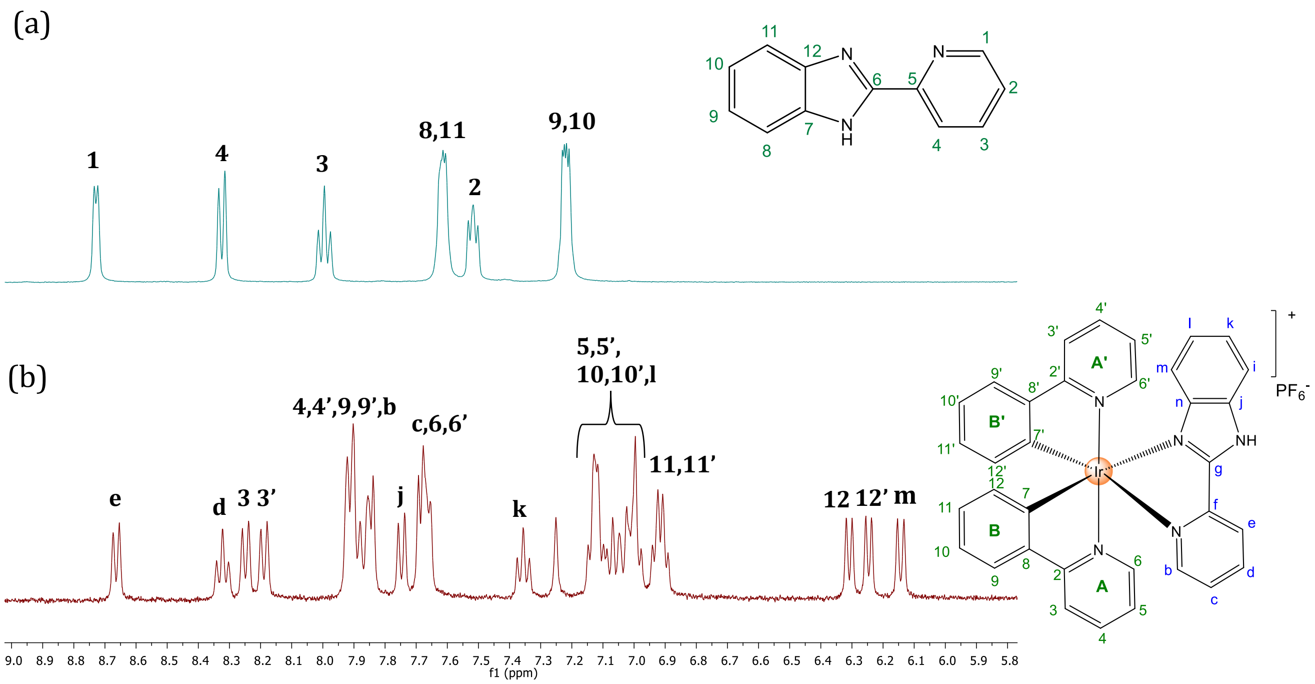

Figure 2.11. Stacked ^{1}H NMR spectra over the aromatic regions of (a) ligand **L1** and (b) complex **C1**, in DMSO-d_6.

In addition to NMR spectroscopy, infrared spectroscopy was used to further verify coordination of the benzimidazole ligand (**L1**) onto the iridium(III) centre. In the infrared spectrum of complex **C1** (Figure 2.12), the characteristic N-H stretching frequency occurs at 3132 cm^{-1} and the C=N bands occur at 1612 cm^{-1} and 1476 cm^{-1} for the imine and pyridyl moieties, respectively. Compared to the respective stretching frequencies that are observed in ligand **L1**, it is evident that there is an overall shift towards higher wavenumbers for the C=N stretching bands for complex **C1**. This observation suggests a shortening of the C=N bonds upon ligand coordination to the metal centre, which is expected due to the strong *trans*-influence exerted by the cyclometalated carbon donors of the 2-phenylpyridyl ligands. The *trans*-influence occurs in the thermodynamic ground state of either square-planar or *pseudo*-octahedral *d*-block complexes whereby tightly bonded ligands selectively lengthen the metal-ligand bonds that are in a *trans* orientation to them.[29] Thus, the *trans*-influence of the 2-phenylpyridyl carbon donors of complex **C1** weakens the Ir-N bonds of the *N^N* ancillary ligand, which in turn results in the strengthening of the C=N bonds, causing these bonds to resonate at a higher frequency.

Furthermore, complex **C1** is cationic in nature, possessing reduced electron density at the metal centre, when compared to the neutral ancillary benzimidazole ligand (**L1**). As a consequence, there is less retro-back donation from the *d*-orbitals of the iridium(III) centre into the empty π* orbitals of the benzimidazole ligand. Backdonation results in lengthened Ir-$N_{benzimidazole}$ bonds and an increased C=N bond order. The diminished occurrence of the *synergic effect* could also be attributed to a considerable difference in the energy gap between the HOMO of the iridium(III) centre and LUMO of the ligand, thus reducing the π-backdonation.[30] However, further analysis of the frontier molecular orbitals and DFT calculations should be performed to garner a deeper understanding of this phenomenon. The shift of the C=N absorbance band in imine and pyridyl moieties to higher wavenumbers upon complexation has been reported for other complexes.[31] Finally, intense stretching bands are observed at 828 cm^{-1} and 734 cm^{-1} which correspond to P-F stretching frequencies and this further corroborates a successful metathesis reaction, as these stretching frequencies are indicative of the PF_6 counter-ion being present.

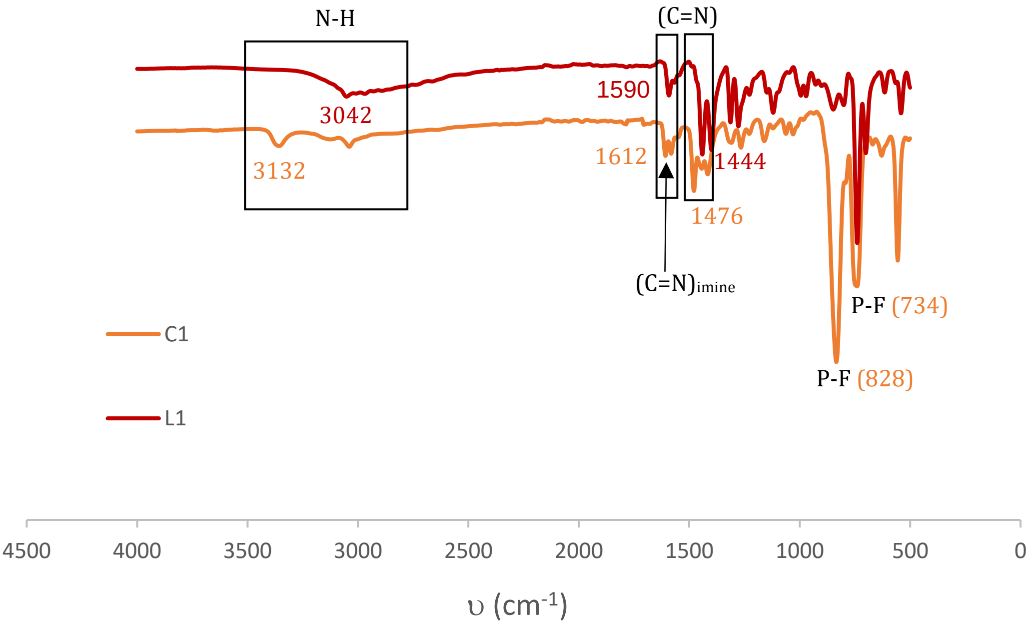

Figure 2.12. Stacked infrared spectra of complex **C1** and ligand **L1.**

2.7 Synthesis and characterisation of the 1-benzyl-2-(pyridin-2-yl)-1*H*-benzo[*d*]imidazole iridium(III) complex (C2)

The reaction scheme depicting the synthesis of the new cationic iridium(III) 1-benzyl-2-(pyridin-2-yl)-1*H*-benzo[*d*]imidazole complex (**C2**) is outlined in Scheme 2.7. The motivation behind the synthesis of complex **C2** was to vary the functional group on the amine nitrogen of the imidazole portion of the benzimidazole scaffold. As discussed in the introduction (2.1) of this chapter, modifications at this position could influence the photophysical and the electrochemical properties of the iridium(III) photosensitiser. Complex **C2** was synthesised in a similar manner to complex **C1**. In the first step, the *N^N* ancillary ligand, 1-benzyl-2-(pyridin-2-yl)-1*H*-benzo[*d*]imidazole underwent a metalation reaction with $[Ir(ppy)_2(\mu\text{-}Cl)]_2$, followed by an anion exchange reaction with ammonium hexafluorophosphate to afford complex **C2** as a yellow powder, in a moderate yield of 68%.

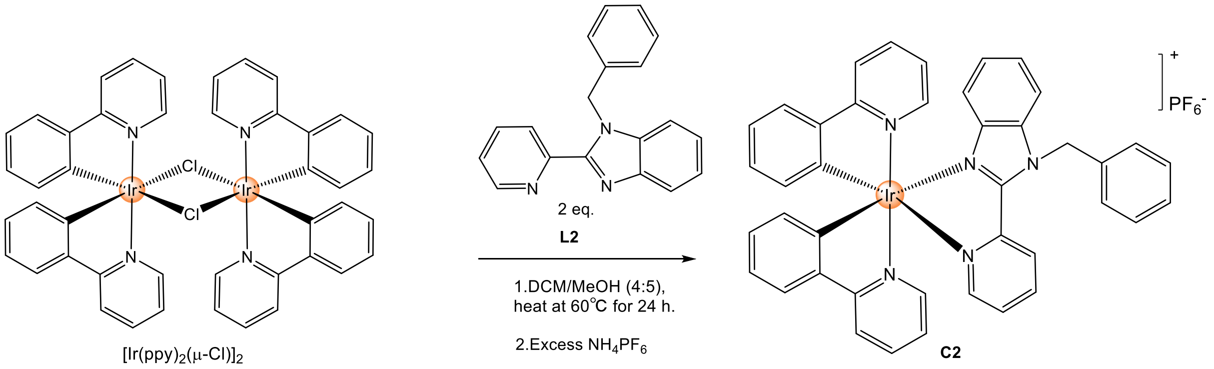

Scheme 2.7. Outline for the synthesis of the cationic iridium(III) 1-benzyl-2-(pyridin-2-yl)-1*H*-benzo[*d*]imidazole complex, **C2.**

Examination of the ^{1}H NMR spectra (Figure 2.13) confirms the successful *N^N* coordination of ligand **L2** to the iridium(III) centre, to afford the new functionalised benzimidazole complex (**C2**). Integration over the aromatic region correlates to the expected number of 31 protons, where the proton signals are observed in the correct multiplicities and ratios. Upon coordination of ligand **L2** to the iridium(III) centre, an upfield shift of proton H_1/H_b, that is *ortho* to the metal-coordinated nitrogen, is observed once again.

This shielding effect is seen for proton H_m as well as the protons *ortho* to the cyclometalated 2-phenylpyridyl ligands (H_{12}-$H_{12'}$). Furthermore, there is an overall downfield shift for the other protons of complex **C2**, relative to the free ancillary ligand, (**L2**) which was similarly seen for complex **C1**. Again, this attests to the cationic nature of complex **C2**, which possesses reduced electron density compared to the neutral ancillary ligand (**L2**). The proton assignments for complex **C2** were made by comparing the respective proton signals to that of the previously synthesised iridium(III) mononuclear complex, **C1** and are confirmed *via* 2D NMR COSY experiments (Figure A25). Furthermore, an interesting observation was made when looking at the methylene signal corresponding to proton H_o. This signal for the -CH_2 group does not occur as a singlet as it did in the ancillary ligand **L2.** Rather, the methylene signal occurs as mutually coupled doublets. The diastereotopicity of the -CH_2 protons is attributed to helical chirality and asymmetric nature (C_1 symmetry) of the tris-bidentate *pseudo*-octahedral complex, **C2.** This phenomenon has been observed in structurally similar iridium(III) complexes reported in literature.[4, 28]

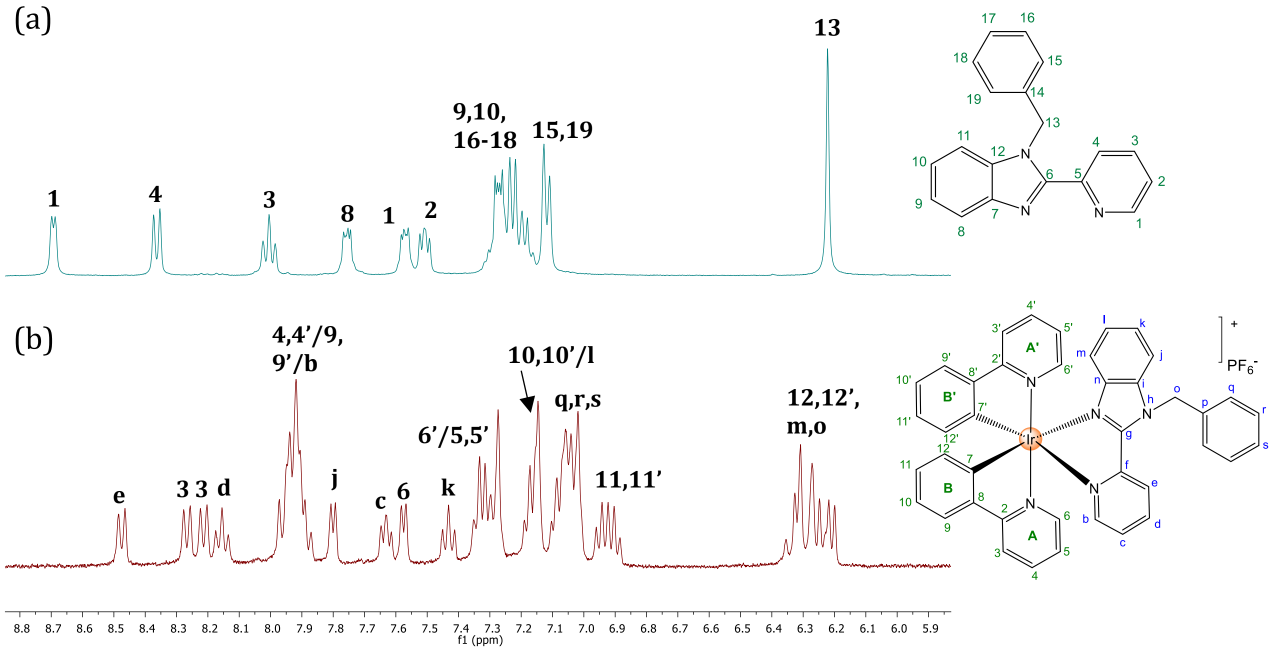

Figure 2.13. Stacked ^{1}H NMR spectra over the aromatic region of (a) ligand **L2** and (b) complex **C2**, in DMSO-d_6.

The infrared spectrum of complex **C2** (Figure 2.14) displays the characteristic C=N imine and pyridyl stretching frequency bands at 1626 cm^{-1} and 1502 cm^{-1}, respectively. A shift to higher wavenumbers for the appropriate C=N bands is observed once again, when comparing the infrared spectrum of the ancillary ligand **L2** to that of complex **C2**. This is due to the *trans*-effect of the 2-phenylpyridyl ligands and cationic nature of complex **C2**. The characteristic P-F stretches are also present at 854 cm^{-1} and 756 cm^{-1}, which is indicative of a successful metathesis reaction.

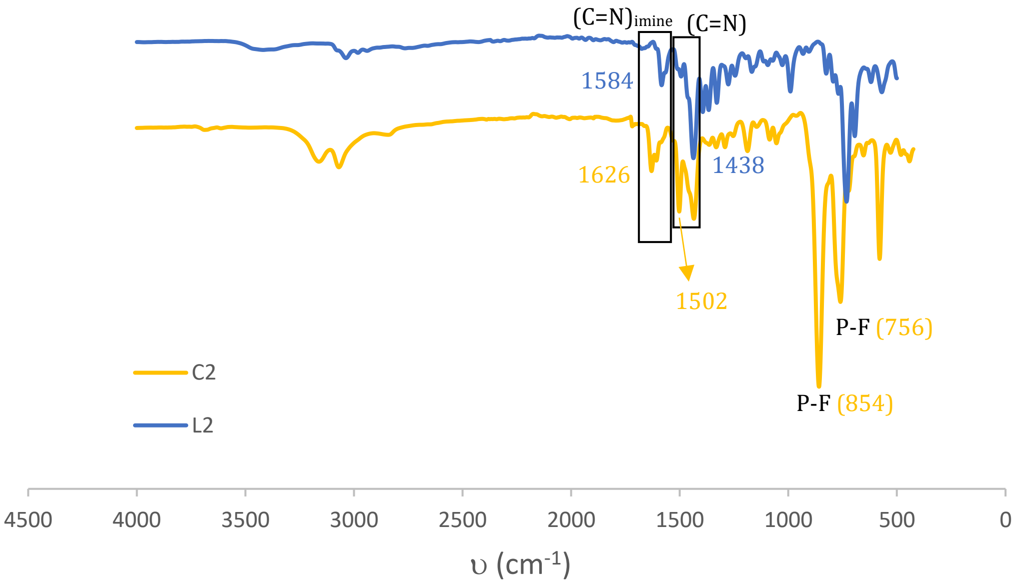

Figure 2.14. Stacked infrared spectra of compounds **C2** and **L2**.

The iridium(III) complex, **C2** was also analysed *via* mass spectrometry (Figure 2.15). High-Resolution Electrospray Ionisation Mass Spectrometry analysis of complex **C2** revealed a molecular ion peak at *m/z*=786.2205 (calculated value: *m/z*=786.2209) that corresponds to the $[M - PF_6]^+$ ion and confirms the formation of the cationic complex **C2**.

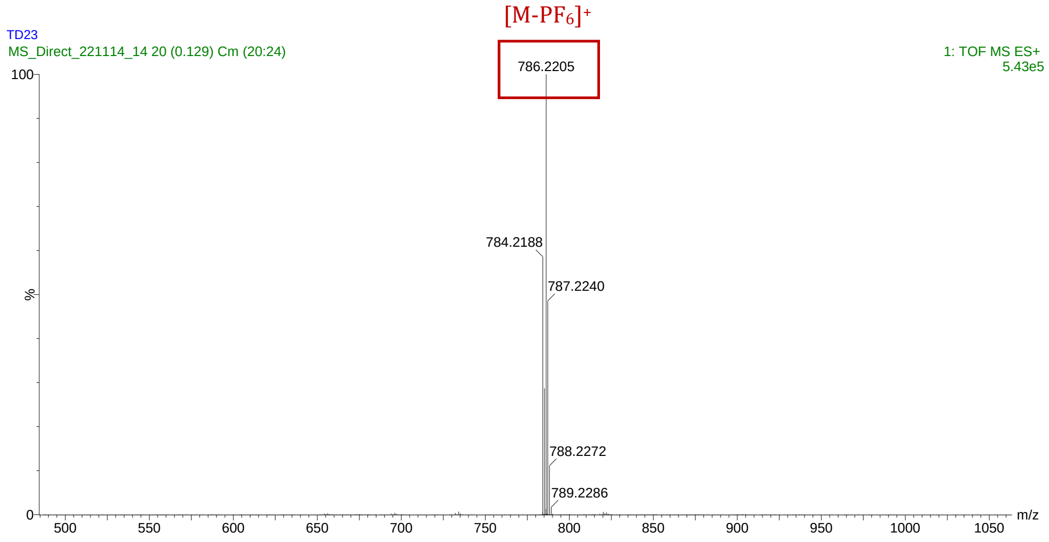

Figure 2.15. High-Resolution ESI Mass Spectrum of complex **C2** recorded in the positive-ion mode.

Finally, single crystal X-ray diffraction (XRD) confirmed the molecular structure of complex **C2** (Figure 2.16). Suitable single crystals of complex **C2** were obtained by slow diffusion of diethyl ether into a solution of dichloromethane/methanol, at room temperature. Additional crystallographic data is presented in Table 2.1 and selected bond lengths and angles, with estimated standard deviations, are collated in Table 2.2.

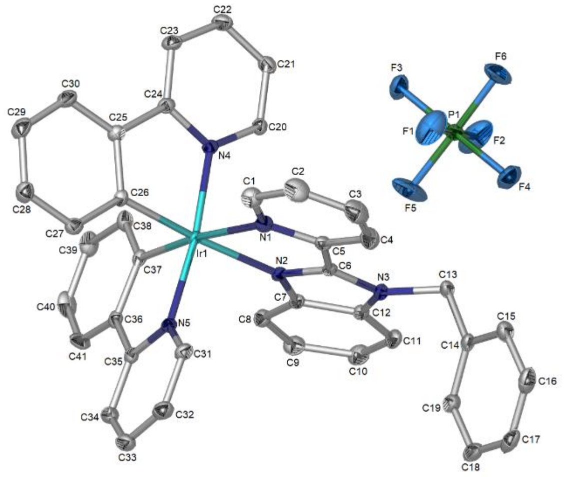

Figure 2.16. X-ray crystallographic ORTEP diagram of complex **C2** with the PF_6^- counterion also shown. Thermal ellipsoids are at the 50% probability level and hydrogen atoms are omitted for clarity.

The complex **C2** crystallises in a P2$_1$/c space group with a monoclinic system, where four molecules (two Δ and two Λ isomers) are present within the unit cell. The unit cell displaying the two pairs of enantiomers for complex **C2** is presented in Figure A58.

Table 2.1: Crystallographic data and refinement parameters for complex **C2**

Complex C2	
Chemical formula	$C_{41} H_{31} F_6 Ir N_5 P$
Formula weight	930.90
Crystal system	monoclinic
Space group	P2$_1$/c
a, b, c (Å)	8.6687(5), 37.359(2), 11.0662(7)
α, β, γ (°)	90, 98.584(2), 90
V (Å^3)	3543.7(4)
Z	4
D (g.cm^{-3})	1.745
μ (mm^{-1})	3.884
F (000)	1832
Crystal size (mm)	0.18 x 0.20 x 0.26
T (K)	100
Scan range (°)	1.9 < θ < 28.3
Unique reflections	8822
R$_{int}$	0.033
Reflections used [I>2σ(I)]	8454
R indices (all data)	R 0.0185, wR 2 0.0378, S 1.12
Goodness-of-fit	1.12
Max, Min Δρ (e Å^{-3})	-0.91, 1.84

The molecular structure of complex **C2** displays a *pseudo*-octahedral geometry around the iridium(III) centre, which is evidenced by the bond bite angles between the bidentate ligands being less than the expected 90˚, with respect to the metal centre.

The ancillary *N^N* ligand exhibits a N_1-Ir_1-N_2 bite angle of 75.36(7)°, whereas the C-Ir-N bite angles for the *C^N* ligands are about 80°. These respective bite angles are in agreement with literature for similar complexes.[1, 4, 32]

The predicted *trans*-N,N and *cis*-C,C arrangement for the cyclometalated *C^N* phenylpyridyl ligands (Figure 2.16) is also observed. Upon analysis of the Ir-N bond lengths listed in Table 2.2, it appears that the Ir-N bond distance for the *N^N* ancillary ligand (2.1323(17)-2.1548(17) Å) is longer than that of the Ir-N bond distance of the *C^N* phenylpyridyl ligands (2.0426(17)-2.0508(17) Å). This is due to the strong *trans* influence that is exerted by the carbon donors of the cyclometalated 2-phenylpyridyl ligands, that was discussed earlier in this chapter (Section 2.6). Noteworthy, is that the crystal data corroborates the infrared data obtained for complex **C2**. It was hypothesised that the strong *trans*-influence of the cyclometalated ligands would weaken (lengthen) the Ir-N bonds of the *N^N* ligand and in so doing, result in the strengthening of the C=N bonds, which would cause these C=N bonds to resonate at a higher frequency. Moreover, these bond lengths are comparable to what is reported in literature for similar cyclometalated iridium(III) complexes, possessing an *N^N* ancillary ligand.[1, 4, 33]

The differences in the π-donor ability of the benzimidazole and pyridine moieties within the 2,2'-pyridylbenzimidazole ligand can be observed too. The Ir-$N_{benzimidazole}$ bond length is shorter (Ir_1-N_2: 2.1323(17) Å) than that of the Ir-$N_{pyridine}$ bond (Ir_1-N_1: 2.1548(17) Å). The difference in these respective bond lengths is likely due to the higher π-donor ability of the benzimidazole portion (which possesses greater electron density) compared to pyridine, which has been corroborated by structurally similar complexes described in literature.[3, 4]

The Ir-C bonds (2.0008(19) -2.013(2) Å) also have standard bond lengths. Furthermore, the N-C-C-C torsion angles (0.2(2)- 2.9(2)°) for the *C^N* ligands and the N-C-C-N torsion angles (-2.7(2)- 0.5(2)°) for the *N^N* ligand are small, which imparts a high degree of planarity on the ligands of complex **C2**. Coplanarity has been reported to be a characteristic attribute of ionic transition metal complexes which possess five-atom chelate rings, as is the case for complex **C2**.[34]

Table 2.2: Selected Bond lengths (Å) and Angles (°) for complex **C2**

Complex C2	
Bond lengths (Å)	
Ir1-N1	2.1548(17)
Ir1-N2	2.1323(17)
Ir1-N4	2.0508(17)
Ir1-N5	2.0426(17)
Ir1-C26	2.013(2)
Ir1-C37	2.0008(19)
Bond angles (°)	
N1-Ir1-N2	75.36(7)
N4-Ir1-C26	80.51(7)
N5-Ir1 -C37	80.42(7)
Torsion angles (°)	
N1-C5-C6-N2	-2.7(2)
N2-C7-C12-N3	0.5(2)
N4-C24-C25-C26	0.2(2)
N5-C35-C36-C37	2.9(2)

2.8 Synthesis and characterisation of the 1,3,5-tris((2-(pyridin-2-yl)-1*H*-benzo[*d*]imidazol-1-yl)methyl)benzene iridium(III) complex (C3)

The new trinuclear iridium polypyridyl complex, **C3** was obtained in a good yield of 75% by refluxing 1.5 equivalents of $[Ir(ppy)_2(\mu\text{-}Cl)]_2$ with 1 equivalent of the trimeric benzimidazole ligand **L3**, followed by an anion exchange reaction with ammonium hexafluorophosphate. Complex **C3** was synthesised to investigate the influence of polymetallic complexes in the scope of photoredox catalysed reactions. The overall reaction for the trinuclear complex (**C3**) is represented in Scheme 2.8.

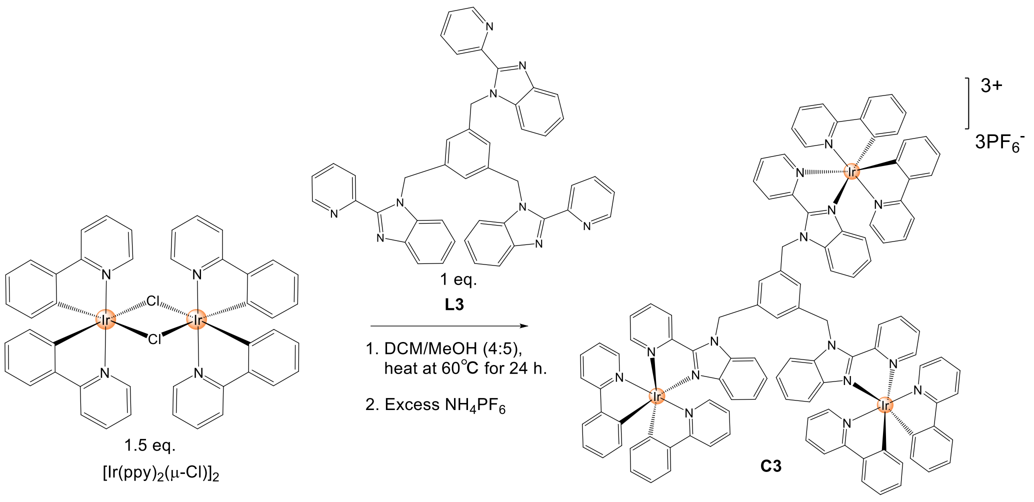

Scheme 2.8. Outline for the synthesis of the cationic trinuclear iridium(III) 1,3,5-tris((2-(pyridin-2-yl)-1*H*-benzo[*d*]imidazol-1-yl)methyl)benzene complex, **C3**.

Upon initial examination of the ^{1}H NMR spectrum (Figure 2.17) of complex **C3**, it is evident that it is a rather complicated spectrum, which is expected for such a large and complex molecule. That is, large complexes such as complex **C3** exhibit slow rotation in solution, which results in the averaging of signals in similar environments on the NMR timescale where overlapping and broadened signals result, as is observed in Figure 2.17. Importantly, this broadening of signals has been reported for other large trinuclear complexes reported in literature.[12] Additionally, as discussed above, helical chirality innate to tris-bidentate *pseudo*-octahedral complexes such as complex **C3**, renders the 2-phenylpyridyl ligands inequivalent, as well as the methylene protons diastereotopic, which adds to the complexity of definitively assigning the ^{1}H NMR spectrum of complex **C3**. Thus, only the distinguishable signals of the ^{1}H NMR spectrum were assigned (Figure 2.17).

Proton H_e was assigned as the most downfield doublet, which was based on the proton assignments of complexes **C1** and **C2**, where this proton occurred as the most downfield signal for these complexes. Subsequently, the general assignments for protons H_c-H_d were made *via* analysis of the COSY spectrum of complex **C3** (Figure A30). The broad assignments for the more shielded aromatic protons occurring in the region of 6.05-6.48 ppm were also made with the ^{1}H NMR spectra of complexes **C1** and **C2** in mind, as protons $H_{12}/H_{12'}$, H_m and H_o all occurred as the more upfield protons signals.

Analysis of the HSQC-DEPT spectrum (Figure A31) of complex **C3** aided in confirming the assignment for the methylene protons, H_o. Importantly, integration over the region of 6.05-6.48 ppm amounts to 15 protons, which is in agreement with the expected number of protons for $H_{12}/H_{12'}$, H_m and H_o for all three arms of the trinuclear complex, **C3**. Furthermore, from the 1D and 2D NMR analysis of complex **C3** it can be postulated that the three arms of **C3** are all in different chemical environments. The doublet assigned to H_e, only integrates for one proton, which is indicative of the assignment of this proton for only one of the arms of the trinuclear complex. This observation once again ties in with previous arguments, whereby there are three chiral metal centres in complex **C3**, with 2^3 possible stereoisomers present, which are indistinguishable in NMR experiments. Noteworthy, is the fact that the integration over the entire ^1H NMR spectrum of complex **C3** integrates to 81 protons, as well as the appearance of the expected proton signals, which are labelled in Figure 2.17, which are also observed in the 1D and 2D NMR spectra for this complex (**C3**), and attests to the successful synthesis of complex **C3**.

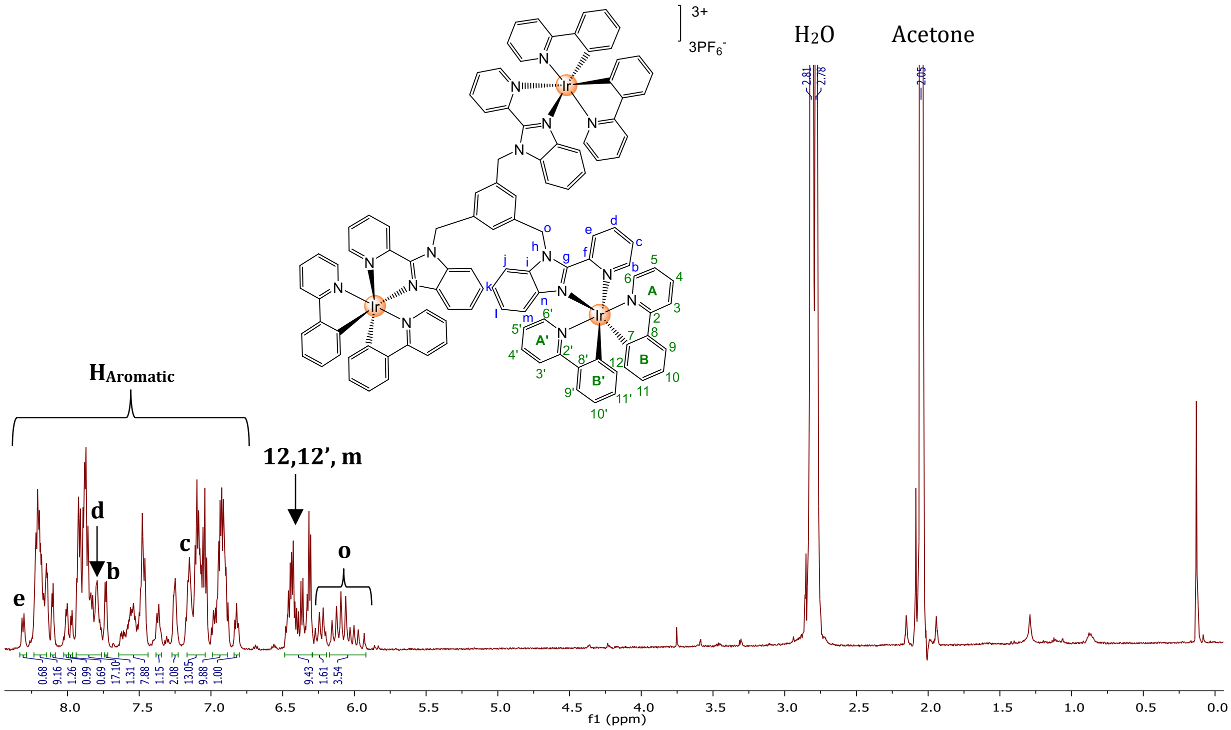

Figure 2.17. ^1H NMR spectrum of the trinuclear complex **C3**, in Acetone-d_6.

The infrared spectrum of complex **C3** presented in Figure 2.18 shows the expected C=N stretching frequencies at 1608 cm^{-1} and 1482 cm^{-1}, which are respectively due to the imine and pyridyl moieties. Once again, the C=N bands in complex **C3** exhibit a shift towards higher wavenumbers when compared to the respective stretching bands in the infrared spectrum of the ancillary ligand, **L3.** This is a result of the three cationic metal centres in complex **C3** as well as the *trans*-effect of the 2-phenylpyridyl ligands. Further corroborating the successful metathesis reaction are the P-F stretching bands observed at 834 cm^{-1} and 738 cm^{-1} (Figure 2.18).

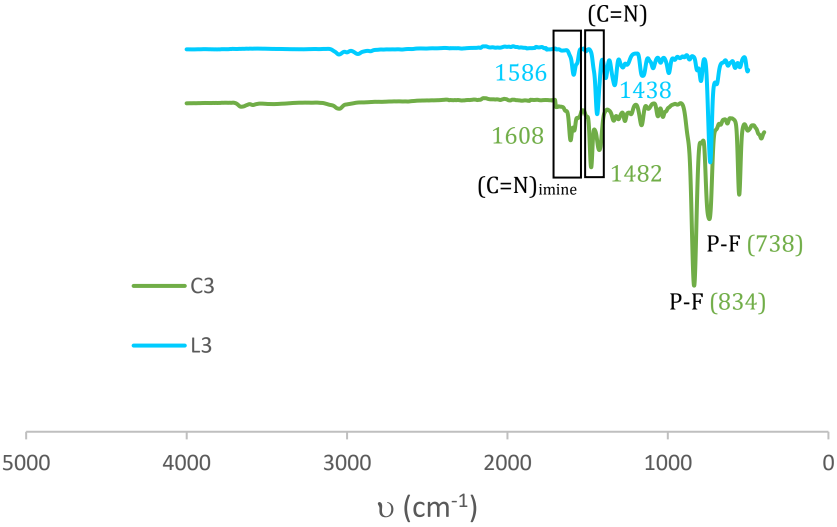

Figure 2.18. Stacked infrared spectra of compounds **C3** and **L3**.

Finally, supporting the spectroscopic and analytical data is the HR ESI mass spectrometry data for the trinuclear cationic iridium(III) complex **C3** (Figure 2.19). Figure 2.19 reveals a molecular ion base peak at *m/z*=733.5249 (calculated: *m/z*=733.5221) that corresponds to the $[M-3PF_6]^{3+}$ ion, substantiating the successful synthesis of complex **C3**. The peak at *m/z*=850.7424 correlates to the dinuclear iridium(III) structure (excluding its two PF_6 counterions) overlayed on the mass spectrum depicted in Figure 2.19. The calculated *m/z* value for this latter dicationic structure is *m/z*=850.7372.

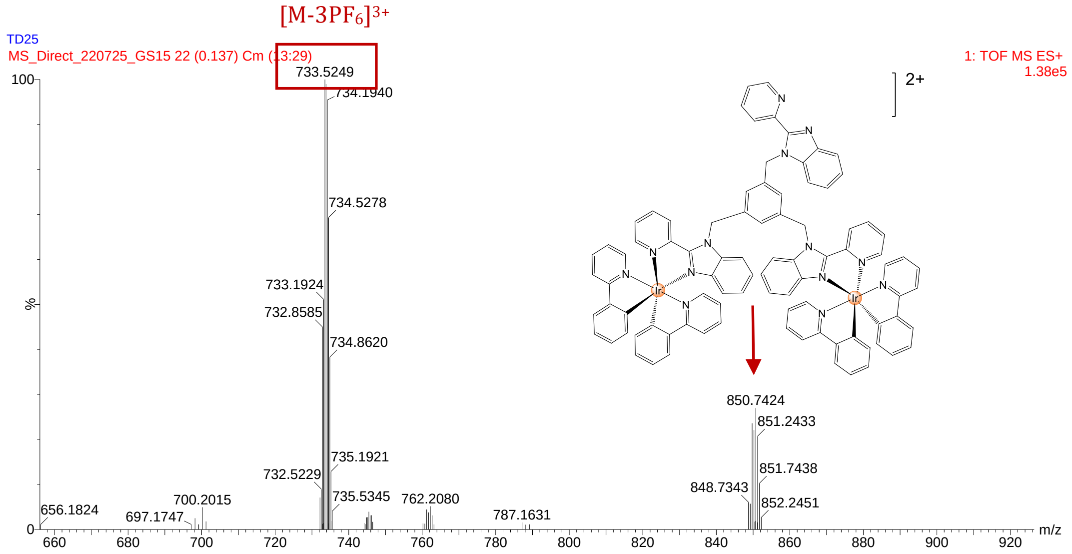

Figure 2.19 High-Resolution ESI Mass Spectrum of complex **C3** recorded in the positive-ion mode.

2.9 Summary

In summary, a series of substituted benzimidazole ligands and their respective cationic, bis-cyclometalated iridium(III) complexes is reported. A precursor benzimidazole ligand (**L1**) was synthesised *via* the reaction of *o*-phenylenediamine and 2-pyridinecarboxylic acid in the presence of an acid catalyst, PPA, in a cyclisation-condensation reaction. This precursor ligand was used in two N-alkylation reactions with either benzyl bromide or 1,3,5-tris(bromomethyl)benzene to respectively afford a monomeric ligand (**L2**) or a trimeric ligand (**L3**). Ligands (**L1-L3**) were obtained in moderate to high yields of 59-95%. The benzimidazole ligands were subsequently reacted with the synthesised iridium(III) chlorobridged dimer, $[Ir(ppy)_2(\mu\text{-}Cl)]_2$ to afford two mononuclear bis-cyclometalated iridium(III) complexes (**C1**, **C2**) and a trinuclear iridium(III) complex, (**C3**). The iridium complexes (**C1-C3**) were obtained in good yields (68-76%), and as racemic mixtures (Λ, Δ isomers) which is an attribute of the helical chirality, inherent to these types of tris-bidentate *pseudo*-octahedral complexes. Characterisation of the synthesised ligands and complexes was achieved by ^{1}H NMR, ^{13}C{^{1}H} NMR spectroscopy, infrared spectroscopy and high-resolution mass spectrometry.

Additionally, a cyrstal structure was obtained for complex (**C2**). Cyrstallographic data obtained for **C2** revealed that this complex displayed a *pseudo*-octahedral geometry around the iridium(III) centre, which was evidenced by the bond bite angles between the bidentate ligands (less than 90°). The cyclometalated *C^N* phenylpyridyl ligands adopt a *trans*-N,N and *cis*-C,C arrangement around the metal centre. Furthermore, the strong *trans* influence exerted by the carbon donors of the cyclometalated ligands resulted in lengthened Ir-N bonds for the *N^N* chelated benzimidazole ligand. The spectroscopic and analytical data thus substantiates and corroborates the structural integrity of ligands (**L1-L3**) and the structures of complexes (**C1-C3**).

2.10 References

1. M. Martínez-Alonso, J. Cerdá, C. Momblona, A. Pertegás, J. M. Junquera-Hernández, A. Heras, A. M. Rodríguez, G. Espino, H. Bolink and E. Ortí, *Inorg. Chem.*, 2017, **56**, 10298-10310.
2. C. D. Sunesh, G. Mathai and Y. Choe, *ACS Appl. Mater. Interfaces*, 2014, **6**, 17416-17425.
3. E. Zafon, I. Echevarría, S. Barrabés, B. R. Manzano, F. A. Jalón, A. M. Rodríguez, A. Massaguer and G. Espino, *Dalton Trans.*, 2022, **51**, 111-128.
4. I. Echevarría, M. Vaquero, B. R. Manzano, F. A. Jalón, R. Quesada and G. Espino, *Inorg. Chem.*, 2022, **61**, 6193-6208.
5. M. S. Lowry and S. Bernhard, *Chem. Eur. J.*, 2006, **12**, 7970-7977.
6. F. Monti, A. Baschieri, L. Sambri and N. Armaroli, *Acc. Chem. Res.*, 2021, **54**, 1492-1505.
7. J. C. Deaton and F. N. Castellano, in *Iridium(III) in Optoelectronic and Photonics Applications*, John Wiley & Sons Inc., Chichester, West Sussex, 2017, pp. 1-69.
8. Y. You and W. Nam, *Chem. Soc. Rev.*, 2012, **41**, 7061-7084.
9. S. DiLuzio, V. Mdluli, T. U. Connell, J. Lewis, V. Van Benschoten and S. Bernhard, *J. Am. Chem. Soc.*, 2021, **143**, 1179-1194.
10. J.-H. Kim, S.-Y. Kim, Y.-J. Cho, H.-J. Son, D. W. Cho and S. O. Kang, *J. Phys. Chem. C.*, 2018, **122**, 4029-4036.

11. S. DiLuzio, T. U. Connell, V. Mdluli, J. F. Kowalewski and S. Bernhard, *J. Am. Chem. Soc.*, 2022, **144**, 1431-1444.
12. N. M. Motimani, S. Ngubane and G. S. Smith, *Polyhedron*, 2022, **212**, 115616.
13. R. O. Reithmeier, S. Meister, A. Siebel and B. Rieger, *Dalton Trans.*, 2015, **44**, 6466-6472.
14. A. M. Cancelliere, F. Puntoriero, S. Serroni, S. Campagna, Y. Tamaki, D. Saito and O. Ishitani, *Chem. Sci.*, 2020, **11**, 1556-1563.
15. N. V. Likhanova, R. Martínez-Palou, M. A. Veloz, D. J. Matías, V. E. Reyes-Cruz, H. Höpfl and O. Olivares, *J. Heterocycl. Chem.*, 2007, **44**, 145-153.
16. O. Dayan, M. Tercan and N. Özdemir, *J. Mol. Struct.*, 2016, **1123**, 35-43.
17. S. Mohanty, A. Khuntia, N. Yellasubbaiah, C. Ayyanna, B. Sudha, S. Harika and N. Y. Subbaiah, *Beni-Suef Univ. J. Basic Appl. Sci.*, 2018, **7**.
18. M. Vaquero, N. Busto, N. Fernández-Pampín, G. Espino and B. García, *Inorg. Chem.*, 2020, **59**, 4961-4971.
19. M. Redrado, M. Miñana, M. P. Coogan, M. Concepción Gimeno and V. Fernández-Moreira, *ChemMedChem*, 2022, **17**, e202200244.
20. B. Wang, J. Fang, B. Li, H. You, D. Ma, Z. Hong, W. Li and Z. Su, *Thin Solid Films*, 2008, **516**, 3123-3127.
21. F. Monti, A. Baschieri, I. Gualandi, J. J. Serrano-Pérez, J. M. Junquera-Hernández, D. Tonelli, A. Mazzanti, S. Muzzioli, S. Stagni, C. Roldan-Carmona, A. Pertegás, H. J. Bolink, E. Ortí, L. Sambri and N. Armaroli, *Inorg. Chem.*, 2014, **53**, 7709-7721.
22. G. W. Parshall, *Acc. Chem. Res.*, 1970, **3**, 139-144.
23. S. Sprouse, K. A. King, P. J. Spellane and R. J. Watts, *J. Am. Chem. Soc.*, 1984, **106**, 6647-6653.
24. K. A. King, P. J. Spellane and R. J. Watts, *J. Am. Chem. Soc.*, 1985, **107**, 1431-1432.
25. S. Dholakia, R. D. Gillard and F. L. Wimmer, *Inorg. Chim. Acta.*, 1983, **69**, 179-181.
26. R. J. Hoare and O. S. Mills, *J. Chem. Soc., Dalton Trans.*, 1972, 2138-2141.
27. J. M. Patrick, A. H. White, M. I. Bruce, M. J. Beatson, D. S. C. Black, G. B. Deacon and N. C. Thomas, *J. Chem. Soc., Dalton Trans.*, 1983, 2121-2123.
28. N. U. Prajith, P. V. Priyanka and V. Alexander, *J. Biol. Inorg. Chem.*, 2022, **27**, 357-372.

29. M. Gregson, E. Lu, D. P. Mills, F. Tuna, E. J. L. McInnes, C. Hennig, A. C. Scheinost, J. McMaster, W. Lewis, A. J. Blake, A. Kerridge and S. T. Liddle, *Nat. Commun.*, 2017, **8**, 14137.
30. P. S. Zinman, MSc Thesis, University of Cape Town, 2023.
31. C. C. Scarborough and K. Wieghardt, *Inorg. Chem.*, 2011, **50**, 9773-9793.
32. G. E. Schneider, A. Pertegás, E. C. Constable, C. E. Housecroft, N. Hostettler, C. D. Morris, J. A. Zampese, H. J. Bolink, J. M. Junquera-Hernández, E. Ortí and M. Sessolo, *J. Mater. Chem, C.*, 2014, **2**, 7047-7055.
33. W. Lin, Q. Zhao, H. Sun, K. Y. Zhang, H. Yang, Q. Yu, X. Zhou, S. Guo, S. Liu and W. Huang, *Adv. Opt. Mater.*, 2015, **3**, 368-375.
34. P. Pla, J. M. Junquera-Hernández, H. J. Bolink and E. Ortí, *Dalton Trans.*, 2015, **44**, 8497-8505.

Chapter 3: Photophysical and electrochemical properties of the iridium(III) photosensitisers

3.1 Introduction

Photoredox catalysis has revolutionised the field of photochemistry and more specifically, synthetic radical chemistry, in that it has created a means for a milder energy source (visible light), to drive reactions.[1, 2] Upon excitation by visible light irradiation of a particular wavelength, photoredox catalysts initiate single electron transfer (SET) events to/from a stable substrate and in so doing, results in the formation of a highly reactive excited-state species that can be involved in reaction pathways that were previously not possible under thermal control.[1,3] The ubiquitous octahedral d^6 polypyridyl complexes of ruthenium(II) and iridium(III) are of the most utilised photosensitisers owing to their favourable photophysical and reversible electrochemical properties that were extensively discussed in Section 1.2.3.[4]

Heteroleptic cyclometalated iridium(III) complexes bearing a diimine N^N ancillary ligand (Figure 3.1(i)) are renowned photosensitisers due to the strong spin-orbit coupling (SOC) of the iridium(III) centre which affords complexes with enhanced photostability and relatively long-lived photoexcited state lifetimes.[5-7] Moreover, the high quantum number of the iridium(III) d electrons result in large ligand field-splitting and the strong σ-donating ability of the cyclometalated carbon atoms significantly destabilise the metal centred antibonding (e_g) orbitals when compared to other 5d and 4d transition metal complexes.[8] As a result, the e_g orbitals are raised in energy above the π^* orbitals of the ligands (Figure 3.1(ii)), and thus inhibits thermal population of the deactivating metal centred (^{3}MC) excited state, which is notorious for being non-emissive or to undergo photodissociation.[9, 10]

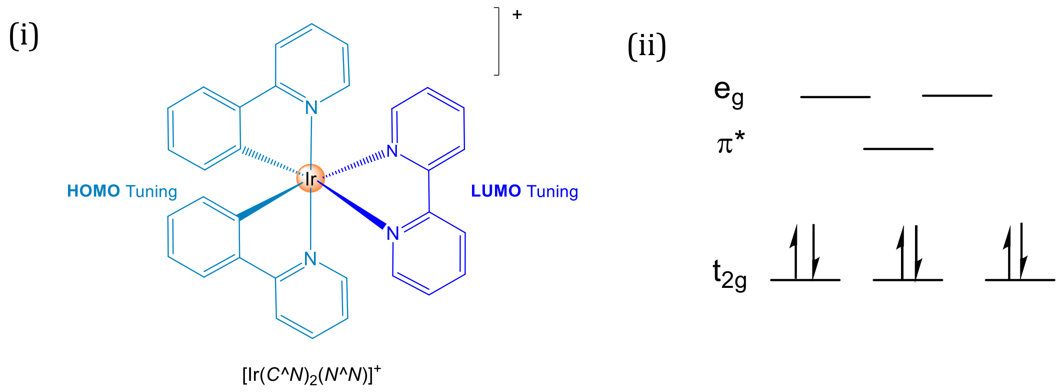

Figure 3.1 (i) Archetypical heteroleptic cationic iridium(III) complex with a diimine *N^N* ancillary ligand.[10] (ii) Electronic configuration diagram typical of low-spin octahedral 5d^6 iridium(III) complexes.[10]

The photophysical and electrochemical properties of $[Ir(C^\wedge N)_2(N^\wedge N)]^+$ complexes can be synthetically tuned *via* judicious tuning of the energy levels of the complexes HOMO and LUMO.[10] The HOMO of $[Ir(C^\wedge N)_2(N^\wedge N)]^+$ complexes is largely localised on the iridium(III) *d* orbitals as well as the π orbitals of the phenyl ring of the cyclometalated ligand, whereas the LUMO is predominantly located on the π* orbitals of the *N^N* ligand.[9, 10] Tuning of the HOMO-LUMO gap can be achieved by functional group modification of the cyclometalated ligand or the ancillary ligand, respectively.[10] The addition of electron-withdrawing substituents has a stabilising effect, while electron-donating groups destabilise the corresponding molecular orbital levels.[7] Thus, the triplet states of iridium(III) offer more advantages when compared to other d^6 transition metal complexes, as the tunability of the charge transfer characteristics for iridium(III) complexes is over a wider range. This is an important factor for photochemical applications, such as photoredox catalysis.

In this chapter the photophysical and electrochemical properties of the synthesised iridium(III) benzimidazole complexes (**C1**-**C3**) is elucidated and described. The effects of ligand modification of the basis *N^N* chelated benzimidazole ligand (**L1**) on the photophysical and electrochemical properties is also discussed herein. Furthermore, the photophysical and electrochemical properties of complexes (**C1**-**C3**) were compared to the model photocatalyst, $[Ir(ppy)_2(dtbbpy)]PF_6$ as this was the photocatalyst that yielded the best catalytic results for the photoredox reaction investigated in this study.

3.2 Photophysical properties

3.2.1 UV-visible absorption spectra

The overlaid UV-vis absorption spectra (Figure 3.2) of complexes (**C1-C3**) as well as the model photoredox catalyst [Ir(ppy)$_2$(dtbbpy)]PF$_6$, were recorded at room temperature in acetonitrile solutions. The absorption spectra are typical of cyclometalated iridium(III) complexes.[11, 12] That is, the overlaid spectra for the respective complexes exhibit intense absorption peaks in the region of 250-330 nm, which correspond to the spin-allowed intraligand, ^{1}LC $\pi \rightarrow \pi^*$ transitions of the π-conjugated *C^N* and *N^N* ligands. Less intense absorption bands are observed at *ca*. 390 nm which correspond to the spin-allowed, $d\pi$ (Ir)→ π^* ^{1}MLCT transitions as well as the ligand-to-ligand charge transfer (^{1}LLCT) transitions. ^{1}LLCT transitions are attributed to the electron transitions from the cyclometalated ligands to the diimine ancillary ligand. Finally, the weak absorption bands trailing off towards the end of the spectra at above 450 nm correspond to the spin-forbidden, $d\pi$ (Ir) → π^* ^{3}MLCT and ^{3}LC transitions. These latter transitions are possible due to the high SOC of the iridium(III) centre (ζ= 3903 cm^{-1}).[13] Importantly, classification of the ^{1}LC, ^{1}LLCT, ^{1}MLCT and ^{3}MLCT states merely serve as a general guideline as it has been reported that mixing between the different states by configuration interaction can occur and spin-orbit coupling can play a significant role in mixing between the electronic states too.[12]

The UV-visible data suggests that the iridium(III) complexes (**C1-C3**) are well-suited to undergo photoredox catalysed reactions under blue LED light irradiation. The absorption bands at 390-450 nm fall within the wavelength range of commercial blue LED lights used for photocatalysis.

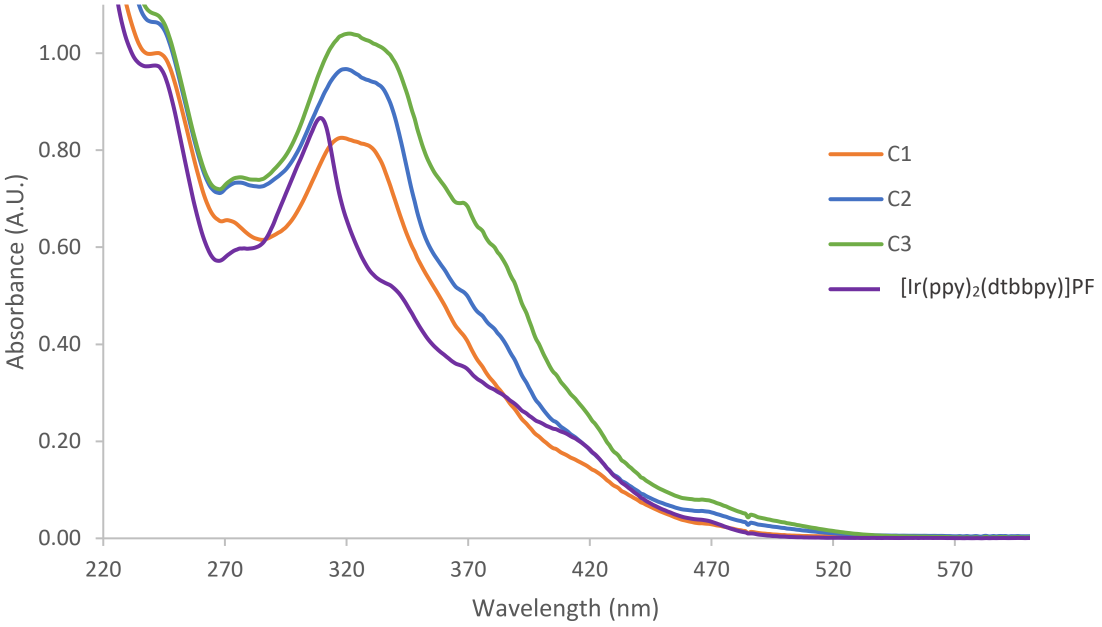

Figure 3.2. Overlaid UV-visible absorption spectra for iridium(III) complexes (**C1**-**C3**) and [Ir(ppy)$_2$(dtbbpy)]PF$_6$ in CH$_3$CN at room temperature. Prepared concentrations of 0.5 × 10^{-4} M for complexes (**C1**, **C2**), [Ir(ppy)$_2$(dtbbpy)]PF$_6$ and 0.25 × 10^{-4} M for complex **C3**.

3.2.2 Emission studies

The emission spectra (Figure 3.3 (i)-(iv)) of complexes (**C1**-**C3**) and [Ir(ppy)$_2$(dtbbpy)]PF$_6$ were recorded in anhydrous acetonitrile solutions at room temperature and at various crossover wavelengths as reported in Table 3.1. Additional photophysical data, which includes the emission band maxima is collated in Table 3.1. The first observation upon examination of the emission spectra presented in Figure 3.3 is that all the iridium(III) complexes display broad and unstructured emission bands. This is a characteristic feature of complexes of high charge transfer nature.[11] Additionally, strong SOC of the iridium(III) centre results in almost unitary intersystem crossing efficiency from the ^{1}MLCT state to the ^{3}MLCT state and thus the emissions of these types of complexes are attributed to spin-forbidden phosphorescence (transition from ^{3}MLCT to the ground state).[14]

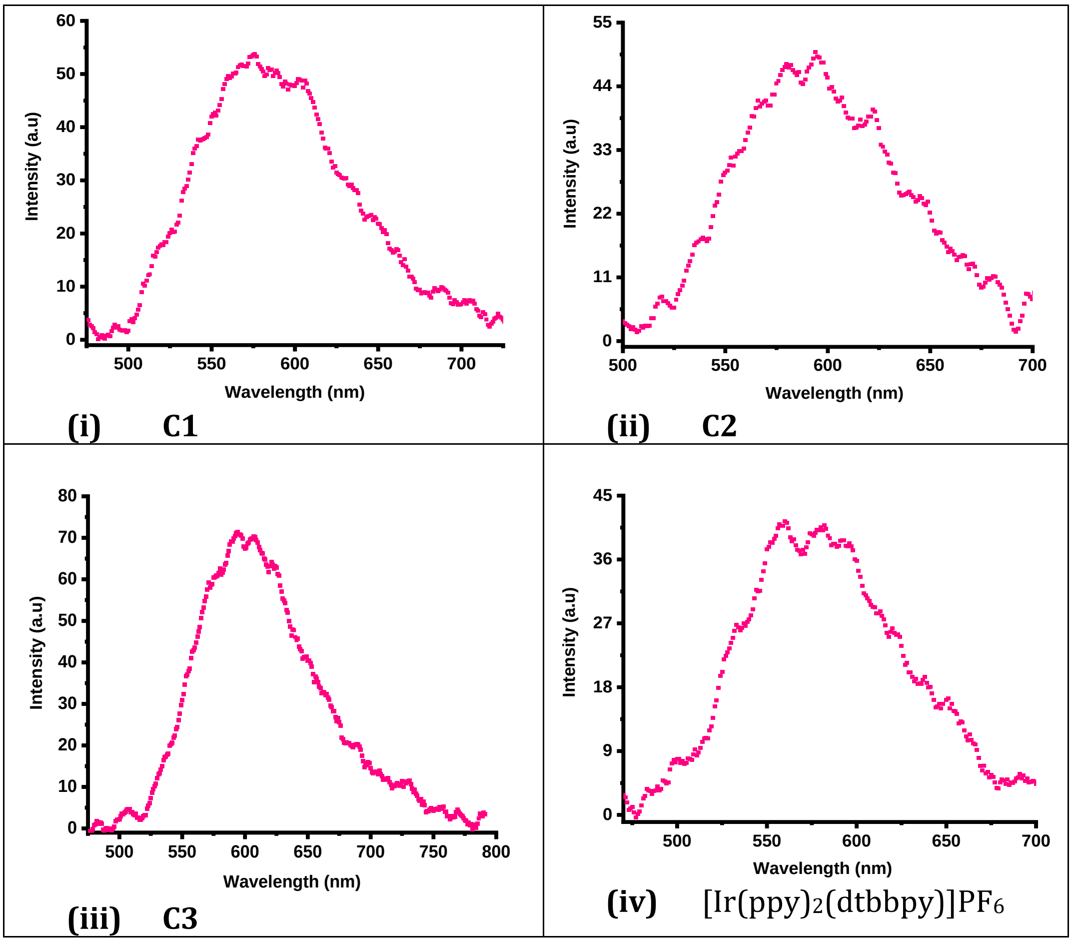

Figure 3.3. Emission spectra of the synthesised iridium(III) complexes (**C1-C3**) and $[Ir(ppy)_2(dtbbpy)]PF_6$ in anhydrous CH_3CN at room temperature.

The emission band maxima for the respective iridium complexes are recorded in Table 3.1, where it is evident that the mononuclear benzimidazole complexes **C1** (582 nm) and **C2** (585 nm) emit in the yellow region, which is also the case for the model photosensitiser, $[Ir(ppy)_2(dtbbpy)]PF_6$ (588 nm). However, the trinuclear complex (**C3**) exhibits orange luminescence (597 nm), which demonstrates the variable emission colours of iridium(III) complexes. Furthermore, there is only a minor red-shift observed upon functionalising the benzimidazole ligand with the benzyl moiety. DFT calculations conducted by Echevarría *et al.* on their structurally similar functionalised benzimidazole iridium(III) complexes to (**C1-C3**), revealed that the alkyl substituents on the *N^N* ancillary ligand do not actually participate in the LUMO orbital that is generally associated with the *N^N* ligand.[15]

Hence, it can be deduced that the benzyl group present on complexes **C2** and **C3** does not play a significant role in emission tuning for these complexes. This was also observed in work done by Sunesh *et al.* where they varied the alkyl chain length on the functionalised imidazole portion of the benzimidazole ancillary ligand of their iridium(III) complexes, which were being developed as LECs.[16] Sunesh *et al.* reported that for their iridium(III) complexes with modified alkyl chains, their complexes displayed similar emission characteristics with yellow emission and they went on to confirm that varying the alkyl chain lengths does not influence the emission maxima.[16] Thus, in the case for complexes **C2** and **C3**, the benzyl group may serve as a protecting shield for the photo-excited photosensitiser during photon absorption and emission processes and in so doing, suppress self-quenching processes, which has been postulated for other iridium(III) complexes that possess alkyl substituents on the *N^N* ligand.[15, 17]

More significant emission tuning *via* the *N^N* ligand could possibly be achieved by modifying the ancillary ligand in such a way, where the modification has a more direct influence on the LUMO. In literature, this has been done by changing the 2-pyridyl group attached to the benzimidazole scaffold to a more electron-donating thiazolyl group.[18] Alternatively, significantly red-shifted emission spectra have been obtained by extending the π-conjugation of the benzimidazole ligand.[19] Moreover, it is important to note that DFT calculations should be performed on the iridium(III) complexes (**C1**-**C3**) in an attempt to fully rationalise these trends and to provide a deeper understanding of these photophysical properties (as well as the subsequent electrochemical properties).

Table 3.1: Photophysical emission properties and ΔG_{ES} for complexes (**C1**-**C3**) as well as the model photoredox catalyst, $[Ir(ppy)_2(dtbbpy)]PF_6$.

Complex	**Crossover** λ (nm)	λ_{em} (nm) (Φ_{Em})[a]	τ_T (μs)	ΔG_{ES} (eV)
C1	447	582 (0.052)	0.272	2.26
C2	451	585 (0.076)	0.191	2.12
C3	442	597 (0.084)	0.241	2.08
$[Ir(ppy)_2(dtbbpy)]PF_6$	441	588 (0.032)	0.416	2.17

Parameters λ_{em} /nm, Φ_{Em}, and τ_T were measured in spectroscopic CH_3CN at ambient temperature. The crossover wavelength is the excitation wavelength, determined by the overlap of the respective UV-Vis absorption spectra. [a]$[Ru(bpy)_3]Cl_2$ (Φ_{Em} = 0.097) was used as the reference.[20, 21]

The emission quantum yields (Φ_{Em}) reported in Table 3.1 for the iridium(III) complexes were obtained using equation 3.1 and $[Ru(bpy)_3]Cl_2$ as a standard following the comparative literature method.[20, 21]

$$\Phi_{Em} = \Phi_{Em}^{Std} \left(\frac{F\, A_{std}\, n^2}{F_{std} A\, (n_{std})^2}\right) \tag{3.1}$$

The parameters of equation (3.1) include Φ_{Em}^{Std} which denotes the emission quantum yield of the Ru(II) standard, F/ F_{std} respectively refer to the areas under the emission curve for the tested complex and standard, and A/A_{std} are the absorbances of the tested complex and standard at the crossover wavelength. Finally, n/n_{std} denote the refractive indices of the solvent (acetonitrile) used for the tested complex and standard, respectively. The emission quantum yield is defined as the ratio of photons absorbed relative to the photons that are emitted *via* fluorescence or phosphorescence quenching.[22] That is, upon the absorption of a photon of light, a photosensitiser is energetically excited to a higher energy singlet (S_1) excited state, as is depicted in the Jablonski diagram in Figure 3.4.

Fluorescence exclusively refers to the radiative emission of light, which is associated with a spin allowed radiative electronic transition ($S_1 \rightarrow S_0$).[23] In the case of phosphorescence, emission is associated with the transition from $T_1 \rightarrow S_0$, where population of the T_1 state is achieved *via* ISC.[23] Upon analysis of the values of the emission quantum yields recorded in Table 3.1, it is evident that the iridium(III) complexes (**C1**-**C3**) and $[Ir(ppy)_2(dtbbpy)]PF_6$ have lower Φ_{em} (0.032-0.084) values when compared to the reference ruthenium(II) complex (Φ_{em} = 0.097). The values of Φ_{em} for complexes (**C1**-**C3**) are notably lower than the respective values of Φ_{Em} for structurally similar mononuclear and trinuclear benzimidazole functionalised ruthenium(II) photosensitisers that were synthesised by Prajith *et al.* (Φ_{em} range 0.096-0.117 in CH_3CN).[24] This could once again be attributed to the strong SOC of the iridium(III) centre compared to ruthenium(II) (ζ= 3903 *vs* 1042 cm^{-1} respectively),[13] which facilitates ISC from the S_1 state to triplet, T_1 state (Figure 3.4) and as a result there is a reduction of fluorescence or non-radiative processes for the iridium(III) complexes. In a photoredox catalysis context, population of the lower-energy triplet state (T_1) is desired, as it is associated with longer-lived excited states that are susceptible to electrochemical quenching with an appropriate electron donor/acceptor substrate, that is involved in the photocatalytic cycle.[23]

Another pertinent observation that can be made upon further examination of the quantum emission yields of complexes (**C**-**C3**), is that Φ_{Em} for the unfunctionalised benzimidazole complex **C1** (0.052), is lower than that of the two functionalised complexes **C2** (0.076) and **C3** (0.084). The greater Φ_{Em} value of complexes **C2** and **C3** could be due to the intramolecular rotation of the benzyl substituent in solution, which involves the dissipation of energy and therefore, with less energy, it makes it more challenging for the respective complexes to undergo ISC to the harder to access spin forbidden T_1 state. Consequently, spin allowed emissions *via* fluorescence are more probable. The dissipation of energy could be amplified in the trinuclear complex **C3**, where this complex has intramolecular rotation over three arms, accounting for the highest Φ_{Em} value seen across all of the iridium(III) complexes being investigated. Importantly, these photophysical dynamics are rather complex and thus these postulations do warrant deeper computational analysis.

Furthermore, the phenomenon whereby N-alkyl groups exhibit intramolecular rotation has been described in literature for structurally similar iridium(III) complexes.[15] It can thus be postulated that the nature of the functional group on the *N^N* ancillary ligand influences the efficiency of emission processes.[15]

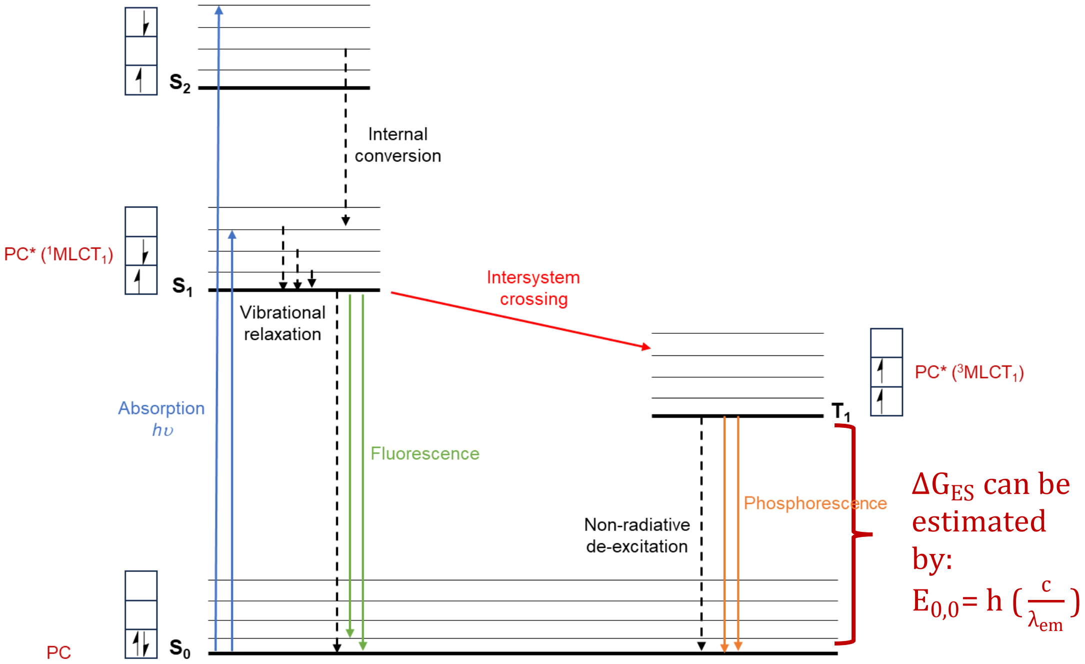

Figure 3.4. Jablonski diagram depicting the photophysical processes that occur in a transition metal photocatalyst upon excitation by light irradiation. Radiative and non-radiative processes are respectively represented by solid and dashed arrows. Modified from Omary *et al.*[23]

Another discernible trend in the photophysical properties listed in Table 3.1 is that lower Φ_{Em} values correspond to an increased triplet excited state lifetime. This is particularly noteworthy in the case of the model photosensitiser. [Ir(ppy)$_2$(dtbbpy)]PF$_6$ has the lowest Φ_{Em} reading (0.032), and the highest excited state lifetime (0.416 μs) when compared to the synthesised benzimidazole functionalised complexes (**C1**-**C3**). Notably, the excited state lifetime of the model photosensitiser is about double than that of the triplet lifetimes of complexes (**C1**-**C3**), which lie within a range of 0.191-0.272 μs.

Upon functionalising the benzimidazole ligand of complex **C1** (τ_T= 0.272 μs) to the corresponding mononuclear (**C2**) and trinuclear (**C3**) complexes, there is a decrease in the length of the triplet lifetimes to 0.191 μs and 0.241 μs respectively, and the decrease is accompanied by an increase in Φ_{Em} for each complex. The decrease in the triplet excited state lifetime upon *N*-functionalisation could also be a result of the intramolecular rotation of the benzyl substituent as discussed above. Although the iridium(III) complexes (**C1**-**C3**) do not have triplet excited state lifetimes that are as high as the lifetime for $[Ir(ppy)_2(dtbbpy)]PF_6$, their τ_T values are comparable to cyclometalated iridium(III) complexes reported in literature,[9] which have been sufficiently long-lived to undergo certain photocatalysed reactions.[15] The triplet state lifetime decay curves for the respective iridium(III) complexes are included in the appendix, Figures A35 (i)-(iv).

Moreover, the above photophysical properties highlight how essential appropriate ligand structure is when designing a photosensitiser. According to Caspar *et al.*, who performed in-depth photophysical studies on precious metal-based complexes, the goal when designing an efficient photosensitiser (efficient with respect to longer excited state lifetimes and higher luminescence quantum yields) is to increase the energy gap between the lowest lying MLCT state and the electronic ground state.[25] Following on from this point, the MC states of a photosensitiser should ideally lie above the lowest-lying MLCT state, so that emissive states can result.[9] In many precious metal polypyridyl complexes, these properties are enhanced by incorporating strong field ligands and rigid coordination environments.[26] Strong ligand fields can be achieved by incorporating strong σ-donors such as the cyclometalated 2-phenylpyridyl ligands, and strong π-acceptors (diimine ancillary ligand). Strong σ-donors act on the metal based e_g orbitals and raise their energy, whereas robust π-acceptors influence the metal's $t_{2}g$ orbitals and lower their energy.[26] Typically, complex rigidity is obtained by utilising bi-or tridentate chelated ligands, which offer limited degrees of conformational freedom upon coordination to the metal centre.[27] With these principles in mind, we can attempt to rationalise why the photophysical properties of the model photosensitiser, $[Ir(ppy)_2(dtbbpy)]PF_6$ are superior to that of the synthesised benzimidazole complexes (**C1**-**C3**).

Firstly, all these iridium complexes possess the same strong field σ-donating cyclometalated ligand, which means that this ligand should not significantly account for the observed differences in the Φ_{Em} values and triplet excited state lifetimes. However, these complexes obviously differ in the nature of their N^N π-acceptor ligand (4,4-di-*tert*-butyl-bipyridine ligand *vs* a benzimidazole motif). Benzimidazole ligands may be stronger π donors (i.e. weaker π acceptors) than pyridine. This is corroborated by crystal data that has been reported for other iridium(III) complexes bearing the 2,2'-pyridylbenzimdazole scaffold, as well as the crystallographic data obtained for complex **C2**.[15, 28] That is, within the 2,2'-pyridylbenzimdazole scaffold, the Ir-N$_{\text{benzimidazole}}$ bond length is shorter than that of the Ir-N$_{\text{pyridine}}$ bond.[15, 28] For complex **C2**, the Ir-N$_{\text{benzimidazole}}$ bond length was found to be 2.1323(17) Å and the Ir-N$_{\text{pyridine}}$ length was 2.1548(17) Å. The difference in these observed bond lengths is likely due to the higher π-donor ability of the benzimidazole portion (which possesses greater electron density) compared to pyridine.[15,28] Additionally, according to the spectrochemical series of ligands, bipyridines are renowned π-acceptors and occur higher up in the series than imidazole.[29] Secondly, the increase in conformational freedom due to rotational motion of the benzyl substituent means that the ideal rigid environment around the metal centre isn't as well maintained in complexes **C2** and **C3**, compared to **C1** and the model photosensitiser. Thus, the stronger π-acceptor ability and higher degree of rigidity of the N^N ancillary ligand in [Ir(ppy)$_2$(dtbbpy)]PF$_6$ could explain the more favourable photophysical properties that are observed for this complex. Again, these postulations do warrant further computational analysis and DFT calculations of the iridium(III) complexes.

Finally, the Gibbs free energy of the excited state (ΔG_{ES}) which is reported in the last column of Table 3.1, can be approximately calculated ($E_{0,0} = h(\frac{c}{\lambda_{em}})$) as it is based on the zero-zero excitation energy (E$_{0,0}$). This is the energy difference between the photoexcited photosensitiser in the triplet (T$_1$) state and the ground state (S$_0$), taking the maximum emission wavelength of the photosensitiser into account (Figure 3.4).[5] Ideally, as discussed above, these values should be larger to obtain a more broadly applicable photosensitiser. The calculated ΔG_{ES} of [Ir(ppy)$_2$(dtbbpy)]PF$_6$ (2.17 eV) is greater than the values obtained for complexes **C2** (2.12 eV) and **C3** (2.08 eV). This once again emphasises the importance of appropriate ligand choice in designing a photosensitiser, to obtain favourable photophysical properties. Furthermore, ΔG_{ES} assists in calculating the excited state redox potentials of the iridium(III) complexes, which is discussed in section 3.4 below.

3.3 Photostability experiments under visible light irradiation

The photostability of the benzimidazole functionalised iridium(III) complexes (**C1**-**C3**) in solution was monitored by ^{1}H NMR spectroscopy. The stacked ^{1}H NMR spectra (Figures 3.5-3.7) for the respective iridium(III) complexes (**C1**-**C3**) were recorded over a 48 hour period under blue LED light irradiation (405 nm, 18 W) in acetonitrile solutions at room temperature, with fan cooling on. These photostability experiments were performed in the EvoluChem™ PhotoRedOx Box, to mimic the conditions of the photocatalytic reactions. The results from the photostability study (Figures 3.5-3.7) show that the iridium(III) benzimidazole complexes appear to be remarkably stable for the 48 hour irradiation time period, with very little (complex **C1**) or no apparent structural change or degradation events occurring (complexes **C2** and **C3**). Furthermore, these results suggest that the synthesised iridium(III) complexes, (**C1**-**C3**) are well-suited to undergo the photocatalysed reactions under visible light (blue LED) irradiation at 405 nm, as they should not decompose during the course of the appropriate photocatalytic reactions.

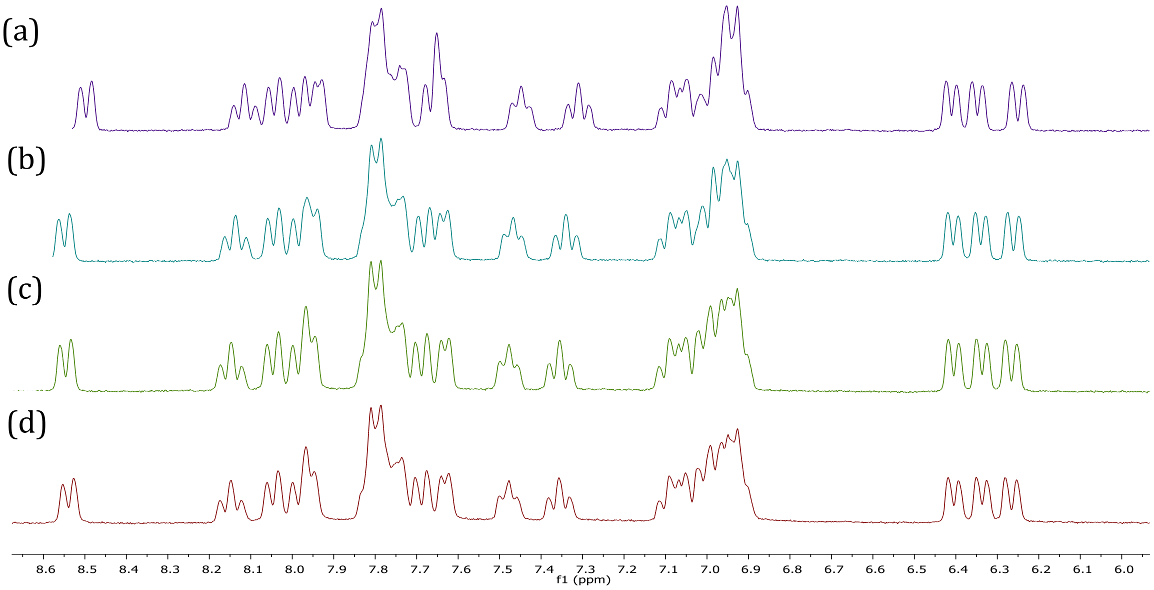

Figure 3.5. Stacked ^{1}H NMR spectra over the aromatic region of complex **C1** in CD_3CN. (a) t= 0 h, (b) t= 7.5 h, (c) t= 24 h and (d) t= 48 h.

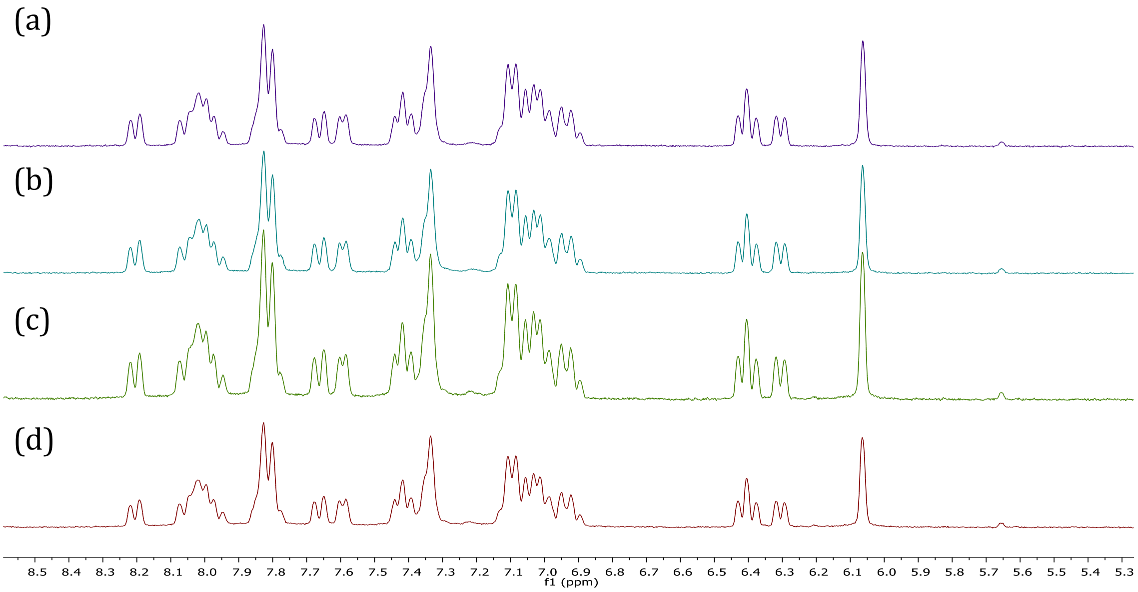

Figure 3.6. Stacked ^1H NMR spectra over the aromatic region of complex **C2** in CD_3CN. (a) t= 0 h, (b) t= 7.5 h, (c) t= 24 h and (d) t= 48 h.

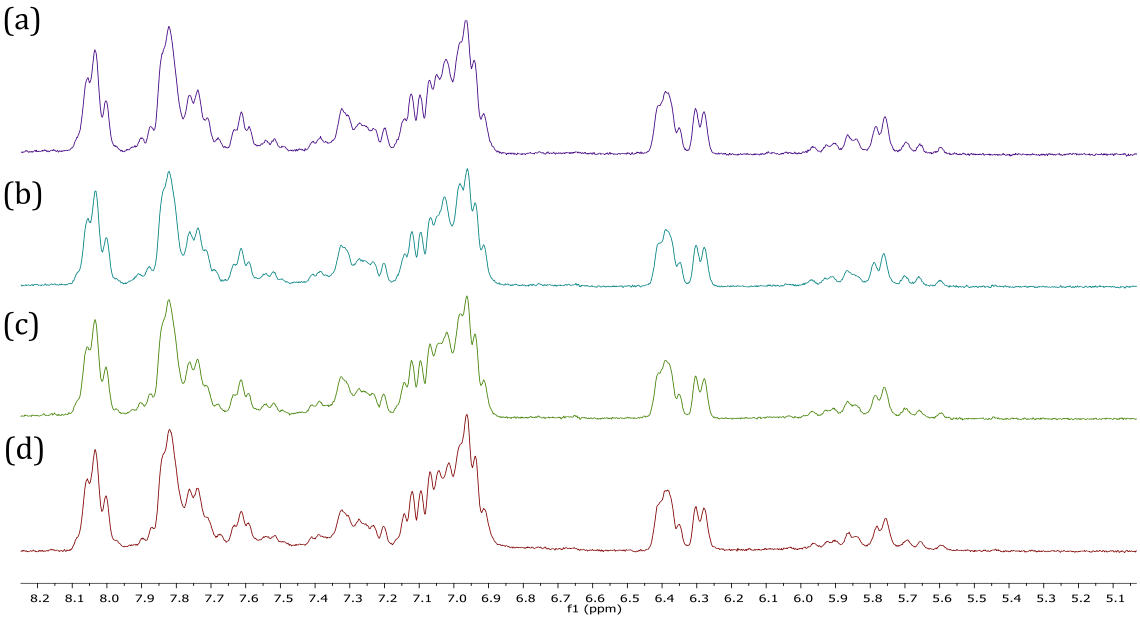

Figure 3.7. Stacked ^1H NMR spectra over the aromatic region of complex **C3** in CD_3CN. (a) t= 0 h, (b) t= 7.5 h, (c) t= 24 h and (d) t= 48 h.

3.4 Electrochemical properties

The electrochemical properties and redox potentials for complexes (**C1-C3**) as well as two prototypical complexes, [Ir(ppy)$_3$] and [Ir(ppy)$_2$(dtbbpy)]PF$_6$ were examined by cyclic voltammetry (Figure 3.8). Cyclic voltammetry was used to ascertain the oxidation and reduction abilities of the complexes' ground and excited states, and to determine whether these complexes display appropriate reversible electrochemical behaviour to undergo photoredox catalysed reactions. From the obtained voltammograms (Figure 3.8), it is evident that all three iridium(III) complexes (**C1-C3**) as well as [Ir(ppy)$_2$(dtbbpy)]PF$_6$ show a single reversible Ir^{III+}/Ir^{IV+} redox couple in the anodic region between +0.928 and +0.947 V (E$_{1/2}$ *vs* Ag/Ag$^+$ in CH$_3$CN). In the case of [Ir(ppy)$_3$], the reversible Ir^{III+}/Ir^{IV+} redox couple occurs at a much lower potential of +0.304 V (E$_{1/2}$ *vs* Ag/Ag$^+$) and an irreversible oxidative couple is observed at +0.882 V. DFT calculations performed for similar cationic cyclometalated iridium(III) complexes possessing a diimine ancillary ligand in literature, report that the HOMO is a mixture of the iridium(III) *d* orbitals (t$_2$g) and π orbitals of the *C^N* ligands.[11, 30]

Accordingly, the oxidation events can be ascribed to oxidation of the iridium(III) centre, to afford the [Ir^{IV}(*C^N*$^-$)$_2$(*N^N*)]$^{2+}$ ion or oxidation at one of the cyclometalated ligands to afford [Ir^{III}(C^N$^-$)(C^N$^\cdot$)(N^N)]$^{2+}$. The lower oxidative redox couples of [Ir(ppy)$_3$] when compared to the other iridium(III) complexes which possess a more π-withdrawing diimine ancillary ligand, could be due to the more electron-rich and σ-donating nature of the *N^C*-phenylpyridyl ligand in [Ir(ppy)$_3$] which increases the electron density at the metal centre and as a result, allows for easier oxidation. Furthermore, this emphasises how modification of the electrochemical properties can be achieved by judicious choice of ligand.

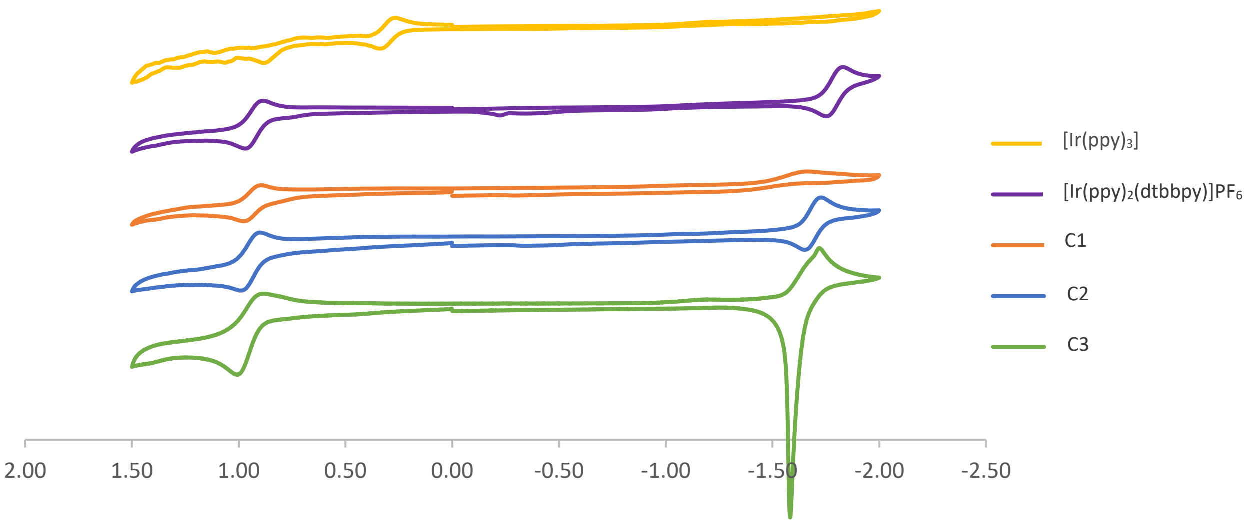

Figure 3.8. Cyclic voltammograms of the iridium(III) complexes (**C1-C3**) as well as the voltammograms for the prototypical complexes [Ir(ppy)$_3$] and [Ir(ppy)$_2$(dtbbpy)]PF$_6$ recorded in anhydrous CH_3CN solutions. $TBAPF_6/CH_3CN$ (0.1 M) electrolyte at room temperature with glassy carbon working electrode, Pt-wire counter electrode, Ag/$AgNO_3$ reference electrode and at a scan rate of 100 mV/s.

In the cathodic regions of the voltammograms it is apparent that complex **C2** and [Ir(ppy)$_2$(dtbbpy)]PF$_6$ display completely reversible Ir^{III+}/Ir^{II+} redox couples at -1.69 V and -1.79 V ($E_{1/2}$ *vs* Ag/Ag^+ in CH_3CN) respectively. An irreversible Ir^{III+}/Ir^{II+} redox couple is observed at -1.66 V for complex **C1** and no Ir^{III+}/Ir^{II+} redox couples are observed for [Ir(ppy)$_3$]. A rather unusual reduction peak is exhibited in the case of the trinuclear complex **C3**. That is, a very sharp and electrochemically unstable reduction event is observed at -1.65 V ($E_{1/2}$ *vs* Ag/Ag^+ in CH_3CN). Subsequently, the electrochemical properties of complex **C3** were also analysed *via* differential pulse voltammetry (Figure 3.9). In the cathodic region of Figure 3.9, a shoulder in the differential pulse voltammogram for complex **C3** is indeed observed at *ca* -1.63 V which could indicate that there is more than one electrochemically active species present upon the reduction of the trinuclear complex, **C3**.

Moreover, based on the topology of the LUMO, which has been reported to be localised predominantly on the *N^N* ancillary ligand, the Ir^{III+}/Ir^{II+} redox couples are attributed to step-wise reduction events centred in the *N^N* ligand.[11, 30] The source of these reduction events occurring on the *N^N* ligand is further substantiated by the cyclic voltammogram of [Ir(ppy)$_3$]. The absence of an *N^N* chelated ligand in [Ir(ppy)$_3$] is possibly why no reduction redox events are observed for this homoleptic triscyclometalated complex.

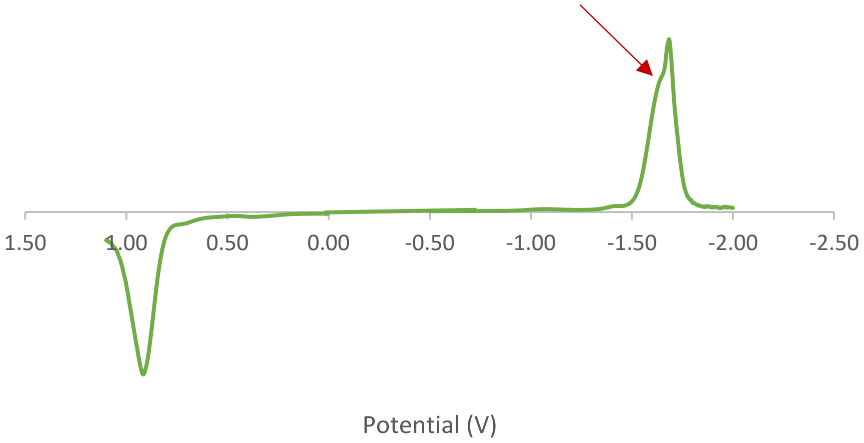

Figure 3.9. Differential pulse voltammogram of complex **C3**. TBAPF$_6$/CH$_3$CN (0.1 M) electrolyte at room temperature with glassy carbon working electrode, Pt-wire counter electrode, Ag/AgNO$_3$ reference.

The unusual reduction event of complex **C3** was subjected to further electrochemical experiments. Reithmeier *et al.* found a similar phenomenon occurring for their trinuclear iridium(III) complex, which displayed a reduction event that led to an almost three-fold negatively charged complex, that was no longer soluble in the acetonitrile electrolyte they were using.[31] Hence, they postulated that the trinuclear iridium species remained adsorbed on the surface of the electrode at a limited potential window, which resulted in the sharp intense feature upon reversing the direction of the potential scan.[31] Reithmeier *et al.* went on to confirm the adsorption behaviour by performing rotating disk electrode experiments in acetonitrile, where they found that the magnitude of the peak rose with increasing rotation rate, which is related to an increased concentration of the reduced species on the electrode surface.[31]

Subsequently, to avoid this adsorption behaviour, they changed their electrolyte to DMF where their highly reduced trinuclear complex remained stable. The findings of Reithmeier *et al*. were applied to the trinuclear complex (**C3**) of this study. The cyclic voltammogram of complex **C3** was rerun using anhydrous DMF as the electrolyte (Figure 3.10), where it is observed that the once highly unstable reduction event is now stabilised in the different electrolyte. Thus, complex **C3** must have previously been getting adsorbed on the electrode surface in acetonitrile, as was confirmed by the works of Reithmeier *et al*. Moreover, Figure 3.10 reveals a reversible Ir^{III+}/Ir^{II+} redox couple at -1.07 V ($E_{1/2}$ *vs* Ag/Ag^+ in DMF). The irreversible reduction event occurring at - 1.78 V could be due to the very unstable two electron reduction of the metal centre to the Ir(I) ion.

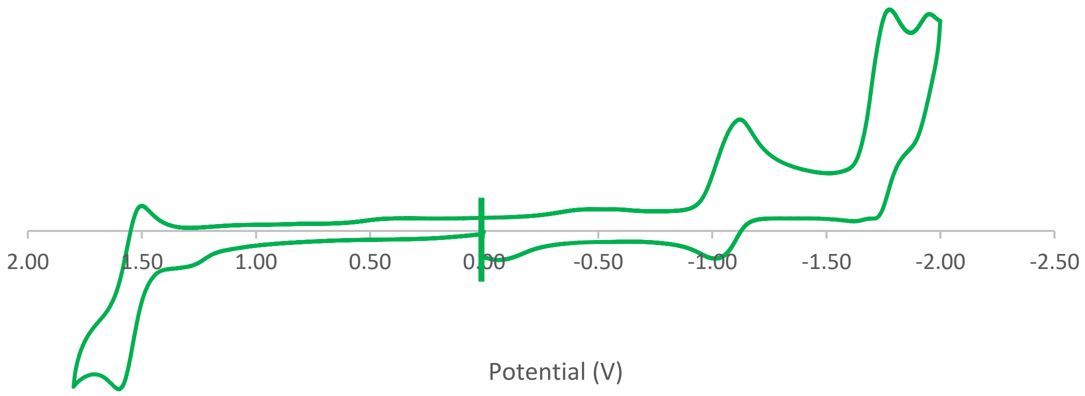

Figure 3.10. Cyclic voltammogram of trinuclear complex **C3** recorded in anhydrous DMF. $TBAPF_6$/DMF (0.1 M) electrolyte at room temperature with glassy carbon working electrode, Pt-wire counter electrode, $Ag/AgNO_3$ reference.

The concept of electrochemical reversibility is important in the context of photoredox catalysis. A photoredox catalyst needs to be adequately stable in its oxidised or reduced form for it to be regenerated over the course of the catalytic cycle. Additionally, the reversibility that is displayed in the Ir^{III+}/Ir^{II+} redox couple for complexes **C2** and **C3** compared to the irreversible Ir^{III+}/Ir^{II+} couple for complex **C1** shows the stabilising effect that the benzyl substituent has on the redox behaviour of the iridium(III) benzimidazole complexes *vs* the N-H moiety.

Table 3.2 summarises the electrochemical data obtained from the cyclic voltammograms for the ground state complexes, as well as including the potentials for the excited state iridium complexes. The approximate excited state redox potentials were calculated by relating ΔG_{ES} obtained from the emission studies to the ground state potentials from the voltammograms, using equations 3.2 and 3.3.[32]

$$E^{o\prime}(\mathrm{Ir}^{\mathrm{III+*/II+}}) = E^{o\prime}(\mathrm{Ir}^{\mathrm{III+/II+}}) + \Delta G_{\mathrm{ES}} \qquad \text{for reduction} \qquad (3.2)$$

$$E^{o\prime}(\mathrm{Ir}^{\mathrm{III+/IV+*}}) = E^{o\prime}(\mathrm{Ir}^{\mathrm{(III+/IV+}}) - \Delta G_{\mathrm{ES}} \qquad \text{for oxidation} \qquad (3.3)$$

Table 3.2: Half-wave potentials for the ground and excited states of the iridium(III) complexes

Complex	$E_{1/2}$(V) *vs* Ag/Ag$^+$ (V)					
	E_{ox1}	**E_{ox2}**	**$^*E_{ox}$**	**E_{Red1}**	**E_{Red2}**	**$^*E_{Red}$**
[Ir(ppy)$_3$]	+0.304	+0.882 (irrev.)	-1.94	-	-	-
[Ir(ppy)$_2$(dtbbpy)]PF$_6$	+0.928	-	-1.24	-1.79	-	+0.380
C1	+0.937	-	-1.32	-1.66 (irrev.)	-	+0.600
C2	+0.943	-	-1.18	-1.69	-	+0.430
C3	+0.947	-	-1.13	-1.65	-	+0.430
[a]**C3**	+1.55	-	-0.53	-1.12	-1.78 (irrev.)	+0.960

Data acquired in anhydrous 0.1 M CH_3CN solutions containing TBAPF$_6$ supporting electrolyte and analyte. $\mathrm{Ir}^{\mathrm{III+/IV+*}} = \mathrm{Ir}^{\mathrm{III+/IV+}} - \Delta G_{\mathrm{ES}}$. $\mathrm{Ir}^{\mathrm{III+*/II+}} = \mathrm{Ir}^{\mathrm{III+/II+}} + \Delta G_{\mathrm{ES}}$. Potentials were corrected to Ag/Ag$^+$ through an external ferrocene reference. [a]Data acquired in anhydrous 0.1 M DMF solution containing TBAPF$_6$ supporting electrolyte and analyte.

All the benzimidazole functionalised complexes (**C1**-**C3**), display reversible $\mathrm{Ir}^{\mathrm{IV+}}/\mathrm{Ir}^{\mathrm{III+}}$ redox couples which means they are able to undergo the oxidative quenching photoredox catalytic cycle.

However, for the photocatalytic reaction that was investigated in this study, the reversible Ir^{III+}/Ir^{II+} is the important redox couple to note as the photoredox catalyst is postulated to undergo a reductive quenching step upon reacting with the sacrificial electron donor, *N,N*-dicyclohexylmethylamine (Cy_2NMe).[33] Thus, the synthesised iridium(III) complexes (**C2** and **C3**) exhibit the ideal reversible electrochemical behaviour for photoredox reactions that undergo the reductive quenching cycle, and the photocatalytic reaction investigated herein (*vide infra*, Chapter 4). Furthermore, the excited-state oxidative redox potentials of the benzyl-substituted complexes **C2** (+0.430 V) and **C3** (+0.430 V) reveal that these complexes are marginally better oxidants when compared to the model photocatalyst, $[Ir(ppy)_2(dtbbpy)]PF_6$ (+0.380 V), and highlights the versatile electrochemical nature of the synthesised iridium(III) complexes. Finally, it is important to note that the electrochemical properties are only one indicator of whether a complex is a good photoredox catalyst or not. Additional thermodynamic factors (such as ΔG for the photoinduced electron transfer) can play an important role during the photocatalytic reaction too.[34] There are altogether a number of photophysical and electrochemical properties to keep in mind when designing a good photosensitiser.

3.5 Summary

In this chapter, the photophysical and electrochemical properties of the synthesised iridium complexes (**C1**-**C3**) was described. The UV-visible absorption spectra revealed that the iridium(III) complexes (**C1**-**C3**) absorb light in the visible region, with absorption bands in the 390-450 nm range. Accordingly, these complexes can be photoexcited upon the irradiation of blue light. Complexes (**C1**-**C3**) displayed unstructured emission bands, with the emission band maxima falling in the range of 582-597 nm and the emission of these complexes was attributed to the transition from the ^3MLCT state to the ground state. Quantum emission yields (0.052-0.084) and the triplet excited state lifetimes (0.191-0.272 μs) of the iridium(III) complexes (**C1**-**C3**) were found to be more favourable than similar ruthenium(II) complexes reported in literature, but inferior to that of the model photosensitiser, $[Ir(ppy)_2(dtbbpy)]PF_6$ (Φ_{Em}= 0.032 and τ_T= 0.416 μs).

The increased Φ_{Em} values and lower triplet excited state lifetimes of complexes (**C1**-**C3**) was ascribed to intramolecular rotations of the benzyl moiety in complexes **C2** and **C3**, as well as the difference in π-acceptor ability of the benzimidazole *vs* bipyridine motif. Furthermore, complexes (**C1**-**C3**) exhibit remarkable photostability under irradiation of 405 nm blue LED light for 48 h, which highlights their robust structure.

Regarding the electrochemical properties, the iridium(III) complexes (**C1**-**C3**) all displayed reversible $Ir^{III+/IV+}$ couples, which was assigned to oxidation of the metal centre or events centred on the *C^N* ligands. Reversible $Ir^{III+/II+}$ couples were only observed in the model photosensitiser and in complexes **C2** and **C3**, upon functionalisation of the benzimidazole ligand with the benzyl moiety. This demonstrated the stabilising influence of the benzyl group on the electrochemical properties. Complexes **C2** and **C3** were revealed to be marginally better oxidants than $[Ir(ppy)_2(dtbbpy)]PF_6$ ((+0.430 V *vs* +0.380 V, respectively for $^*E_{Red}$). The versatile and reversible electrochemical behaviour of complexes **C2** and **C3** underscores their potential as photoredox catalysts.

Finally, the photophysical and electrochemical properties discussed herein show the importance of judicious ligand choice when designing a photosensitiser. More noticeable influences on the photophysical properties, with respect to emission tuning could be achieved by direct ligand modifications which would form part of the *N^N* LUMO topology. Thus, the properties elucidated in this chapter, are altogether important to take into consideration as the efficiency of a photosensitiser is not determined by a single factor.

3.6 References

1. G. E. M. Crisenza and P. Melchiorre, *Nat. Commun.*, 2020, 11, 803.
2. T. M. Monos and C. R. J. Stephenson, in *Iridium(III) in Optoelectronic and Photonics Applications*, John Wiley & Sons Inc., Chichester, West Sussex, 2017, pp. 541-581.
3. M. H. Shaw, J. Twilton and D. W. C. MacMillan, *J. Org. Chem.*, 2016, 81, 6898-6926.
4. B. M. Hockin, C. Li, N. Robertson and E. Zysman-Colman, *Catal. Sci. Technol.* , 2019, 9, 889-915.

5. J. C. Deaton and F. N. Castellano, in *Iridium(III) in Optoelectronic and Photonics Applications*, John Wiley & Sons Inc., Chichester, West Sussex, 2017, pp. 1-69.
6. J. M. Younker and K. D. Dobbs, *J. Phys. Chem. C.*, 2013, 117, 25714-25723.
7. J.-H. Kim, S.-Y. Kim, Y.-J. Cho, H.-J. Son, D. W. Cho and S. O. Kang, *J. Phys. Chem. C.*, 2018, 122, 4029-4036.
8. J.-H. Kim, S.-Y. Kim, S. Jang, S. Yi, D. W. Cho, H.-J. Son and S. O. Kang, *Inorg. Chem.*, 2019, 58, 16112-16125.
9. F. Monti, A. Baschieri, L. Sambri and N. Armaroli, *Acc. Chem. Res.*, 2021, 54, 1492-1505.
10. S. DiLuzio, V. Mdluli, T. U. Connell, J. Lewis, V. VanBenschoten and S. Bernhard, *J. Am. Chem. Soc.*, 2021, 143, 1179-1194.
11. R. D. Costa, E. Ortí, H. J. Bolink, F. Monti, G. Accorsi and N. Armaroli, *Angew. Chem. Int. Ed.*, 2012, 51, 8178-8211.
12. T. Hofbeck and H. Yersin, *Inorg. Chem.*, 2010, 49, 9290-9299.
13. M. Montalti, A. Credi, L. Prodi and M. T. Gandolfi, 2006.
14. L. Flamigni, A. Barbieri, C. Sabatini, B. Ventura and F. Barigelletti, in *Photochemistry and Photophysics of Coordination Compounds II*, eds. V., Springer Berlin, Heidelberg, 2007, pp. 143-203.
15. I. Echevarría, M. Vaquero, B. R. Manzano, F. A. Jalón, R. Quesada and G. Espino, *Inorg. Chem.*, 2022, 61, 6193-6208.
16. C. D. Sunesh, G. Mathai and Y. Choe, *ACS Appl. Mater. Interfaces*, 2014, 6, 17416-17425.
17. W. He, D.-j. Zu, D.-m. Liu and R. Cheng, *Inorg. Chim. Acta*, 2011, 365, 78-84.
18. M. Martínez-Alonso, J. Cerdá, C. Momblona, A. Pertegás, J. M. Junquera-Hernández, A. Heras, A. M. Rodríguez, G. Espino, H. Bolink and E. Ortí, *Inorg. Chem.*, 2017, 56, 10298-10310.
19. L. He, J. Qiao, L. Duan, G. Dong, D. Zhang, L. Wang and Y. Qiu, *Adv. Funct. Mater.*, 2009, 19, 2950-2960.
20. B. Liu, S. Monro, M. A. Jabed, C. G. Cameron, K. L. Colón, W. Xu, S. Kilina, S. A. McFarland and W. Sun, *Photochem. Photobiol. Sci.* , 2019, 18, 2381-2396.
21. K. Suzuki, A. Kobayashi, S. Kaneko, K. Takehira, T. Yoshihara, H. Ishida, Y. Shiina, S. Oishi and S. Tobita, *Phys. Chem. Chem. Phys.*, 2009, 11, 9850-9860.

22. C. Würth, M. Grabolle, J. Pauli, M. Spieles and U. Resch-Genger, *Nat. Protoc.*, 2013, 8, 1535-1550.
23. M. Omary and H. H. Patterson, in *Luminescence Theory*, 2016, pp. 636-653.
24. N. U. Prajith, P. V. Priyanka and V. Alexander, *J. Biol. Inorg. Chem.*, 2022, 27, 357-372.
25. J. V. Caspar and T. J. Meyer, *J. Phys. Chem.*, 1983, 87, 952-957.
26. N. Sinha and O. S. Wenger, *J. Am. Chem. Soc.*, 2023, 145, 4903-4920.
27. C. Förster and K. Heinze, *Chem. Soc. Rev.*, 2020, 49, 1057-1070.
28. E. Zafon, I. Echevarría, S. Barrabés, B. R. Manzano, F. A. Jalón, A. M. Rodríguez, A. Massaguer and G. Espino, *Dalton Trans.*, 2022, 51, 111-128.
29. S. Yoichi, *Bull. Chem. Soc. Jpn.*, 1988, 61, 693-698.
30. R. D. Costa, E. Ortí, H. J. Bolink, S. Graber, S. Schaffner, M. Neuburger, C. E. Housecroft and E. C. Constable, *Adv. Funct. Mater.*, 2009, 19, 3456-3463.
31. R. O. Reithmeier, S. Meister, A. Siebel and B. Rieger, *Dalton Trans.*, 2015, 44, 6466-6472.
32. J. W. Tucker and C. R. J. Stephenson, *J. Org. Chem.*, 2012, 77, 1617-1622.
33. X. Fan, X. Gong, M. Ma, R. Wang and P. J. Walsh, *Nat. Commun.*, 2018, 9, 4936.
34. M. R. Schreier, B. Pfund, D. M. Steffen and O. S. Wenger, *Inorg. Chem.*, 2023.

Chapter 4: Evaluation of the iridium(III) complexes (C1-C3) as photosensitisers in the photoredox catalysed carboxylation of ketimines

4.1 Introduction

CO_2 emissions reached an alarming level of 34.9 Gt in 2021.[1] The vast excess of CO_2 in the atmosphere contributes to the greenhouse effect which in turn exacerbates the effects of global warming and climate change.[2] Climate change threatens the balance of natural ecosystems as well as endangering the lives of many species and humans.[3] In light of these environmental issues and with the 12 principles of Green Chemistry in mind, it is thus of utter importance that strategies are developed in an attempt to reduce the high atmospheric CO_2 concentrations. The difficulty however, in employing CO_2 storage or utilisation technologies lies in the inherently inert nature of CO_2.[4, 5] That is, CO_2 is the most oxidised form of carbon, is thermodynamically stable and kinetically inert and thus large energy input is required for the transformation of CO_2.[4] In the context of organic CO_2 transformation reactions, very reactive reagents are required in order for the direct incorporation of CO_2 into organic substrates.[5] Additionally, CO_2 fixation methods have been restrictive in that these methods required stoichiometric amounts of organometallic reductants or harsh reaction conditions.[6] There have been various alternative strategies explored in an attempt to circumvent the above mentioned difficulty, with photocatalytic techniques being at the forefront in this regard.[6]

Recently, photoredox catalysis has paved a way for the direct incorporation of CO_2 into organic molecules.[7] Photoredox catalysis has applications in direct carboxylation reactions and other variations of CO_2 fixation techniques into organic moieties, to afford an array of valuable synthetic building blocks such as amino acids, carboxylic acids, esters and heterocycles.[6] These transformations are possible because photoredox catalysis involves the creation of reactive intermediates (*via* SET events) which can readily react with CO_2, where this is not as easily achieved with other catalytic systems.[6]

Following on from the above mentioned CO_2 carboxylation reactions, is the photoredox catalysed fixation of CO_2 to afford unnatural α-amino acids.[8-13] Unnatural amino acids do not form part of the 20 naturally occurring amino acids, but many of them are chemically synthesised and they have an important role in medicinal chemistry.[14] Here, these unnatural amino acids act as key building blocks for complex molecules, fundamental components of peptidomimetic drugs and potential drugs on their own.[9, 15, 16] The "proof-of-concept" photocatalytic reaction investigated in the context of this project was based on the work of Walsh and coworkers,[7] the visible light mediated photoredox catalysed carboxylations of ketimines using CO_2, to afford valuable unnatural amino acid precursors. This overall photocatalytic reaction is depicted in Scheme 4.1.

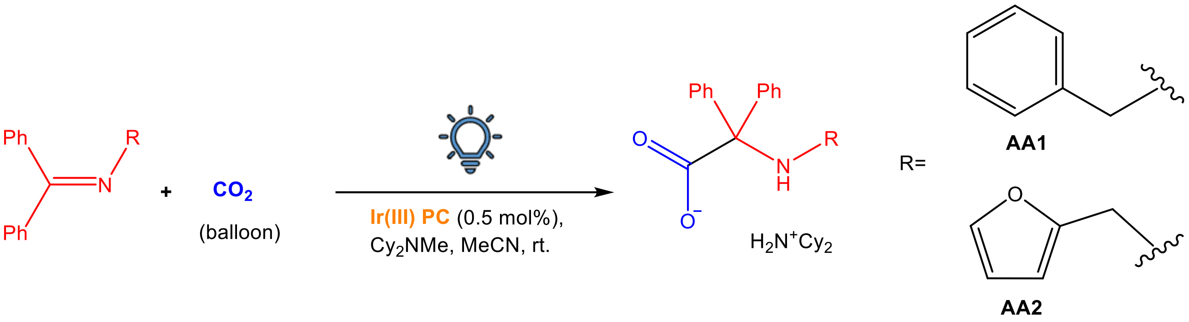

Scheme 4.1. Visible-light mediated photoredox catalysed carboxylations of ketimines utilising CO_2.[7]

A noteworthy aspect about this selected photocatalytic reaction is the greenness and great simplicity of the experimental setup. That is, a sustainable C1 source is utilised (1 atm. CO_2) which means that specialised equipment such as autoclaves are not necessary.[7] Additionally, the precipitation of the desired product allows for a straightforward work-up, where the product is obtained by vacuum filtration and tedious chromatographic purification is avoided.[7] Hence, valuable unnatural α-amino acid precursors can be synthesised *via* a reaction pathway that aligns with Green Chemistry principles. The photocatalytic activity of the synthesised benzimidazole complexes (**C1**-**C3**) in the context of the reaction presented in Scheme 4.1 is the focus of this chapter.

The catalytic activity was benchmarked against [Ir(ppy)$_2$(dtbbpy)]PF$_6$, which was the photocatalyst that yielded the best results for the reaction being investigated, as was discovered in the optimisation experiments conducted by Walsh and coworkers.[7] Our aim was to investigate the effect of a trinuclear photocatalyst (*vs* a mononuclear photocatalyst) on the photocatalytic activity, as well as the influence of the *N^N* ancillary ligand (bpy motif *vs* benzimidazole) on the photocatalytic activity and in doing so, evaluate the potential of cyclometalated benzimidazole iridium(III) complexes as photoredox catalysts.

4.2 Synthesis and characterisation of the ketimine precursors

The benzyl (**K1**) and furfuryl (**K2**) substituted ketimine precursors were synthesised following a standard Schiff-base condensation reaction, as outlined in Scheme 4.2.[17, 18] Ketimine precursors (**K1**) and (**K2**) were obtained in good yields of 70% and 51%, respectively. The postulated mechanism for this reaction is presented in Scheme 4.3.

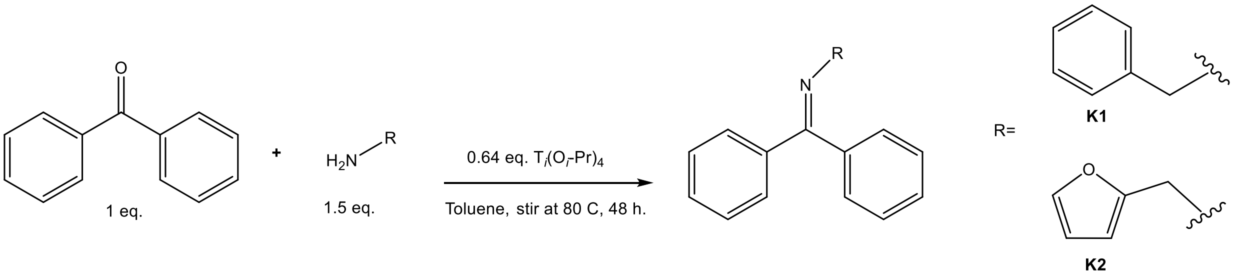

Scheme 4.2. Synthetic outline for the ketimine precursors, **K1** and **K2**.

The reaction is initiated by a nucleophilic attack of the lone pairs of electrons on the respective amine nitrogen at the electrophilic carbonyl centre of benzophenone. A proton transfer occurs, in which the negatively charged carbonyl oxygen accepts a proton from the positively charged R-N$^+$H$_2$ moiety. Thereafter, an iminium ion is formed and a hydroxyl group is eliminated. Once free, the hydroxyl group deprotonates the positively charged imine nitrogen, which results in the formation of the appropriate ketimine products (**K1, K2**) with water as a by-product. Furthermore, titanium isopropoxide (TTIP/T*i*(O*i*-Pr)$_4$) plays a crucial role during the course of the reaction.

That is, ketones are generally less reactive than aldehydes due to the carbonyl carbon being sterically hindered by the surrounding substituents, and the more electron-donating nature of alkyl substituents attached to the carbonyl centre render the carbonyl centre slightly less electrophilic. TTIP is highly Lewis acidic in nature- having the ability to accommodate 18 electrons and Ti(IV) is highly oxophilic in nature. Consequently, the titanium atom in TTIP can coordinate to the ketone oxygen of benzophenone and in so doing, make the carbonyl carbon more electrophilic and thus more susceptible to nucleophilic attack by the amine. Additionally, the reactions are carried out in an aprotic solvent toluene, where the "promoting" effect of TTIP could be enhanced as the aprotic environment allows for better coordination of the ketone oxygen with the titanium atom, which has been reported in literature.[19] Finally, the oxophilicity and Lewis acidic nature of TTIP result in it possessing excellent water scavenging abilities and thus TTIP is postulated to act as a dehydrating agent during the course of the reaction as well.[19, 20]

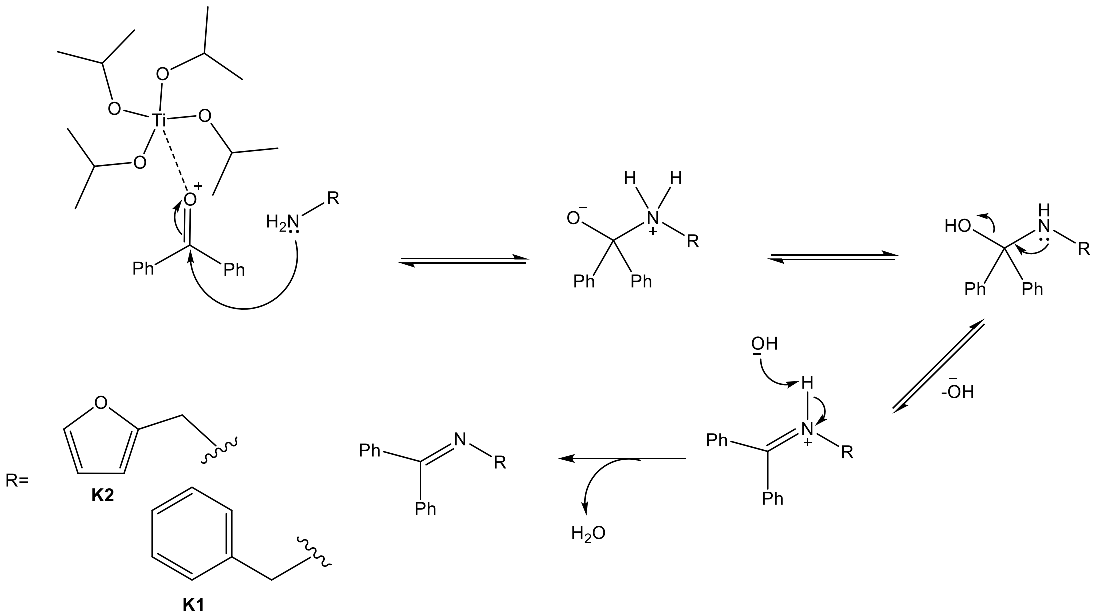

Scheme 4.3. Postulated mechanism for the synthesis of ketimine precursors, **K1** and **K2**.

Analysis of the ^{1}H NMR spectra (Figures 4.1 and 4.2) attests to the successful synthesis of the respective ketimine precursors, **K1** and **K2**. In both spectra the diagnostic methylene proton signals are present, integrating for two protons each and integration over the respective aromatic regions correlates with the expected number of aromatic protons. The ^{1}H NMR data also corroborates with the spectral data reported in literature for the respective ketimine compounds.[17, 18]

Infrared spectra (Figures A36 and A37) of compounds **K1** and **K2** reveal the characteristic $(C{=}N)_{imine}$ absorption bands at 1620 cm^{-1} and 1618 cm^{-1} respectively, which further substantiates the successful synthesis of the desired ketimine precursors.

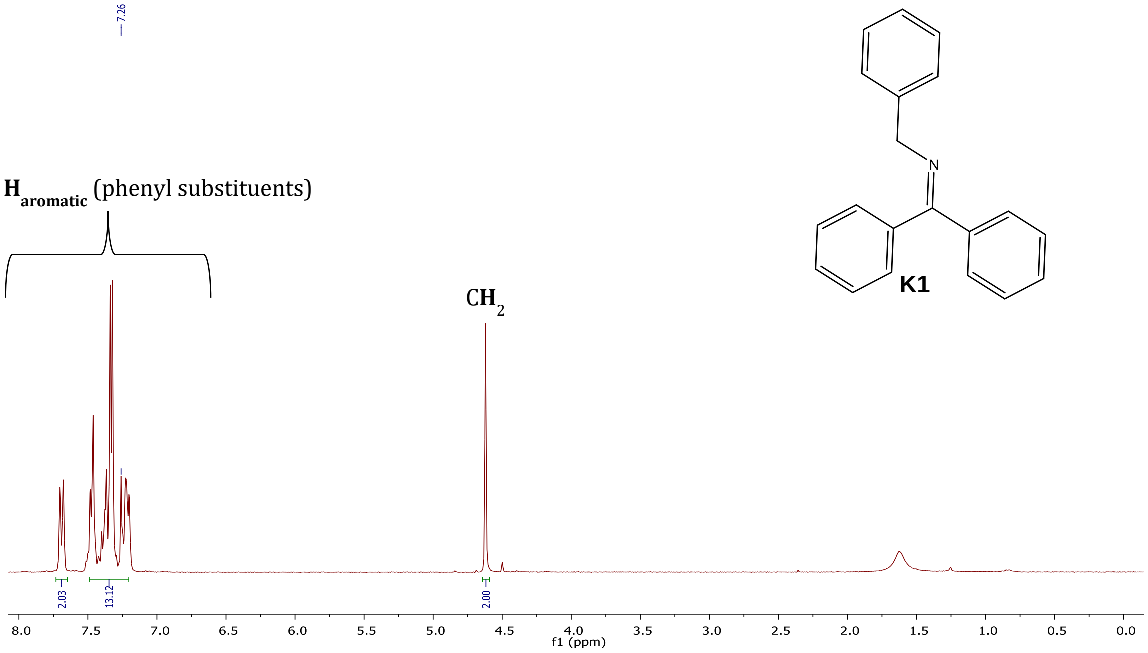

Figure 4.1. ^{1}H NMR spectrum of ketimine **K1**, in $CDCl_3$.

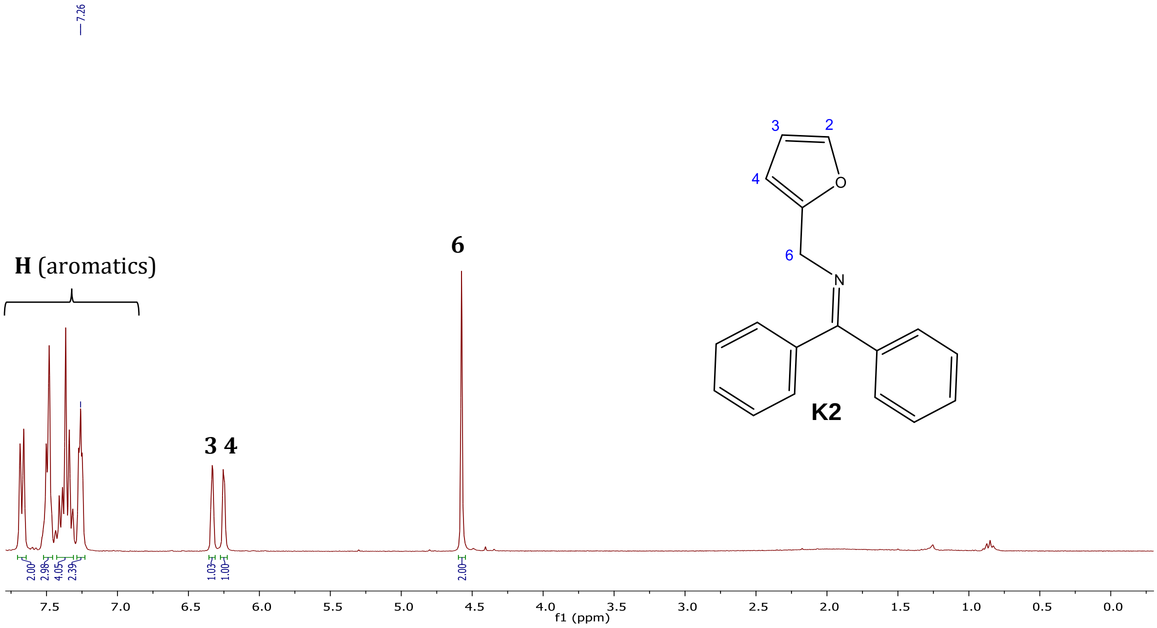

Figure 4.2. ^{1}H NMR spectrum of ketimine **K2**, in $CDCl_3$.

4.3 Photocatalytic results and discussion

4.3.1 Optimisation experiments and control photocatalytic reactions

A series of optimisation and control photocatalytic experiments were performed in order to obtain a standardised set of experimental conditions for the photocatalytic set-up used in our lab. Within the field of photoredox catalysis, a downfall of these light-mediated reactions is that crucial factors such as reproducibility, scalability and standardised light sources are often overlooked.[21] Key parameters that need to be taken into account for reaction optimisation include, the nature of the light source (wavelength and intensity), light uniformity, the reactor geometry as well as the temperature of the reaction.[21] Additionally, there is an increasing number of photoredox catalysed reactions reported to require a narrow temperature range for optimal results.[21-23] With these factors taken into consideration, we performed a series of optimisation experiments in the EvoluChem™ PhotoRedOx Box (Figure 4.3). This standardised set-up allowed for constant irradiance, uniform light irradiation (with limited diffraction), as well as a form of temperature control (fan cooling function). Optimisation studies were performed with the model photoredox catalyst, $[Ir(ppy)_2(dtbbpy)]PF_6$, a 405 nm (18 W) blue LED light source and with the benzyl substituted ketimine precursor (**K1**). Table 4.1 summarises the results obtained from these experiments.

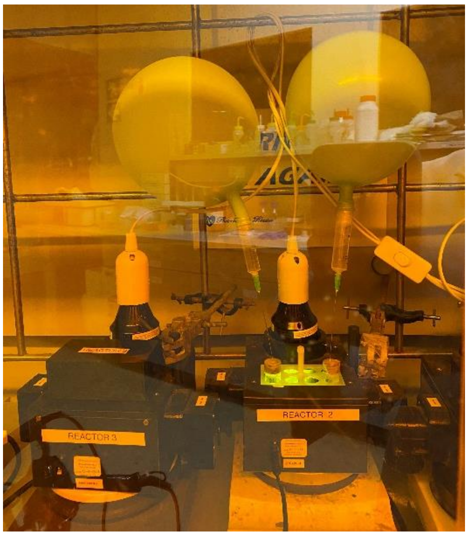

Figure 4.3. Typical set-up of the photocatalytic experiments performed in the EvoluChem™ PhotoRedOx Box.

Table 4.1: Optimisation experiments of the photoredox catalysed carboxylation reactions of the benzyl substituted ketimine (**K1**) using CO_2

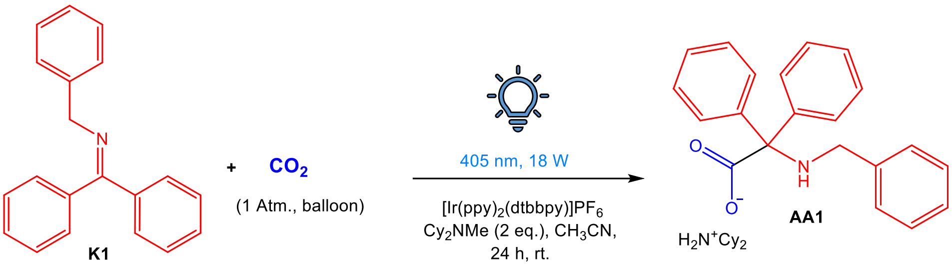

Entry	Ketimine K1 (1 eq.)	Cy_2NMe (2 eq.)	CH_3CN (mL)	Catalyst loading	Yield (%) of product AA1
1	0.0541 g, 0.199 mmol	85.4 μL 0.398 mmol	1.20	1.0 mol% 1.82 mg	60
2	0.0529 g, 0.195 mmol	83.5 μL 0.390 mmol	2.00	1 mol% 1.80 mg	60
3	0.0545 g, 0.201 mmol	86.0 μL 0.402 mmol	2.00	0.5 mol% 0.940 mg	57
4	0.0571 g, 0.210 mmol	90.1 μL 0.420 mmol	2.00	0.5 mol% 0.96 mg	62
5	0.0524 g, 0.193 mmol	82.7 μL 0.386 mmol	2.00	0.5 mol% 0.88 mg	67
6	0.102 g, 0.374 mmol	160.4 μL 0.749 mmol	4.00	0.5 mol% 1.71 mg	58
7	0.507 g, 1.87 mmol	0.800 mL 3.73 mmol	18.4	0.5 mol% 8.53 mg	65

Optimisation experiments conducted with $[Ir(ppy)_2(dtbbpy)]PF_6$, under irradiation with a 405 nm (18 W) blue LED light over 24 h. Fan cooling on during the 24 h irradiation time.

There are a number of observations that can be made upon examination of the experimental data collated in Table 4.1. Changing the concentration of the reaction mixture (1.2 mL *vs* 2.0 mL CH_3CN) does not significantly affect the reaction yields, and this is also the case when the iridium(III) photocatalyst loading is doubled from 0.5 mol% to 1.0 mol%. Noteworthy, entries 1-5 of Table 4.1 reveal a consistent set of results over multiple reaction run times when reactions were performed on a *ca* 50 mg scale, with yields of the amino acid salt product (**AA1**) occurring in the range of 57-67%. Additionally, increasing the scale of the reaction to *ca* 100 mg and 500 mg (entries 6 and 7 respectively), yield the desired amino acid product in respective yields of 58% and 65%, which is in line with the yields obtained for entries 1-5. This highlights the reproducible and practical nature of the proof-of-concept reaction. The benzyl substituted amino acid salt product (**AA1**) was obtained as a white solid and the ^1H NMR spectrum of this product is presented in Figure 4.4. Analysis of the ^1H NMR data (Figure 4.4) reveals that the aromatic protons corresponding to the phenyl substituents are present, integrating for 15 protons and there has been an upfield shift of the methylene protons (*) from 4.64 ppm in the ketimine precursor (**K1**) to 3.35 ppm in the amine-functionalised product. This is due to the more electron-withdrawing nature of the ketimine when compared to the amine functional group (more electron-donating).

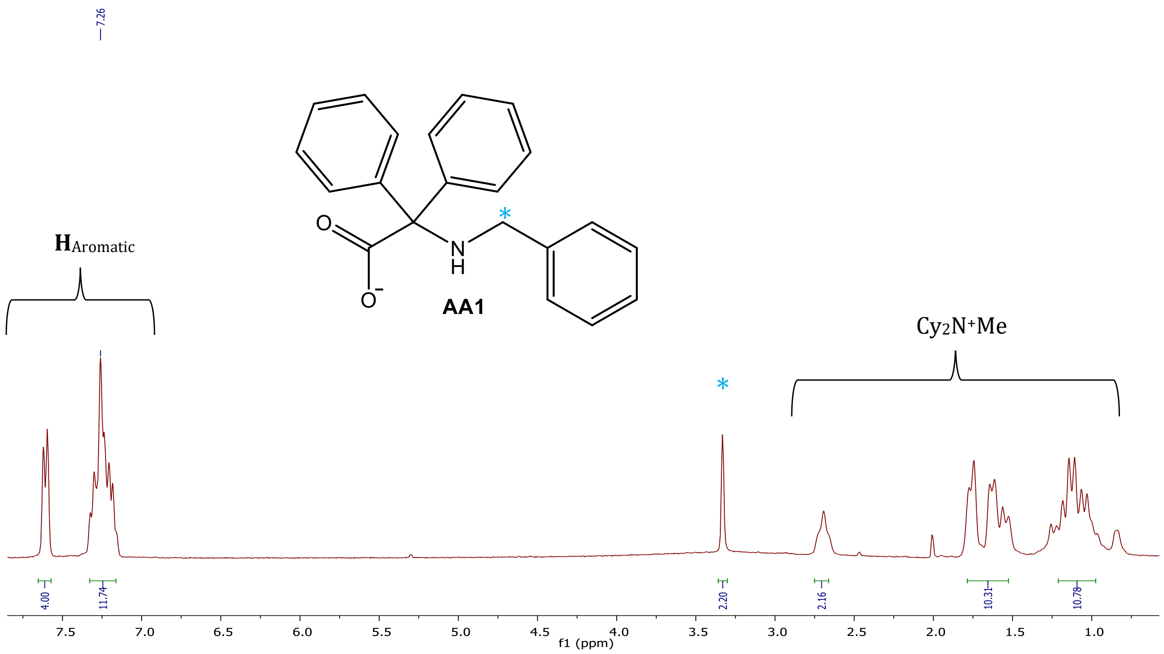

Figure 4.4. ^1H NMR spectrum of the benzyl substituted amino acid salt product (**AA1**), in $CDCl_3$.

Moreover, the spectral data correlates with what has been reported in literature for this compound.[7] With the optimised conditions established, the substrate scope of the reaction was expanded to the furfuryl substituted ketimine (**K2**). Table 4.2 summarises the results obtained from the reaction runs with ketimine **K2**.

Table 4.2: Results obtained from the photoredox catalysed carboxylation reactions of the furfuryl substituted ketimine (**K2**).

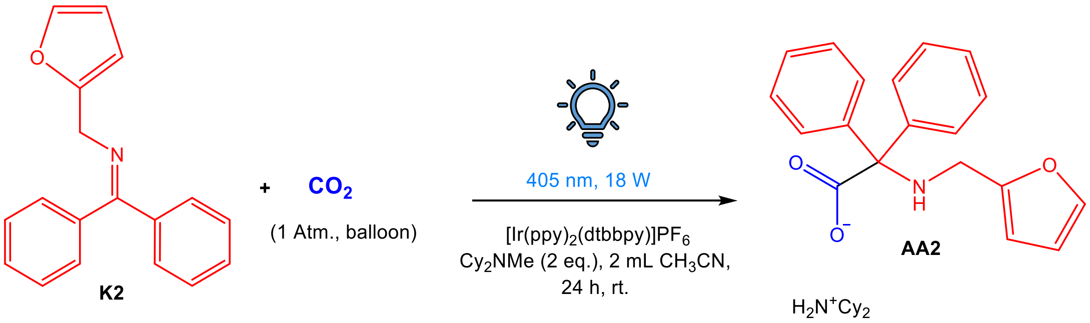

Entry	**Ketimine K2 (1 eq.)**	**Cy_2NMe (2 eq.)**	**CH_3CN (mL)**	**Catalyst loading**	**Yield (%) of product AA2**
1	0.0546 g, 0.209 mmol	89.5 mL 0.418 mmol	2.00	0.5 mol% 0.96 mg	66
2	0.0551 g, 0.211 mmol	90.3 mL 0.422 mmol	2.00	0.5 mol% 0.99 mg	76
3	0.0556 g, 0.213 mmol	91.1 mL 0.426 mmol	2.00	0.5 mol% 0.98 mg	63

Optimised conditions (based on a ~50 mg scale of ketimine): 2 eq. Cy_2NMe, 2 mL CH_3CN, 0.5 mol% loading of $[Ir(ppy)_2(dtbbpy)]PF_6$ and irradiation with a 405 nm (18 W) blue LED light over 24 h. Fan cooling on during the 24 h irradiation time.

The desired furfuryl substituted amino acid salt product (**AA2**) was obtained as a white solid in yields ranging from 63-76% over the three reaction runs, as outlined in Table 4.2. The ^{1}H NMR spectrum of the product obtained from reaction runs 1-3 with the furfuryl substituted ketimine is depicted in Figure 4.5 and supports the successful synthesis of the desired product, **AA2**. The aromatic protons can be accounted for, as well as the presence of the furfuryl moiety which is evidenced by the peaks occurring at 6.25 ppm (H_3) and 6.11 ppm (H_4). The ^{1}H NMR data also corroborates with what has been reported in literature for this compound.[7] Furthermore, the results that are collated in Table 4.2, again attest to the reproducible nature of this photoredox catalysed reaction, particularly when varying the substrate scope of the reaction.

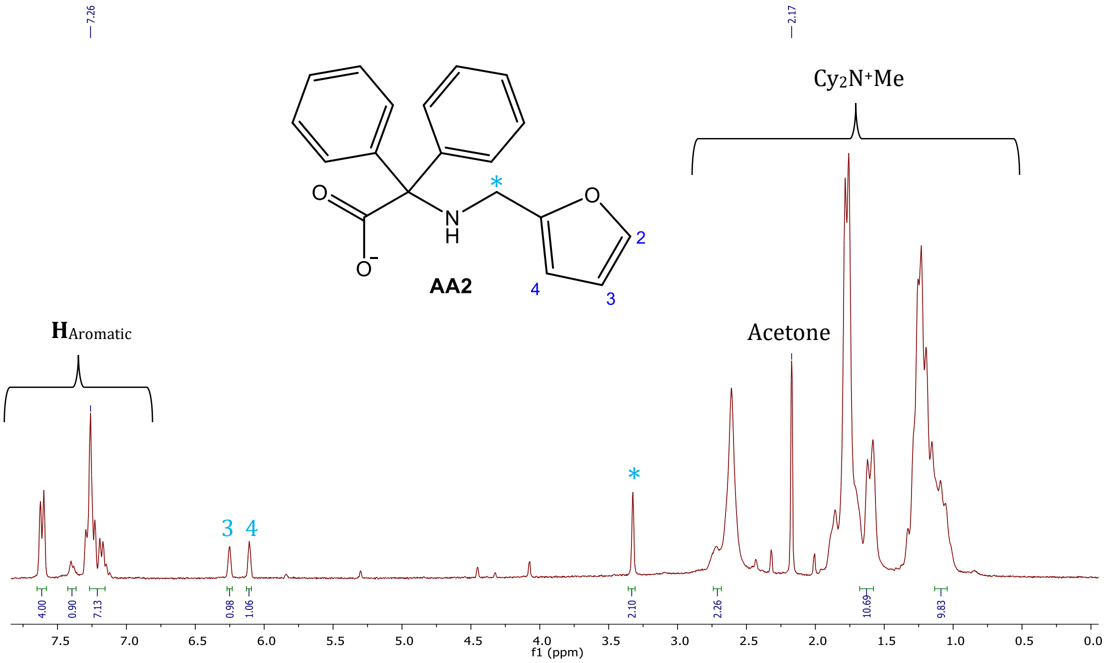

Figure 4.5. ^{1}H NMR spectrum of the furfuryl substituted amino acid salt product (**AA2**), in $CDCl_3$.

The yields for the benzyl substituted amino acid salt product (**AA1**) obtained for our reactions (57-67% range) are lower than the yield reported in literature (91%).[7] This trend was also observed with the furfuryl substituted amino acid product (**AA2**) with our yields ranging between 63-76% *vs* 95% obtained in literature.[7]

The lower product yields for the photocatalytic reactions we performed may be attributed to differences in the experimental set-up. Although we kept our experimental parameters as close as possible to the details reported in literature, our blue LED light source was of slightly lower intensity (18 W) compared with the light utilised by Walsh and coworkers (20 W). The variable nature of photoredox catalysed reactions as discussed above, where certain reactions require a highly specific set of conditions could be another contributing factor for the difference in these observed yields. More importantly, from our optimisation experiments, we established a consistent and reproducible set of results from the photocatalytic setup.

The choice of sacrificial electron donor, *N,N*-dicyclohexylmethylamine (Cy_2NMe) was based on previous optimisation studies by Walsh and coworkers,[7, 17] where they tested a series of other amines (trimethylamine, triethylamine and *N,N*-diisopropylethylamine). Cy_2NMe is obviously the most sterically hindered amine compared to the other amines tested and it was found that the sterically bulky nature of this amine (Cy_2NMe) serves to protect the amino acid product from decarboxylation.[7, 17] Consequently, during the course of these photocatalytic reactions, the amino acid salt product precipitates out of the initially homogeneous reaction solution. This precipitation of the desired product was not detected in the case of the other, less sterically hindered amines.

Finally, a series of control reactions was conducted using our PhotoRedOx Box photocatalytic setup to rule out any underlying factors that could be influencing the results. Again, the benzyl substituted ketimine (**K1**) and the model photoredox catalyst, $[Ir(ppy)_2(dtbbpy)]PF_6$ were utilised (except in the reaction with no photosensitiser). Four independent control reactions were performed with no photoredox catalyst, in the absence of light, with no sacrificial electron donor (Cy_2NMe) and with no CO_2. The ^1H NMR spectra (Figures A44-A47) of the products from these individual studies show that there is no formation of the desired amino acid salt product. That is, the spectral data presented in Figures A44-47, correlate with the ketimine and/or the Cy_2NMe starting materials. Thus, the control reactions confirm that the photocatalyst, light source, sacrificial electron donor and CO_2 are all together important for the reaction to occur and that the reaction is not independently promoted by each of these individual variables.

4.3.2 Photocatalytic reaction results with complexes C1-C3 as photoredox catalysts

With a set of consistent and reproducible results obtained from the optimisation studies, and the control experiments, the synthesised benzimidazole complexes (**C1**-**C3**) were evaluated in the context of the visible light mediated photoredox catalysed carboxylation reaction of ketimines (**K1** and **K2**). The reactions conducted with complexes (**C1**-**C3**) were all performed twice and with the established optimised conditions, as presented in Scheme 4.4.

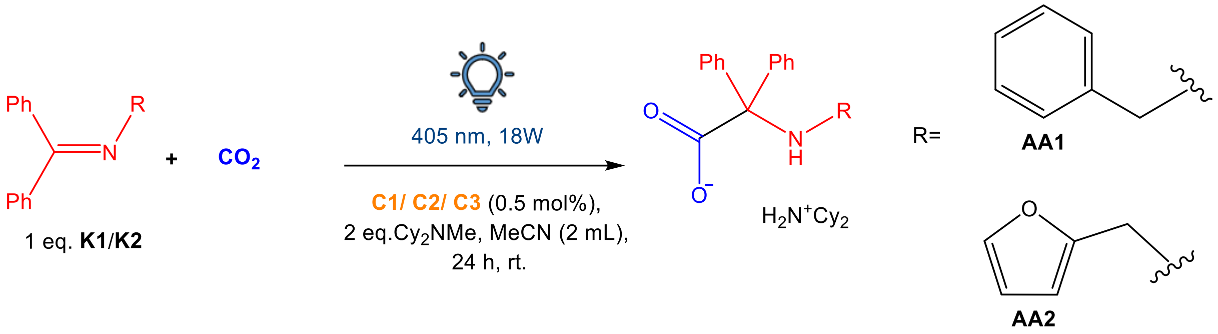

Scheme 4.4. Visible light mediated photoredox catalysed carboxylation reaction of ketimines, with the optimised reaction conditions.

4.3.2.1 Results obtained from complex (C1) as the photoredox catalyst

The stacked ^{1}H NMR spectra obtained from the two reaction runs with complex **C1** as the photoredox catalyst, and the benzyl substituted ketimine (**K1**) is shown in Figure 4.6. The products from the two respective reactions were obtained as white solids, after filtration. An interesting observation upon analysis of the stacked spectra presented in Figure 4.6, is that the product obtained from the reaction runs with complex **C1** as the photoredox catalyst, does not correlate with the structure of the desired (benzyl substituted) amino acid salt. Additionally, the product obtained from complex **C1** is different to the ketimine precursor, **K1**. These two observations suggest that there is a photocatalytic reaction occurring but something different (mechanistically) must be happening in order to obtain the distinct product. The mechanism, proposed by Walsh and coworkers for the selected proof-of-concept reaction is presented in Scheme 4.5.[7]

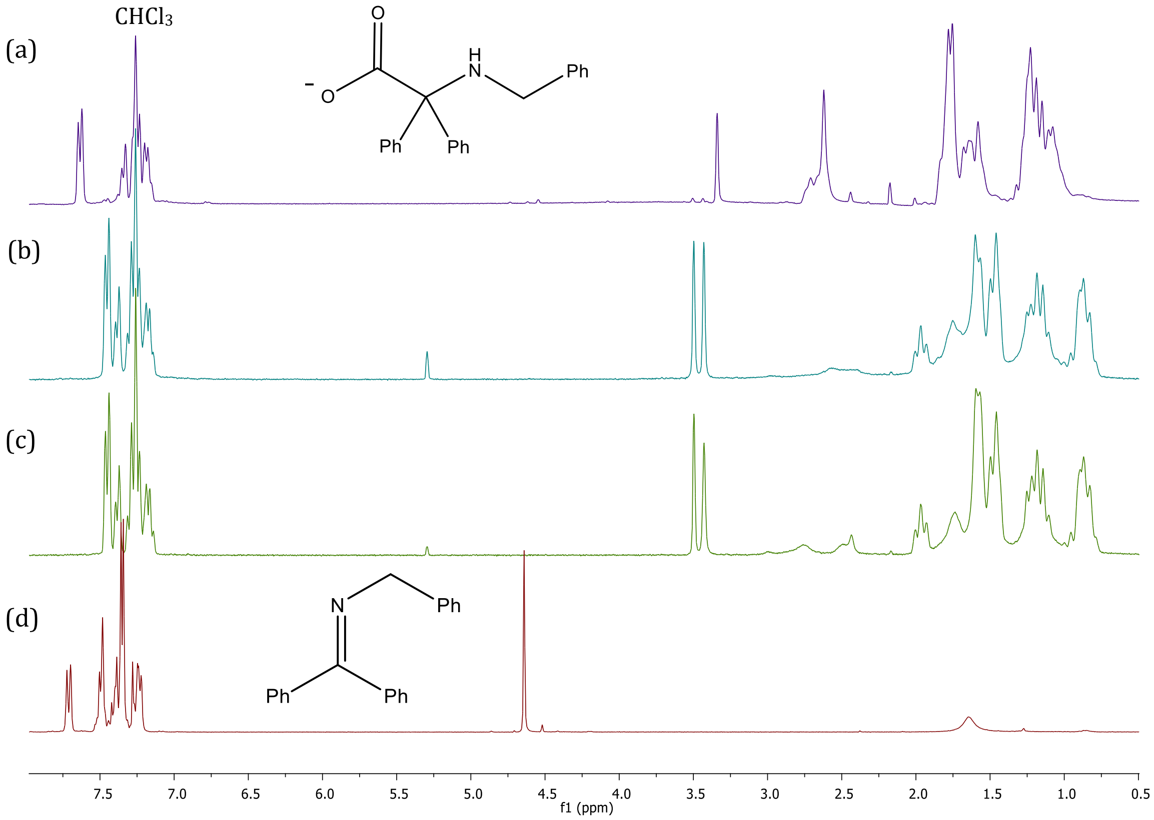

Figure 4.6. Stacked ^{1}H NMR spectra of (a) benzyl substituted amino acid product, (b) reaction run 1 product with complex **C1**, (c) reaction run 2 product with complex **C1** and (d) benzyl substituted ketimine precursor **K1**, in $CDCl_3$.

The reaction is initiated by the absorption of visible light (blue LED) by the $[Ir]^{3+}$ photocatalyst to form its excited state ion, $[Ir]^{3+*}$. In its excited state, the iridium(III) photoredox catalyst can accept an electron from the sacrificial electron donor, Cy_2NMe in a SET process, to afford the radical cation intermediate, $[Cy_2NMe]^+$. The resulting amine radical cation ($[Cy_2NMe]^+$) is proposed to coordinate with the ketimine to form a 2-centre-3-electron bond, which facilitates reduction by $[Ir]^{2+}$ to form the key radical anion intermediates A/B and in so doing, regenerating the ground state catalyst, $[Ir]^{3+}$. Due to the high reactivity of the N-radical resonance contributor B, it is postulated that B is quickly quenched by the amine radical cation *via* a hydrogen atom transfer (HAT), to afford the α-amino carbanion intermediate, C. Finally, intermediate C acts as a strong nucleophile and attacks CO_2 to yield the amino acid salt product, and the iminium ion ($Cy_2N^+CH_2$) is proposed to react with adventitious water to generate the counter ion, $Cy_2N^+H_2$.[7]

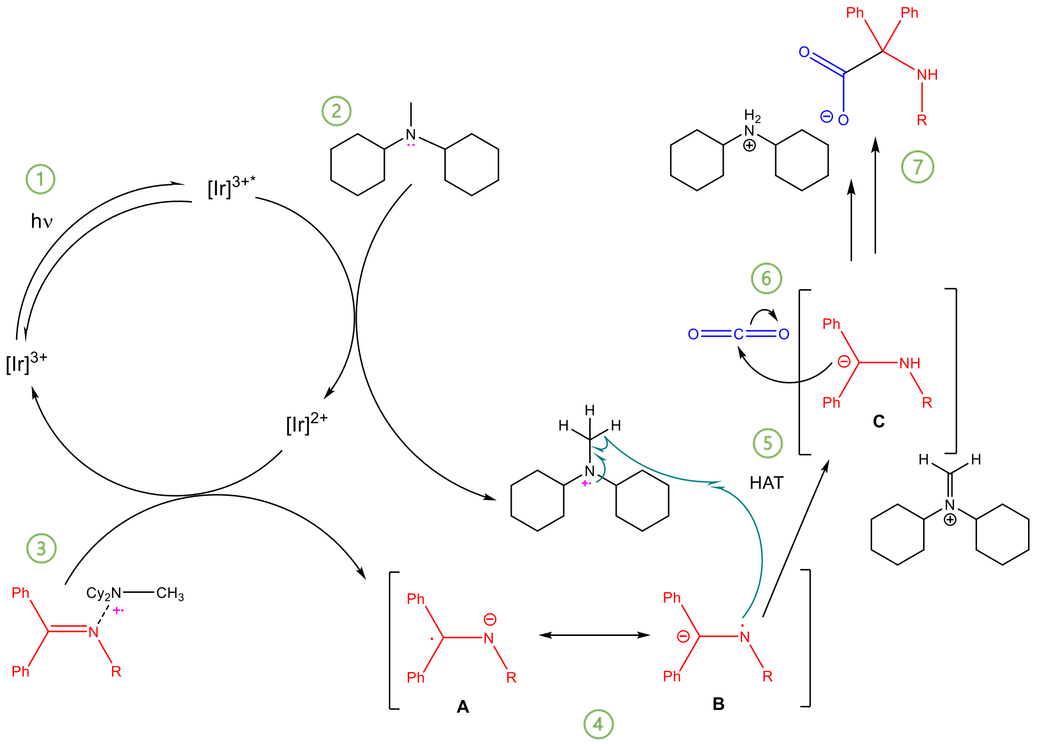

Scheme 4.5. Proposed mechanism for the visible light mediated photoredox catalysed carboxylations of ketimines using CO_2.[7]

The electrochemical properties that were determined for complex **C1** assist in rationalising the above photocatalytic reaction outcome. That is, the unfunctionalised benzimidazole complex, **C1** was found to display an irreversible Ir^{III+}/Ir^{II+} reduction couple at -1.66 V (Section 3.4, Chapter 3) and as seen in Scheme 4.5, the reaction is postulated to undergo the reductive quenching photocatalytic cycle. As discussed in Section 3.4, the concept of reversibility is import in the context of photoredox catalysis specifically, as a photoredox catalyst needs to be adequately stable in its oxidised or reduced form for it to be regenerated over the course of the catalytic cycle. Thus, in the above photocatalytic reaction when complex **C1** is reduced to Ir^{II+}, its irreversible (reduction) electrochemical behaviour may result in this complex being unable to be regenerated back to its starting Ir^{III+} oxidation state. This would in turn influence the product obtained during the photocatalytic cycle. Consequently, the expected benzyl substituted amino acid salt product (**AA1**) is not formed when complex **C1** is used as the photoredox catalyst for this tested reaction.

Furthermore, when the reaction substrate was changed to the furfuryl substituted ketimine (**K2**), a similar product outcome is obtained, as was observed in the reactions performed with complex **C1** above (with the benzyl substituted ketimine). That is, from the stacked ^{1}H NMR spectra presented in Figure 4.7 it is evident that once again, a distinct product is formed from the two reaction runs with complex (**C1**) used as the photoredox catalyst. The products obtained from reaction runs 1 and 2 are "distinct" in that the spectroscopic data for these products do not corroborate with the desired furfuryl substituted amino acid salt product and they differ from the ketimine precursor. Thus, the above photocatalytic results obtained with the complex **C1** highlights the importance of the concept of reversible electrochemical behaviour, which is a requirement to obtain the desired amino acid products (**AA1** and **AA2**), specifically.

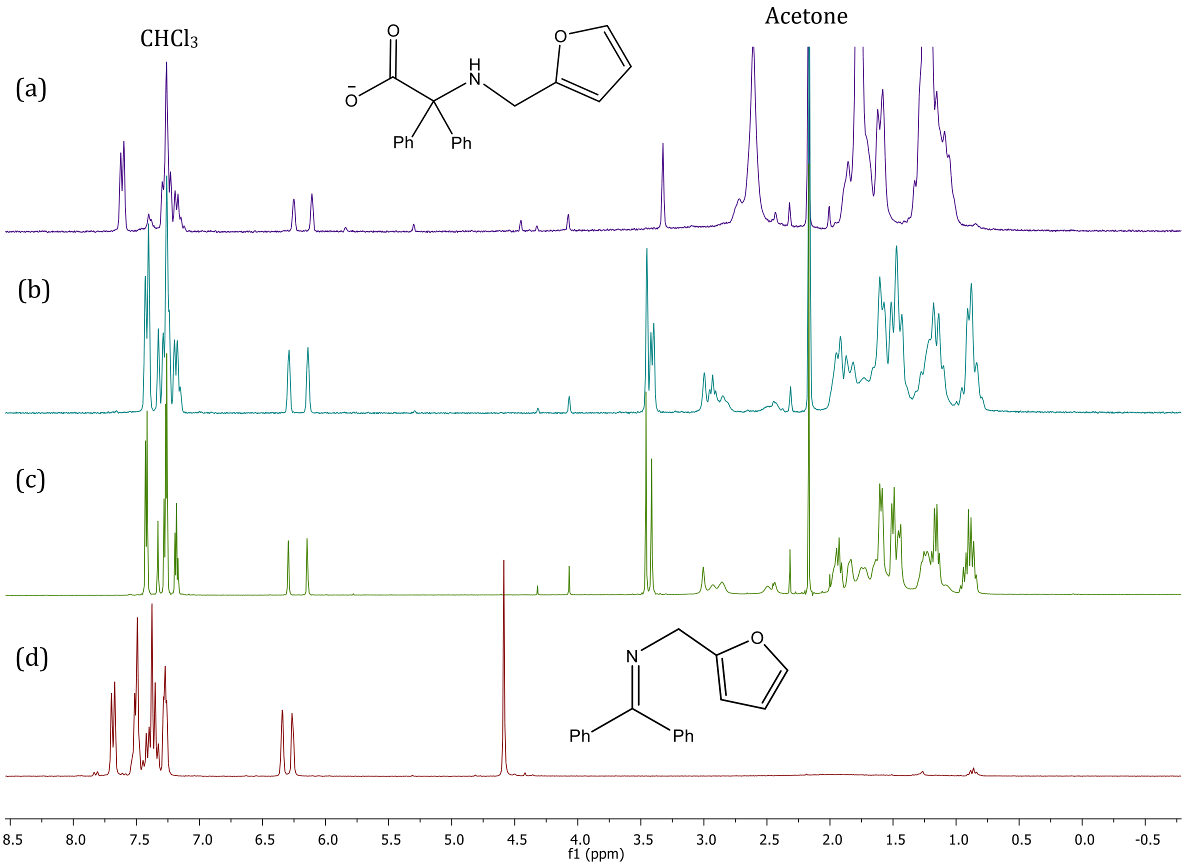

Figure 4.7. Stacked ^{1}H NMR spectra of (a) furfuryl substituted amino acid product, (b) reaction run 1 product with complex **C1**, (c) reaction run 2 product with complex **C1** and (d) furfuryl substituted ketimine precursor **K2**, in $CDCl_3$.

4.3.2.2 Results obtained from complex (C2) as the photoredox catalyst

The benzyl functionalised benzimidazole complex (**C2**) was the next photosensitiser evaluated in the selected proof-of-concept photocatalytic reaction. As before, the first substrate to be investigated in the context of this reaction was the benzyl substituted ketimine precursor (**K1**). The stacked ^{1}H NMR spectra from the two reaction runs performed with complex **C2** as the photoredox catalyst are shown in Figure 4.8. Examination of the ^{1}H NMR spectra (Figure 4.8), shows two products being formed during the respective photocatalytic reaction runs. The first product correlates with the desired benzyl substituted amino acid product, with the diagnostic peaks being the most downfield doublet at ~7.60 ppm (integrating for four protons) and the methylene singlet integrating for two protons at ~3.35 ppm. The spectroscopic data for the second product, interestingly, correlates with the product that was obtained when complex **C1** was used as the photoredox catalyst, with the benzyl substituted ketimine (Figure 4.6 above).

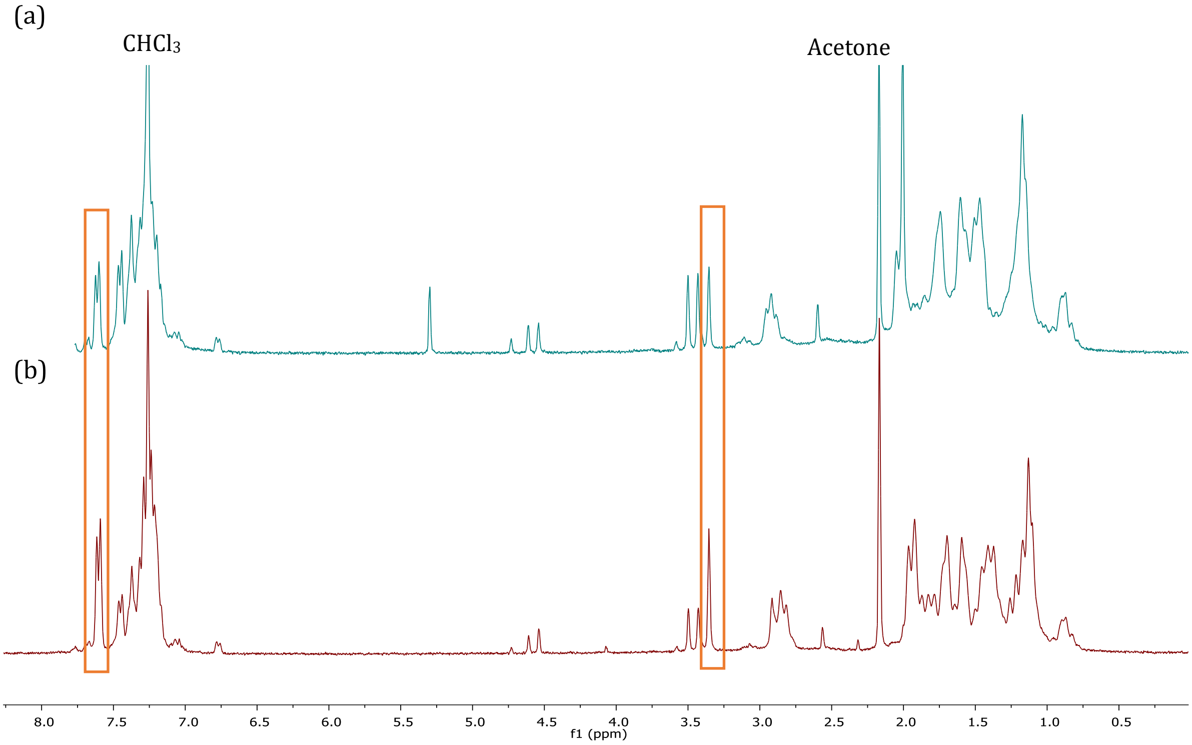

Figure 4.8. Stacked ^{1}H NMR spectra obtained of (a) reaction run 1 product, (b) reaction run 2 product with complex **C2**, and the benzyl substituted ketimine precursor, in $CDCl_3$. The orange boxes correspond to the diagnostic peaks of the benzyl substituted amino acid product.

When the substrate scope of the reaction was modified to the furfuryl substituted ketimine (**K2**), a similar product trend is observed. That is, two products are obtained once again (Figure 4.9), where the spectral data of the first product correlates with the furfuryl substituted amino acid salt and the second product corresponds to the other product that is exclusively obtained when complex **C1** is utilised in the context of this reaction (Figure 4.7 above). Again, the presence of the furfuryl amino acid product being formed is evidenced by the most deshielded doublet in the aromatic region (at *ca* 7.62 ppm), integrating for four protons and the methylene proton signal integrating for two protons at 3.35 ppm. Another observation that can be made upon further examination of the ^{1}H NMR spectra from the respective reaction runs with complex **C2** are the intensity of the peaks for the two products being formed (Figures 4.8 and 4.9). Namely, the intensity of the peaks for the amino acid product is approximately equal to or greater than the peaks corresponding to the other product being formed. This is the case for both the benzyl and furfuryl substrates being evaluated, over their respective reaction runs.

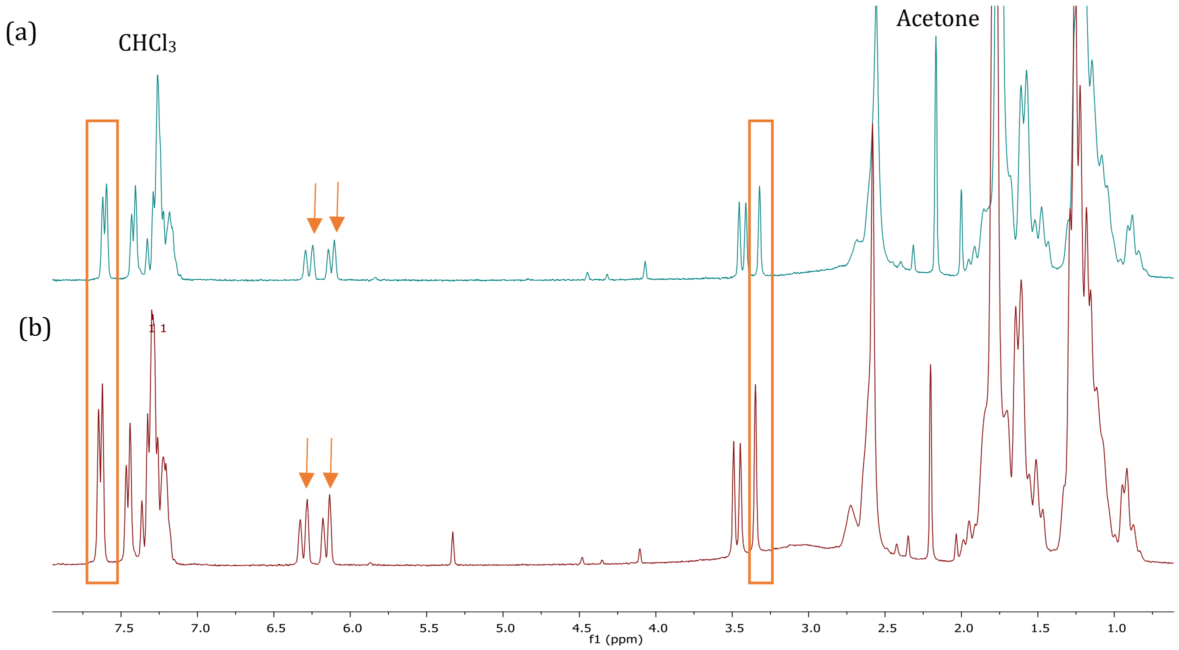

Figure 4.9. Stacked ^{1}H NMR spectra obtained of (a) reaction run 1 product, (b) reaction run 2 product with complex **C2**, and the furfuryl substituted ketimine precursor, in $CDCl_3$. The orange boxes/arrows correspond to the diagnostic peaks of the furfuryl substituted amino acid product.

We can attempt to rationalise why two different products are being formed when complex **C2** is evaluated as the photoredox catalyst, by taking the electrochemical and photophysical properties of complex **C2** into consideration. As discussed above in (Subsection 4.3.2.1), this photoredox catalysed reaction is proposed to undergo the reductive quenching cycle, which was supported by experiments conducted by Walsh and coworkers.[7] Upon functionalising the benzimidazole ligand of complex (**C1**) with the benzyl substituent that's present on complex (**C2**), we saw the stabilising effect this benzyl group had on the electrochemical behaviour on the iridium(III) complex, in that complex **C2** displayed a reversible $Ir^{III+/II+}$ redox couple at -1.69 V ($E_{1/2}$ *vs* Ag/Ag^+ in CH_3CN, Section 3.4, Chapter 3). This reversible $Ir^{III+/II+}$ redox couple was not observed for complex **C1**. Thus, upon undergoing the reductive quenching step for the photocatalytic reaction investigated herein, complex **C2** has the electrochemical ability to regenerate the Ir^{III+} starting oxidation state. Consequently, the desired (benzyl and furfuryl) amino acid product can be formed when complex **C2** is the photoredox catalyst for the reaction.

Furthermore, the photophysical properties (Φ_{Em} and τ_T) determined for complex **C2** could explain why the respective (benzyl and furfuryl) amino acid products are not exclusively formed when this complex (**C2**) is selected for the photocatalytic reaction. Complex **C2** was reported to have a Φ_{Em} value of 0.076 and a triplet excited state lifetime of 0.191 μs (Section 3.2.2, Chapter 3). The model photoredox catalyst, $[Ir(ppy)_2(dtbbpy)]PF_6$, has a lower Φ_{Em} value of 0.032 and an excited state lifetime of τ_T = 0.416 μs, which is more than double than the lifetime of complex **C2**. Hence, for complex **C2**, the triplet excited state lifetime for this photosensitiser may be too short lived to get complete conversion to the desired amino acid product exclusively and a competitive side reaction may be taking place (*vide infra* Section 4.4). Consequently, an additional (alternative) product is being formed too.

4.3.2.3 Results obtained from complex (C3) as the photoredox catalyst

The final photosensitiser that was evaluated in the context of the photoredox catalysed carboxylation reaction of ketimines with CO_2 was the trinuclear complex, **C3**. The stacked ^{1}H NMR spectra from the two reaction runs performed with complex **C3** as the photoredox catalyst with the benzyl substituted ketimine are presented in Figure 4.10. As was the case for complex **C2**, a mixture of two products is obtained once again where the first product corresponds to the desired benzyl amino acid salt and the second structure correlates to the distinct product which is formed when complex **C1** is used as the photosensitiser. The same trend is discerned when the substrate of the reaction is changed to the furfuryl substituted ketimine (Figure 4.11). Additionally, from Figures 4.10 and 4.11 it is evident that the peaks corresponding to the respective amino acid products are of lower intensity than the peak corresponding to the alternative product being formed. This phenomenon is different from what was observed with complex **C2** above.

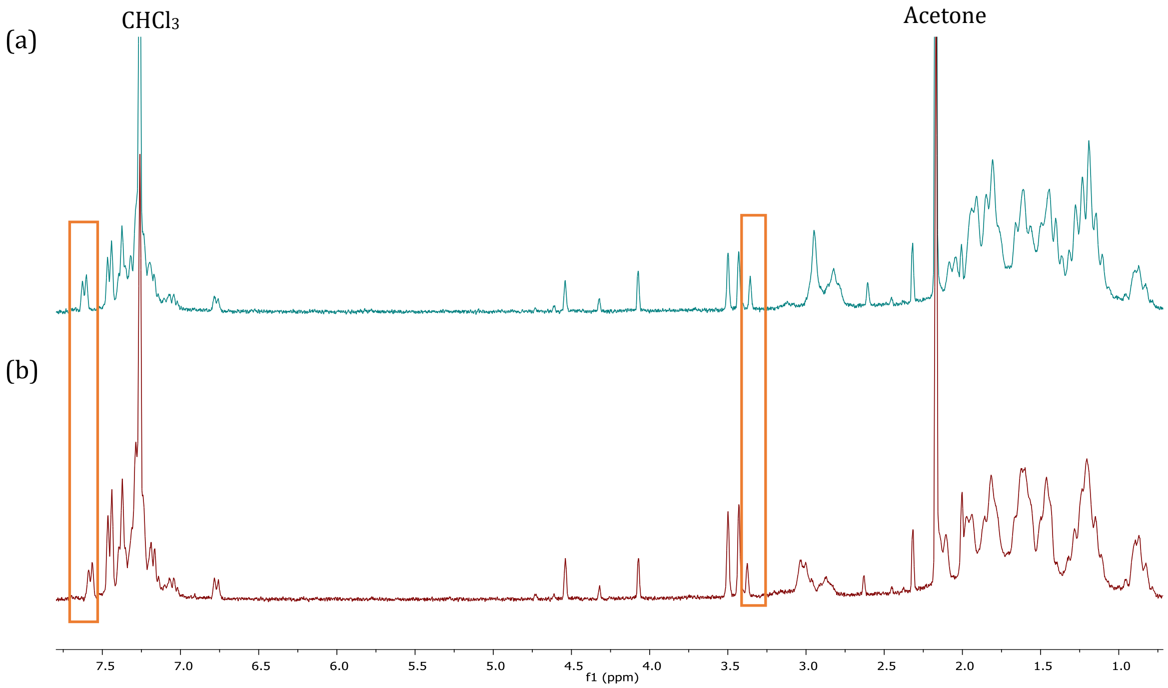

Figure 4.10. Stacked ^{1}H NMR spectra obtained of (a) reaction run 1 product, (b) reaction run 2 product with complex **C3**, and the benzyl substituted ketimine precursor, in $CDCl_3$. The orange boxes correspond to the diagnostic peaks of the benzyl substituted amino acid product.

Complex **C3** was reported to display a reversible Ir$^{III+/II+}$ redox couple at (-1.07 V, E$_{1/2}$ *vs* Ag/Ag$^+$ in DMF, Section 3.4, Chapter 3), which means that complex (**C3**) displays the appropriate electrochemical behaviour to take part in this photoredox catalysed reaction. This is evidenced by the formation of the two desired amino acid products. However, complex **C3** showed the poorest photophysical properties when compared to complexes (**C1**, **C2**) and [Ir(ppy)$_2$(dtbbpy)]PF$_6$. That is, complex **C3** exhibited the highest Φ_{Em} value of 0.084 and an excited state lifetime of 0.241 μs (Section 3.2.2, Chapter 3). Accordingly, the respective amino acid products are formed in a lower ratio compared to the additional side product that is also being formed during the photocatalytic reaction. The inferior photophysical properties of complex **C3** may again favour a competing side reaction that is taking place.

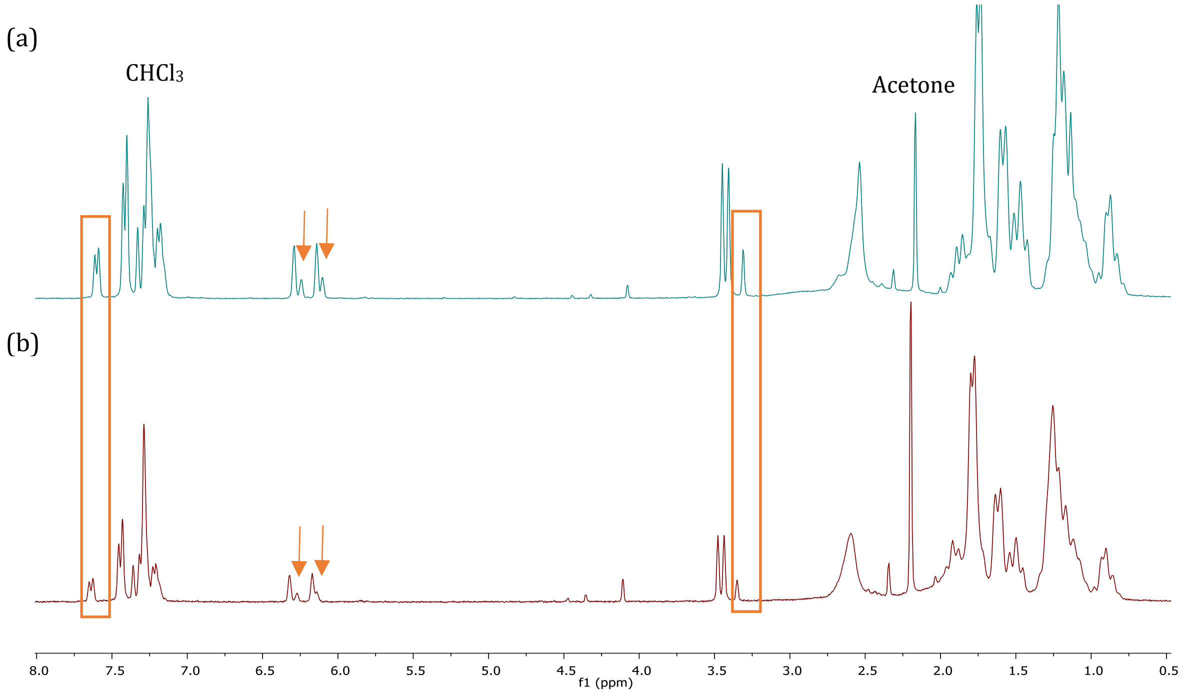

Figure 4.11. Stacked ^{1}H NMR spectra obtained of (a) reaction run 1 product, (b) reaction run 2 product with complex **C3**, and the furfuryl substituted ketimine precursor, in CDCl$_3$. The orange boxes/arrows correspond to the diagnostic peaks of the furfuryl substituted amino acid product.

Thus, the photocatalytic results obtained for complexes (**C1**-**C3**) reveal that the benzimidazole scaffold may not be the most well-suited *N^N* ligand for this photoredox catalysed reaction, when compared to the bipyridine motif. These results have also demonstrated the importance of both the electrochemical properties and photophysical properties for an efficient photosensitiser. Furthermore, the reduced structural rigidity of complexes **C2** and **C3**, due to the intramolecular rotation of the benzyl group needs to be considered too, as it was previously discussed that this could be a contributing factor for the inferior photophysical properties that is observed for these complexes. Therefore, all these important attributes should be taken into consideration to do a fairer comparison of the photocatalytic activity of a mononuclear complex *vs* a trinuclear complex.

4.4 Identification of the additional product being formed for complexes (C1-C3)

The unique umpolung activity that is displayed by ketimines and ketones under photoredox catalysed conditions remains to be a rather underexplored topic.[24] Yu and co-workers were the first group to achieve the photocatalytic hydrocarboxylation of enamides and imines with CO_2, to generate valuable α,α-disubstituted amino acids.[25, 26] Closely following on their work, was the photocatalytic reaction investigated herein, by Walsh and coworkers.[7] It has been reported that efficient cross-coupling reactions between imines and carbonyl compounds under photoredox catalysed conditions remains to be a challenging transformation reaction due to prevailing radical coupling mechanisms, necessitating the formation of two distinct radical intermediates (Figure 4.12) under the same conditions and the high chemoselectivity of these reactions.[27] With this in mind, further spectroscopic analysis of the alternative product obtained with complexes **C1**-**C3** was conducted. Thus, the final studies of the photocatalytic reaction investigated in the scope of this project, involved elucidating the structure of the alternative product being formed when complexes **C1**-**C3** were selected as the photoredox catalysts. In so doing, this would provide further mechanistic insight into possible competitive side reactions that may be taking place in this selected proof-of-concept reaction.

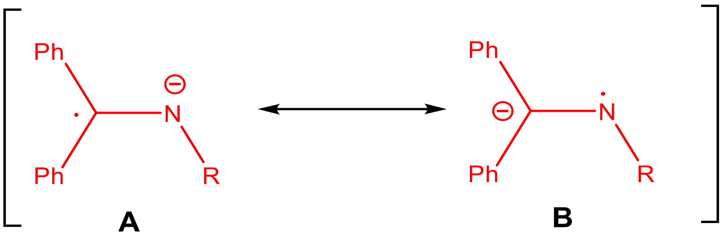

Figure 4.12. The two radical intermediates of ketimines that are formed under photoredox catalysed conditions. The umpolung activity of ketimines is highlighted in intermediate B.[7, 27]

The first postulation as to what the respective benzyl/furfuryl substituted additional product could be, was the main decarboxylated products (as proposed by Walsh and coworkers) presented in Figure 4.13.[7, 17] However, the ^{1}H NMR data obtained of the additional products formed with complexes **C1-C3** above, does not correlate with the spectroscopic data of the structures depicted in Figure 4.13.[28, 29]

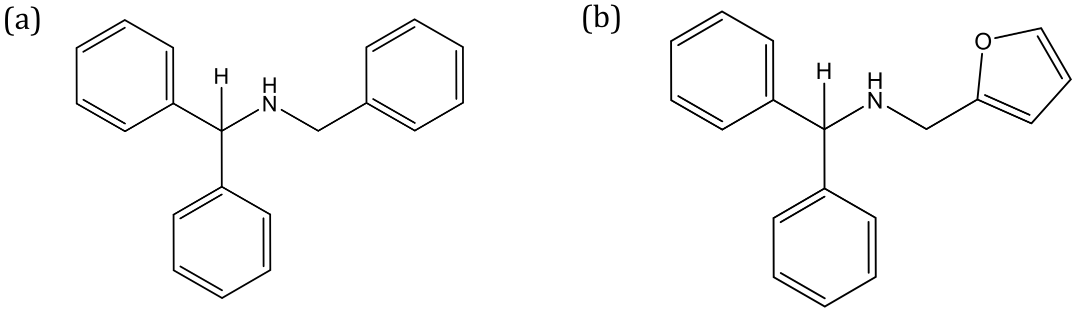

Figure 4.13. Proposed structures of the main decarboxylated products. (a) Product from the benzyl substituted ketimine and (b) product from the furfuryl substituted ketimine.[7,17]

In line with the thought of a possible decarboxylated product, infrared spectra as well as ^{13}C {^{1}H} NMR spectra were acquired for the isolated respective additional benzyl/ furfuryl substituted products. The stacked infrared spectra for the desired benzyl/furfuryl amino acid product as well as the corresponding additional products are presented in Figures 4.14 and 4.15 respectively.

Firstly, upon analysis of the infrared spectra (Figures 4.14 and 4.15) it is evident that the respective additional products display amine absorption bands in the region of ~2920 cm^{-1} and ~2850 cm^{-1}, which is also observed for the two desired amino acid products. Hence, it can be deduced that there is indeed a reduction of the ketimine precursor to an amine functionalised product in the photocatalytic reactions with complexes (**C1**-**C3**). This is further corroborated by looking at the infrared spectra of the respective ketimine precursors (Figures A36 and A37), where no N-H bands are observed.

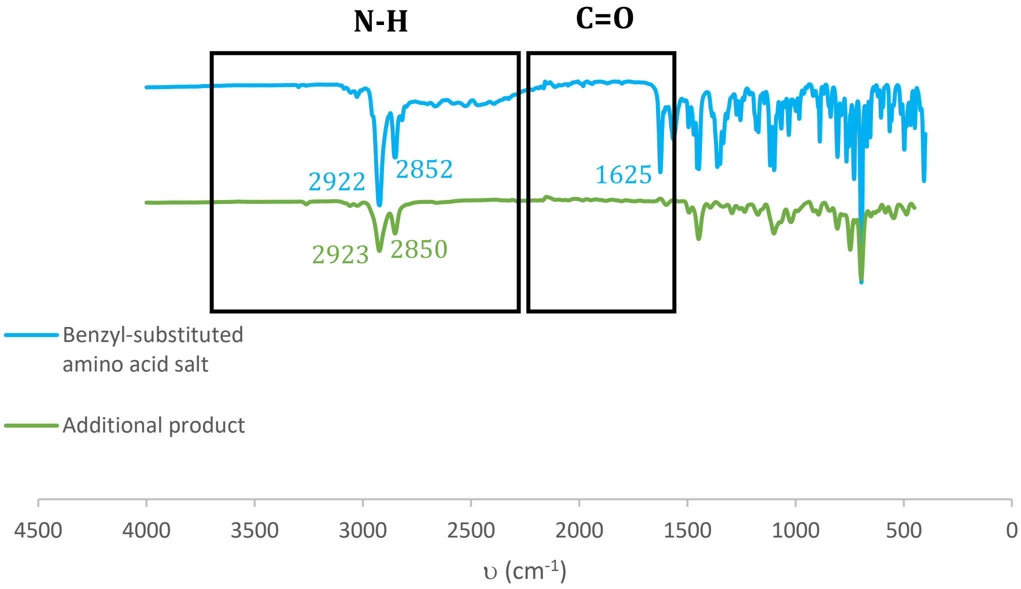

Figure 4.14. Stacked infrared spectra of the desired benzyl substituted amino acid salt product as well as the additional benzyl substituted product that is formed when complexes (**C1**-**C3**) are selected as photoredox catalysts.

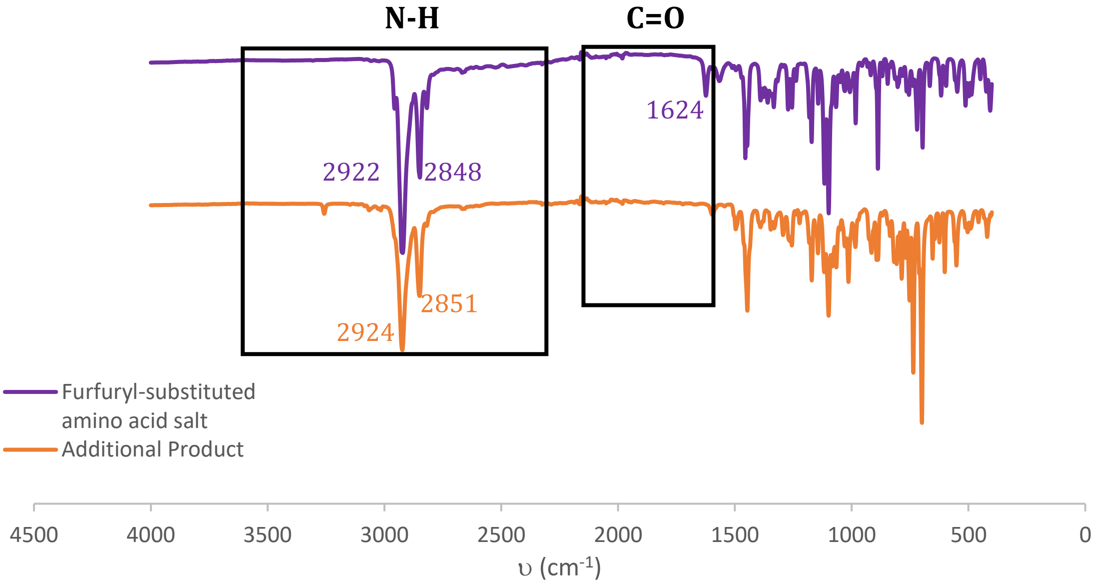

Figure 4.15. Stacked infrared spectra of the desired furfuryl substituted amino acid salt product as well as the additional furfuryl substituted product that is formed when complexes (**C1**-**C3**) are selected as photoredox catalysts.

Secondly, analysis of the infrared spectra of the additional products also reveals that are in fact no carbonyl (C=O) absorption bands in the region of *ca* 1625 cm^{-1}, which is seen for the respective desired amino acid products. This observation points to the notion that the additional products formed with complexes (**C1**-**C3**) must be a decarboxylated species and that the nucleophilic intermediate B (Figure 4.12) is not reacting with CO_2. Moreover, the absence of the carboxyl group was confirmed by ^{13}C {^1H} NMR analysis of the two additional products (Figures 4.16 and 4.17). The diagnostic carboxyl peaks that are present at 177.15 ppm and 176.91 ppm respectively for the benzyl and furfuryl amino acid products are not observed for the corresponding additional products being formed (Figures 4.16 and 4.17).

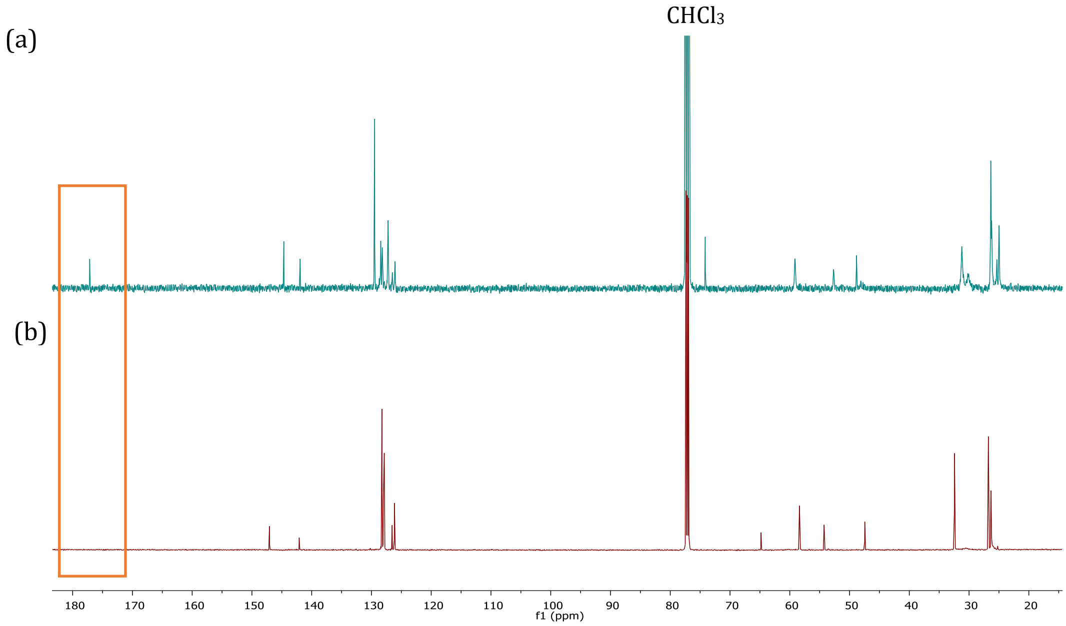

4.16. Stacked $^{13}C\ \{^{1}H\}$ NMR spectra of (a) the desired benzyl substituted amino acid salt product and (b) the additional product obtained with the benzyl substituted ketimine precursor and photoredox catalysts (**C1**-**C3**), in $CDCl_3$.

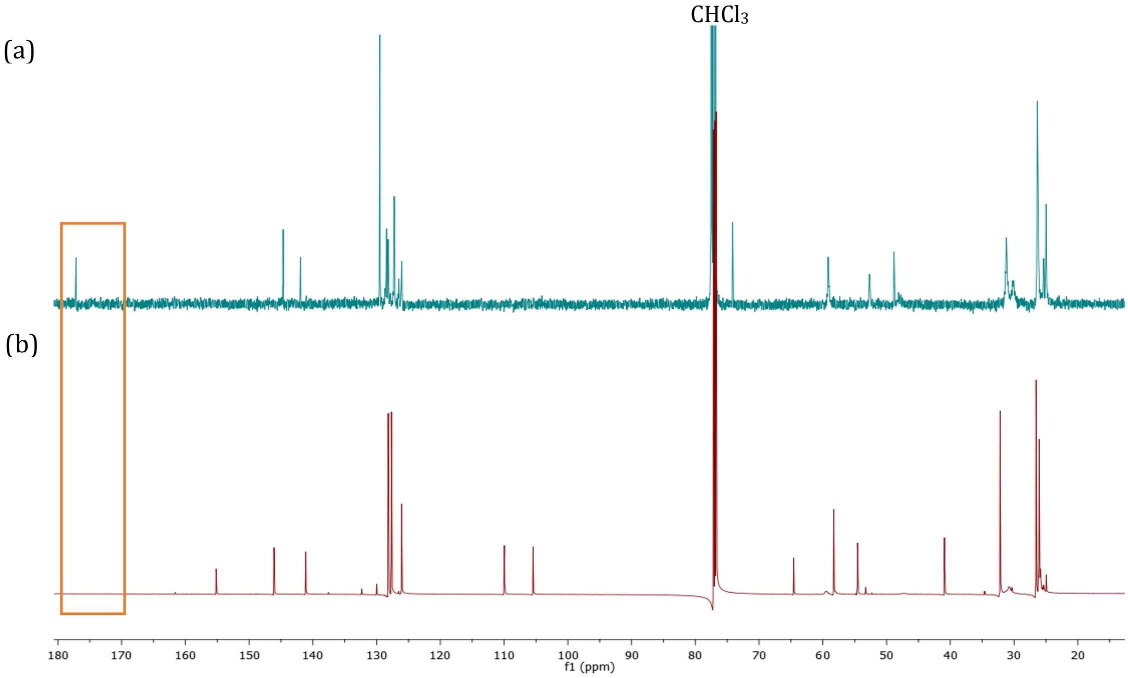

4.17. Stacked $^{13}C\ \{^{1}H\}$ NMR spectra of (a) the desired furfuryl substituted amino acid salt product and (b) the additional product obtained with the furfuryl substituted ketimine precursor and photoredox catalysts (**C1**-**C3**), in $CDCl_3$.

The next piece of crucial spectroscopic data was from 2D NMR analysis conducted on the additional products. HSQC-DEPT spectra of the two isolated additional products obtained from the reactions with complexes (**C1**-**C3**) were recorded. The respective HSQC-DEPT spectra are depicted in Figures 4.18 and 4.19. The diagnostic information from the 2D analysis is that the two singlets in the aliphatic region, occurring at 3.49 ppm and 3.42 ppm for the product obtained from the benzyl substituted ketimine as well as the singlets appearing at 3.42 ppm and 3.39 ppm for the product obtained from the furfuryl substituted ketimine are methylene carbons (-CH_2). This finding was particularly significant in that it enabled us to confirm that there were two methylene groups present in each of the respective additional products being obtained with complexes (**C1**-**C3**). Additionally, it allowed for us to assign these signals in the proton spectra and in so doing, integrate over the respective ^{1}H NMR spectra correctly. The integrated ^{1}H NMR spectra of the two additional products being formed with complexes (**C1**-**C3**) as the photoredox catalysts are presented in Figures 4.20 and 4.21.

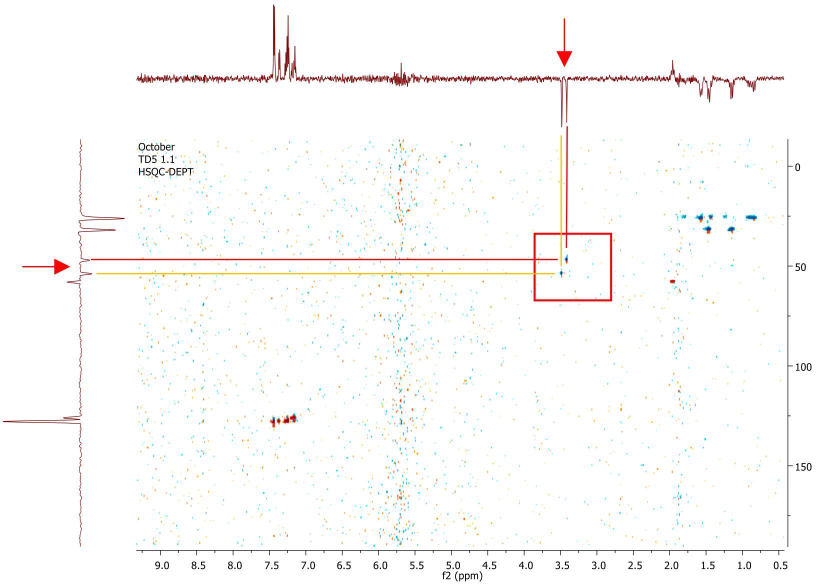

Figure 4.18. HSQC-DEPT spectrum of the additional product obtained with the benzyl substituted ketimine precursor and photoredox catalysts (**C1**-**C3**), in $CDCl_3$.

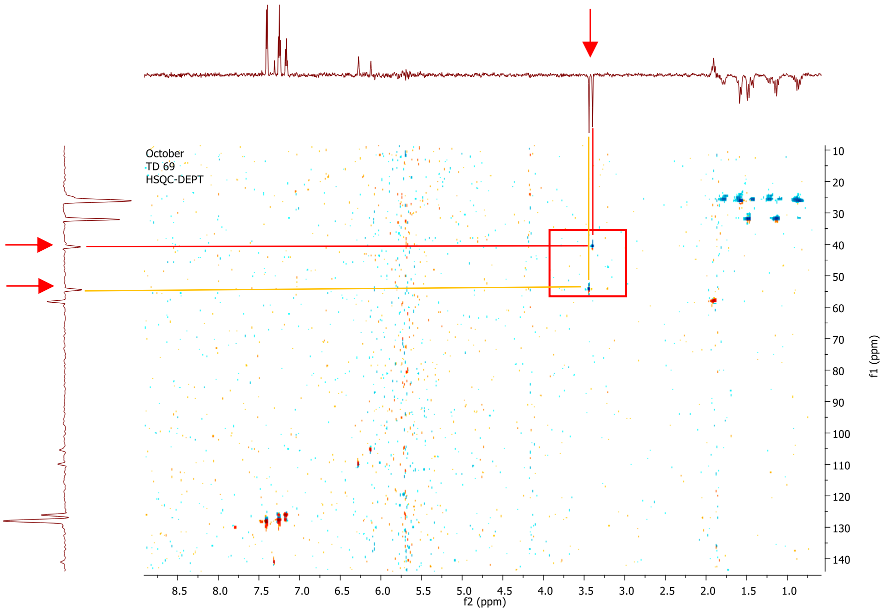

Figure 4.19. HSQC-DEPT spectrum of the additional product obtained with the furfuryl substituted ketimine precursor and photoredox catalysts (**C1**-**C3**), in $CDCl_3$.

Integration over the aromatic region of the ^1H NMR spectrum (Figure 4.20) amounts to 16 protons (including the $CHCl_3$ solvent peak). It was postulated that the 15 protons could be attributed to the presence of three phenyl rings in the additional product being formed in the reactions involving the benzyl substituted ketimine and complexes (**C1**-**C3**). Furthermore, the proton signals occurring in the broad region of 1.98-0.83 ppm in Figure 4.20 point to the idea that there is a structural component of the amine, $Cy_2N^+CH_2$ that may form part of the additional product. This is further substantiated by the HSQC-DEPT data for this additional product (Figure 4.18), where in the region of 1.98-0.83 ppm, it is evident that there are CH_2 moieties present, which could be due to the cyclohexyl groups of the sacrificial amine.

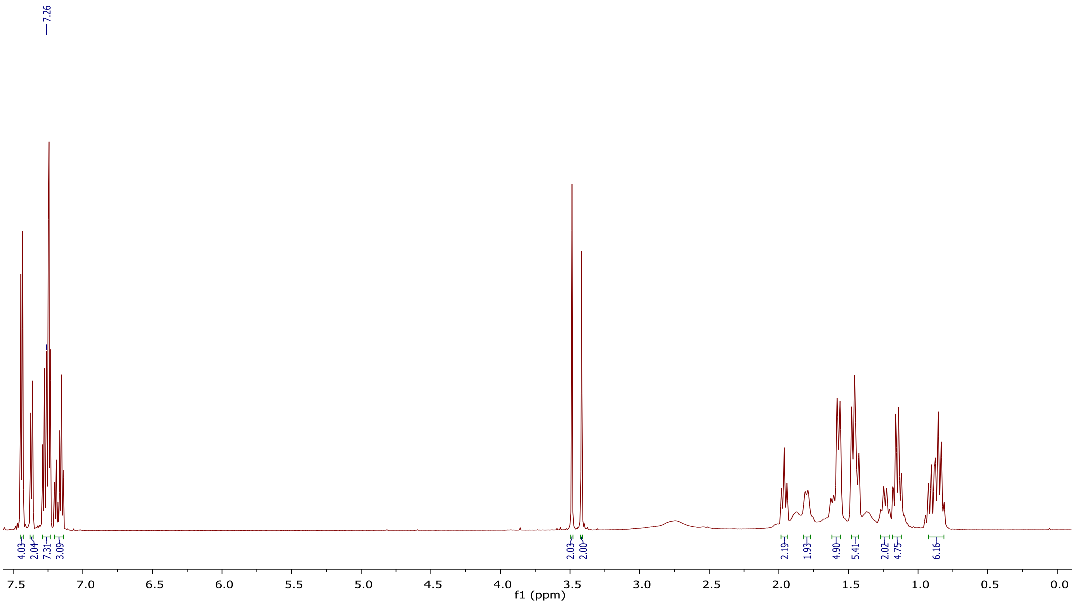

Figure 4.20. ^{1}H NMR spectrum of the additional product obtained with the benzyl substituted ketimine precursor and photoredox catalysts (**C1**-**C3**), in $CDCl_3$.

In the case of the additional product obtained from the reactions performed with the furfuryl substituted ketimine and complexes (**C1**-**C3**), integration over the aromatic region of the ^{1}H NMR spectrum (Figure 4.21) corresponds to 14 protons (including the $CHCl_3$ solvent peak). This observation, along with the proton signals at 6.27 ppm and 6.13 ppm, lead to the postulation that within this additional product, there must be two phenyl groups present and a furfuryl substituent. Again, in the most upfield region of 1.93-0.84 ppm, there is evidence of the structural component of the amine, $Cy_2N^+CH_2$ forming part of the additional product. This latter observation is corroborated by the HSQC-DEPT spectrum of this product (Figure 4.19).

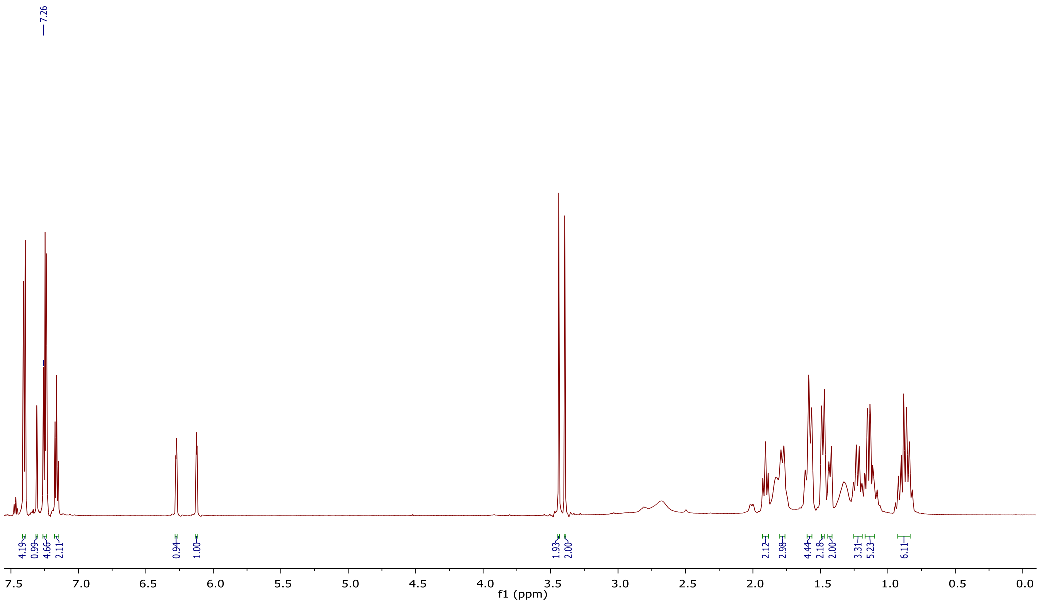

Figure 4.21. ^{1}H NMR spectrum of the additional product obtained with the furfuryl substituted ketimine precursor and photoredox catalysts (**C1**-**C3**), in $CDCl_3$.

Taking all the above spectroscopic data (infrared data, ^{13}C {^{1}H} NMR spectra, ^{1}H NMR and 2D NMR analysis) collated for the respective additional products formed in the presence of complexes **C1**-**C3** into account, the structures of these respective compounds could be proposed. The proposed structures of the additional products obtained from the reactions with either the benzyl or furfuryl substituted ketimines and with complexes **C1**-**C3** as the photoredox catalysts is presented in Figure 4.22. The postulated structures correlate with a decarboxylated product, but a product where, interestingly, a new C-C bond has been formed.

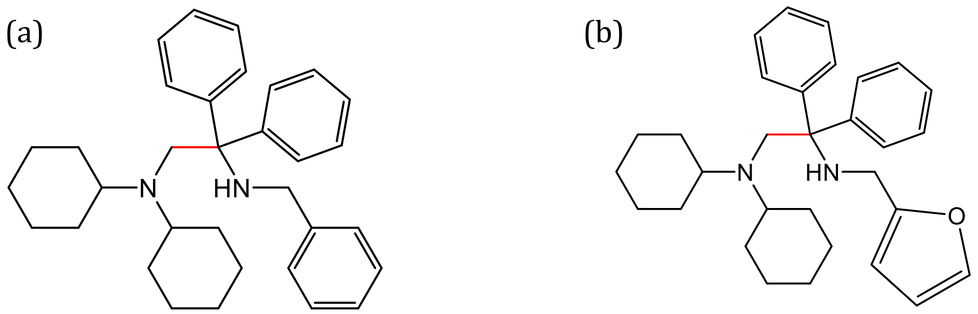

Figure 4.22. Proposed structures of the additional products being formed when complexes **C1**-**C3** are selected as the photoredox catalyst. (a) Product from the benzyl substituted ketimine and (b) product from the furfuryl substituted ketimine. Red bonds highlight the proposed new C-C bond formed.

Briefly, to summarise all the spectroscopic data which attests to the proposed structures of the respective additional products in Figure 4.22. The infrared spectra (Figures 4.14 and 4.15) display N-H absorption bands at *ca* 2920 cm^{-1} and *ca* 2850 cm^{-1} which correlates with a reduction of the ketimine precursor taking place to form an amine functionalised product. The infrared spectra for the isolated additional products don't reveal any characteristic carbonyl stretches (Figures 4.14 and 4.15), which is confirmed by the ^{13}C {^{1}H} NMR spectra (Figures 4.16 and 4.17). Importantly, the ^{13}C {^{1}H} NMR data for these respective additional products correlates with the proposed structures in Figure 4.22, where the carbons of the postulated structures are correctly accounted for. The two -CH$_2$ groups that are present in each of the respective additional products (Figure 4.22), as well as the formation of the new C-C bond, are supported by the HSQC-DEPT spectra recorded for each respective product (Figures 4.18 and 4.19). Examination of the ^{1}H NMR spectra (Figures 4.20 and 4.21) of the respective additional products support the postulation of the phenyl and/or the furfuryl groups being present in the structure. ^{1}H NMR analysis also corroborates the presence of the cyclohexyl substituents on the proposed structures. The final piece of analytical data that substantiates the postulated structures of the two additional/alternative products depicted in Figure 4.22, are the LC-MS traces obtained for the respective products. The LC-MS traces are shown in Figure 4.23. For the proposed benzyl substituted additional product, its LC-MS trace (Figure 4.23 (a)) reveals a molecular base peak, *m/z*= 467.3, which accurately corresponds to the protonated molecular ion [M+H]$^{+}$.

A similar result is observed for the furfuryl substituted additional product. The LC-MS trace for this product (Figure 4.23 (b)) shows a molecular base peak *m/z*= 457.3, which is in agreement with the protonated molecular ion [M+H]$^+$. Furthermore, the LC-MS traces of both products display very similar fragmentation patterns. Both spectra (Figures 4.23 (a) and (b)) have a peak at *m/z*= 360.2, in an abundance of *ca* 18%. This latter peak corresponds to the fragmented structure shown in Figure 4.24. Thus, the extensive spectroscopic data collated for the respective additional products that are formed in the photocatalytic reactions with complexes (**C1**-**C3**), strongly attest to the proposed structures as presented in Figure 4.22.

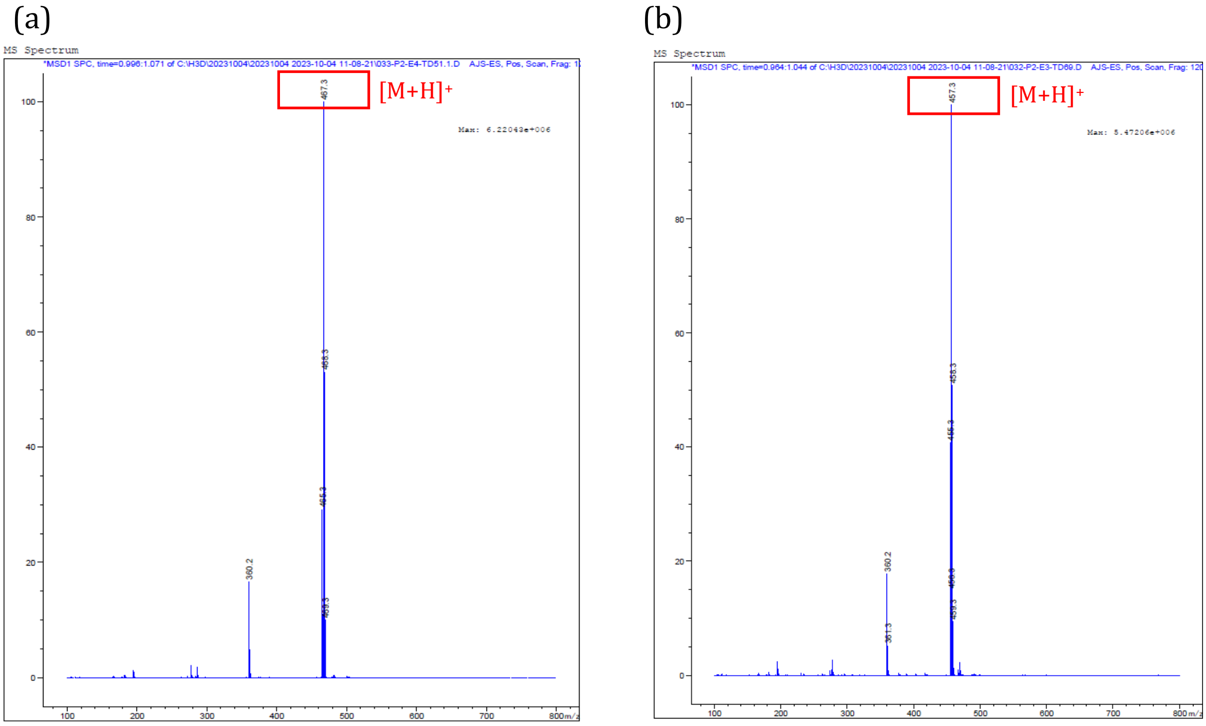

Figure 4.23. LC-MS traces of the additional/alternative products being formed when complexes **C1-C3** are selected as the photoredox catalyst. (a) Product from the benzyl substituted ketimine and (b) product from the furfuryl substituted ketimine.

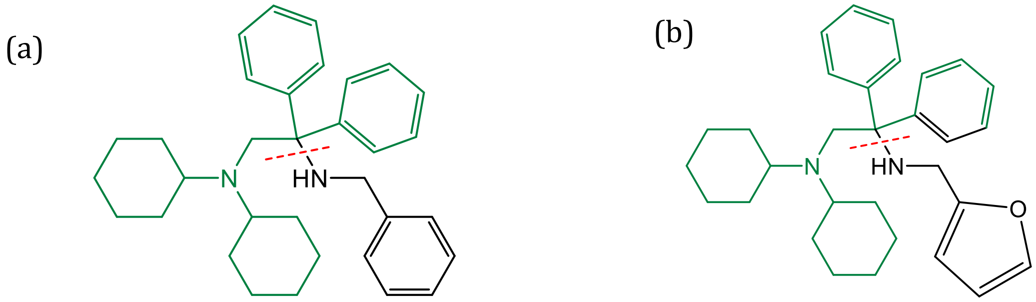

Figure 4.24. Structures displaying the fragmentation which gives rise to peak at *m/z*= 360.2, highlighted in green. The dashed red line represents the point of fragmentation. (a) Product from the benzyl substituted ketimine and (b) product from the furfuryl substituted ketimine.

Finally, the postulated mechanism for the competitive reaction taking place, to form the additional products is presented in Scheme 4.6. It is proposed that steps 1-5, of the original photocatalytic reaction, as postulated by Walsh and coworkers,[7] are still taking place with complexes (**C1**-**C3**). The formation of the crucial anionic intermediate B is evidenced by computational evidence previously conducted by Walsh's group where it was found that that for the radical intermediate, B, there is greater spin density on nitrogen (0.37) than the carbon atom C3, which has a spin density of 0.18.[30] Thus, indicating that carbon C3 possesses more anionic character.[30] Furthermore, the more anionic nature of C3 has also been supported by other studies involving the electrochemical and photochemical reduction of ketimines.[17, 31] The key difference in the proposed mechanism involved in the formation of the additional products (with complexes **C1-C3**), is that in step 6, instead of the negatively charged intermediate B attacking the neutral molecule CO_2, B is attacking the inherently positively charged tertiary amine, $Cy_2N^+CH_2$. The main driving force behind this postulated side reaction could be due to the favourable electrostatic interaction between the anionic intermediate B and the positively charged amine. Additionally, the electrostatic driving force may be more favoured than the reaction of $Cy_2N^+CH_2$ and adventitious water (to form the $Cy_2N^+H_2$ counterion), as proposed by Walsh's group.[7] Interestingly, the additional products that have been reported herein pose an attractive strategy to generate C-C bonds *via* a photoredox catalysed mechanism.

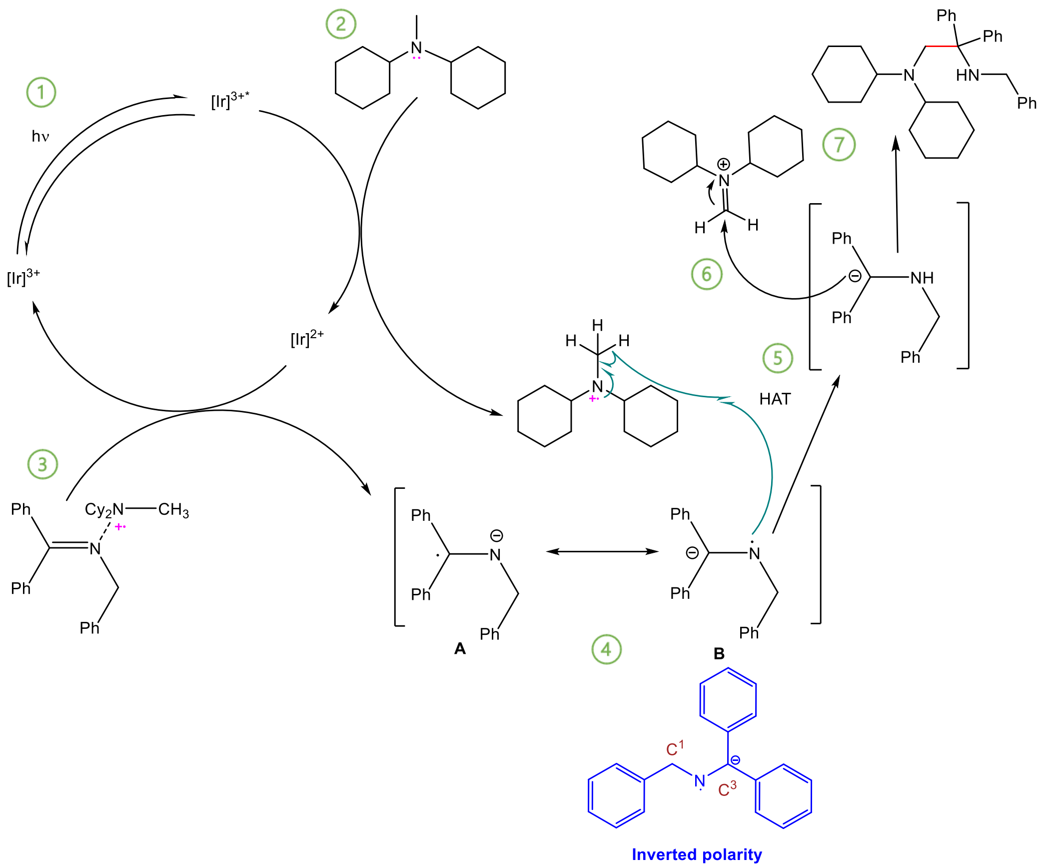

Scheme 4.6. Proposed mechanism for the competitive reaction resulting in the formation of the benzyl substituted additional product, obtained with complexes (**C1-C3**) as photoredox catalysts. The furfuryl substituted additional product is formed in an analogous manner. The inverted polarity of the ketimine is highlighted in step 4.[7]

Compared to the main proposed reduction reaction products which generates C–H bonds (Figure 4.13), the formation of C–C bonds (Figure 4.22) is more desirable, in that it increases molecular complexity and it allows for construction of potential new functional molecules. Moreover, it is important to note that further in-depth mechanistic studies and computational analysis should be conducted to fully rationalise why the postulated side reaction is taking place predominately when complexes **C1-C3** are selected as the photoredox catalysts for this particular reaction. However, it is evident that for the photoredox catalysed carboxylation reaction of ketimines with CO_2, this photocatalytic reaction requires a photosensitiser with a relatively longer-lived triplet excited state lifetime, lower Φ_{Em} value and a reversible $Ir^{III+/II+}$ reduction couple to get complete conversion to the desired amino acid product.

That is, a photosensitiser such as [Ir(ppy)$_2$(dtbbpy)]PF$_6$, which possess a longer excited state lifetime (0.416 μs), a lower Φ_{Em} value (0.032) and the appropriate reversible electrochemical behaviour shows conversion to the desired amino acid product exclusively. This outcome stands in contrast to the photocatalytic outcome with complexes **C1**-**C3**, which have shorter triplet excited state lifetimes (0.191-0.272 μs range) and higher Φ_{Em} values (0.052-0.084 range) and consequently produce an additional product during the course of the photocatalytic outcomes. Only complexes **C2** and **C3**, which display reversible $Ir^{III+/II+}$ redox couples produce a mixture of the amino acid product and the additional product. Again, the photocatalytic results emphasise the importance of judicious photosensitiser design for a particular photochemical application.

4.5 Summary

In this chapter, the photocatalytic activity of the synthesised benzimidazole complexes (**C1**-**C3**) was evaluated in the proof-of-concept reaction, the photoredox catalysed carboxylation reaction of ketimines utilising CO_2. The synthesis and the characterisation of the benzyl (**K1**) and furfuryl (**K2**) substituted ketimine precursors was described. Optimisation and control reactions were performed with the benzyl substituted ketimine and model photoredox catalyst, [Ir(ppy)$_2$(dtbbpy)]PF$_6$. A consistent and reproducible set of results were obtained in our photocatalytic setup which in turn allowed for us to evaluate the photocatalytic activity of complexes **C1**-**C3**, with the two ketimine substrates. Additionally, the results from the control reactions aided in ruling out any potential underlying factors that could influence the photocatalytic outcomes.

Complexes **C1**-**C3** revealed a rather interesting photocatalytic outcome. For complex **C1**, a distinct product was formed, which was different from the ketimine precursor and did not correlate with the desired amino acid product either. In the photocatalytic reactions with complexes **C2** and **C3**, a mixture of two products were obtained. The spectroscopic data of the first product corroborated with the appropriate desired amino acid product (**AA1** or **AA2**) and the spectroscopic data of the second product matched the data of the distinct product obtained when complex **C1** was utilised as the photoredox catalyst.

This trend was observed across both the benzyl and furfuryl substituted ketimine substrates in the reactions with complexes **C2** and **C3**. The differences in the photocatalytic activity of the model photoredox catalyst, $[Ir(ppy)_2(dtbbpy)]PF_6$ and the synthesised iridium(III) complexes (**C1**-**C3**), was attributed to the difference in the photophysical (τ_T and Φ_{Em}) and electrochemical properties of the respective photosensitisers. $[Ir(ppy)_2(dtbbpy)]PF_6$ exhibited the longest excited state lifetime, lowest value of Φ_{Em} compared to complexes **C1**-**C3**, and the model photoredox catalyst displayed appropriate reversible electrochemical behaviour.

Furthermore, the structure of the additional product obtained in the reactions with complexes **C1**-**C3** was proposed (Figure 4.22), and a mechanism for this product formation was postulated too (Scheme 4.6). The photocatalytic results herein demonstrate that complexes **C1**-**C3** may not be the most ideal choice of photosensitiser for this particular photoredox catalysed reaction due to the more difficult nature of the reaction, involving the activation of CO_2. These unexpected photocatalytic results also made it difficult to appropriately compare the activity of trinuclear photoredox catalysts *vs* their mononuclear congeners. However, complexes (**C1**-**C3**) could be better suited for a different photoredox catalysed reaction, where a fairer comparison could be made. Finally, these results once again highlight how photophysical and electrochemical properties of a photosensitiser influence the photochemical application, and emphasise how these properties are altogether important to take into consideration for the efficiency of a photosensitiser.

4.6 References

1. Z. Liu, Z. Deng, S. J. Davis, C. Giron and P. Ciais, *Nat. Rev. Earth Environ.*, 2022, 3, 217-219.
2. T. F. Stocker, D. Qin, G.-K. Plattner, M. Tignor, S. K. Allen, J. Boschung, A. Nauels, Y. Xia, V. Bex and P. M. Midgley (eds.), *Contribution of Working Group I to the Fifth Assessment Report of the Intergovernmental Panel on Climate Change.* Cambridge University Press, Cambridge, United Kingdom and New York, NY, USA.
3. D.-G. Yu and L.-N. He, *Green Chem.*, 2021, 23, 3499-3501.
4. T. Sakakura, J.-C. Choi and H. Yasuda, *Chem. Rev.*, 2007, 107, 2365-2387.
5. T. Baran, A. Dibenedetto, M. Aresta, K. KruczaBa and W. Macyk, *ChemPlusChem*, 2014, 79, 708-715.
6. S. Pradhan, S. Roy, B. Sahoo and I. Chatterjee, *Chemistry*, 2021, 27, 2254-2269.
7. X. Fan, X. Gong, M. Ma, R. Wang and P. J. Walsh, *Nat. Commun.*, 2018, 9, 4936.
8. L. Wang, A. Brock, B. Herberich and P. G. Schultz, *Science*, 2001, 292, 498-500.
9. M. A. T. Blaskovich, *J. Med. Chem.*, 2016, 59, 10807-10836.
10. X. Fan, Y. Ge, F. Lin, Y. Yang, G. Zhang, W. S. Ngai, Z. Lin, S. Zheng, J. Wang, J. Zhao, J. Li and P. R. Chen, *Angew. Chem. Int. Ed.*, 2016, 55, 14046-14050. 2254-2269
11. Y. Ge, X. Fan and P. R. Chen, *Chem. Sci.*, 2016, 7, 7055-7060.
12. D. F. Kreitler, D. E. Mortenson, K. T. Forest and S. H. Gellman, *J. Am. Chem. Soc.*, 2016, 138, 6498-6505.
13. M. Jewginski, T. Granier, B. Langlois d'Estaintot, L. Fischer, C. D. Mackereth and I. Huc, *J. Am. Chem. Soc.*, 2017, 139, 2928-2931.
14. T. Narancic, S. A. Almahboub and K. E. O'Connor, *World J. Microbiol. Biotechnol.*, 2019, 35, 67.
15. M. Tanaka, *Chem. Pharm. Bull.*, 2007, 55, 349-358.
16. Y. Ohfune and T. Shinada, *Eur. J. Org. Chem.*, 2005, 5127-5143.
17. R. Wang, M. Ma, X. Gong, G. B. Panetti, X. Fan and P. J. Walsh, *Org. Lett.*, 2018, 20, 2433-2436.
18. K. Li, A. E. Weber, L. Tseng and S. J. Malcolmson, *Org. Lett.*, 2017, 19, 4239-4242.
19. M. Selva, P. Tundo and C. A. Marques, *Synth. Commun.*, 1995, 25, 369-378.
20. G. Liu, D. A. Cogan, T. D. Owens, T. P. Tang and J. A. Ellman, *J. Org. Chem.*, 1999, 64, 1278-1284.

21. T. D. Svejstrup, A. Chatterjee, D. Schekin, T. Wagner, J. Zach, M. J. Johansson, G. Bergonzini and B. König, *ChemPhotoChem*, 2021, 5, 808-814.

22. A. Ruffoni, F. Juliá, T. D. Svejstrup, A. J. McMillan, J. J. Douglas and D. Leonori, *Nat. Chem.*, 2019, 11, 426-433.

23. S. L. Rössler, B. J. Jelier, P. F. Tripet, A. Shemet, G. Jeschke, A. Togni and E. M. Carreira, *Angew. Chem. Int. Ed.*, 2019, 58, 526-531.

24. K. N. Lee, Z. Lei and M.-Y. Ngai, *J. Am. Chem. Soc.*, 2017, 139, 5003-5006.

25. T. Ju, Q. Fu, J. H. Ye, Z. Zhang, L. L. Liao, S. S. Yan, X. Y. Tian, S. P. Luo, J. Li and D. G. Yu, *Angew. Chem. Int. Ed.*, 2018, 57, 13897-13901.

26. Z. Zhang, C.-J. Zhu, M. Miao, J.-L. Han, T. Ju, L. Song, J.-H. Ye, J. Li and D.-G. Yu, *Chin. J. Chem.,* 2018, 36, 430-436.

27. R. Wang, M. Ma, X. Gong, X. Fan and P. J. Walsh, *Org. Lett.*, 2019, 21, 27-31.

28. G. Dilauro, M. Dell'Aera, P. Vitale, V. Capriati and F. M. Perna, *Angew. Chem. Int. Ed.*, 2017, 56, 10200-10203.

29. J. Che and Y. Lam, *Adv. Synth. Catal.*, 2010, 352, 1752-1758.

30. M. Li, O. Gutierrez, S. Berritt, A. Pascual-Escudero, A. Yeşilçimen, X. Yang, J. Adrio, G. Huang, E. Nakamaru-Ogiso, M. C. Kozlowski and P. J. Walsh, *Nat. Chem.*, 2017, 9, 997-1004.

31. A. J. Fry and R. G. Reed, *J. Am. Chem. Soc.*, 1969, 91, 6448-6451.

Chapter 5: Conclusions and future work

5.1 Overall summary and conclusions

The overall aim of this project was to synthesise and fully characterise iridium(III) polypyridyl photosensitisers containing a *N^N*-benzimidazole ancillary ligand. These photosensitisers were evaluated in the context of the visible light mediated photoredox catalysed carboxylation reaction of ketimines using CO_2. Accordingly, a precursor benzimidazole ligand (**L1**) was synthesised *via* the reaction of *o*-phenylenediamine and 2-pyridinecarboxylic acid in the presence of an acid catalyst, PPA. This precursor ligand was used in two N-alkylation reactions with benzyl bromide or 1,3,5-tris(bromomethyl)benzene to respectively afford a monomeric ligand (**L2**) and a trimeric ligand (**L3**). Ligands (**L1**-**L3**) were obtained in moderate to good yields. Subsequently, the benzimidazole ligands (**L1**-**L3**) underwent facile bridge-splitting reactions with the synthesised iridium(III) chloro-bridged dimer, $[Ir(ppy)_2(\mu\text{-}Cl)]_2$ to afford two mononuclear bis-cyclometalated iridium(III) complexes (**C1**, **C2**) and a trinuclear iridium(III) complex (**C3**). Complexes (**C1**-**C3**) were obtained as racemic mixtures in good yields. Characterisation of the synthesised ligands (**L1**-**L3**) and complexes (**C1**-**C3**) was achieved by ^1H NMR, $^{13}C\{^1H\}$ NMR spectroscopy, infrared spectroscopy and high-resolution mass spectrometry. A crystal structure was also obtained for complex (**C2**).

Thereafter, the photophysical and electrochemical properties of the synthesised complexes (**C1**-**C3**) were elucidated. UV-visible absorption spectra revealed that the iridium(III) complexes (**C1**-**C3**) absorb light in the visible region. Complexes (**C1**-**C3**) displayed unstructured emission bands, where the emissions were attributed to the transition from the ^{3}MLCT state to the ground state.[1] Quantum emission yields and the triplet excited state lifetimes of the iridium(III) complexes (**C1**-**C3**) were measured. These values were found to be more favourable than similar ruthenium(II) benzimidazole complexes reported in literature,[2] but inferior to that of the model photosensitiser, $[Ir(ppy)_2(dtbbpy)]PF_6$.

Furthermore, the increased Φ_{Em} values and lower triplet excited state lifetimes of complexes (**C1**-**C3**) was attributed to intramolecular rotations of the benzyl moiety in complexes **C2** and **C3**, as well as the difference in π-acceptor ability of the benzimidazole *vs* bipyridine motif. Notably, complexes (**C1**-**C3**) exhibited remarkable photostability under irradiation of 405 nm blue LED light for 48 h, which highlighted their robust structure. With respect to the electrochemical properties of complexes (**C1**-**C3**), these complexes exhibited reversible $Ir^{III+/IV+}$ couples, which was assigned to oxidation of the metal centre or events centred on the *C^N* ligands. Reversible $Ir^{III+/II+}$ couples were only observed in the model photosensitiser and in complexes **C2** and **C3**, upon functionalisation of the benzimidazole ligand with the benzyl moiety. This demonstrated the stabilising influence of the benzyl group on the electrochemical properties. Moreover, it was concluded that the photophysical and electrochemical properties reported for complexes (**C1**-**C3**) highlighted the importance of judicious ligand choice when designing a photosensitiser and, how these properties (along with other parameters) are altogether important to take into consideration as the efficiency of a photosensitiser is not determined by a single factor.

Finally, the photocatalytic activity of the benzimidazole functionalised complexes (**C1**-**C3**) was evaluated in the proof-of-concept reaction, the photoredox catalysed carboxylation reaction of ketimines utilising CO_2.[3] The synthesis and characterisation of the benzyl (**K1**) and furfuryl (**K2**) substituted ketimine precursors was also described. A consistent and reproducible set of results were obtained in our photocatalytic setup, after optimisation experiments performed with $[Ir(ppy)_2(dtbbpy)]PF_6$, which in turn allowed us to evaluate the photocatalytic activity of complexes (**C1**-**C3**), with the two ketimine substrates. An interesting photocatalytic outcome was reported for the reactions conducted with (**C1**-**C3**) as the photoredox catalysts. A distinct product was formed with complex **C1**, which was different from the ketimine precursor and did not correlate with the desired amino acid product either. Alternatively, a mixture of two products was obtained for the photocatalytic reactions with complexes **C2** and **C3**. The spectroscopic data of the first product correlated with the desired amino acid and the spectroscopic data of the second product matched the data of the distinct product obtained when complex **C1** was utilised as the photoredox catalyst.

It was concluded that the observed differences in the photocatalytic activity of the model photoredox catalyst, $[Ir(ppy)_2(dtbbpy)]PF_6$ and the iridium(III) complexes (**C1**-**C3**), was attributed to the difference in the photophysical (tT and Φ_{Em}) and electrochemical properties of the respective photosensitisers.

The structure of the (benzyl or furfuryl substituted) additional products obtained in the reactions with complexes **C1**-**C3** was proposed, along with a postulated mechanism for the product formation. Moreover, the photocatalytic results demonstrated that complexes **C1**-**C3** may not be the most ideal choice of photosensitiser for the photoredox catalysed reaction investigated in this study. Consequently, these results made it difficult to fairly compare the activity of trinuclear photoredox catalysts *vs* their mononuclear congeners. The photocatalytic results further emphasised how the photophysical and electrochemical properties of a photosensitiser influence the photochemical application, and highlighted how these properties are altogether important to take into consideration for the efficiency of a photosensitiser.

5.2 Future work

The photophysical and electrochemical properties determined for the iridium complexes (**C1-C3**), could benefit from further in-depth studies such as DFT calculations and computational analysis. DFT studies could aid in designing more efficient and versatile photosensitisers, which could possess longer excited state lifetimes and higher luminescent quantum yields. Figure 5.1 suggests a few structural modifications that should be considered when designing an iridium(III) photosensitiser, taking into account the structural considerations as proposed by Caspar *et al.*[4] and Sinha *et al.*[5] and the findings of this work. In this work, it was found that the benzimidazole scaffold and benzyl substituent may not have been the most well-suited modifications in the context of our photocatalytic application. The stronger π-acceptor ability and higher degree of rigidity of the *N^N* (bpy) ancillary ligand in $[Ir(ppy)_2(dtbbpy)]PF_6$ could explain the more favourable photophysical properties, and subsequent better photocatalytic activity that was observed for this archetypical complex.

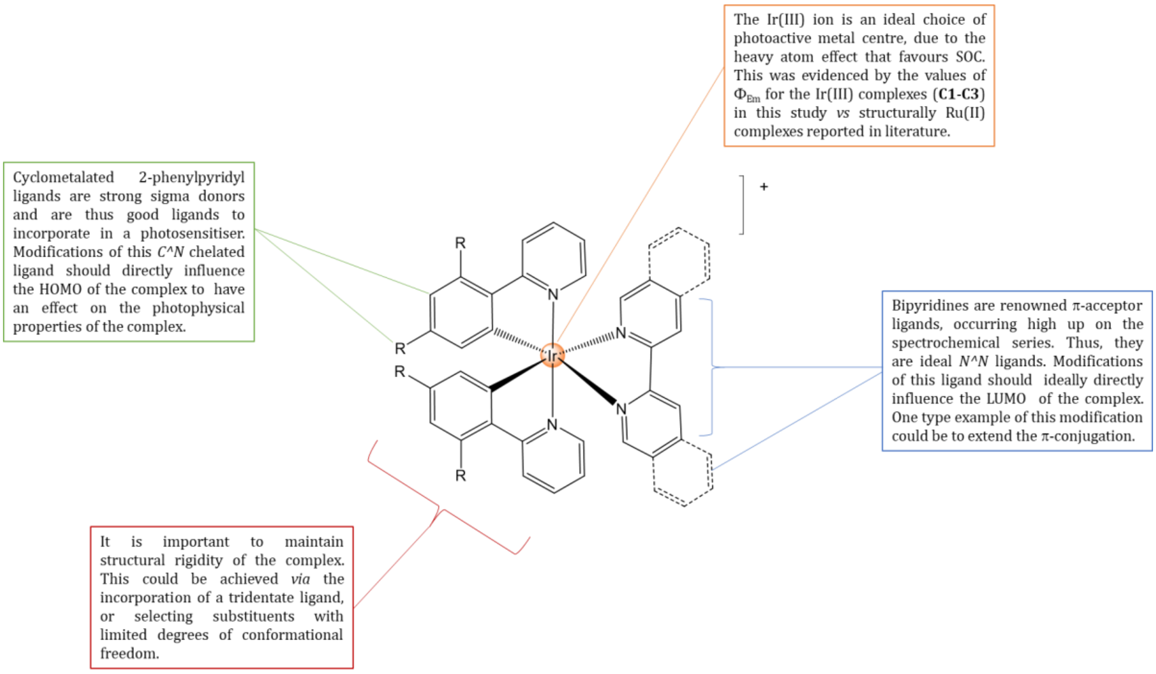

The Ir(III) ion is an ideal choice of photoactive metal centre, due to the heavy atom effect that favours SOC. This was evidenced by the values of Φ_{Em} for the Ir(III) complexes (**C1**-**C3**) in this study *vs* structurally Ru(II) complexes reported in literature.

Cyclometalated 2-phenylpyridyl ligands are strong sigma donors and are thus good ligands to incorporate in a photosensitiser. Modifications of this *C^N* chelated ligand should directly influence the HOMO of the complex to have an effect on the photophysical properties of the complex.

Bipyridines are renowned π-acceptor ligands, occurring high up on the spectrochemical series. Thus, they are ideal *N^N* ligands. Modifications of this ligand should ideally directly influence the LUMO of the complex. One type example of this modification could be to extend the π-conjugation.

It is important to maintain structural rigidity of the complex. This could be achieved *via* the incorporation of a tridentate ligand, or selecting substituents with limited degrees of conformational freedom.

Figure 5.1. Suggested structural modifications that should be considered when designing an efficient photosensitiser.

The noteworthy photostability exhibited for complexes (**C1**-**C3**) over the 48 h irradiation time, the versatile absorption spectra for these complexes (**C1**-**C3**) as well as the reversible electrochemical behaviour of complexes **C2** and **C3,** underscores their potential as photosensitisers for a different photocatalytic reaction or a different photochemical application altogether. The latter application being evaluating complexes (**C1**-**C3**) as potential PDT agents. Although the effect of increasing the number of metal centres (trinuclear *vs* mononuclear complexes) wasn't as significant on the photocatalytic activity that we initially hypothesised, trinuclear complexes do still have relevance in photochemical applications. This is evidenced by their role as photocatalysts in CO_2 reduction reactions as well as organic transformation reactions, which was discussed in Chapter 1 of this thesis.[6-8] Additionally, Prajith *et al.*,[2] as well as Matshitse *et al.*[9] have demonstrated the advantages of polymetallic complexes as PDT agents, where both groups reported a trend of increased cellular uptake as the overall charge (i.e. increased number of metal centres) of the complex increased.

Finally, more in-depth mechanistic studies should be conducted on the photocatalysed reaction investigated herein. Emphasis should be made on the postulated side reaction which affords the additional product obtained when complexes (**C1**-**C3**) are selected as photoredox catalysts, as it poses an interesting strategy to generate new C-C bonds in molecules.

5.3 References

1. L. Flamigni, A. Barbieri, C. Sabatini, B. Ventura and F. Barigelletti, in *Photochemistry and Photophysics of Coordination Compounds II*, eds. V., Springer Berlin, Heidelberg, 2007, pp. 143-203.
2. N. U. Prajith, P. V. Priyanka and V. Alexander, *J. Biol. Inorg. Chem.*, 2022, 27, 357-372.
3. X. Fan, X. Gong, M. Ma, R. Wang and P. J. Walsh, *Nat. Commun.*, 2018, 9, 4936.
4. J. V. Caspar and T. J. Meyer, *J. Phys. Chem.*, 1983, 87, 952-957.
5. N. Sinha and O. S. Wenger, *J. Am. Chem. Soc.*, 2023, 145, 4903-4920.
6. R. O. Reithmeier, S. Meister, A. Siebel and B. Rieger, *Dalton Trans.*, 2015, 44, 6466-6472.
7. A. M. Cancelliere, F. Puntoriero, S. Serroni, S. Campagna, Y. Tamaki, D. Saito and O. Ishitani, *Chem. Sci.*, 2020, 11, 1556-1563.
8. N. M. Motimani, S. Ngubane and G. S. Smith, *Polyhedron*, 2022, 212, 115616.
9. R. Matshitse, N. Nwaji, M. Mananga, E. Prinsloo and T. Nyokong, *J. Photochem. Photobiol. A: Chem.*, 2018, 367, 253-260.

Chapter 6: Experimental

6.1 General details

6.1.1 General experimental details

Solvents and reagents were obtained from commercial sources (Sigma-Aldrich, Merck and Kimix) and were used without any further purification, unless stated otherwise. Anhydrous solvents were degassed with argon prior to use. All reactions were performed using standard Schlenk-line techniques under an argon atmosphere. Reactions were monitored by thin-layer chromatography (TLC) using aluminium-backed Merck precoated silica-gel 60 F_{254} plates, and compounds were visualised under ultraviolet (UV) light. Column chromatography was performed using 60 Å silica gel (7-230 mesh).

6.1.2 Spectroscopic and analytical instrumentation

Nuclear magnetic resonance (NMR) spectra were obtained on either a Bruker XR600 MHz spectrometer (^{1}H at 599.95 MHz and ^{13}C{^{1}H} at 151.0 MHz), a Bruker XR400 spectrometer (^{1}H at 399.95 MHz and ^{13}C{^{1}H} at 100.58 MHz) or a Varian Mercury 300 (^{1}H at 300.08 MHz) spectrometer, with tetramethylsilane (TMS) as the internal standard. Chemical shifts (δ) and *J*-coupling values are reported in units of ppm and Hz respectively. ^{1}H NMR signals are designated as follows: s, singlet; br.s, broad singlet; d, doublet; dd, doublet of doublets; dt, doublet of triplets; t, triplet; m, multiplet.

Infrared spectra were recorded using a Perkin-Elmer Spectrum 100 FT-IR spectrometer equipped with an Attenuated Total Reflectance Infrared Unit (ATR-IR), with bond vibrations measured in reciprocal centimetres (cm^{-1}). Melting points were obtained using a Büchi Melting Point Apparatus B-540 and are uncorrected. High resolution (HR) electrospray ionisation mass spectrometry (ESI- MS) were performed on a Waters Synapt G2 mass spectrometer equipped with an ESI probe and with data recorded using the positive mode. Electronic absorption (UV-Vis) spectra were recorded using the Agilent Cary 8454 Photodiode Array UV-Vis spectrometer. Emission spectra were recorded using a Varian Eclipse spectrofluorometer with a quartz cell of 1 cm at room temperature.

Determination of C/H/N was performed using a Elementar Vario EL Cube Elemental Analyzer. Electrochemical measurements were performed using a BASi EC Epsilon potentiostat connected to a BASi C3 cell stand and subsequently analysed with Epsilon software. A standard three-electrode setup was used which consisted of a glassy carbon working electrode, platinum-wire counter electrode and an Ag/$AgNO_3$ reference electrode. All samples were degassed with argon prior to measurements.

6.2 Synthesis of the benzimidazole ligands and their corresponding iridium(III) complexes

6.2.1 *2-(Pyridin-2-yl)-1H-benzo[d]imidazole* (**L1**)

Ligand (**L1**) was synthesised according to established literature procedures, with minor modifications:[1, 2]

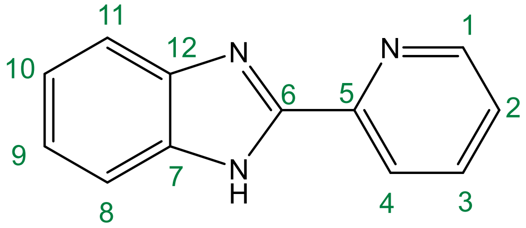

A degassed Schlenk flask was charged with *o*-phenylenediamine (1.05 g, 9.37 mmol) and 2-pyridinecarboxylic acid (1.20 g, 9.75 mmol). Sufficient polyphosphoric acid (*ca* 35 mL) was added to the flask to obtain a stirrable paste, which was heated to 170 °C and stirred for 19 h. Thereafter, the reaction vessel was cooled to 70 °C, water (50 mL) was added and the resulting suspension was left to stir for *ca* 10 min. The reaction mixture was neutralised by slowly pouring the suspension into a beaker containing a cold solution of 10% K_2CO_3 (50 mL, pH 13) while stirring. The reaction vessel and the sides of the beaker were washed with additional cold 10% K_2CO_3 solution, and the resulting neutralised suspension was left in an ice bath for *ca* 10 min. The yellow-brown precipitate that formed was collected *via* vacuum filtration and dried *in vacuo* to afford ligand **L1** as a beige powder. **Yield:** 1.79 g, 95%. **^{1}H NMR** (400 MHz, DMSO) δ (ppm)= 8.73 (d, *J* = 4.6 Hz, 1H, H_1), 8.32 (d, *J* = 7.8 Hz, 1H, H_4), 7.99 (t, *J* = 7.7 Hz, 1H, H_3), 7.64 – 7.60 (m, 2H, H_8, H_{11}), 7.53 – 7.50 (m, 1H, H_2), 7.22 (dd, *J* = 5.8, 3.0 Hz, 2H, H_9, H_{10}). **$^{13}C\{^1H\}$ NMR** (101 MHz, DMSO) δ (ppm)= 150.87, 149.40, 148.62, 137.57, 124.72, 122.47, 121.44, 115.66. **IR/ATR** (ν, cm^{-1}): 3042 (N-H), 1590 $(C=N)_{imine}$,1444 (C=N). **MS (HR-ESI, *m/z*)**: Calculated: 196.0830, Found: 196.0884, (100%, $[M+H]^+$). **Melting point:** 222.9-223.4 °C (literature value: 223 ˚C).

6.2.2 *1-Benzyl-2-(pyridin-2-yl)-1H-benzo[d]imidazole* (**L2**)

Ligand (**L2**) was synthesised according to reported literature procedures, with minor modifications:[3, 4]

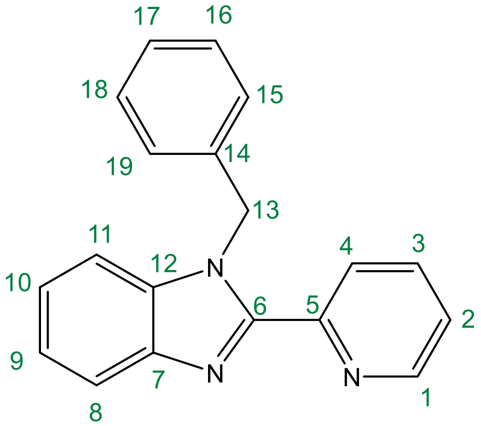

To a degassed Schlenk flask containing ligand **L1** (0.453 g, 2.32 mmol) and K_2CO_3 (0.642 g, 4.65 mmol), anhydrous DMF (10 mL) was added, and the resulting dark yellow suspension was stirred for 30 min at room temperature. Benzyl bromide (0.340 mL, 2.78 mmol) was added and the resulting mixture was stirred for 21 h at room temperature. Thereafter, the reaction was quenched with water (20 mL) and stirred for 5 min. The organic fractions of the mixture were extracted with DCM (4 x 20 mL), and washed with water (4 x 20 mL). The organic fractions were dried over anhydrous $MgSO_4$, filtered by gravity and the solvent of the filtrate was removed under reduced pressure to afford a dark yellow oil that was dried *in vacuo*. After 24 h, an off-white solid in a brown oil resulted. The crude solid-oil suspension was filtered by vacuum filtration and washed with cold pet. ether to afford a reddish-brown solid, ligand **L2**, that was dried *in vacuo*. **Yield:** 0.511 g, 77%. **^1H NMR** (400 MHz, DMSO) δ (ppm)= 8.69 (d, *J* = 4.2 Hz, 1H, H_1), 8.36 (d, *J* = 7.9 Hz, 1H, H_4), 8.00 (t, *J* = 7.8 Hz, 1H, H_3), 7.79 – 7.73 (m, 1H, H_8), 7.57 (dd, *J* = 6.1, 2.8 Hz, 1H, H_{11}), 7.53 – 7.48 (m, 1H, H_2), 7.30 – 7.18 (m, 5H, H_9, H_{10}, H_{16}, H_{17}, H_{18}), 7.12 (d, *J* = 7.3 Hz, 2H, H_{15}, H_{19}), 6.22 (s, 2H, H_{13}). **$^{13}C\{^1H\}$ NMR** (101 MHz, DMSO) δ (ppm)= 150.03, 149.33, 148.94, 142.25, 137.81, 137.65, 136.55, 128.61, 127.34, 126.77, 124.55, 124.49, 123.52, 122.71, 119.70, 111.41, 48.03. **IR/ATR** (v, cm^{-1}): 1584 (C=N)$_{\text{imine}}$, 1438 (C=N). **MS (HR-ESI, *m/z*)**: Calculated: 286.1300, Found: 286.1347, (100%, [M+H]$^+$). **Melting point:** 116.3-117.1 °C (literature value: 116-118 °C).

6.2.3 *1,3,5-Tris((2-(pyridin-2-yl)-1H-benzo[d]imidazol-1-yl)methyl)benzene* (**L3**)

Ligand (**L3**) was synthesised in a similar manner to ligand (**L2**), with the following modifications:

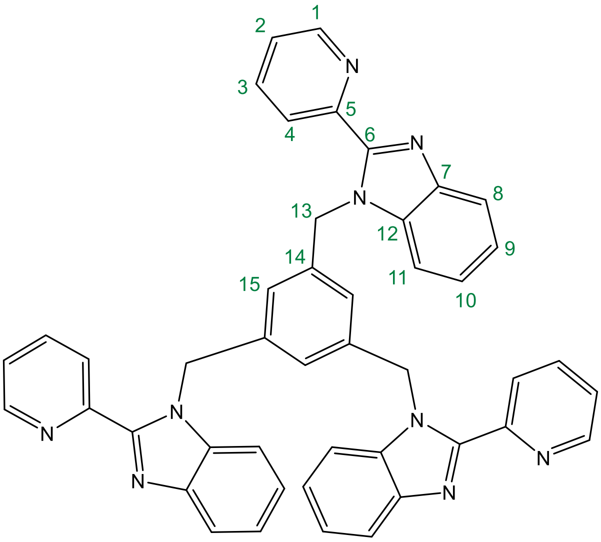

To a degassed Schlenk flask containing ligand **L1** (0.339 g, 1.74 mmol) and K_2CO_3 (0.482 g, 3.49 mmol), anhydrous DMF (10 mL) was added, and the resulting yellow suspension was stirred for 30 min at room temperature. 1,3,5-Tris(bromomethyl)benzene (0.206 g, 0.578 mmol) was added and the resulting mixture was stirred for 48 h at room temperature. Thereafter, the reaction was quenched with water (75 mL). There organic fractions of the mixture were extracted with DCM (4 x 50 mL), and washed with water (4 x 50 mL). Following this step, the organic fractions were dried over anhydrous $MgSO_4$, filtered by gravity and the solvent of the filtrate was removed under reduced pressure to afford a yellow oil. The crude oil was purified by silica gel column chromatography, which afforded the desired compound **L3** (eluent 100% EtOAc) as white flakes. **Yield:** 0.237 g, 59%. **^{1}H NMR** (400 MHz, DMSO) δ (ppm)= 8.23 (d, J = 4.5 Hz, 3H, H_1), 8.12 (d, J = 7.9 Hz, 3H, H_4), 7.86 (t, J = 7.7 Hz, 3H, H_3), 7.72 (d, J = 8.0 Hz, 3H, H_8), 7.38 – 7.33 (m, 3H, H_{11}), 7.32 – 7.22 (m, 6H, H_2, H_9), 7.16 (t, J = 7.6 Hz, 3H, H_{10}), 6.93 (s, 3H, H_{15}), 5.92 (s, 6H, H_{13}). **^{13}C{^{1}H} NMR** (101 MHz, DMSO) δ (ppm)= 149.60, 148.87, 148.34, 142.10, 138.31, 137.25, 136.34, 125.11, 124.20, 124.11, 123.30, 122.50, 119.62, 110.99, 47.75. **IR/ATR** (*v*, cm^{-1}): 1586 (C=N)$_{\text{imine}}$, 1438 (C=N). **MS (HR-ESI, *m/z*)**: Calculated: 700.2892, Found: 700.2933, (100%, [M+H]$^{+}$). **Melting Point:** 217.6-218.5 °C.

6.2.4 *Dichlorotetrakis(2-(2-pyridinyl)phenyl)diiridium(III)*

[Ir(ppy)$_2$(μ-Cl)]$_2$ was synthesised according to an established literature procedure:[5]

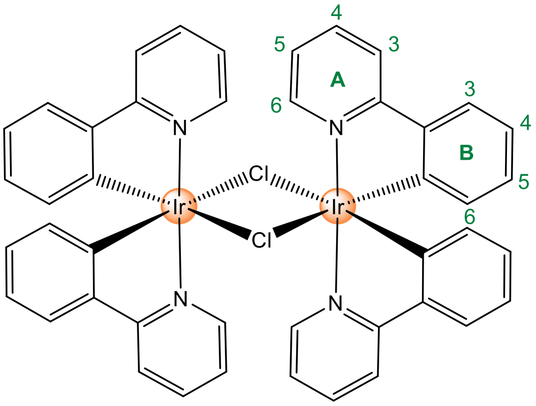

2-Phenylpyridine (0.640 mL, 4.36 mmol) was dissolved in a mixture of 2-ethoxyethanol/water (3:1 *v/v*, 20 mL) and the solution was degassed with argon for 20 min. $IrCl_3$•xH_2O (0.513 g, 1.45 mmol) was added and the mixture was refluxed for 24 h at 140 °C. Thereafter, water (15 mL) was added and the resulting yellow precipitate was collected *via* vacuum filtration and dried *in vacuo* to afford [Ir(ppy)$_2$(μ-Cl)]$_2$ as a bright yellow powder. **Yield**: 0.610 g, 78%. **^{1}H NMR** (400 MHz, $CDCl_3$) δ (ppm)= 9.24 (d, *J* = 6.0 Hz, 4H, H_{6A}), 7.87 (d, *J* = 8.0 Hz, 4H, H_{3A}), 7.73 (t, *J* = 7.8 Hz, 4H, H_{4A}), 7.48 (d, *J* = 8.0 Hz, 4H, H_{3B}), 6.75 (dt, *J* = 14.1, 7.1 Hz, 8H, H_{5A}, H_{5B}), 6.56 (t, *J* = 7.4 Hz, 4H, H_{4B}), 5.93 (d, *J* = 7.6 Hz, 4H, H_{6B}). **^{13}C{^{1}H} NMR** (101 MHz, $CDCl_3$) δ (ppm)= 168.66, 151.81, 145.46, 143.82, 136.29, 130.71, 129.22, 123.78, 122.25, 121.45, 118.53. **IR/ATR** (*v*, cm^{-1}): 1576 (C=N)$_{\text{pyridyl,}}$ 1478 (C=N). **Melting Point**: Compound remains intact upon heating to 410 °C.

6.2.5 *2-(Pyridin-2-yl)-1H-benzo[d]imidazole iridium(III) complex* (**C1**)

Complex (**C1**) was synthesised according to a procedure previously reported in literature:[6]

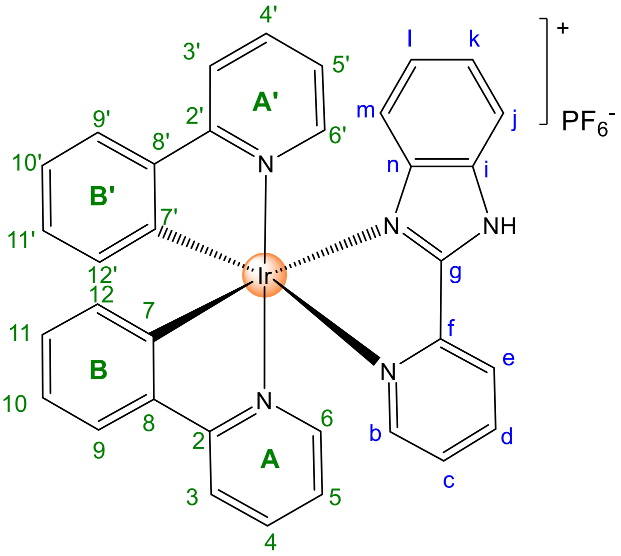

[Ir(ppy)$_2$(μ –Cl)]$_2$ (0.107 g, 0.100 mmol) and 2-(pyridin-2-yl)-1*H*-benzo[*d*]imidazole (**L1**) (0.0394 g, 0.202 mmol) were dissolved in a mixture of anhydrous DCM/anhydrous methanol (4:5 *v/v*, 18 mL), and the resulting solution was stirred at 60 °C for 24 h under an argon atmosphere. Thereafter, the reaction flask was cooled to room temperature, an excess of NH$_4$PF$_6$ (0.0340 g, 0.209 mmol) was added and the mixture was stirred for 2 h at room temperature. The reaction mixture was filtered by gravity to remove the NH$_4$Cl salt, and the solvent of the filtrate was concentrated under reduced pressure. The product was precipitated upon the addition of diethyl ether and then filtered by vacuum filtration. The resulting solid was dried *in vacuo* to afford complex **C1** as a yellow powder. **Yield:** 0.128 g, 76%. **^{1}H NMR** (400 MHz, DMSO) δ (ppm)= 8.66 (d, *J* = 7.9 Hz, 1H, H$_e$), 8.32 (t, *J* = 7.7 Hz, 1H, H$_d$), 8.25 (d, *J* = 8.0 Hz, 1H, H$_3$), 8.19 (d, *J* = 7.9 Hz, 1H, H$_{3'}$), 7.93 – 7.84 (m, 5H, H$_4$, H$_{4'}$, H$_9$, H$_{9'}$, H$_b$), 7.75 (d, *J* = 8.1 Hz, 1H, H$_j$), 7.70 – 7.65 (m, 3H, H$_c$, H$_6$, H$_{6'}$), 7.36 (t, *J* = 7.7 Hz, 1H, H$_k$), 7.13 – 7.01 (m, 5H, H$_5$, H$_{5'}$, H$_{10}$, H$_{10'}$, H$_l$), 6.94 – 6.89 (m, 2H, H$_{11}$, H$_{11'}$), 6.31 (d, *J* = 7.6 Hz, 1H, H$_{12}$), 6.25 (d, *J* = 7.2 Hz, 1H, H$_{12'}$), 6.14 (d, *J* = 8.1 Hz, 1H, H$_m$). **^{13}C{^{1}H} NMR** (101 MHz, DMSO) δ (ppm)= 167.13, 167.03, 153.57, 151.13, 150.36, 149.48, 149.19, 147.43, 147.10, 144.57, 144.32, 140.06, 139.93, 138.62, 138.41, 134.75, 131.82, 131.11, 130.24, 129.57, 128.63 , 125.48, 125.11, 124.75, 124.37, 124.29, 123.91, 123.81, 122.21, 122.11, 119.89, 119.59, 116.56, 114.01. **IR/ATR** (v, cm^{-1}): 3132 (N-H), 1612 (C=N)$_{imine}$, 1476 (C=N), 828 (P-F), 734 (P-F). **MS (HR-ESI, *m/z*)**: Calculated: 696.1739, Found: 696.1740, (100%, [M -PF$_6$]$^+$). **Melting Point**: 349.0 ˚C (decomp.).

6.2.6 *1-Benzyl-2-(pyridin-2-yl)-1H-benzo[d]imidazole iridium(III) complex* (**C2**)

C2 was synthesised according to the following procedure:

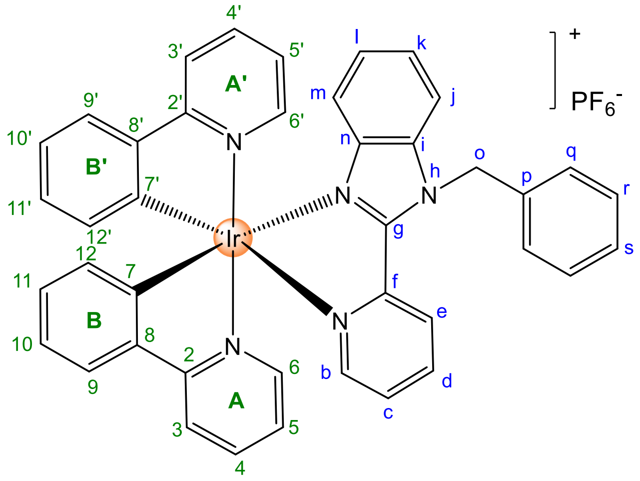

[Ir(ppy)$_2$(μ −Cl)]$_2$ (0.109 g, 0.102 mmol) and 1-benzyl-2-(pyridin-2-yl)-1*H*-benzo[*d*]imidazole (**L2**) (0.0585 g, 0.205 mmol) were dissolved in a mixture of anhydrous DCM/anhydrous methanol (4:5 *v/v*, 18 mL), and the resulting solution was stirred at 60 ˚C for 24 h under an argon atmosphere. Thereafter, the reaction flask was cooled to room temperature, an excess of NH$_4$PF$_6$ (0.0386 g, 0.237 mmol) was added, and the mixture was stirred for 2 h at room temperature. The reaction mixture was filtered by gravity to remove the NH$_4$Cl salt, and the solvent of the filtrate was concentrated under reduced pressure. The product was precipitated upon the addition of cold diethyl ether and filtered. The resulting solid was dried *in vacuo* to afford complex **C2** as a yellow powder. **Yield:** 0.128 g, 68%. **^{1}H NMR** (400 MHz, DMSO) δ (ppm)= 8.47 (d, *J* = 8.3 Hz, 1H, H$_e$), 8.27 (d, *J* = 8.4 Hz, 1H, H$_3$), 8.21 (d, *J* = 8.5 Hz, 1H, H$_{3'}$), 8.15 (t, *J* = 8.1 Hz, 1H, H$_d$), 7.98 – 7.86 (m, 5H, H$_4$, H$_{4'}$, H$_9$, H$_{9'}$, H$_b$), 7.80 (d, *J* = 5.6 Hz, 1H, H$_j$), 7.66 – 7.59 (m, 1H, H$_c$), 7.58 (d, *J* = 5.7 Hz, 1H, H$_6$), 7.43 (t, *J* = 7.6 Hz, 1H, H$_k$), 7.36 – 7.26 (m, 3H, H$_{6'}$, H$_5$, H$_{5'}$), 7.19 – 7.14 (m, 3H, H$_{10}$, H$_{10'}$, H$_l$), 7.11 – 7.00 (m, 5H, H$_q$, H$_r$, H$_s$), 6.97 – 6.88 (m, 2H, H$_{11}$, H$_{11'}$), 6.34

– 6.19 (m, 5H, H_{12}, $H_{12'}$, H_m, H_o). **^{13}C{^{1}H} NMR** (101 MHz, DMSO) δ (ppm)= 167.08, 166.89, 152.57, 151.30, 151.18, 149.54, 148.93, 147.47, 146.16, 144.48, 144.10, 139.72, 138.81, 138.74, 138.58, 136.80, 135.34, 131.81, 131.02, 130.31, 129.69, 129.21, 128.80, 128.05, 126.22, 125.84, 125.75, 125.20, 124.89, 123.94, 123.71, 122.30, 122.21, 120.03, 119.73, 117.18, 112.70, 48.31.**IR/ATR** (ν, cm $^{-1}$): 1626 (C=N)$_{\text{imine}}$, 1502 (C=N), 854 (P-F), 756 (P-F). **MS (HR-ESI, *m/z*)**: Calculated: 786.2209, Found: 786.2205, (100%, [M–PF_6]$^+$). **Melting Point**: 204.4-206.2 °C. **EA** (%): Calculated: C, 49.98; H, 3.55; N, 7.84, Found: C, 52.88; H, 3.36; N, 7.52.

6.2.7 *1,3,5-Tris((2-(pyridin-2-yl)-1H-benzo[d]imidazol-1-yl)methyl)benzene iridium(III) complex* (**C3**)

C3 was synthesised according to the following procedure:

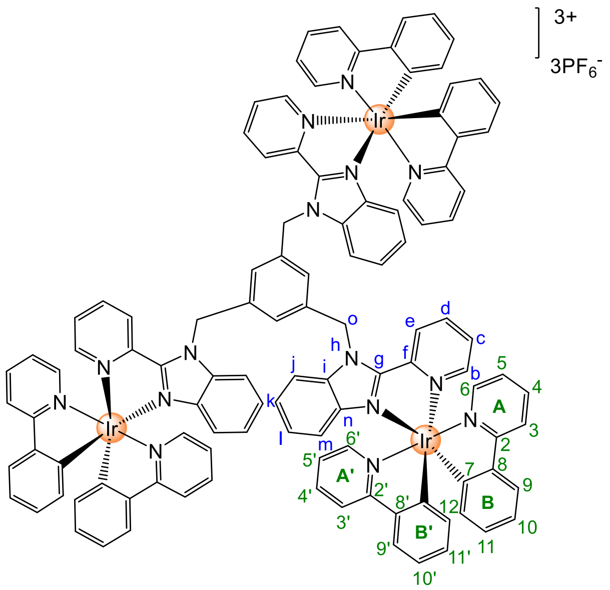

[Ir(ppy)$_2$(μ –Cl)]$_2$ (0.146 g, 0.136 mmol) and 1,3,5-tris((2-(pyridin-2-yl)-1*H*-benzo[*d*]imidazol-1-yl)methyl)benzene (**L3**) (0.0634 g, 0.0906 mmol) were dissolved in a mixture of anhydrous DCM/anhydrous methanol (4:5 *v/v*, 45 mL), and the resulting solution was stirred at 60 °C for 24 h under an argon atmosphere. The reaction flask was cooled to room temperature, an excess of NH_4PF_6 (0.0898 g, 0.551 mmol) was added and the mixture was stirred for 2.5 h at room temperature.

Thereafter, the solvent of the suspension was concentrated under reduced pressure, and the dark-yellow precipitate was filtered and washed with water. Following this step, the crude solid was redissolved in DCM and filtered by gravity. The filtrate was concentrated under reduced pressure and the product was precipitated with cold diethyl ether and collected by filtration. The resulting precipitate was dried *in vacuo* to afford complex **C3** as a yellow solid. **Yield:** 0.178 g, 75%. **^{1}H NMR** (600 MHz, Acetone) δ(ppm)= 8.31 (d, *J* = 8.1 Hz, 1H, H_e), 8.23 – 8.13 (m, 9H, H_{Ar}), 8.10 (d, *J* = 5.0 Hz, 1H, H_{Ar}), 8.01 (d, *J* = 5.7 Hz, 1H, H_{Ar}), 7.97 (d, *J* = 5.4 Hz, 1H, H_{Ar}), 7.94 – 7.77 (m, 17H, H_{Ar}, H_d), 7.73 (d, *J* = 5.2 Hz, 1H, H_b), 7.65 – 7.44 (m, 8H, H_{Ar}), 7.37 (d, *J* = 7.8 Hz, 1H, H_{Ar}), 7.27 – 7.23 (m, 2H, H_{Ar}), 7.17 – 7.01 (m, 13H, H_{Ar}, H_c), 7.00 – 6.88 (m, 10H, H_{Ar}), 6.82 (t, *J* = 7.2 Hz, 1H, H_{Ar}), 6.48 – 6.30 (m, 9H, H_{12}, $H_{12'}$, H_m), 6.23 (dd, *J* = 29.7, 13.7 Hz, 2H, H_o), 6.05 (ddd, *J* = 59.4, 39.7, 21.6 Hz, 4H, H_o). **^{13}C{^{1}H} NMR** (151 MHz, Acetone) δ (ppm)= 206.19, 168.95, 168.80, 153.85, 153.64, 153.57, 153.15, 153.01, 152.97, 151.96, 151.92, 150.77, 150.71, 150.37, 150.31, 150.25, 148.26, 148.22, 147.42, 145.53, 145.16, 140.45, 140.34, 140.08, 139.94, 139.47, 139.33, 139.22, 138.98, 138.87, 137.88, 137.81, 137.72, 133.15, 132.30, 131.37, 130.71, 129.59, 129.48, 127.40, 127.22, 127.17, 127.11, 126.46, 126.38, 126.30, 126.23, 126.08, 125.94, 125.82, 125.63, 125.54, 124.68, 124.51, 124.47, 124.39, 123.45, 123.28, 120.80, 120.49, 119.15, 119.11, 119.03, 112.75, 112.70, 112.54, 112.48, 112.32, 79.25, 79.03, 78.81, 49.76, 49.71, 49.65, 49.59, 29.84. **IR/ATR** (ν, cm^{-1}): 1608 (C=N)$_{imine}$, 1482 (C=N), 834 (P-F), 738 (P-F). **MS (HR-ESI, *m/z*)**: Calculated: 733.5221, Found: 733.5249, (100%, [M–3PF$_6$]$^{3+}$). **Melting Point**: 308.7 °C (decomp.). **EA** (%): Calculated: C, 50.22; H, 3.38; N, 7.78, Found: C, 50.55; H, 3.01; N, 7.97.

6.3. Synthesis of the benzyl (K1) and furfuryl (K2) substituted ketimine precursors

The respective ketimine precursors for the photocatatyic reactions were synthesised following literature procedures.[7, 8]

6.3.1 *Benzyl substituted ketimine* (**K1**)

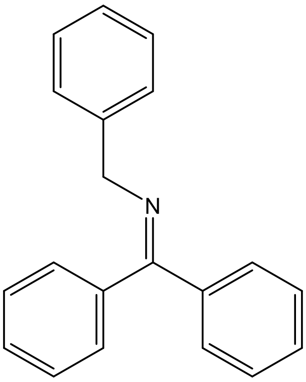

Benzophenone (1.93 g, 10.6 mmol), benzylamine (1.74 mL, 15.9 mmol) and 25 mL anhydrous toluene were charged into a degassed Schlenk flask. To this solution, T*i*(O*i*-Pr)$_4$ (2.00 mL, 6.77 mmol) was added and the resulting mixture was stirred for 48 h at 80 °C. After this period, the reaction flask was cooled to room temperature, 20 mL toluene was added and 2.5 mL water was added to quench the reaction. The resulting mixture was stirred for 30 min at room temperature, during which time a precipitate (TiO_2) formed. Thereafter, the residue was filtered and washed with diethyl ether. The filtrate was dried over anhydrous Na_2SO_4, filtered by gravity and the solvent of the filtrate was removed under reduced pressure to afford a murky-white oil. Recrystallisation of the crude oil was performed by dissolving the oil in minimal hot DCM, adding hexane and placing the resulting suspension in the fridge overnight. The resulting solid was filtered and washed with additional cold hexane before drying *in vacuo* to obtain the benzyl substituted ketimine product (**K1**) as a crystalline white solid. **Yield**: 2.00 g, 70%. **^{1}H NMR** (300 MHz, $CDCl_3$) δ (ppm)= 7.71 (d, *J* = 7.5 Hz, 2H, H_{Ar}), 7.53 – 7.18 (m, 13H, H_{Ar}), 4.64 (s, 2H, CH_2). The ^{1}H NMR data is in agreement with literature.[7] **IR/ATR** (v, cm^{-1}): 1618 (C=N)$_{imine.}$

6.3.2 *Furfuryl substituted ketimine* (**K2**)

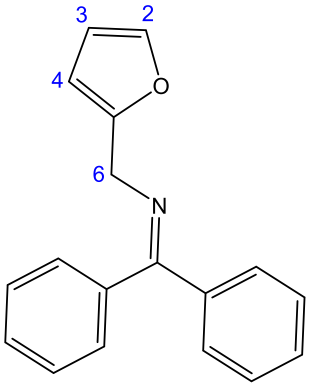

Benzophenone (1.61 g, 8.85 mmol), furfurylamine (1.24 mL, 13.3 mmol) and 30 mL anhydrous toluene were charged into a degassed Schlenk flask. To this solution, T*i*(O*i*-Pr)$_4$ (1.68 mL, 5.66 mmol) was added and the resulting mixture was stirred for 48 h at 80 ˚C. After this period, the reaction flask was cooled to room temperature, 20 mL toluene was added and 2 mL water was added to quench the reaction. The resulting mixture was stirred for 30 min at room temperature, during which time a precipitate (TiO_2) formed. Thereafter, the residue was filtered and washed with diethyl ether. The filtrate was dried over anhydrous Na_2SO_4, filtered by gravity and the solvent of the filtrate was removed under reduced pressure to afford a dark yellow oil. Recrystallisation of the crude oil was performed by dissolving the oil in minimal hot DCM, adding hexane and placing the resulting suspension in the fridge overnight. The resulting solid was filtered and washed with additional cold hexane before drying *in vacuo* to obtain the furfuryl substituted ketimine product (**K2**) as a brown solid. **Yield**: 1.17 g, 51%. **^{1}H NMR** (300 MHz, $CDCl_3$) δ (ppm)= 7.69 (d, *J* = 7.6 Hz, 2H, H_{Ar}), 7.51 (d, *J* = 6.3 Hz, 3H, H_{Ar}), 7.40 (dq, *J* = 15.1, 7.4 Hz, 4H, H_{Ar}), 7.30 – 7.25 (m, 2H, H_{Ar}), 6.35 (d, 1H, H_3), 6.27 (d, *J* = 2.3 Hz, 1H, H_4), 4.60 (s, 2H, H_6). The ^{1}H NMR data is in agreement with literature.[8] **IR/ATR** (ν, cm^{-1}): 1620 (C=N)$_{\text{imine.}}$

6.4. General procedure for the visible-light mediated carboxylation reactions of ketimines using CO_2:[9]

The benchmark photoredox catalyst, $[Ir(ppy)_2(dtbbpy)]PF_6$ was prepared following a literature procedure.[10] Control and optimised reactions were performed with $[Ir(ppy)_2(dtbbpy)]PF_6$ as the photoredox catalyst.

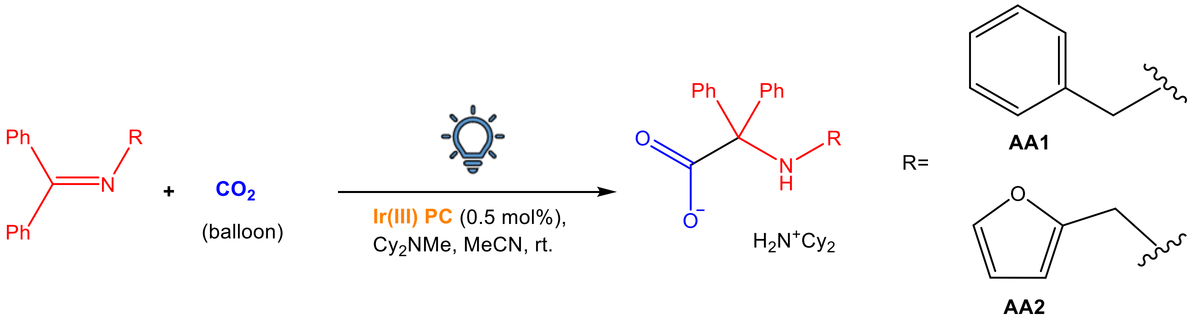

The respective benzyl or furfuryl substituted ketimine (**K1** or **K2**, 1 eq., 50 mg scale), iridium catalyst (**C1**, **C2**, **C3** or $[Ir(ppy)_2(dtbbpy)]PF_6$ (0.5 mol%)), Cy_2NMe (2 eq.) and anhydrous CH_3CN (2.00 mL) were charged into a standard borosilicate glass vial. The vial was sealed and the contents of the vial were purged with argon for 15 min. CO_2 gas (1 atm.) in a balloon was bubbled into the reaction mixture through a needle, under stirring for 35 sec. The needle was lifted up and out of the reaction mixture but kept in the vial during the course of the reaction. Thereafter, the reaction vial was placed in the EvoluChem™ PhotoRedOx Box and irradiated with an EvoluChem™ blue LED light (405 nm, 18 W) and stirred at room temperature, with fan cooling on. A white precipitate appeared as the reaction proceeded. After 24 h, the vial was opened and placed in an ice bath. The work-up procedure involved collecting the precipitate by filtration and washing with cold CH_3CN. The final amino acid salt products (**AA1**, **AA2**) were dried *in vacuo* and obtained as a white solid.

The additional benzyl/furfuryl substituted products were exclusively obtained when complex (**C1**) was utilised as the photoredox catalyst. A mixture of the respective desired amino acid products (**AA1**/**AA2**) and the additional benzyl/furfuryl substituted products was obtained with photocatalysts (**C2** and **C3**). The desired amino acid salt products and the additional products were isolated as white solids, after filtration.

6.4.1 *Benzyl substituted amino acid salt product* (**AA1**):

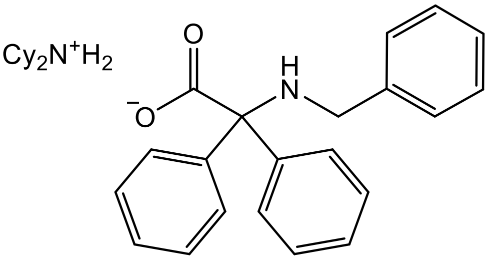

^{1}H NMR (300 MHz, CDCl$_3$) δ (ppm) = 7.61 (d, *J* = 7.4 Hz, 4H, H$_{Ar}$), 7.34 – 7.16 (m, 11H, H$_{Ar}$), 3.33 (s, 2H, C**H$_2$**), 2.69 (t, *J* = 9.5 Hz, 2H, Cy), 1.81 – 1.51 (m, 10H, Cy), 1.21 – 0.98 (m, 10H, Cy). **^{13}C {^{1}H} NMR** (101 MHz, CDCl$_3$) δ (ppm)=177.15, 144.66, 141.93, 129.47, 128.44, 128.18, 127.22, 126.51, 126.06, 77.16, 74.15, 52.66, 48.84, 26.36, 25.36, 24.98. **IR/ATR** (*ν*, cm^{-1}): 2922 (N-H), 2852 (N-H), 1625 (C=O). Spectral data correlates with literature.[9]

6.4.2 *Furfuryl substituted amino acid salt product* (**AA2**):

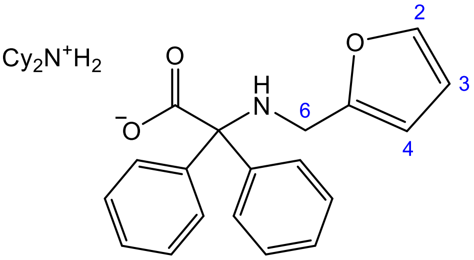

^{1}H NMR (300 MHz, CDCl$_3$) δ (ppm)= 7.61 (d, *J* = 7.4 Hz, 4H, H$_{Ar}$), 7.39 (d, *J* = 4.9 Hz, 1H, H$_{Ar}$), 7.24 – 7.12 (m, 7H, H$_{Ar}$), 6.25 (s, 1H, H$_3$), 6.11 (s, 1H, H$_4$), 3.32 (s, 2H, H$_6$), 2.72 (br.s, 2H, Cy), 1.70 – 1.57 (m, 11H, Cy), 1.14 – 1.02 (m, 10H, Cy). **^{13}C {^{1}H} NMR** (101 MHz, CDCl$_3$) δ (ppm)= 176.91, 155.44, 144.19, 141.26, 129.50, 127.26, 126.15, 110.15, 105.94, 77.16, 73.86, 52.73, 41.83, 26.38, 25.02. **IR/ATR** (*ν*, cm^{-1}): 2922 (N-H), 2848 (N-H), 1624 (C=O). Spectral data correlates with literature.[9]

6.4.3 *Benzyl substituted 'additional' product:*

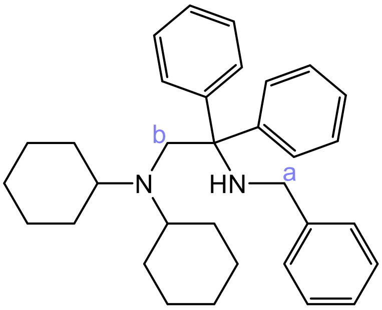

^{1}H NMR (600 MHz, CDCl$_3$) δ (ppm)= 7.44 (d, *J* = 7.6 Hz, 4H, H$_{Ar}$), 7.37 (d, *J* = 7.5 Hz, 2H, H$_{Ar}$), 7.29 – 7.23 (m, *J* = 7.7, 6.3 Hz, 7H, H$_{Ar}$), 7.17 (dt, *J* = 22.5, 7.3 Hz, 3H, H$_{Ar}$), 3.49 (s, 2H, CH$_2$**b**), 3.42 (s, 2H, CH$_2$**a**), 2.00 – 1.93 (m, 2H, Cy), 1.80 (d, *J* = 11.7 Hz, 2H, Cy), 1.59 (dd, *J* = 27.0, 12.6 Hz, 5H, Cy), 1.45 (t, *J* = 15.6 Hz, 5H, Cy), 1.24 (dd, *J* = 25.0, 12.3 Hz, 2H, Cy), 1.19 – 1.12 (m, *J* = 21.8, 7.5 Hz, 5H, Cy), 0.93 – 0.81 (m, *J* = 38.1, 19.1, 11.3 Hz, 6H, Cy). **^{13}C {^{1}H} NMR** (151 MHz, CDCl$_3$) δ (ppm)= 147.06, 142.09, 128.24, 128.01, 127.85, 126.55, 126.15, 77.16, 64.83, 58.38, 54.26, 47.45, 32.44, 26.77, 26.34, 26.22. **IR/ATR** (v, cm^{-1}): 2923 (N-H), 2850 (N-H). **LC-MS (*m/z*)**: Calculated: 467.3, Found: 467.3 (100%, [M+H]$^+$).

6.4.4 *Furfuryl substituted 'additional' product:*

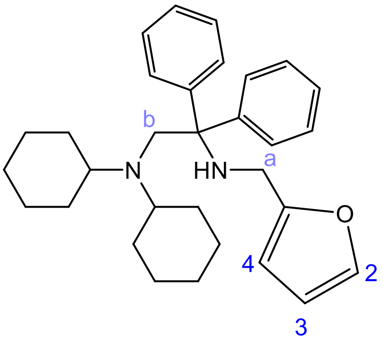

^{1}H NMR (600 MHz, CDCl$_3$) δ (ppm)= 7.40 (d, *J* = 7.6 Hz, 4H, H$_{Ar}$), 7.31 (s, 1H, H$_{Ar}$), 7.26 – 7.23 (m, *J* = 10.2, 5.1 Hz, 5H, H$_{Ar}$), 7.16 (t, *J* = 7.3 Hz, 2H, H$_{Ar}$), 6.28 – 6.26 (m, 1H, H$_3$), 6.12 (d, *J* = 3.0 Hz, 1H, H$_4$), 3.44 (s, 2H, CH$_2$**b**), 3.39 (s, 2H, CH$_2$**a**), 1.93 – 1.88 (m, 2H, Cy), 1.78 (d, *J* = 12.7 Hz, 3H, Cy), 1.58 (d, *J* = 12.8 Hz, 4H, Cy), 1.48 (d, *J* = 11.7 Hz, 2H, Cy), 1.43 (d, *J* = 11.3 Hz, 2H, Cy), 1.22 (dd, *J* = 25.4, 12.4 Hz, 3H, Cy), 1.17 – 1.08 (m, *J* = 19.2, 14.4, 7.6 Hz, 5H, Cy), 0.93 – 0.82 (m, *J* = 25.3, 12.7 Hz, 6H, Cy). **^{13}C {^{1}H} NMR** (151 MHz, $CDCl_3$) δ (ppm)= 155.18, 146.09, 141.11, 128.16, 127.67, 126.08, 109.95, 105.47, 77.16, 76.95, 76.74, 64.56, 58.28, 54.55, 40.90, 32.19, 26.55, 26.07. **IR/ATR** (v, cm^{-1}): 2924 (N-H), 2851 (N-H). **LC-MS (*m/z*)**: Calculated: 457.3, Found: 457.3 (100%, $[M+H]^+$).

6.5 X-ray Crystallography

Suitable single crystals of complex **C2** were obtained by slow diffusion of diethyl ether into a solution of dichloromethane/methanol at room temperature. Single-crystal X-ray diffraction data were collected on a Bruker D8 Venture diffractometer using graphite-monochromated Cu-Kα radiation (χ = 1.54178 Å). Data collection was carried out at 100(2) K. Temperature was controlled by an Oxford Cryostream cooling system (Oxford Cryostat). Cell refinement and data reduction were performed using the program SAINT.[11] The data were scaled and absorption correction performed using SADABS.[12] The structure was solved by direct methods using SHELXS-97[12] and refined by full-matrix least-squares methods based on F^2 using SHELXL-2014[12] and using the graphics interface program X-Seed.[13,14] The programs X-Seed and POV-Ray[15] were used to prepare molecular graphic images. All non-hydrogen atoms were refined anisotropically. All hydrogen atoms were placed in idealised positions and refined in riding models with U_{iso} assigned 1.2 times U_{eq} of their parent atoms and the C-H bond distances were constrained at 0.95 Å and 0.99 Å. The structure was refined to R factor of 0.0185.

6.6 Emission quantum yield (Φ_{Em}) measurements

Emission quantum yields were determined in acetonitrile using a comparative method previously described in the literature.[16] $[Ru(bpy)_3]Cl_2$ (Φ_{Em} = 0.097) was used as the standard.[17, 18]

6.7 Triplet excited-state lifetime experiments

Triplet state lifetimes were recorded in acetonitrile at 470 nm using an Edinburgh Instrument LP980 spectrometer and an Ekspla NT-342B laser equipped with an OPO for precise excitation (using 2.0 mJ excitation energy, 7 nm pulse duration and a 20 Hz repetition rate). Prior to the measurements, sample solutions were purged with nitrogen for 40 min. The absorbances of the samples were maintained at *ca*. 1.2. The acquired decay curve was analysed through exponential curve fitting using OriginPro 98 software.

6.8 References

1. O. Dayan, M. Tercan and N. Özdemir, *J. Mol. Struct.*, 2016, **1123**, 35-43.
2. N. V. Likhanova, R. Martínez-Palou, M. A. Veloz, D. J. Matías, V. E. Reyes-Cruz, H. Höpfl and O. Olivares, *J. Heterocycl. Chem.*, 2007, **44**, 145-153.
3. W. G. Wang, F. Wang, H. Y. Wang, G. Si, C. H. Tung and L. Z. Wu, *Chem. Asian J.*, 2010, **5**, 1796-1803.
4. M. Vaquero, N. Busto, N. Fernández-Pampín, G. Espino and B. García, *Inorg. Chem.*, 2020, **59**, 4961-4971.
5. F. Monti, A. Baschieri, I. Gualandi, J. J. Serrano-Pérez, J. M. Junquera-Hernández, D. Tonelli, A. Mazzanti, S. Muzzioli, S. Stagni, C. Roldan-Carmona, A. Pertegás, H. J. Bolink, E. Ortí, L. Sambri and N. Armaroli, *Inorg. Chem.*, 2014, **53**, 7709-7721.
6. M. Martínez-Alonso, J. Cerdá, C. Momblona, A. Pertegás, J. M. Junquera-Hernández, A. Heras, A. M. Rodríguez, G. Espino, H. Bolink and E. Ortí, *Inorg. Chem.*, 2017, **56**, 10298-10310.
7. R. Wang, M. Ma, X. Gong, G. B. Panetti, X. Fan and P. J. Walsh, *Org. Lett.*, 2018, **20**, 2433-2436.
8. K. Li, A. E. Weber, L. Tseng and S. J. Malcolmson, *Org. Lett.*, 2017, **19**, 4239-4242.
9. X. Fan, X. Gong, M. Ma, R. Wang and P. J. Walsh, *Nat. Commun.*, 2018, **9**, 4936.
10. D. Tordera, M. Delgado, E. Ortí, H. J. Bolink, J. Frey, M. K. Nazeeruddin and E. Baranoff, *Chem. Mater.*, 2012, **24**, 1896-1903.
11. SAINT, Bruker AXS Inc., Madison, WI, USA, v2019.1-0.
12. G. M. Sheldrick, SHELXS-97, SHELXL-2014 and SADABS, Acta Cryst. **C71**,3-8.

13. L. J. Barbour, *J. Supramol. Chem.*, 2001, **1**, 189-191.
14. J. L. Atwood and L. J. Barbour, *Cryst. Growth Des.*, 2003, **3**, 3-8.
15. P. o. V. P. Ltd., Persistence of Vision Raytracer (Version 3.6), retrieved from http://www.povray.org/download/, 2014.
16. Z. Zhao, T. Nyokong and M. D. Maree, *Dalton Trans.*, 2005, 3732-3737.
17. B. Liu, S. Monro, M. A. Jabed, C. G. Cameron, K. L. Colón, W. Xu, S. Kilina, S. A. McFarland and W. Sun, *Photochem. Photobiol. Sci.* , 2019, **18**, 2381-2396.
18. K. Suzuki, A. Kobayashi, S. Kaneko, K. Takehira, T. Yoshihara, H. Ishida, Y. Shiina, S. Oishi and S. Tobita, *Phys. Chem. Chem. Phys.*, 2009, **11**, 9850-9860.

Appendix for: Iridium(III) Photosensitisers for Photoredox Catalysed Carboxylation Reactions of Ketimines

1. Spectroscopic Data for ligands (L1-L3) and their corresponding complexes (C1-C3)

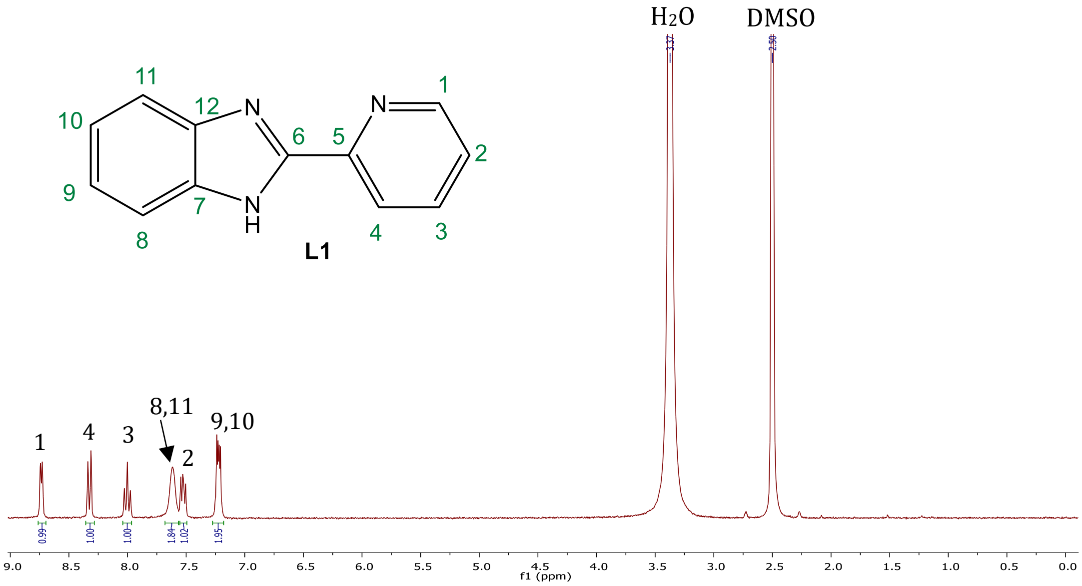

Figure A1. ^{1}H NMR spectrum of compound **L1** in DMSO-d_6.

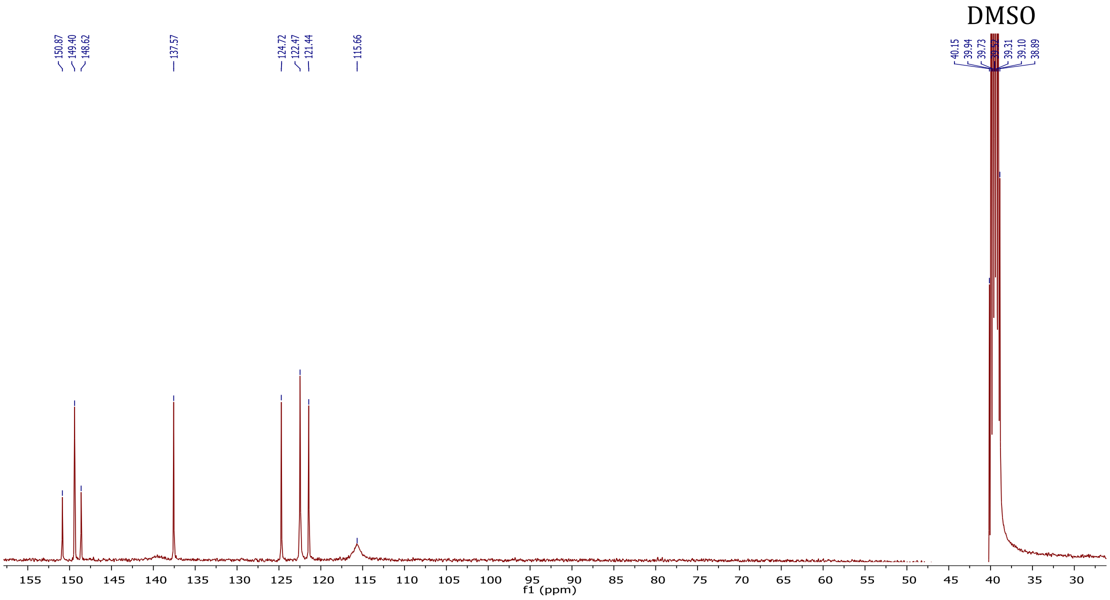

Figure A2. ^{13}C{^{1}H} NMR spectrum of compound **L1** in DMSO-d_6.

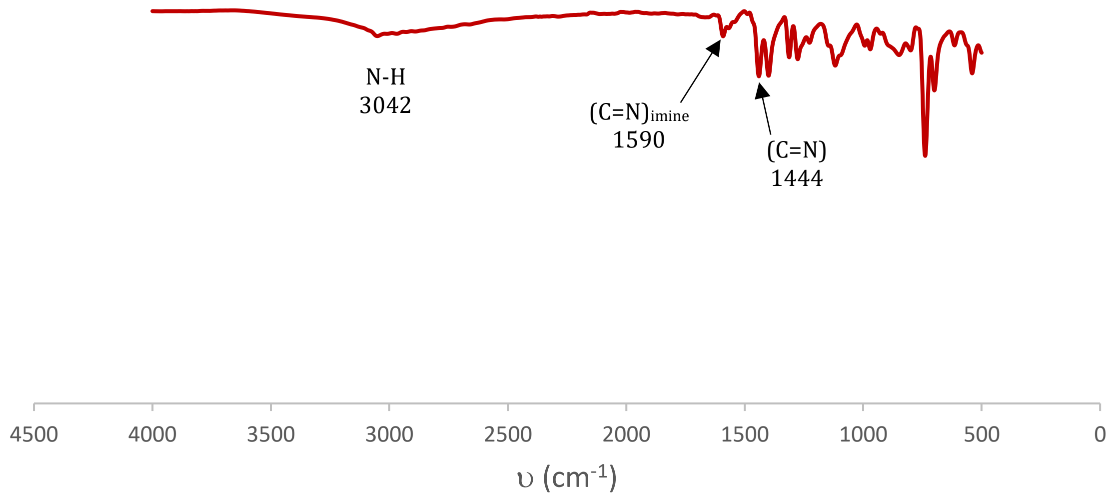

Figure A3. Infrared spectrum of compound **L1**.

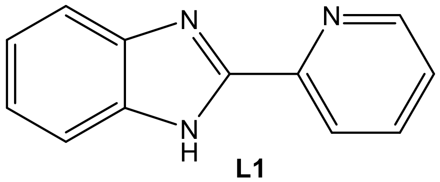

L1

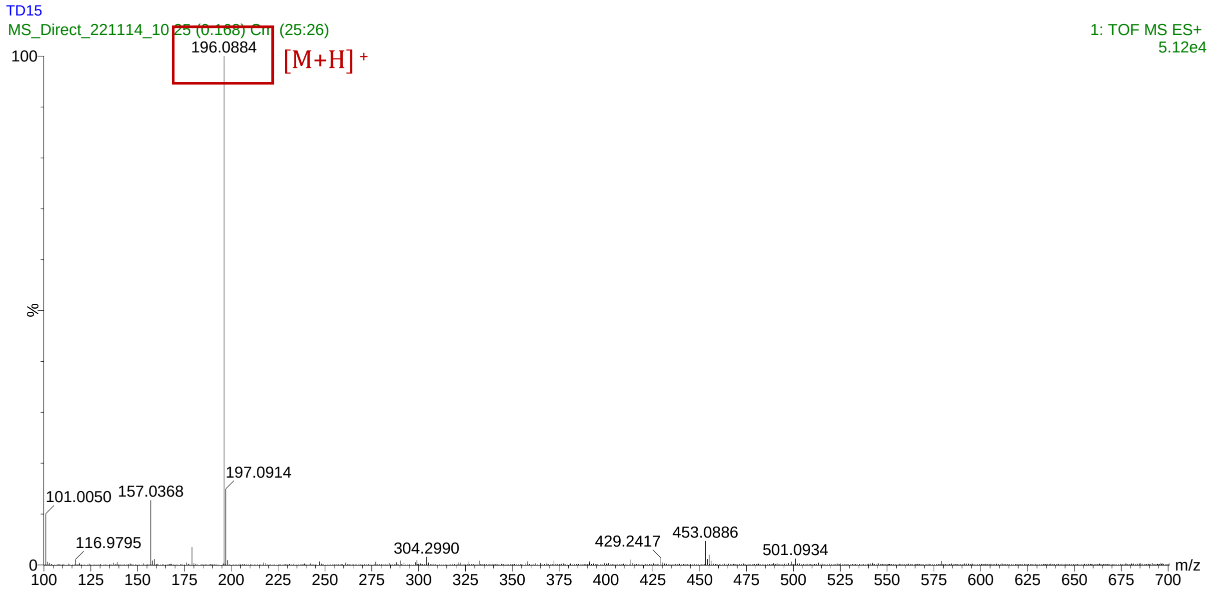

Figure A4. High-Resolution ESI Mass Spectrum of compound **L1** recorded in the positive-ion mode.

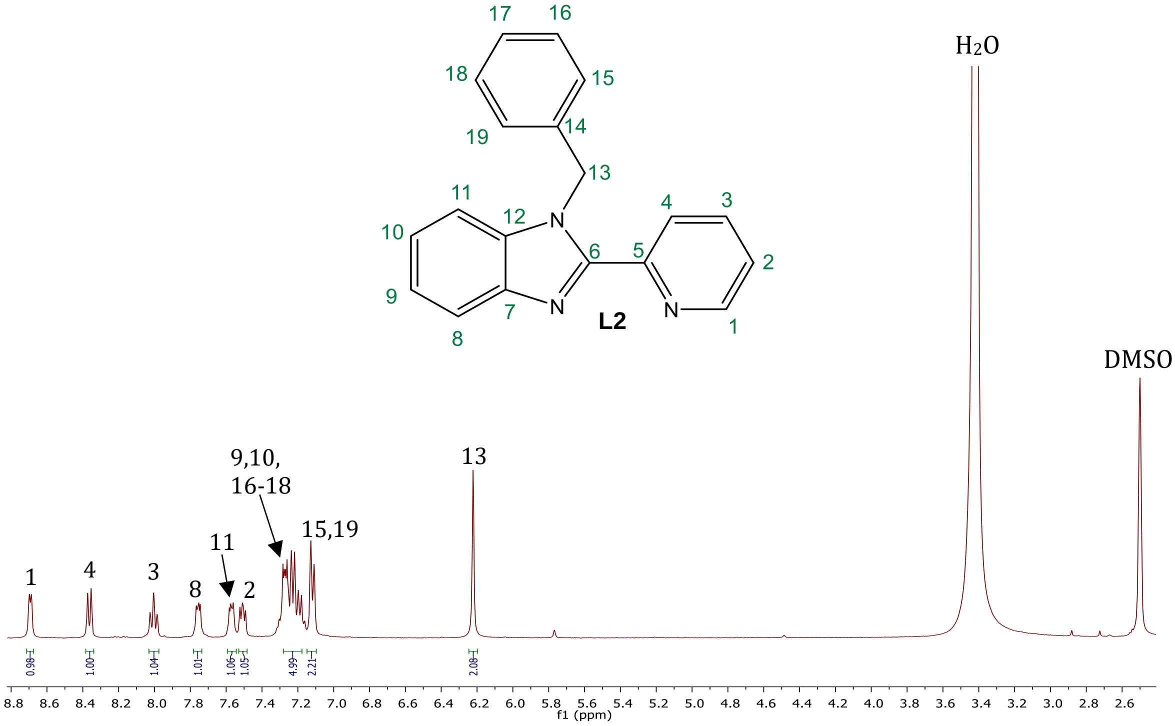

Figure A5. ^{1}H NMR spectrum of compound **L2** in DMSO-d_6.

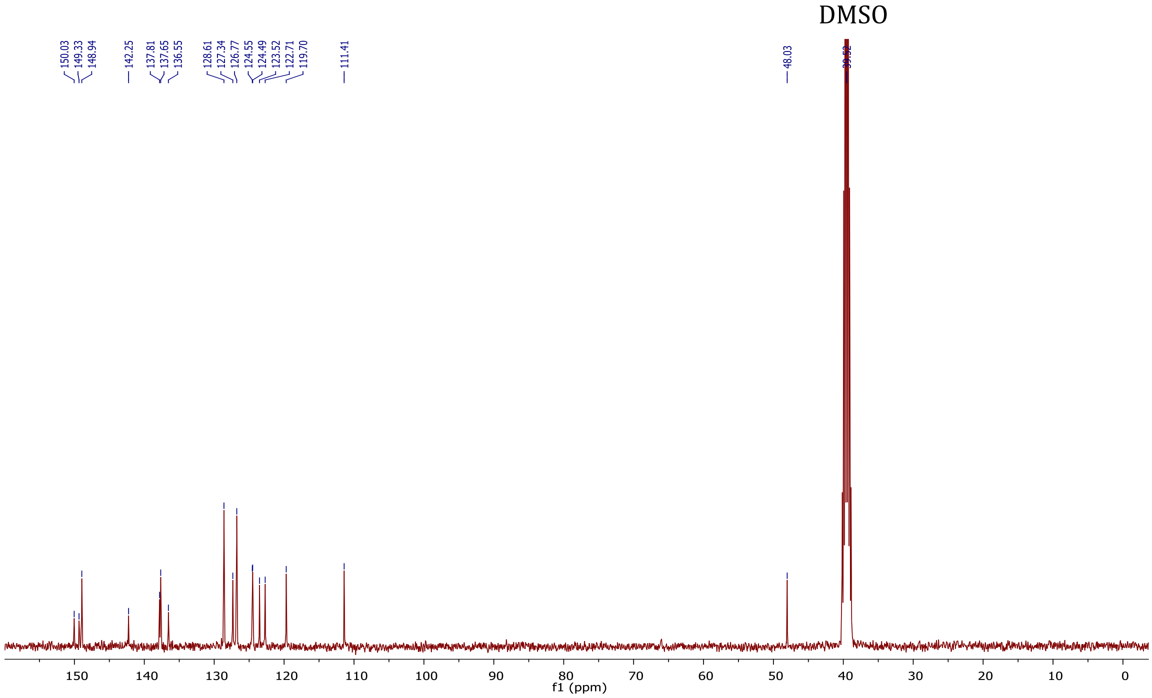

Figure A6. ^{13}C{^{1}H} NMR spectrum of compound **L2** in DMSO-d_6.

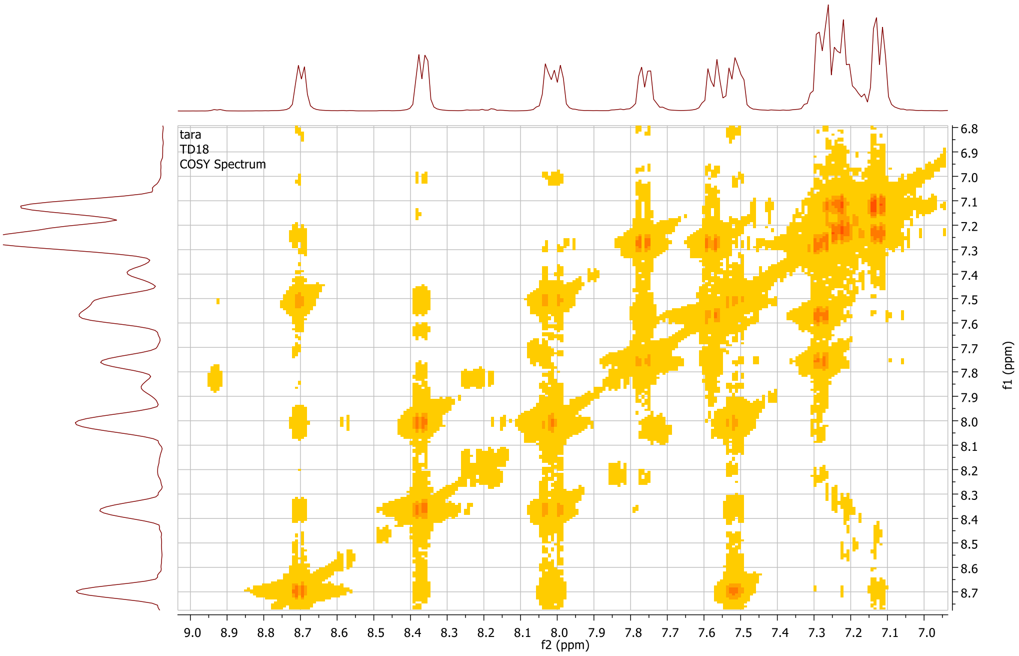

Figure A7. COSY spectrum of compound **L2** in DMSO-d_6.

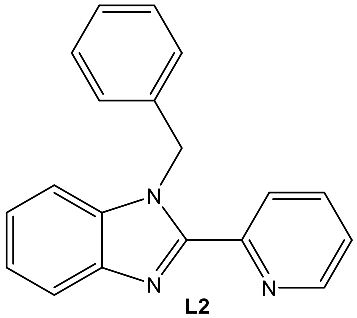

L2

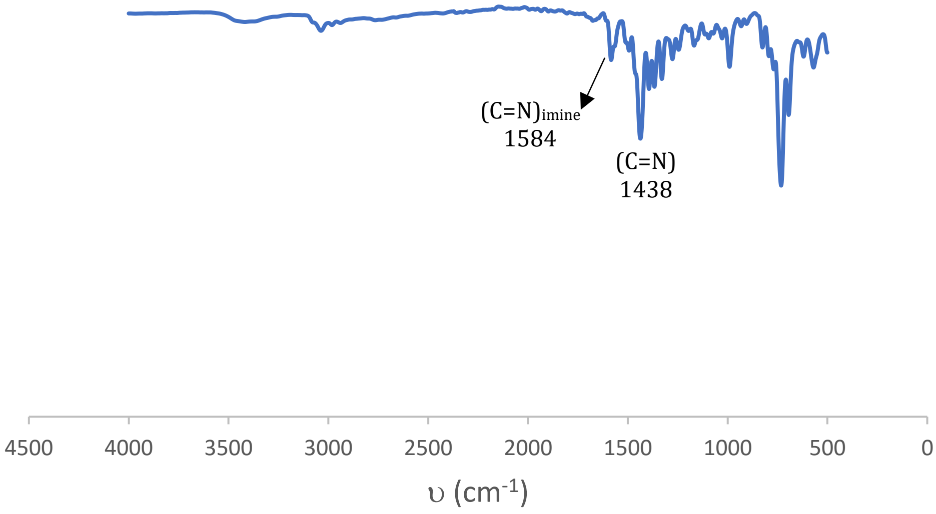

Figure A8. Infrared spectrum of compound **L2**.

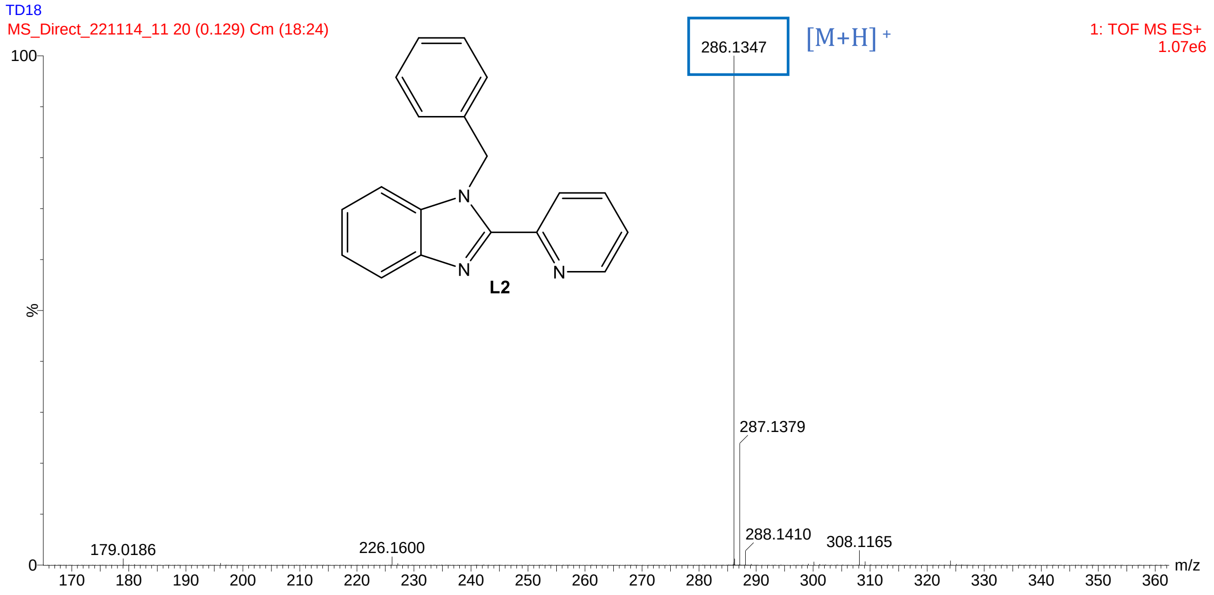

Figure A9. High-Resolution ESI Mass Spectrum of compound **L2** recorded in the positive-ion mode.

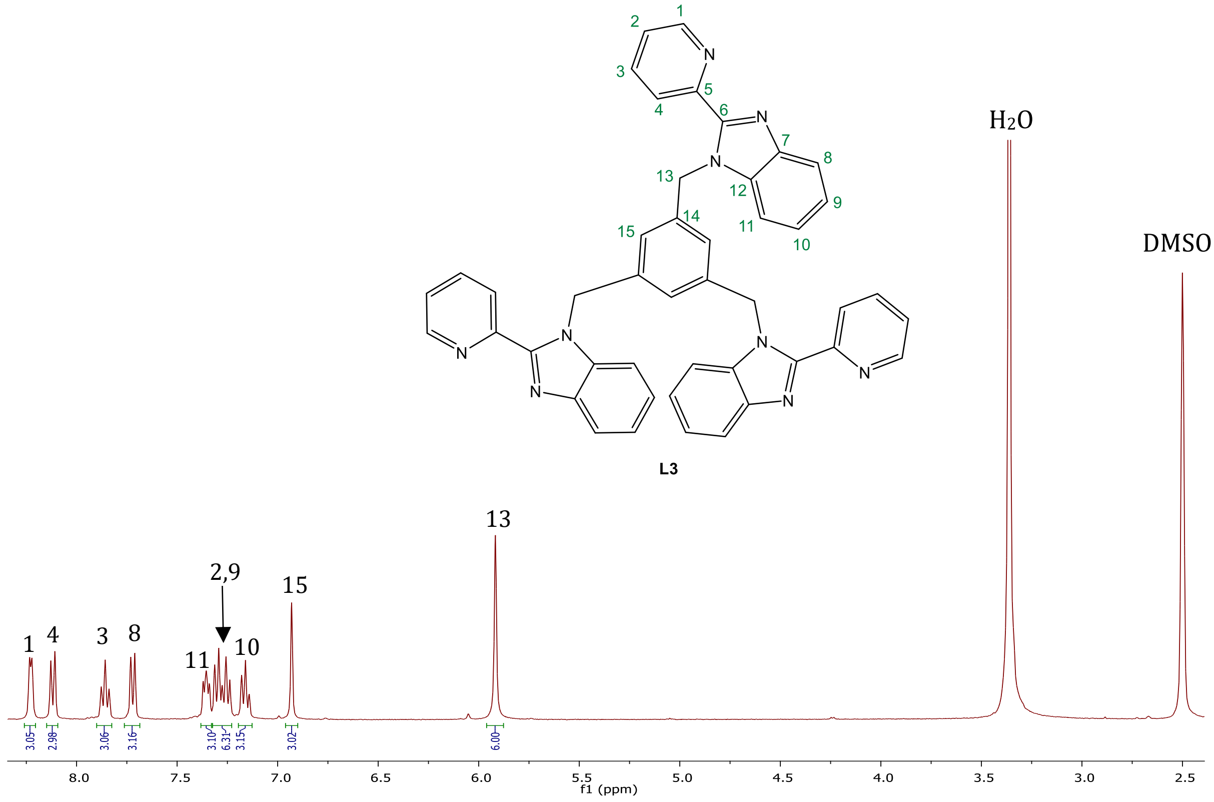

Figure A10. ^{1}H NMR spectrum of compound **L3** in DMSO-d_6.

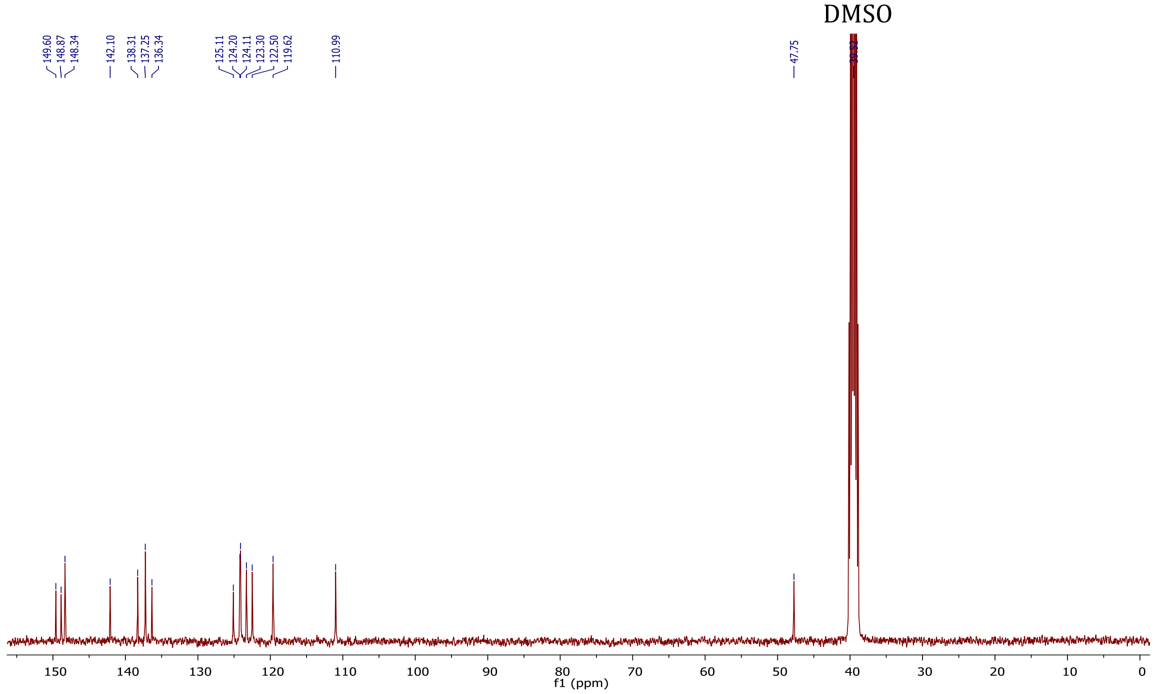

Figure A11. $^{13}C\{^{1}H\}$ NMR spectrum of compound **L3** in DMSO-*d*$_6$.

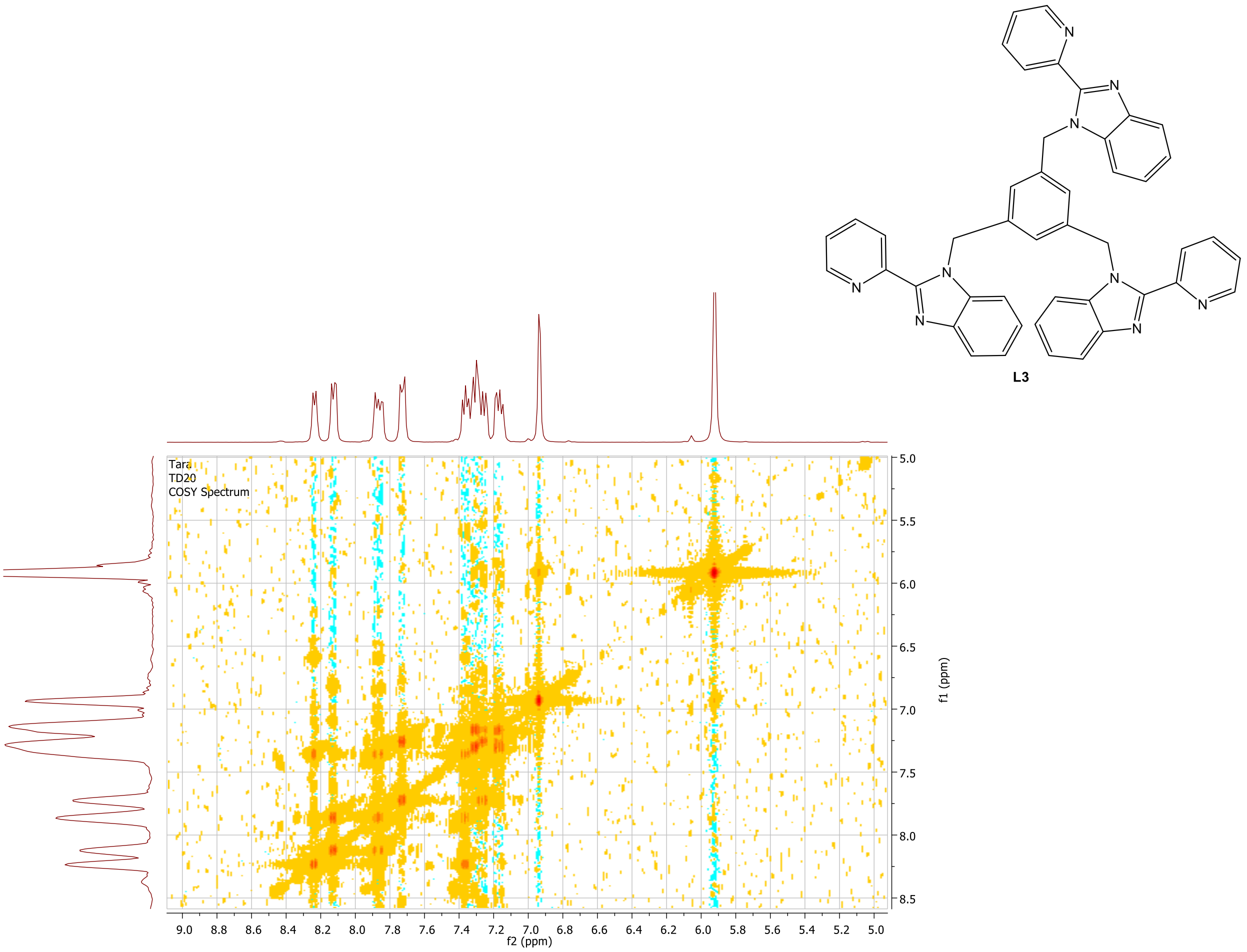

Figure A12. COSY spectrum of compound **L3** in DMSO-*d*$_6$.

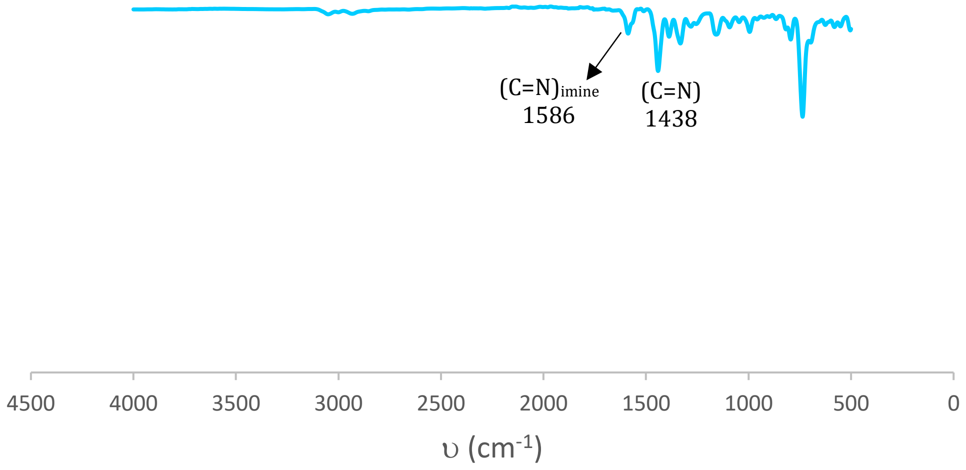

Figure A13. Infrared spectrum of compound **L3**.

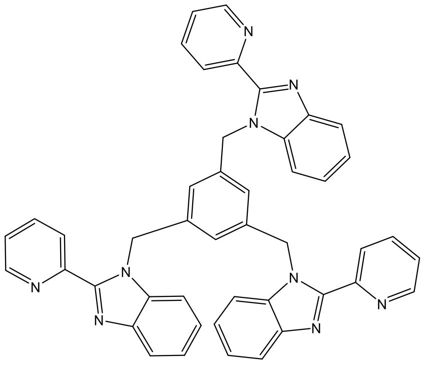

L3

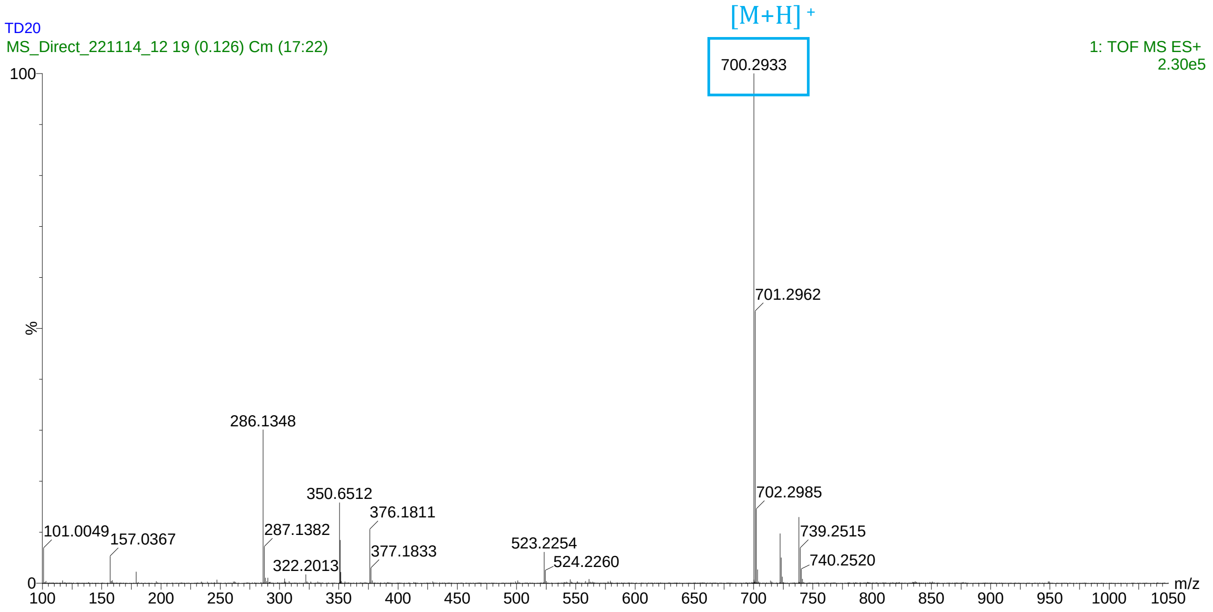

Figure A14. High-Resolution ESI Mass Spectrum of compound **L3** recorded in the positive-ion mode.

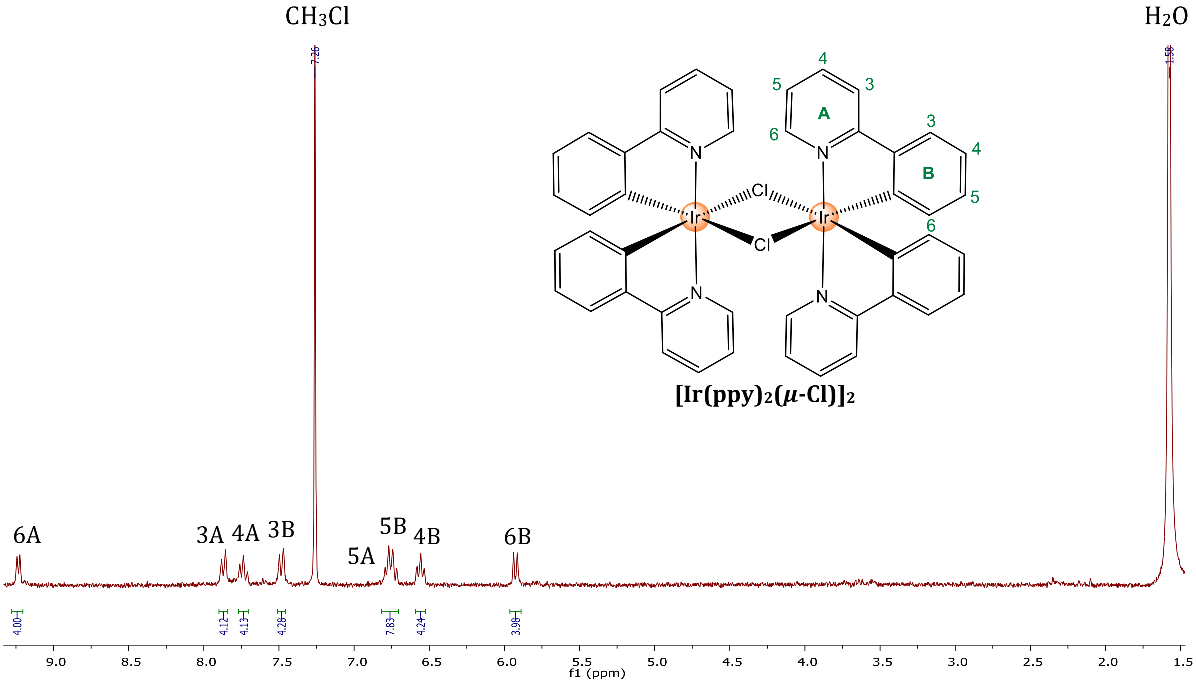

Figure A15. ^{1}H NMR spectrum of $[Ir(ppy)_2(\mu\text{-}Cl)]_2$ in $CDCl_3$.

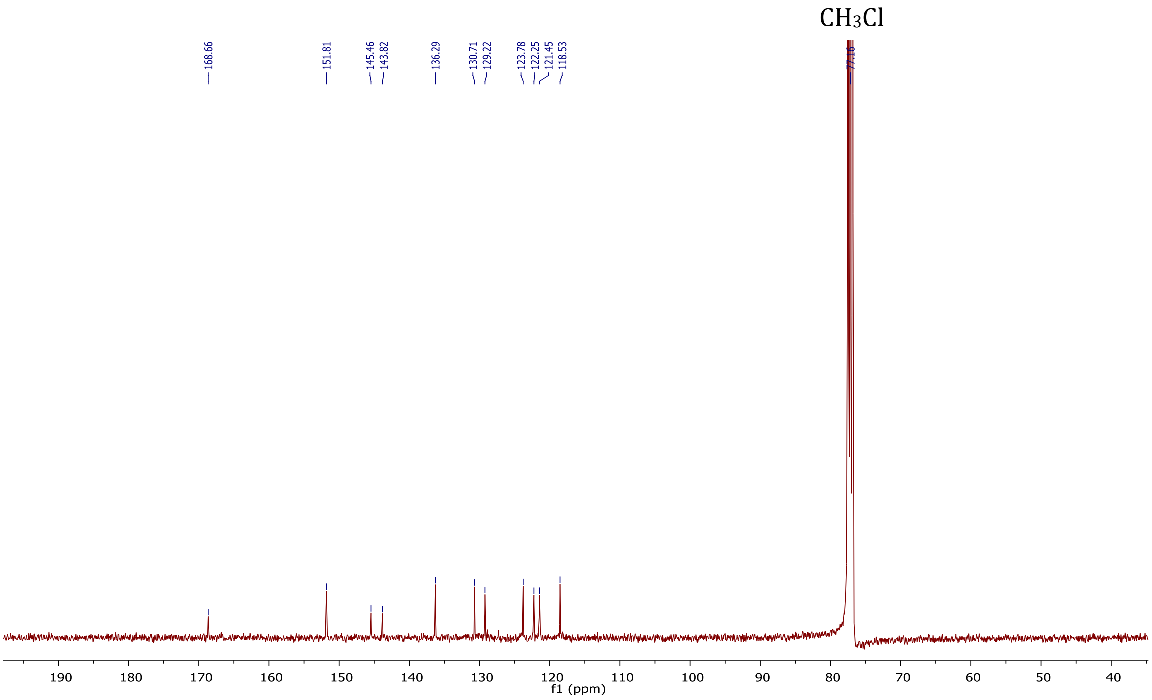

Figure A16. $^{13}C\{^1H\}$ NMR spectrum of $[Ir(ppy)_2(\mu\text{-}Cl)]_2$ in $CDCl_3$.

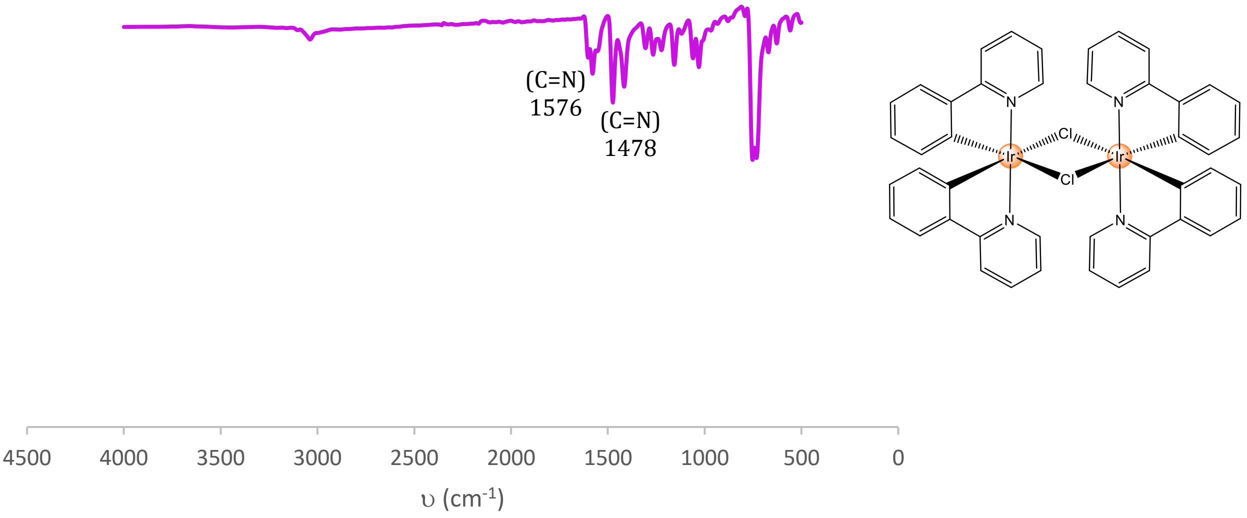

Figure A17. Infrared spectrum of [Ir(ppy)$_2$(μ-Cl)]$_2$.

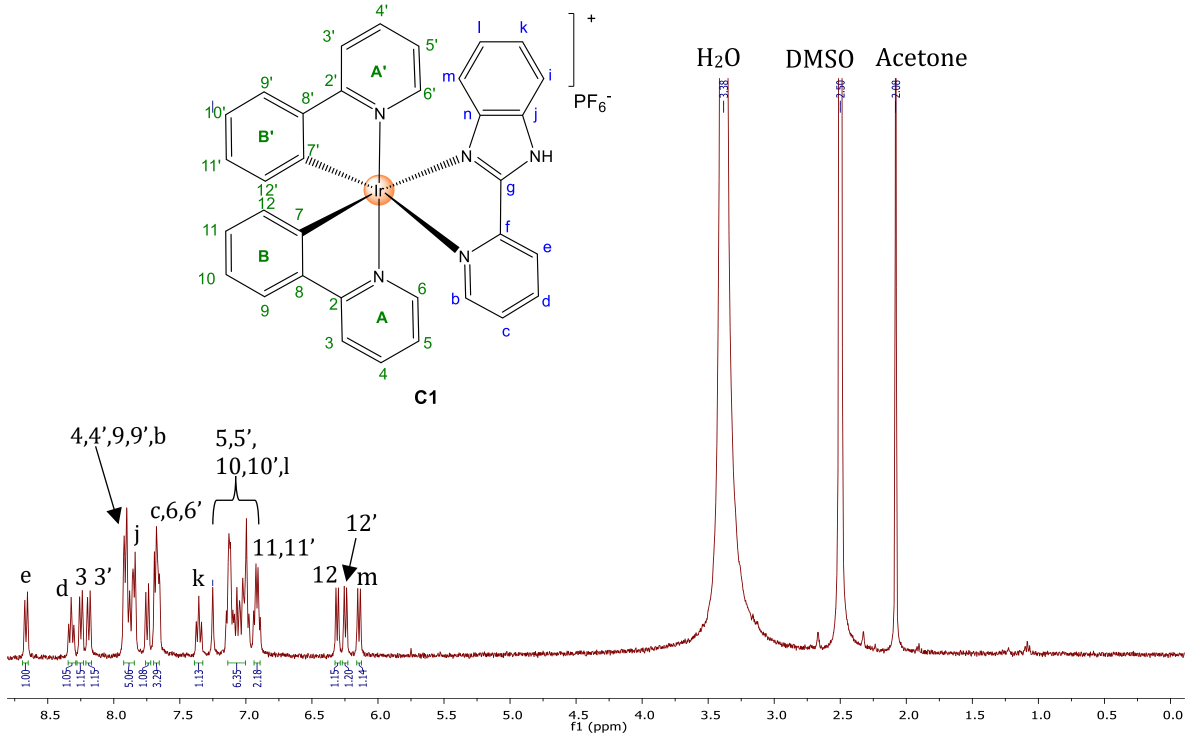

Figure A18. ^{1}H NMR spectrum of complex **C1** in DMSO-d_6.

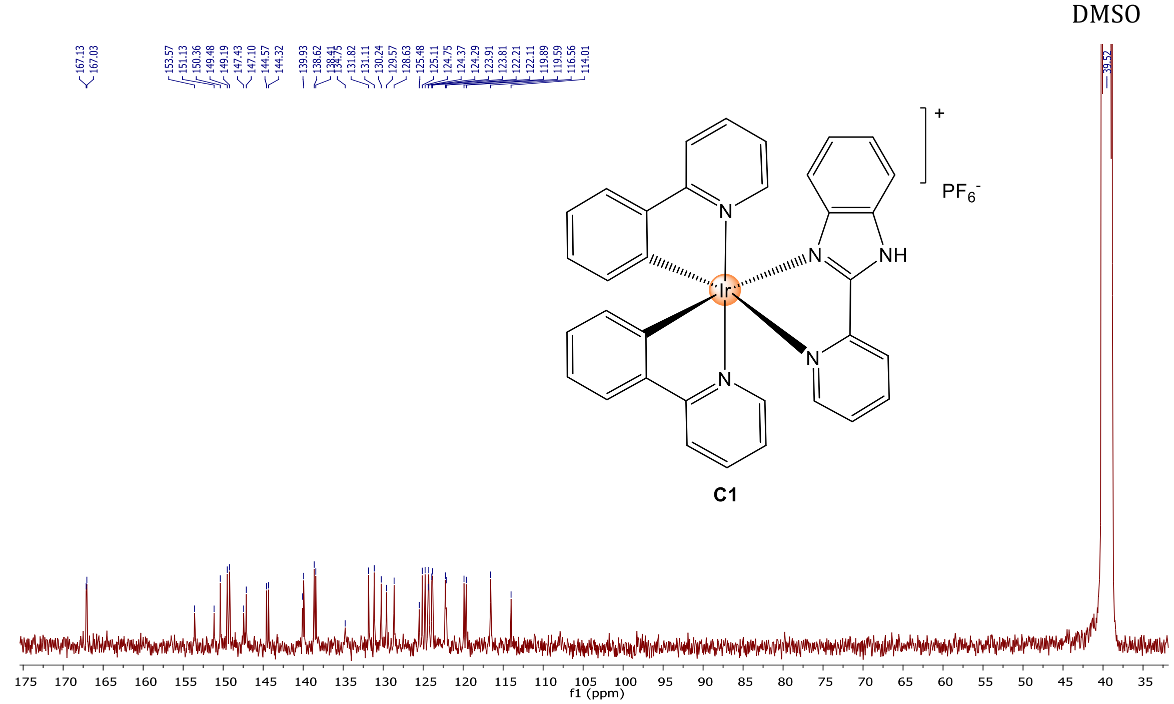

Figure A19. $^{13}C\{^{1}H\}$ NMR spectrum of complex **C1** in DMSO-*d*₆.

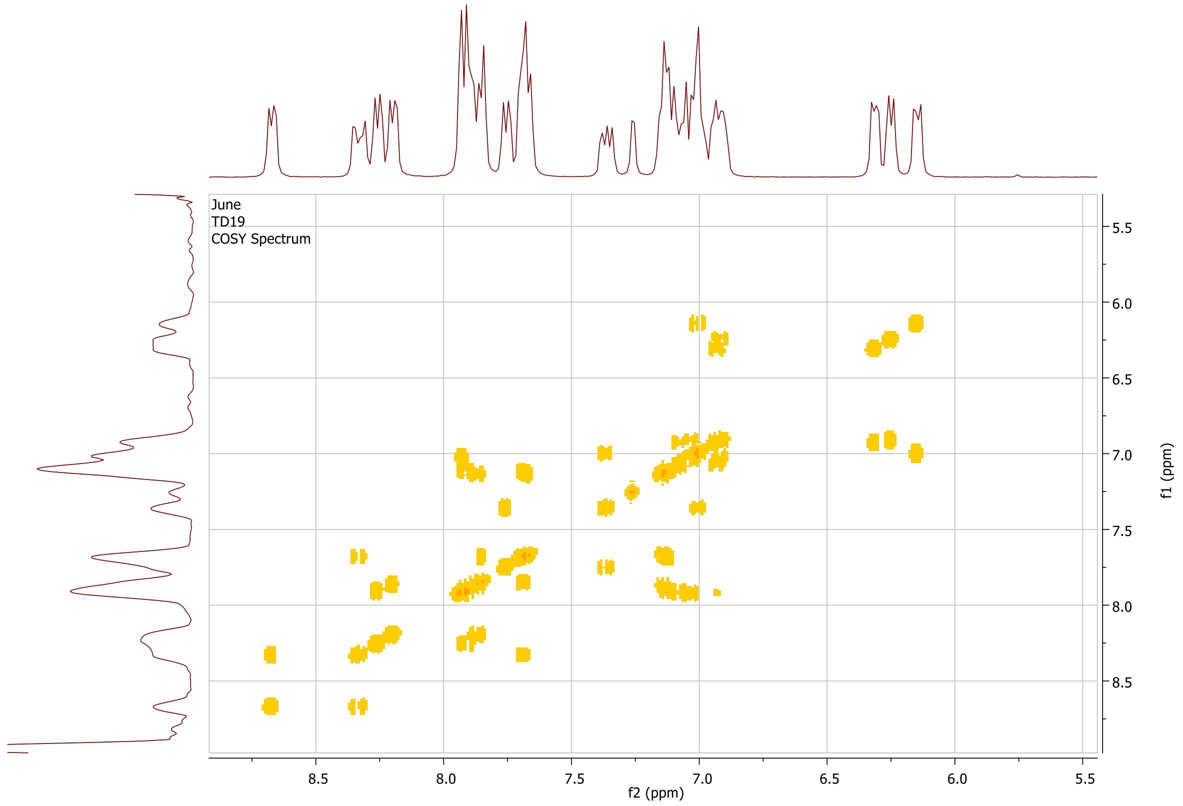

Figure A20. COSY spectrum over the aromatic region of complex **C1** in DMSO-*d*₆.

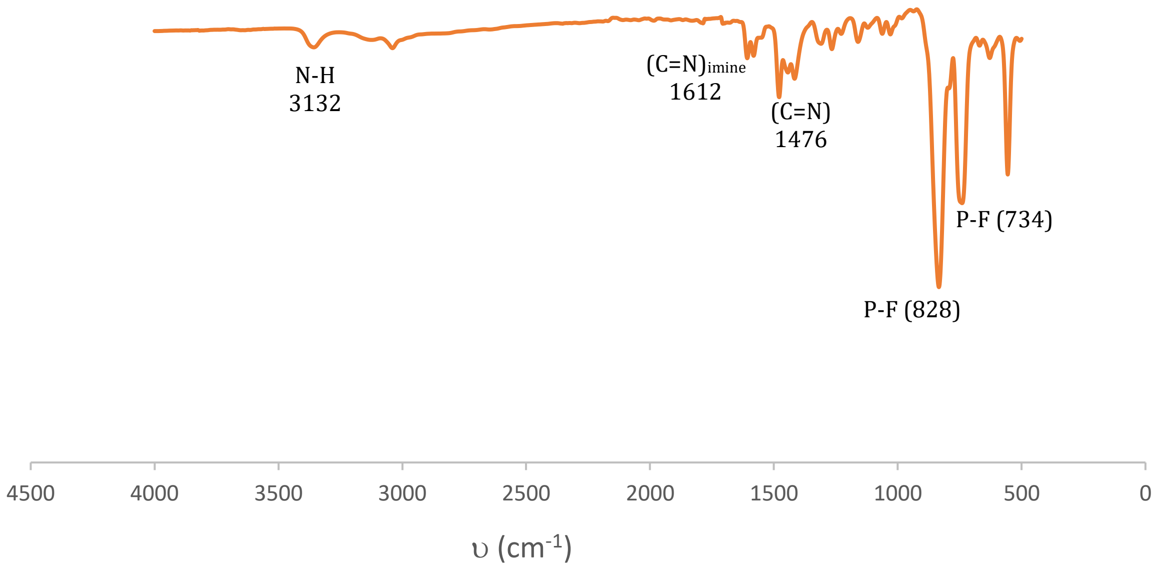

Figure A21. Infrared spectrum of complex **C1**.

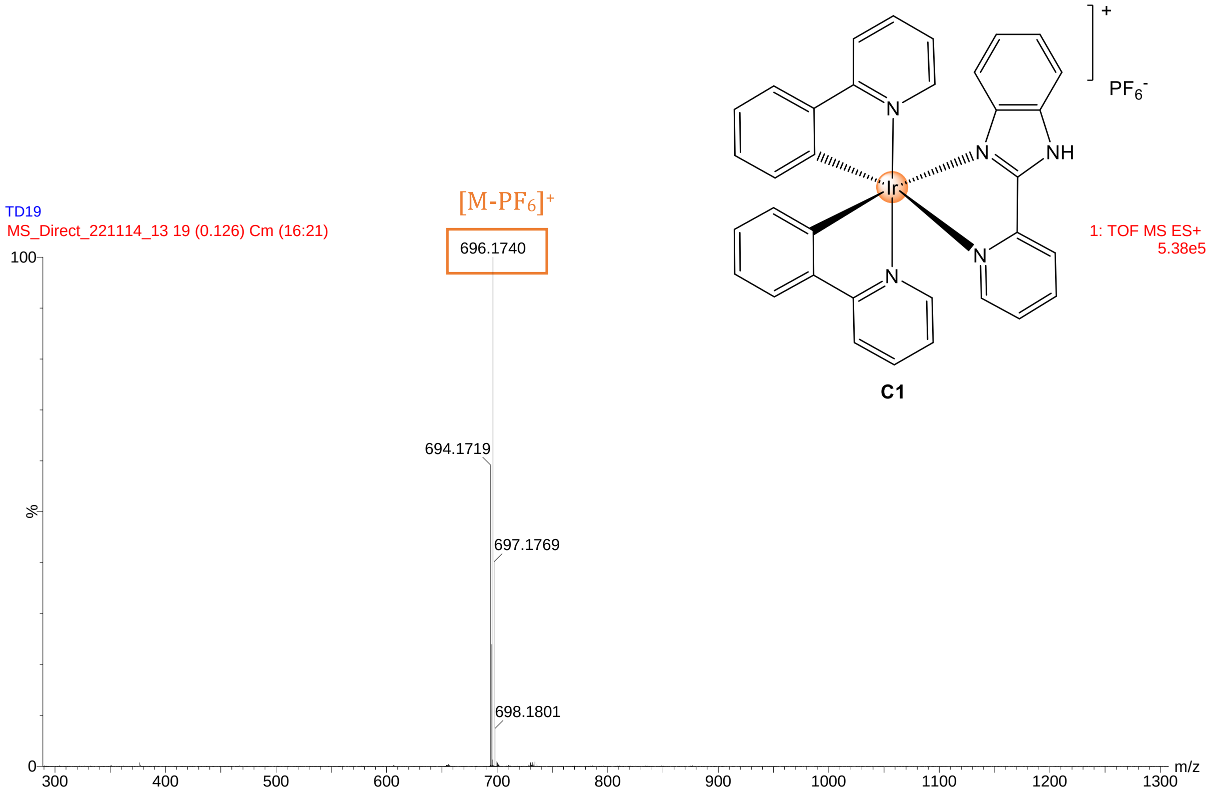

Figure A22. High-Resolution ESI Mass Spectrum of complex **C1** recorded in the positive-ion mode.

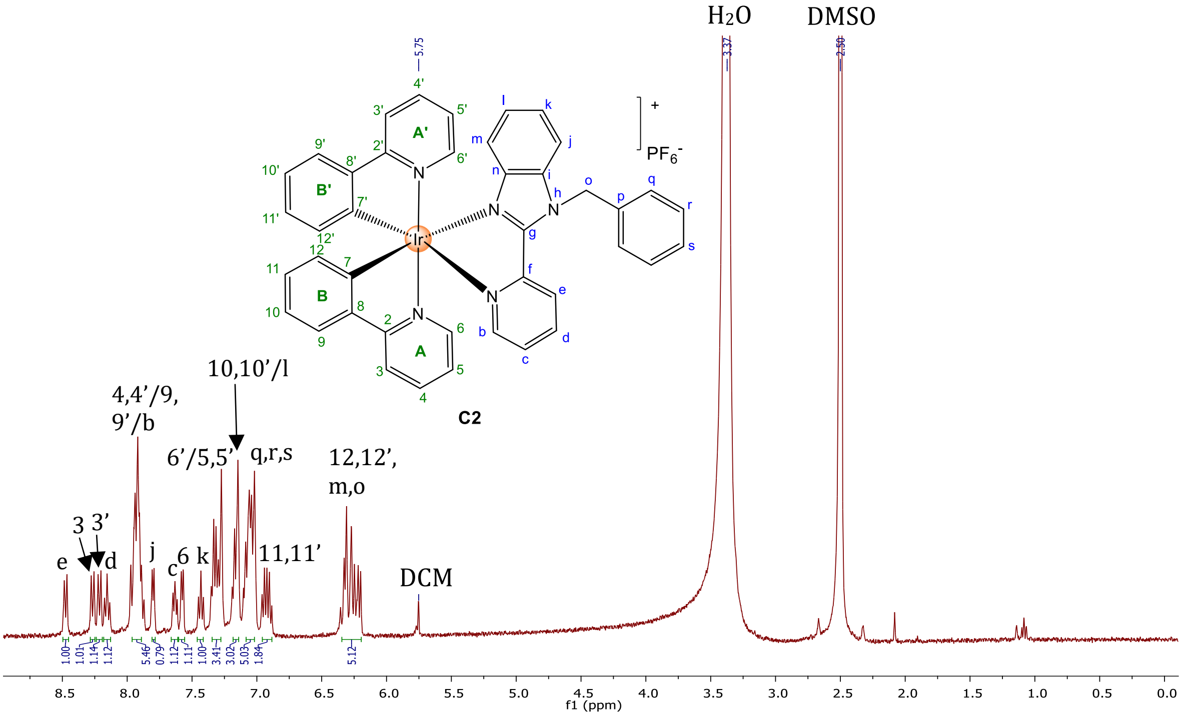

Figure A23. ^{1}H NMR spectrum of complex **C2** in DMSO-d_6.

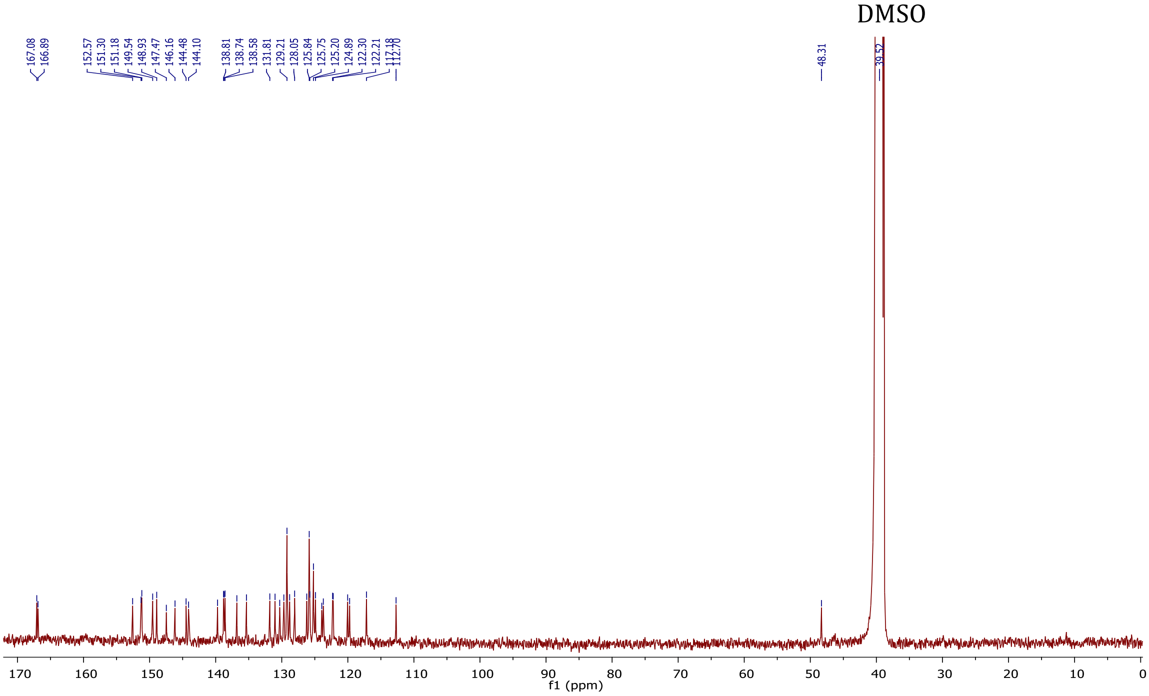

Figure A24. ^{13}C{^{1}H} NMR spectrum of complex **C2** in DMSO-d_6.

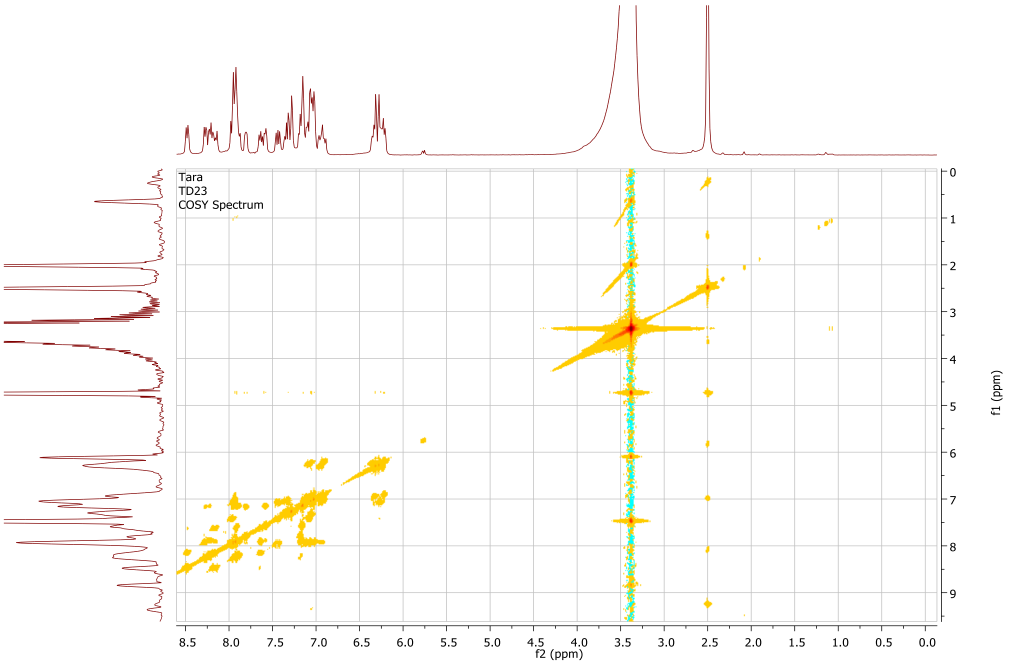

Figure A25. COSY spectrum of complex **C2** in DMSO-d_6.

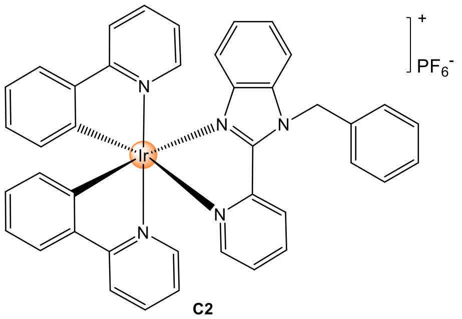

C2

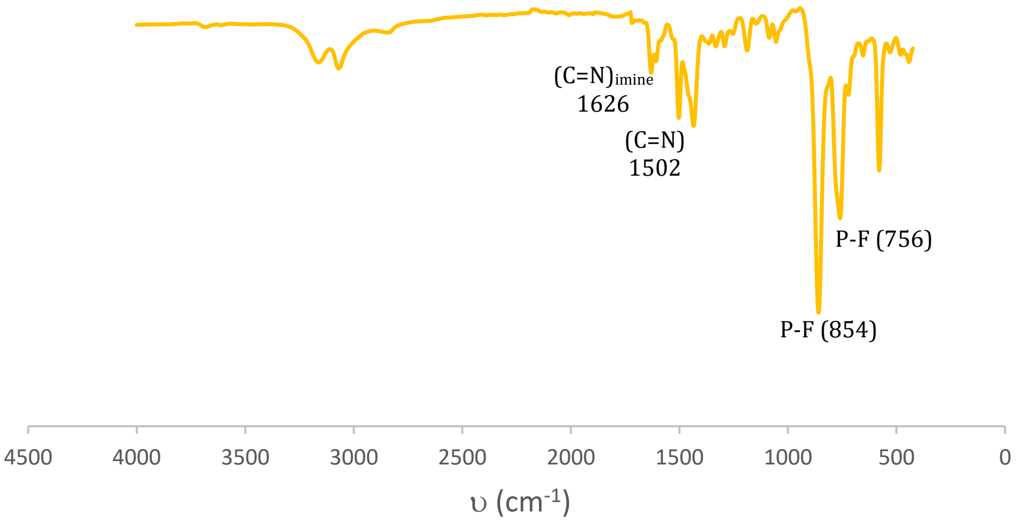

Figure A26. Infrared spectrum of complex **C2**.

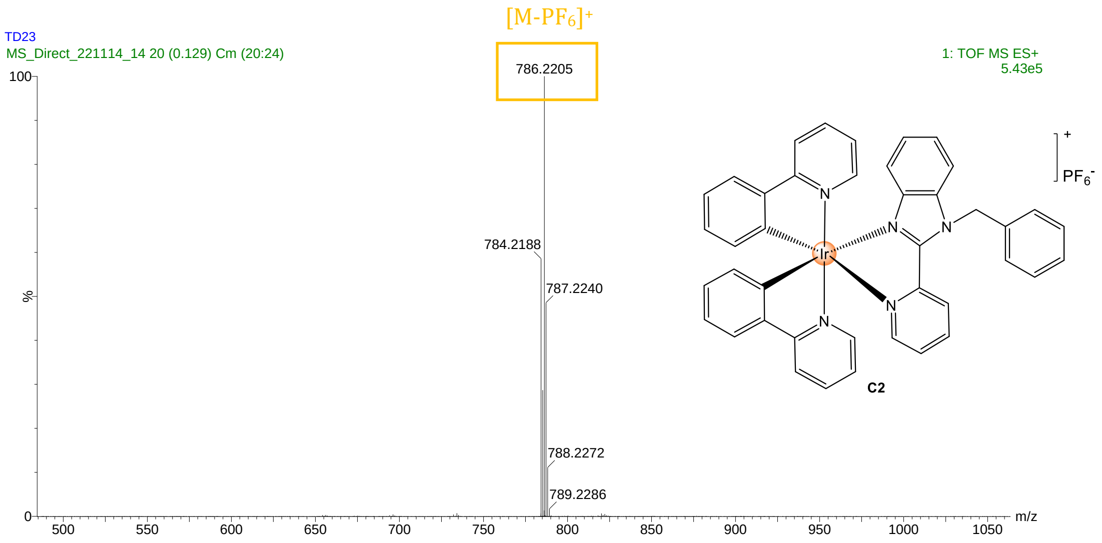

Figure A27. High-Resolution ESI Mass Spectrum of complex **C2** recorded in the positive-ion mode.

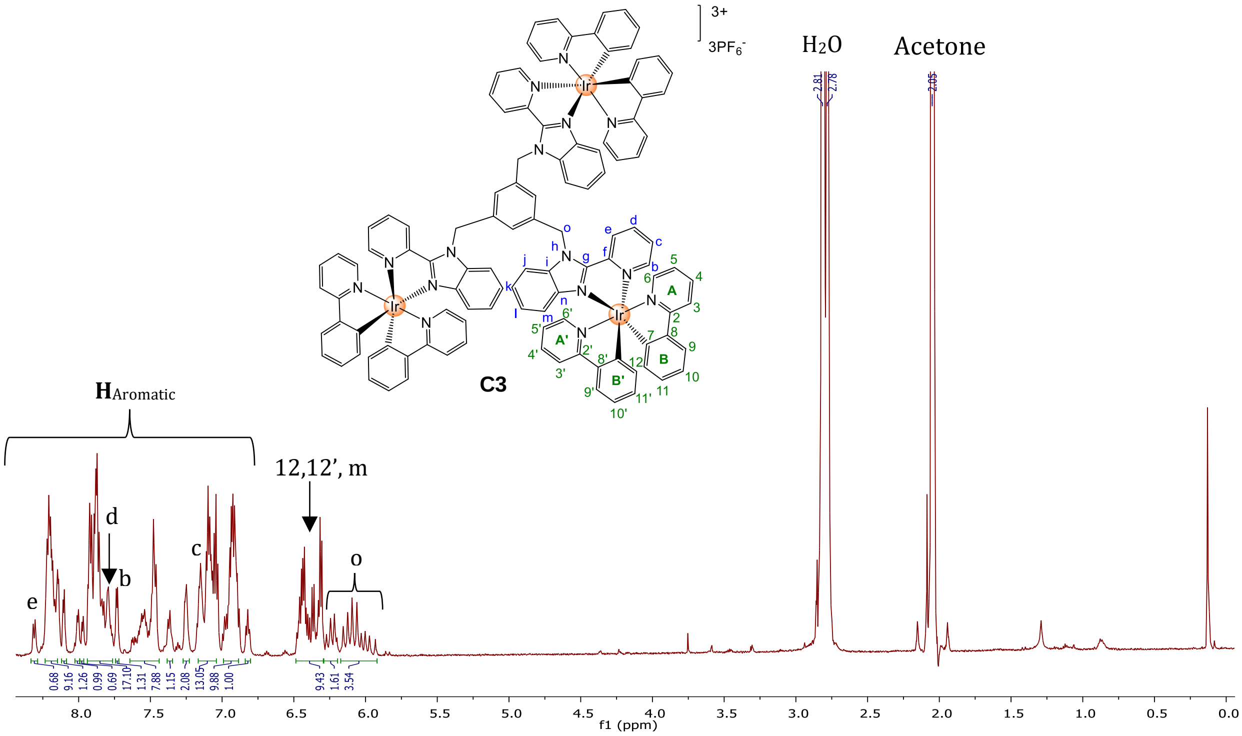

Figure A28. ^1H NMR spectrum of complex **C3** in Acetone-d_6.

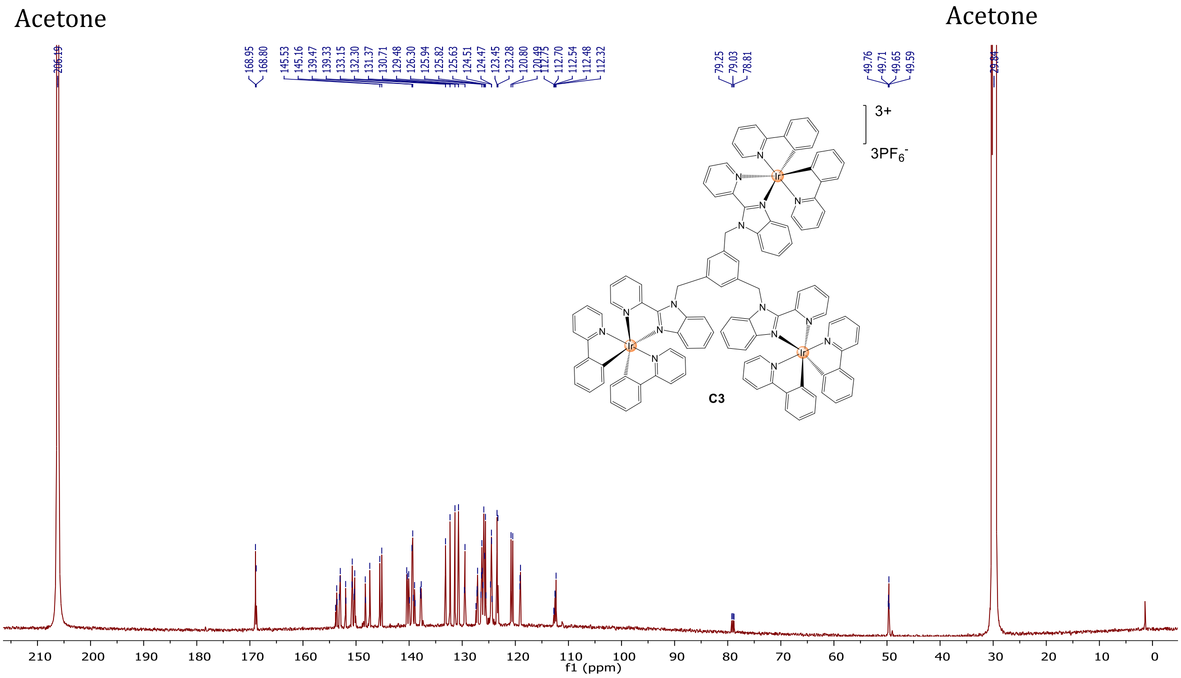

Figure A29. $^{13}C\{^{1}H\}$ NMR spectrum of complex **C3** in Acetone-*d*$_6$.

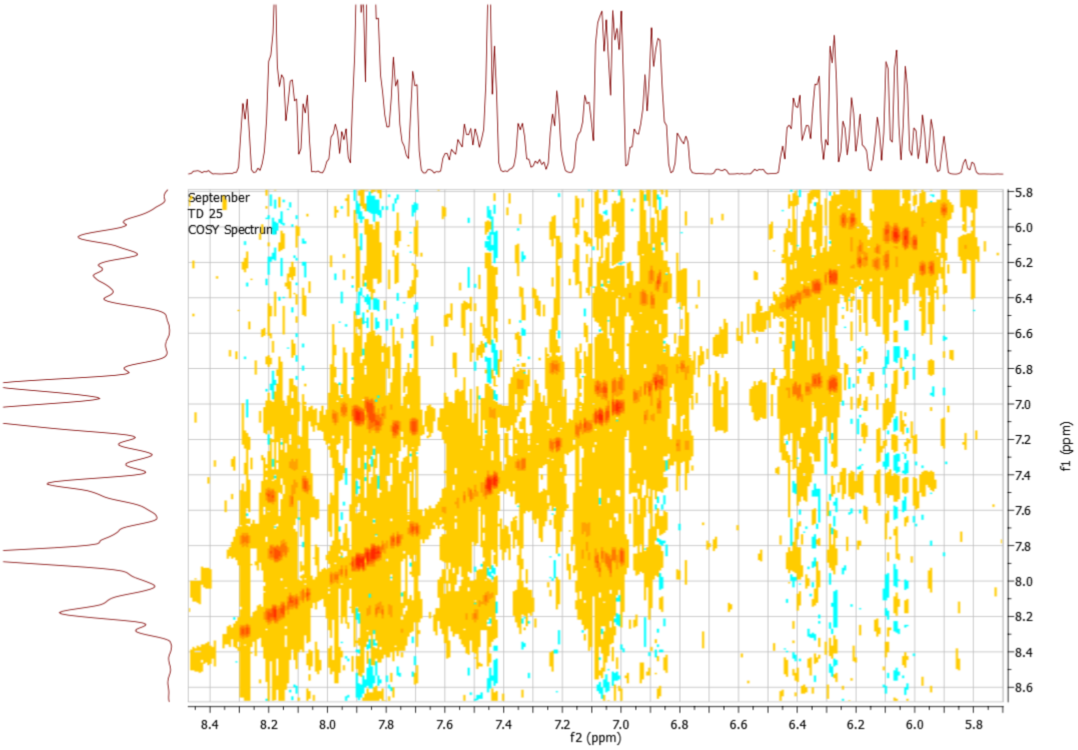

Figure A30. COSY spectrum of complex **C3** in Acetone-*d*$_6$.

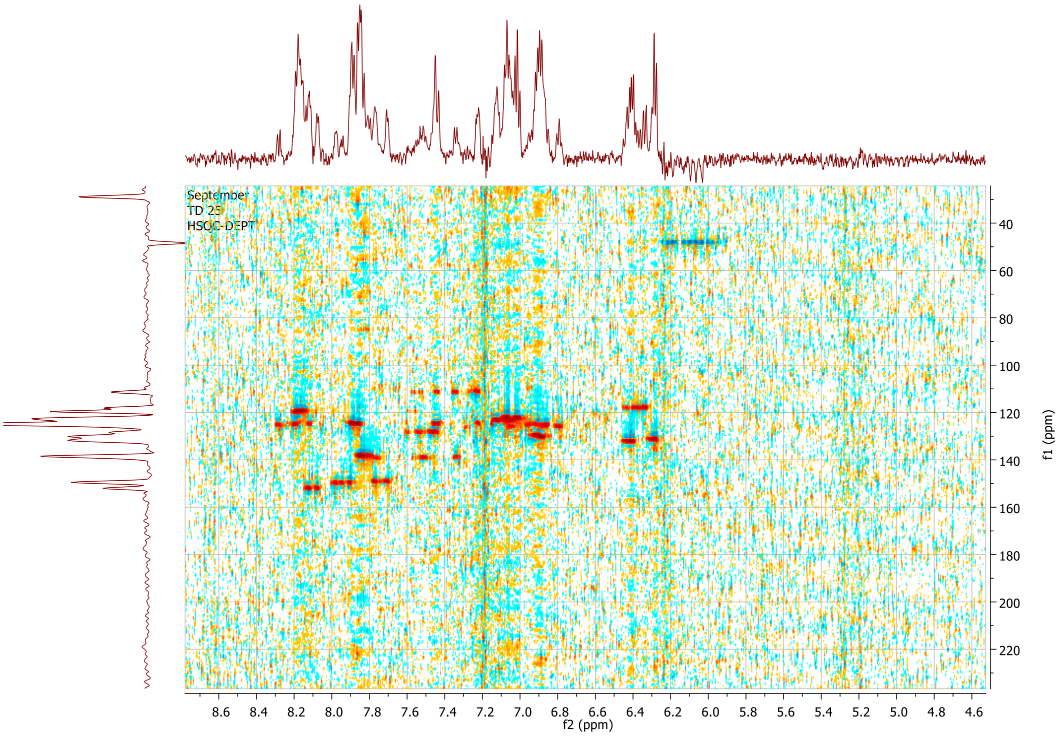

Figure A31. HSQC-DEPT spectrum of complex **C3** in Acetone-*d*6.

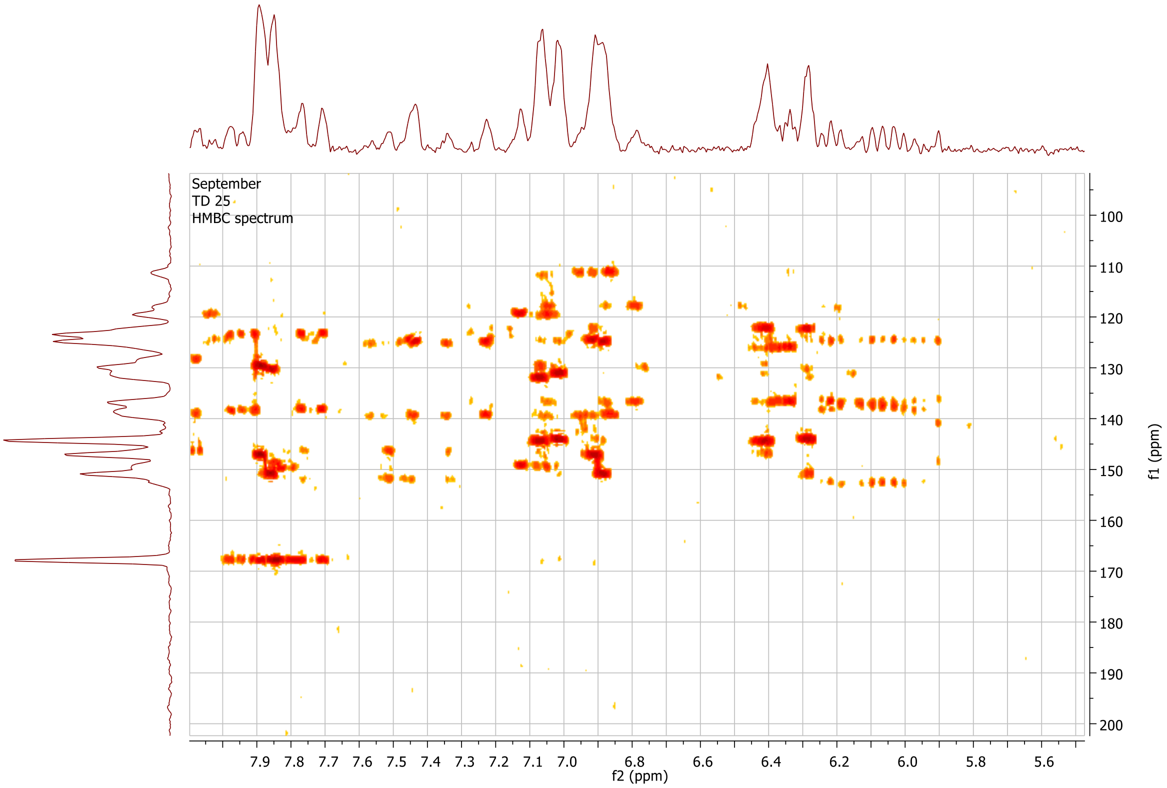

Figure A32. HMBC spectrum of complex **C3** in Acetone-*d*6.

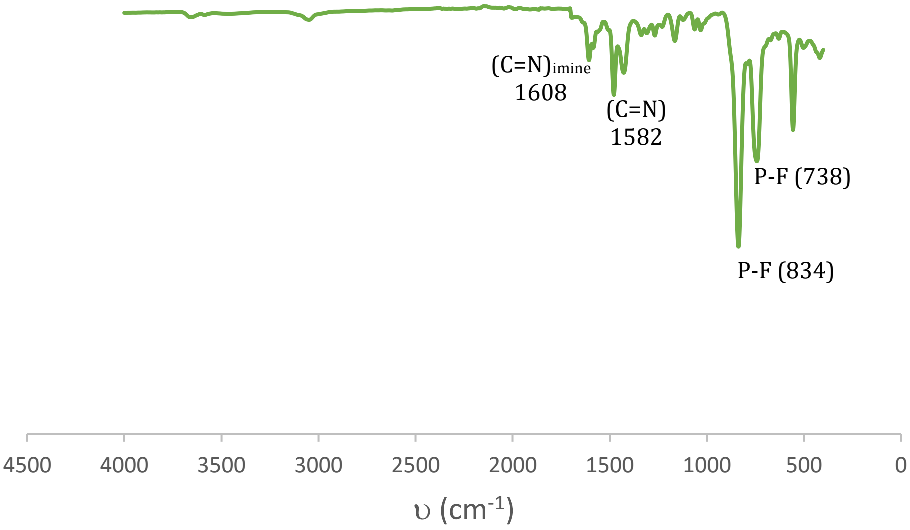

Figure A33. Infrared spectrum of complex **C3.**

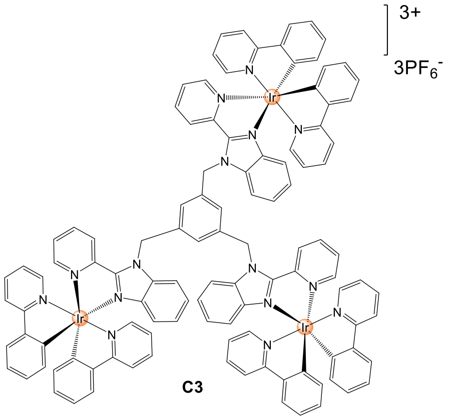

C3

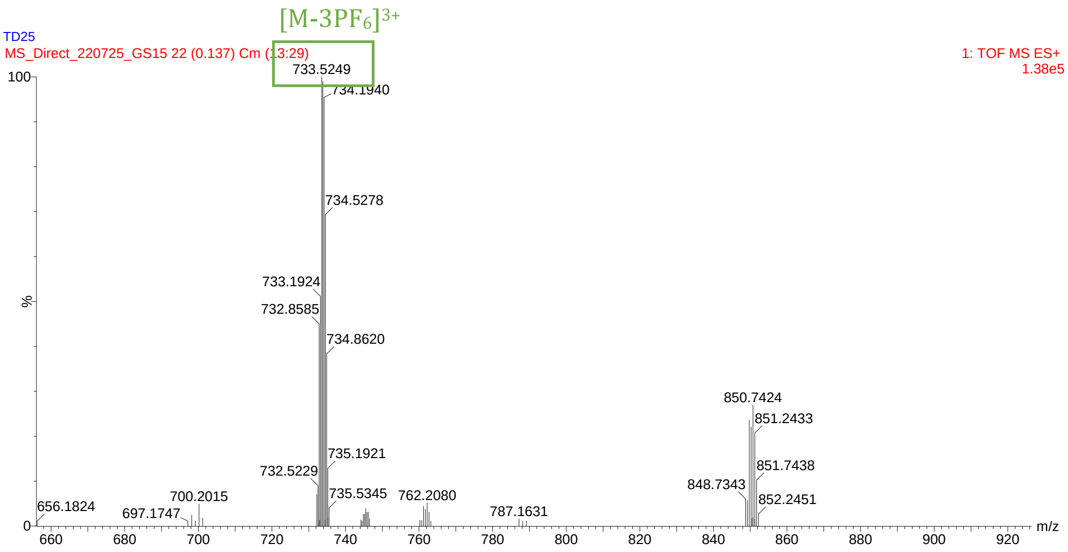

Figure A34. High-Resolution ESI Mass Spectrum of complex **C3** recorded in the positive-ion mode.

2. Triplet state lifetime decay curves

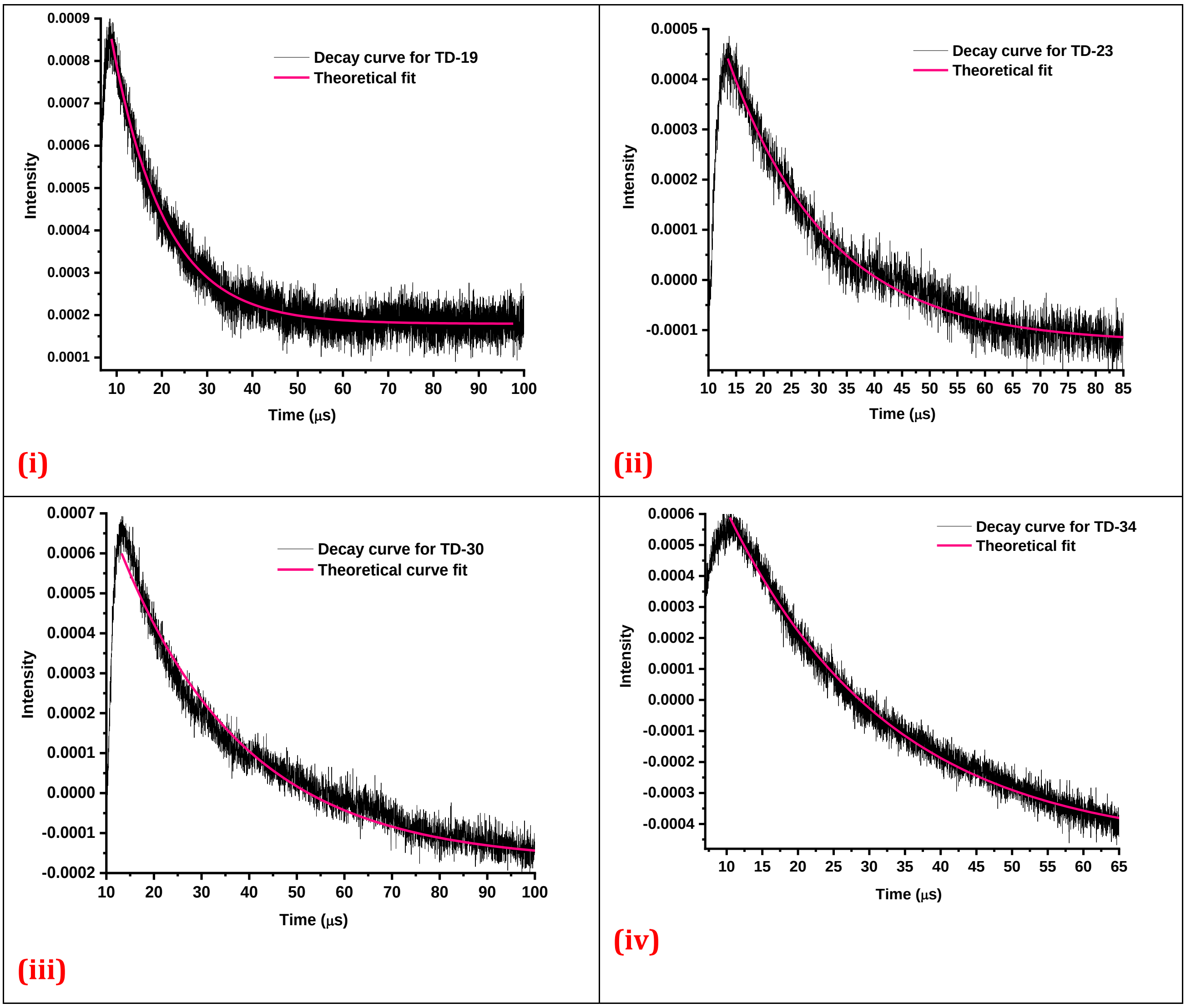

Figure A35. Triplet-state lifetime decay curves for complexes (i) **C1**, (ii) **C2**, (iii) [Ir(ppy)$_2$(dtbbpy)]PF$_6$ and (iv) **C3** in degassed CH$_3$CN at room temperature.

3. Spectroscopic data for the ketimine precursors K1 and K2

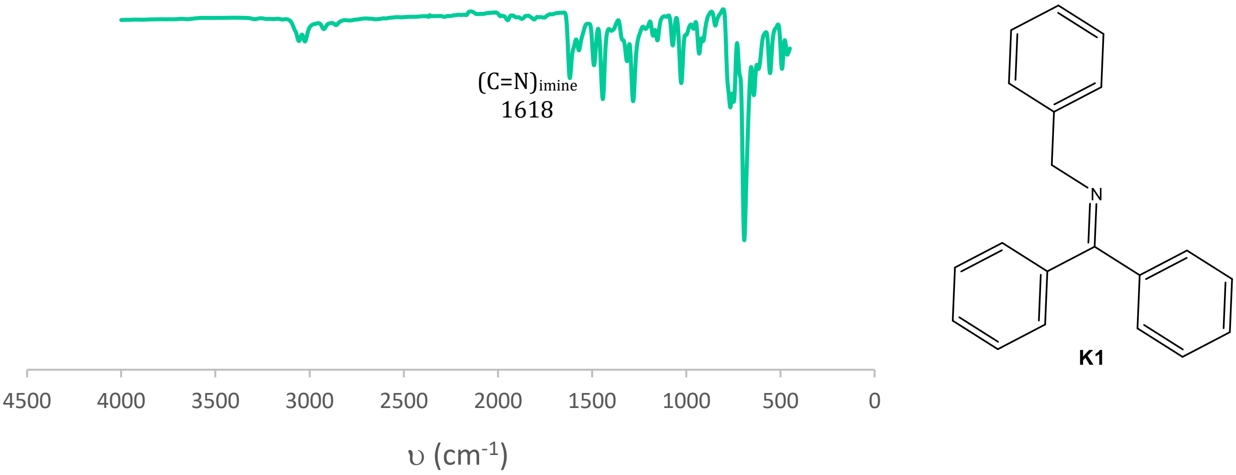

Figure A36. Infrared spectrum of ketimine **K1**.

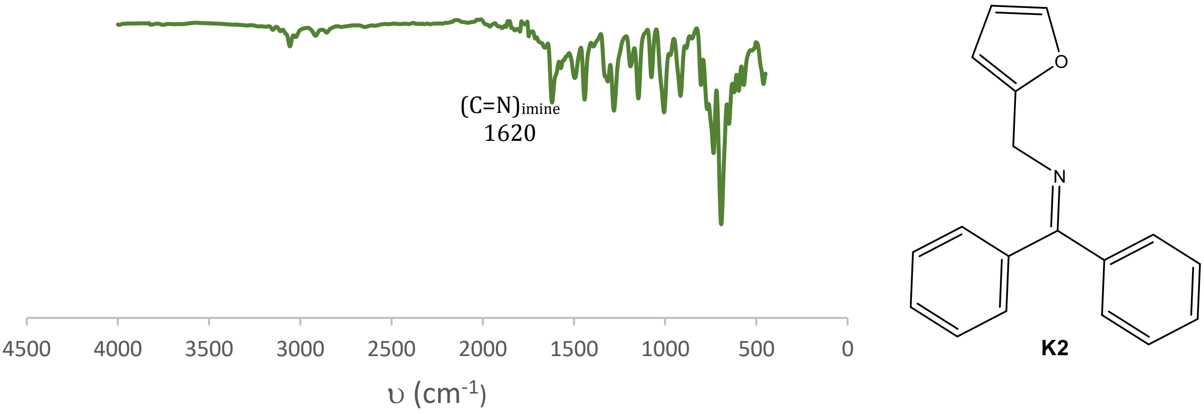

Figure A37. Infrared spectrum of ketimine **K2**.

4. Spectral data of the amino acid salt products

4.1 Data for the benzyl-substituted amino acid salt (AA1)

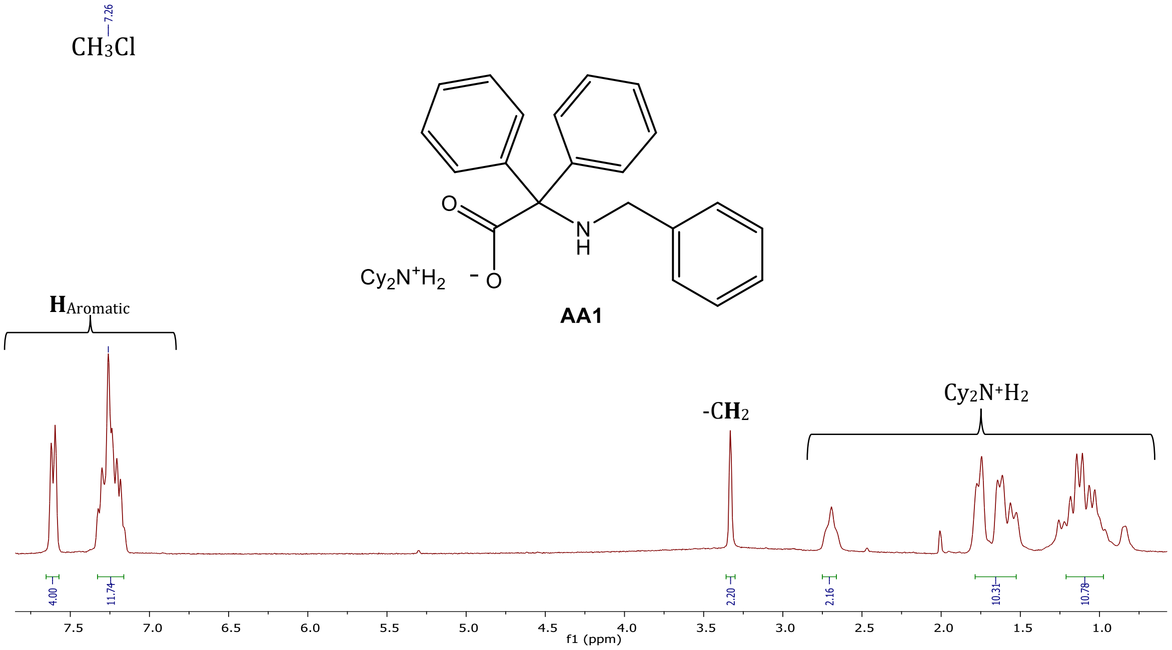

Figure A38. ^{1}H NMR spectrum of the benzyl substituted amino acid salt product in CDCl$_3$.

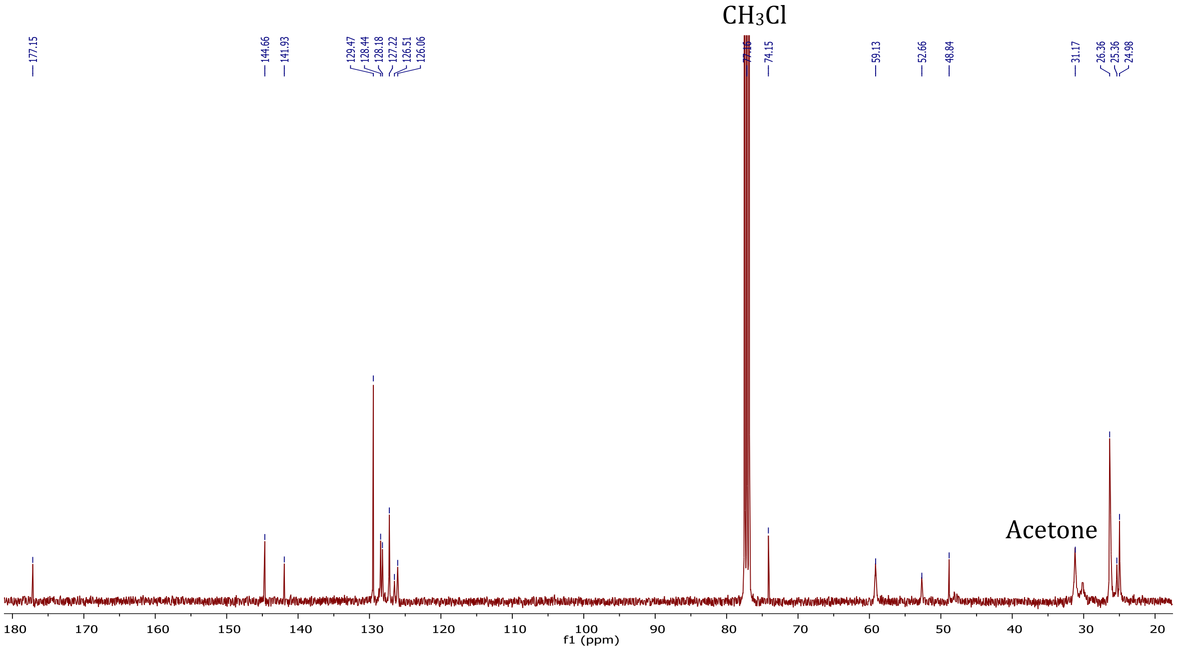

Figure A39. ^{13}C{^{1}H} NMR spectrum of the benzyl substituted amino acid salt product in CDCl$_3$.

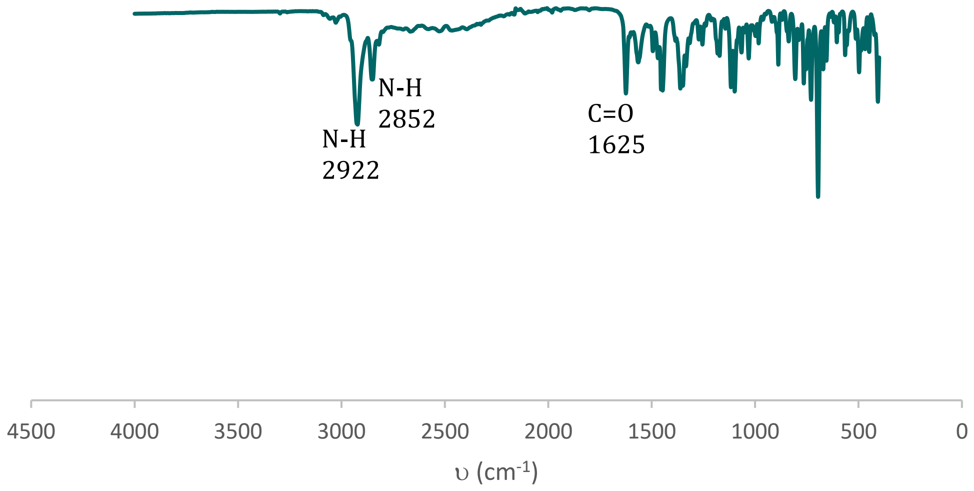

Figure A40. Infrared spectrum of the benzyl substituted amino acid salt.

4.2 Data for the furfuryl-substituted amino acid salt (AA2)

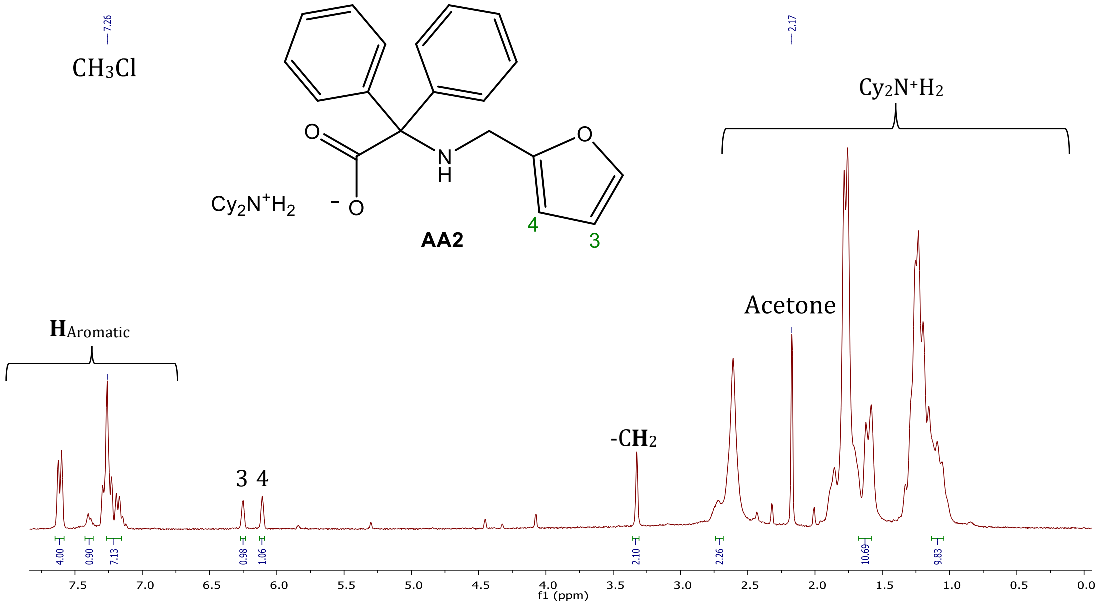

Figure A41. ^{1}H NMR spectrum of the furfuryl substituted amino acid salt product in $CDCl_3$.

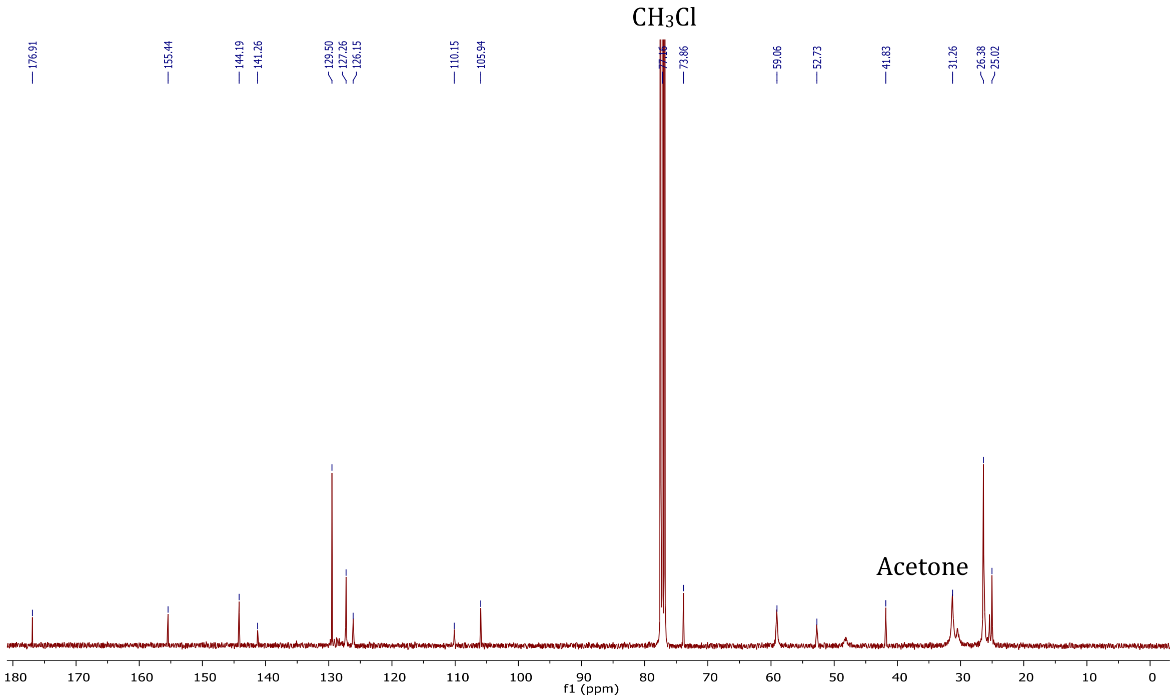

Figure A42. $^{13}C\{^{1}H\}$ NMR spectrum of the furfuryl substituted amino acid salt product in $CDCl_3$.

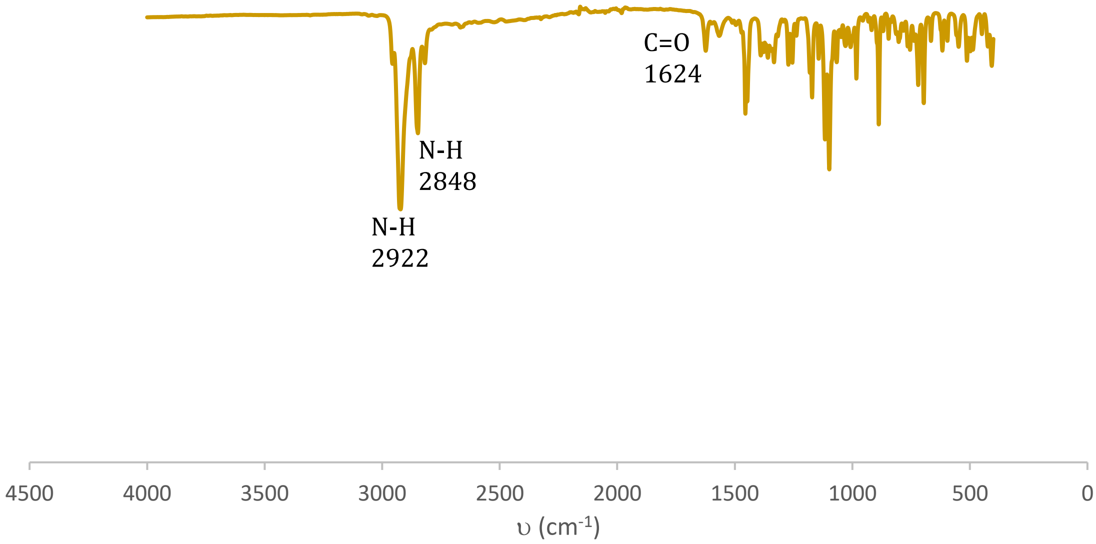

Figure A43. Infrared spectrum of the furfuryl substituted amino acid salt.

5. Control photocatalytic experiments

5.1 No iridium(III) photoredox catalyst

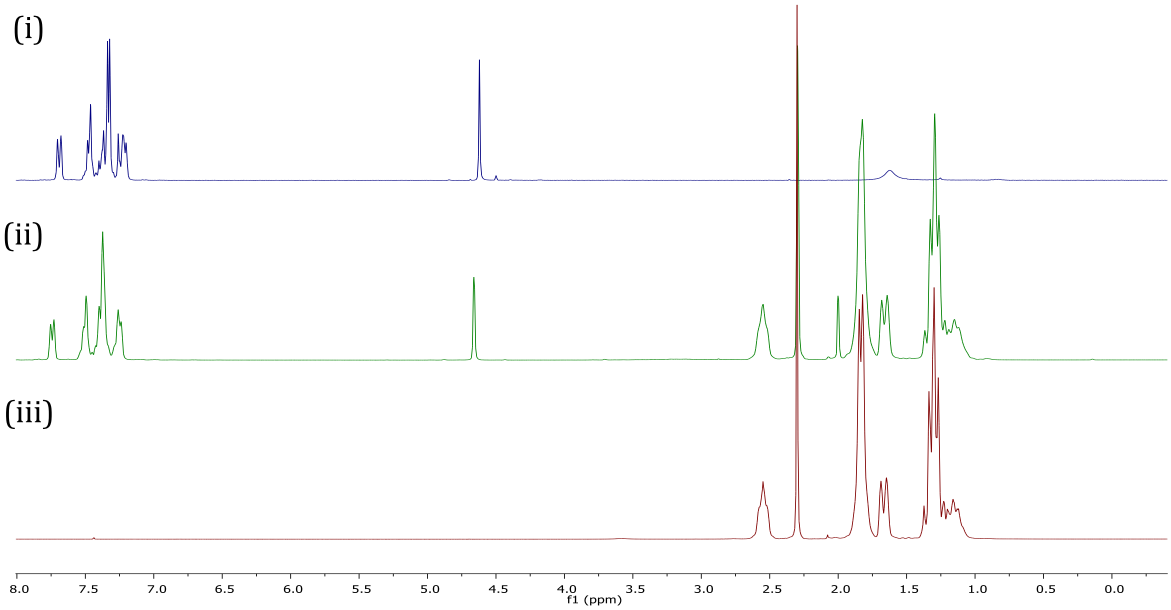

Figure A44. Stacked ^{1}H NMR spectra of (i) ketimine precursor **K1**, (ii) product obtained from the reaction with no Ir(III) photocatalyst and (iii) Cy_2NMe in $CDCl_3$.

5.2 No sacrificial electron donor (Cy_2NMe)

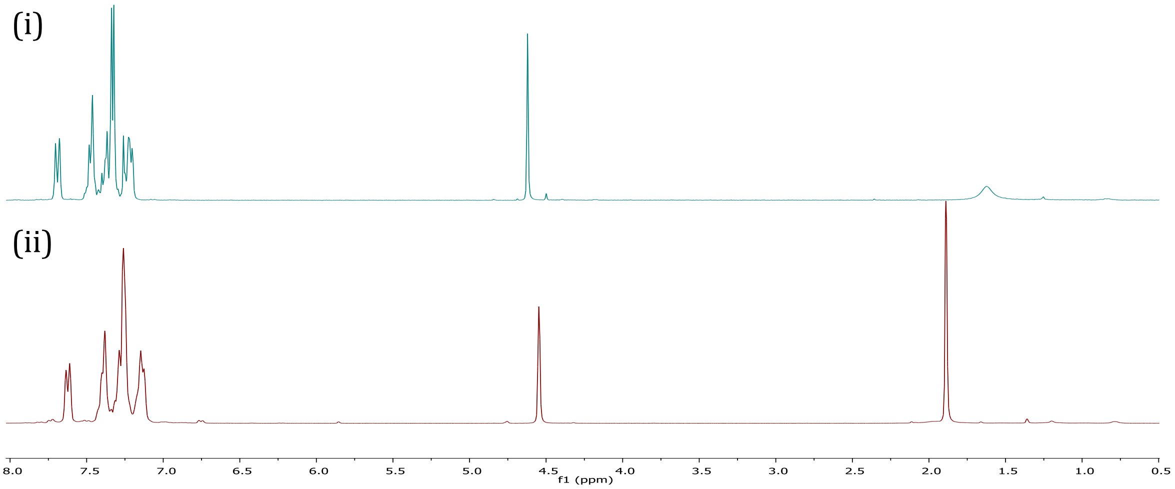

Figure A45. Stacked ^{1}H NMR spectra of (i) ketimine precursor **K1**, (ii) product obtained from the reaction with no Cy_2NMe in $CDCl_3$.

5.3 In the absence of light (i.e. in the dark)

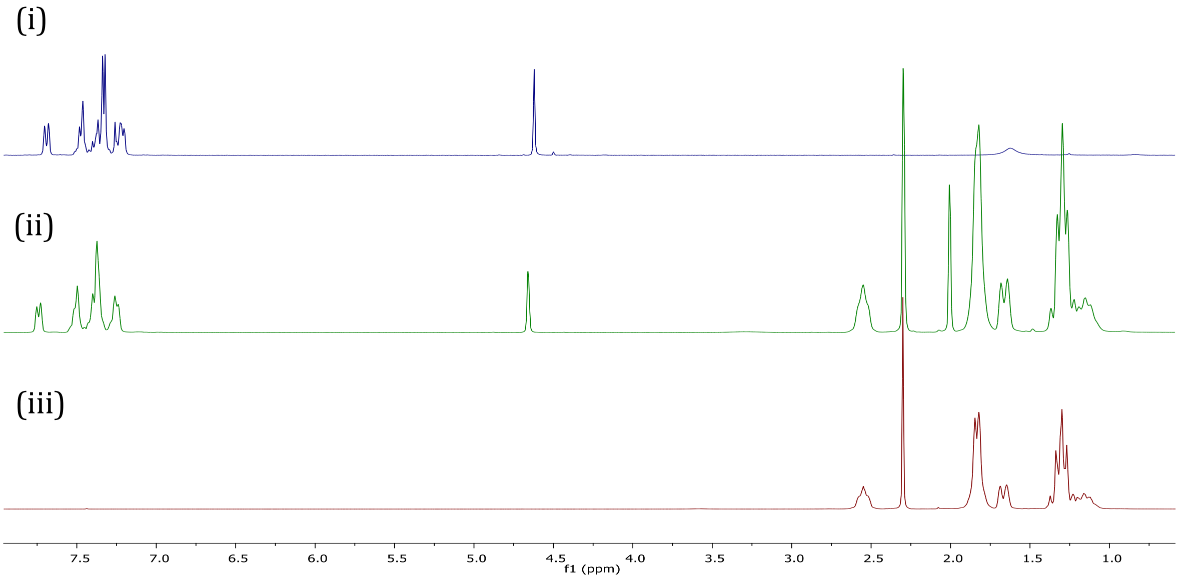

Figure A46. Stacked ^{1}H NMR spectra of (i) ketimine precursor **K1**, (ii) product obtained from the reaction with no light source and (iii) Cy_2NMe in $CDCl_3$.

5.4 No CO_2

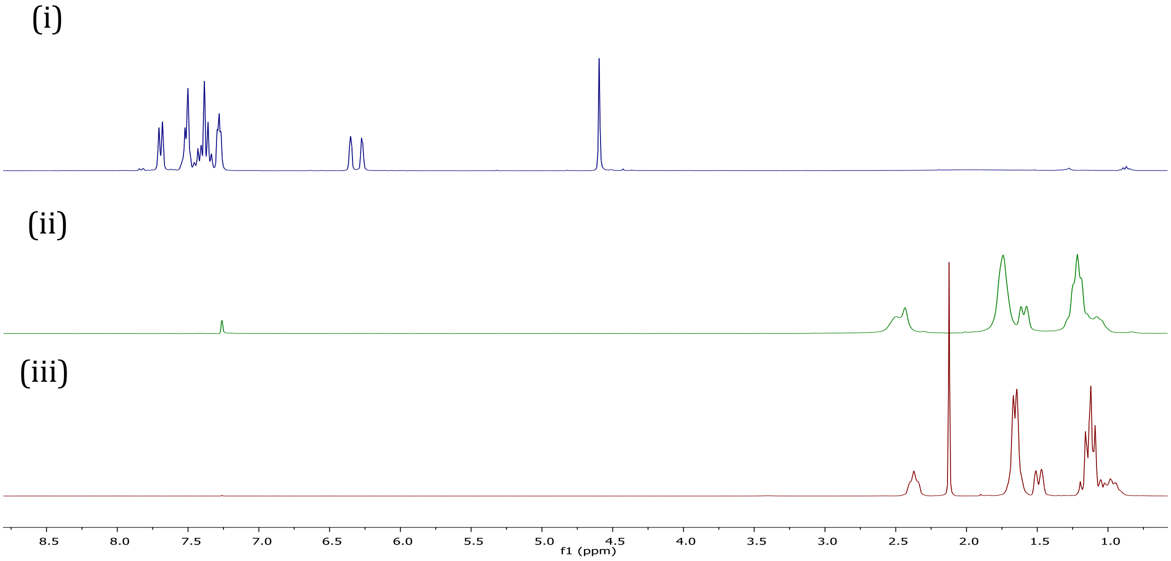

Figure A47. Stacked ^{1}H NMR spectra of (i) ketimine precursor **K2**, (ii) product obtained from the reaction with no CO_2 and (iii) Cy_2NMe in $CDCl_3$.

6. Spectral data for the additional/alternative products formed with complexes C1-C3

6.1 Spectral data for the benzyl substituted additional product

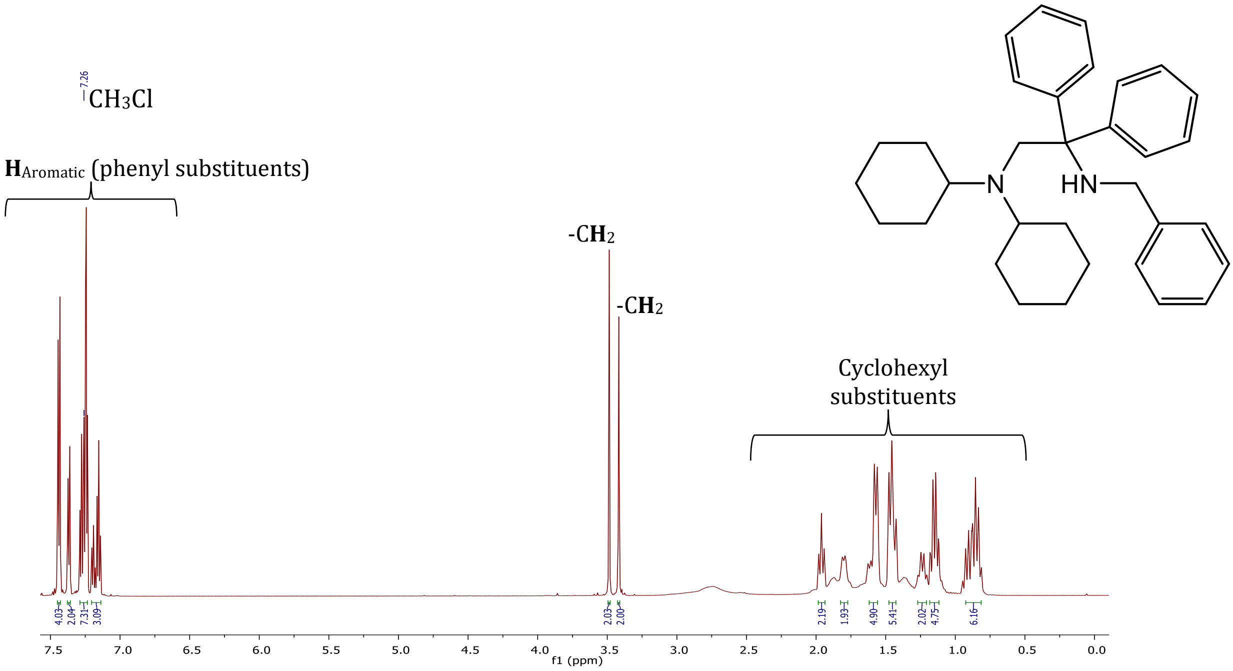

Figure A48. ^1H NMR spectrum of the benzyl substituted additional product in $CDCl_3$.

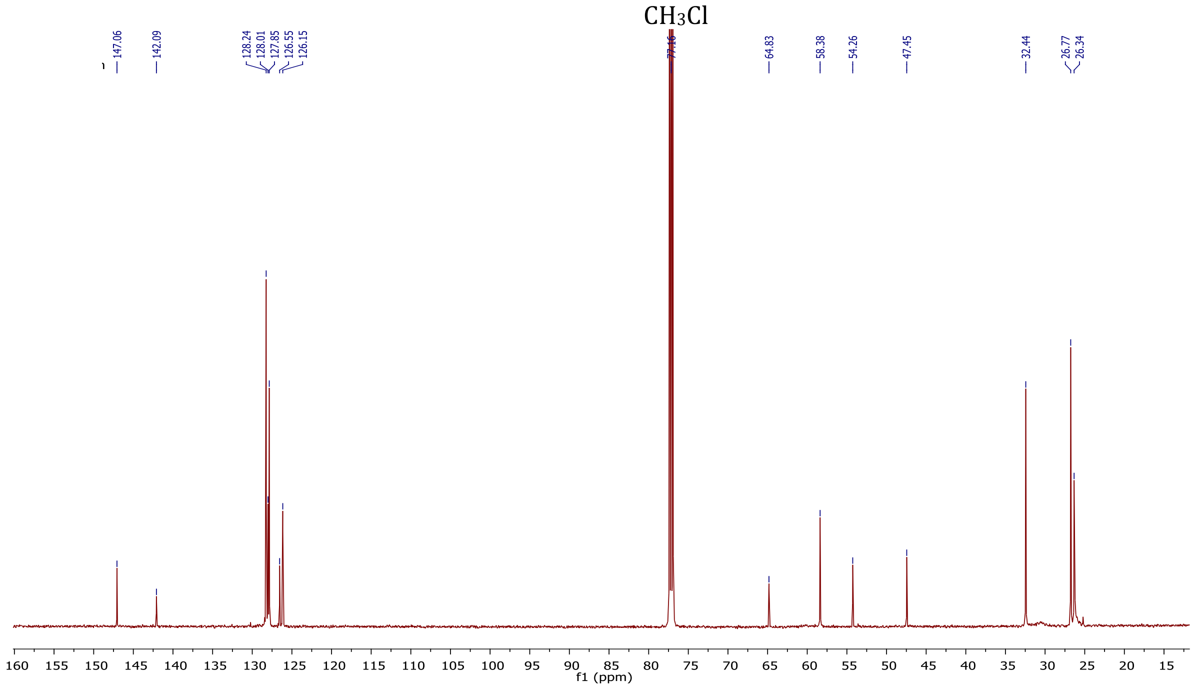

Figure A49. $^{13}C\{^1H\}$ NMR spectrum of the benzyl substituted additional product in $CDCl_3$.

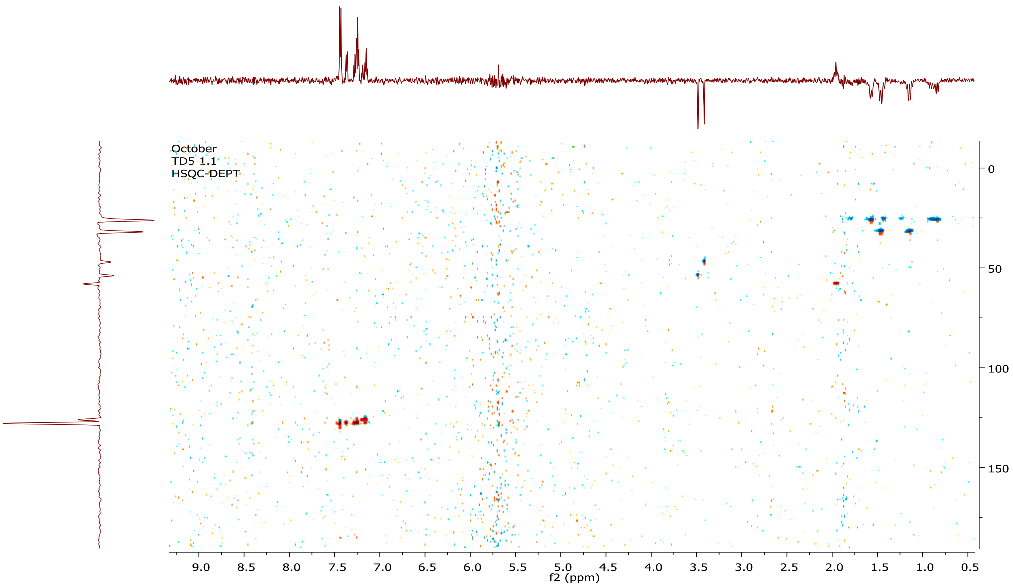

Figure A50. HSQC-DEPT spectrum of the benzyl substituted additional product in $CDCl_3$.

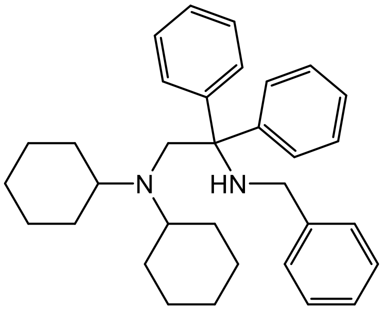

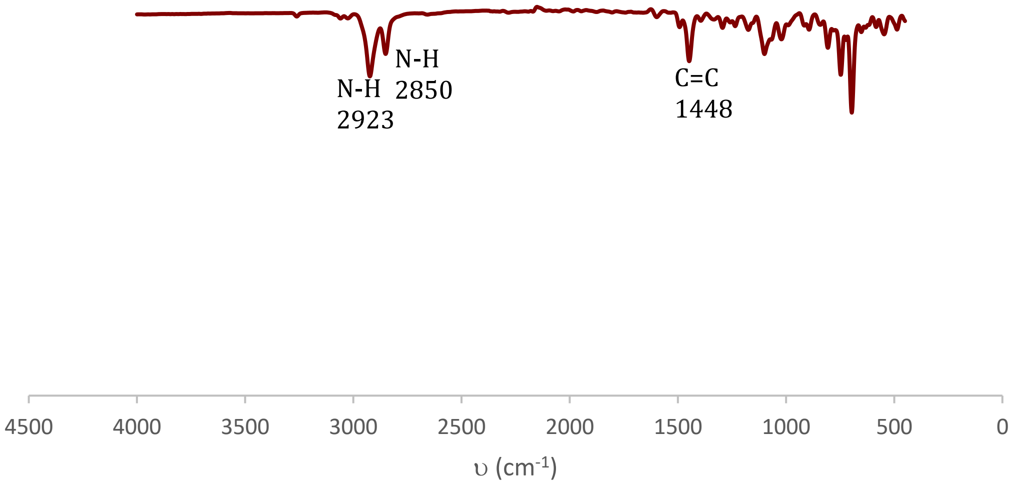

Figure A51. Infrared spectrum of the benzyl substituted additional product.

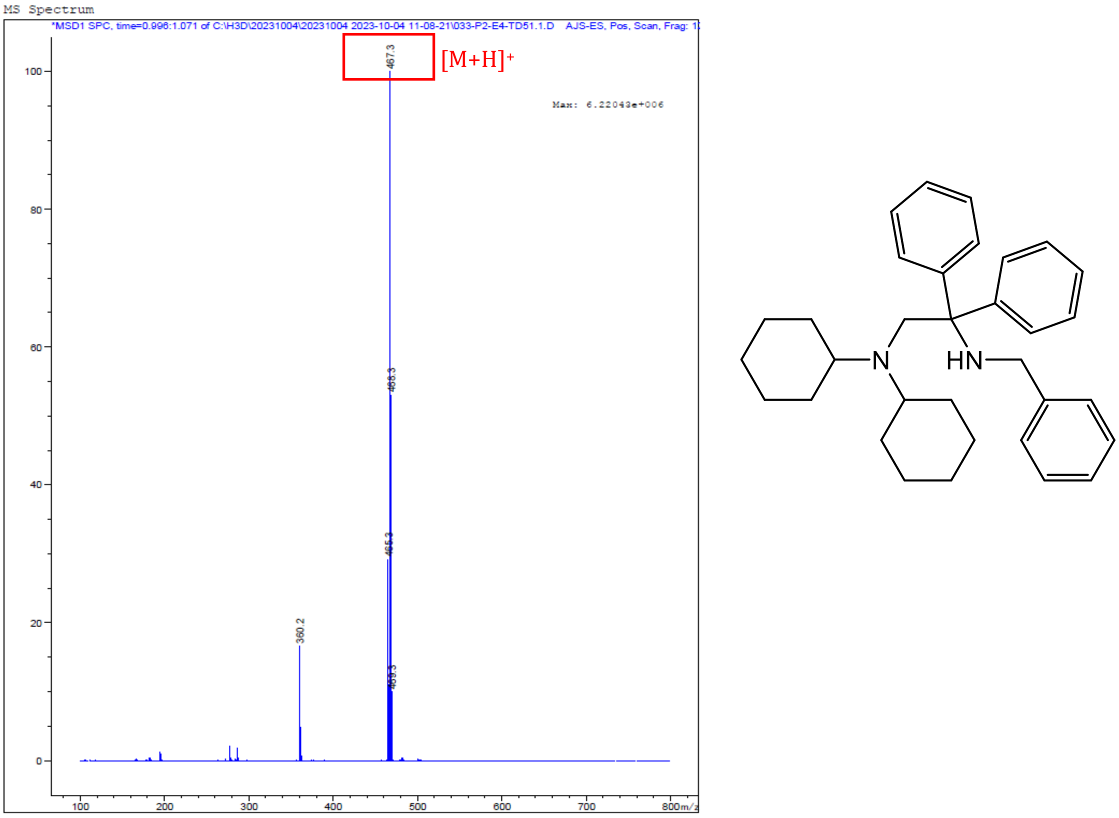

Figure A52. LC-MS trace of the benzyl substituted additional product.

6.2 Spectral data for the furfuryl substituted additional product

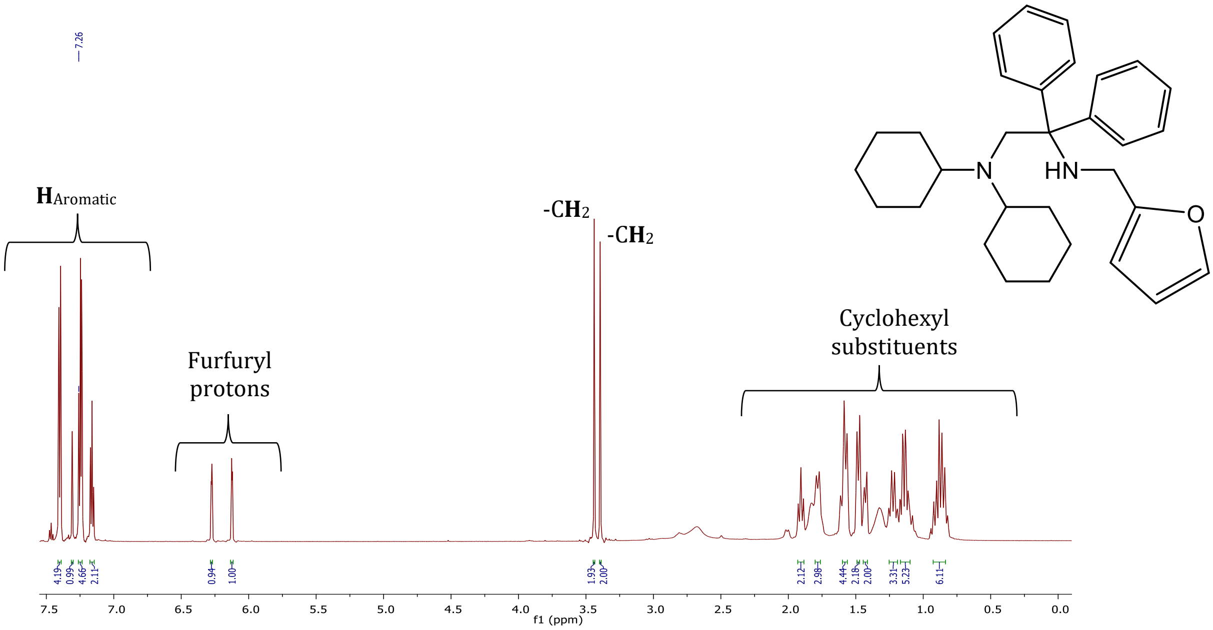

Figure A53. ^{1}H NMR spectrum of the furfuryl substituted additional product in $CDCl_3$.

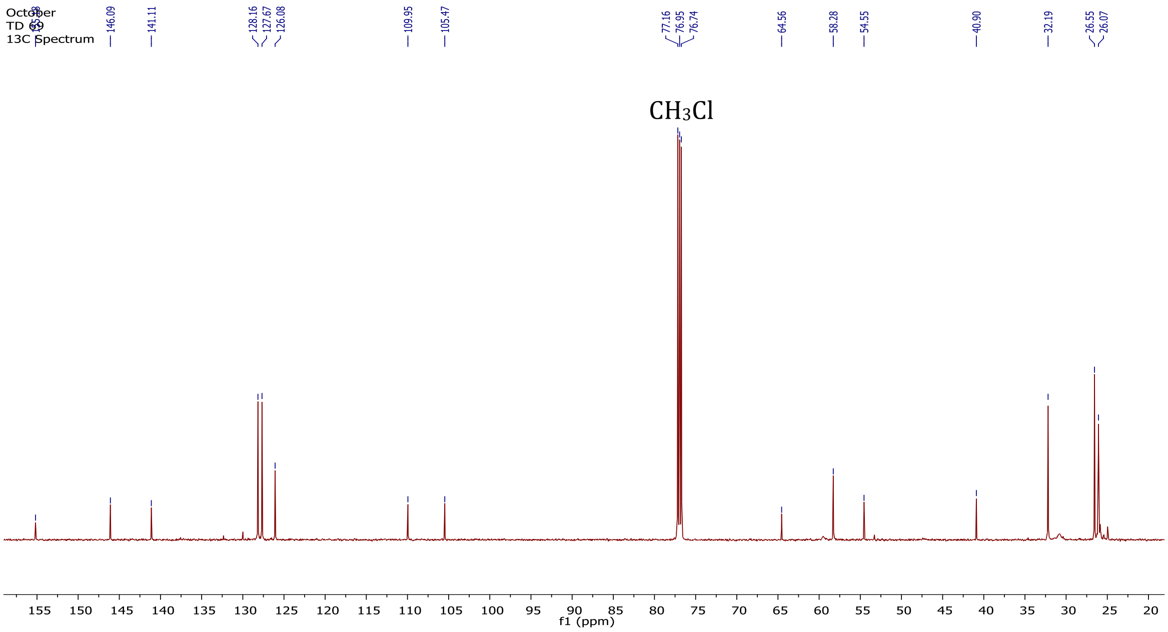

Figure A54. $^{13}C\{^{1}H\}$ NMR spectrum of the furfuryl substituted additional product in $CDCl_3$.

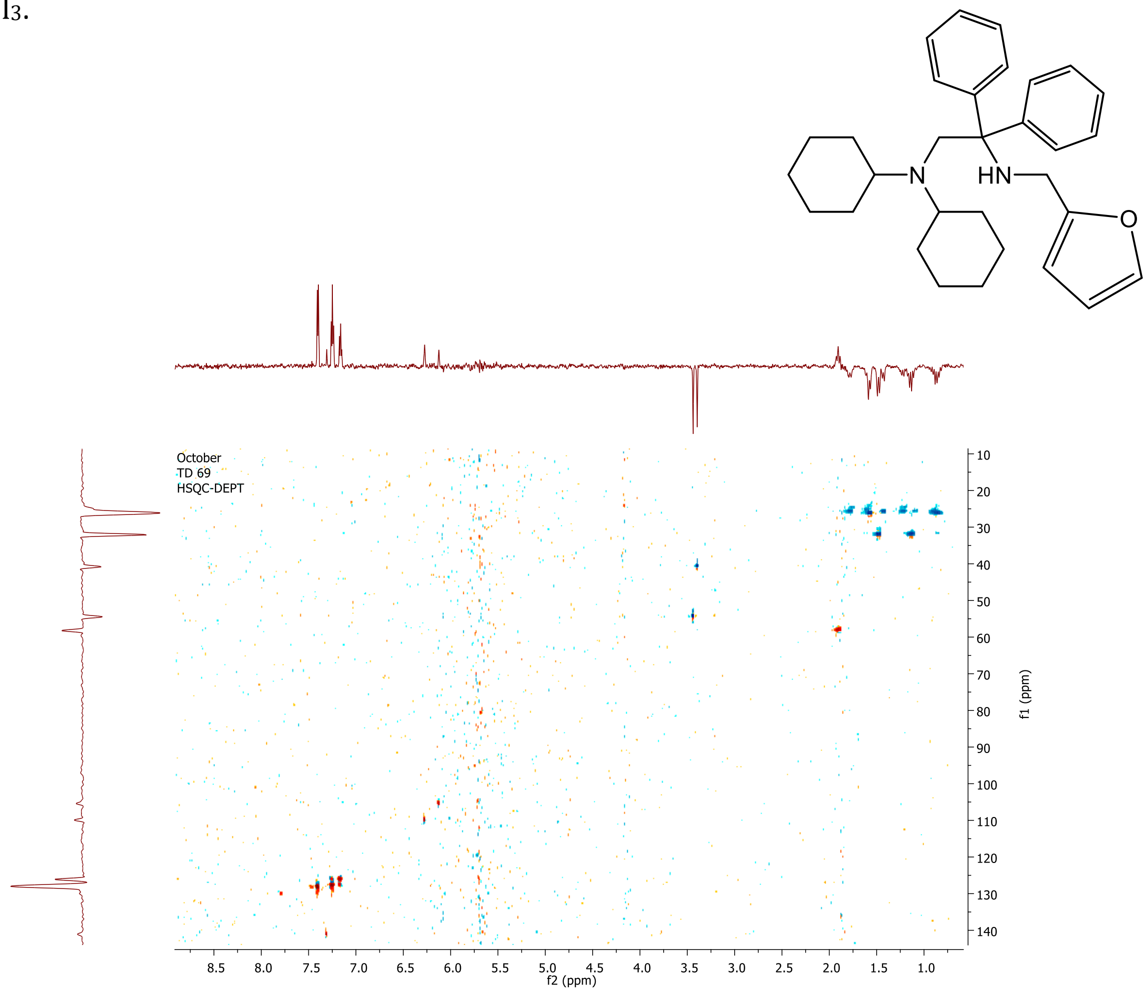

Figure A55. HSQC-DEPT spectrum of the furfuryl substituted additional product in $CDCl_3$.

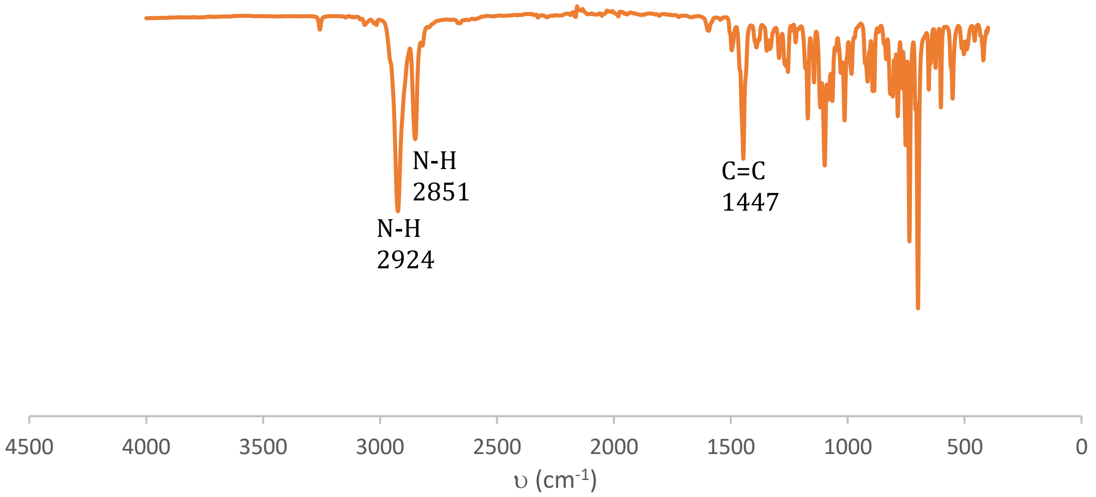

Figure A56. Infrared spectrum of the furfuryl substituted additional product.

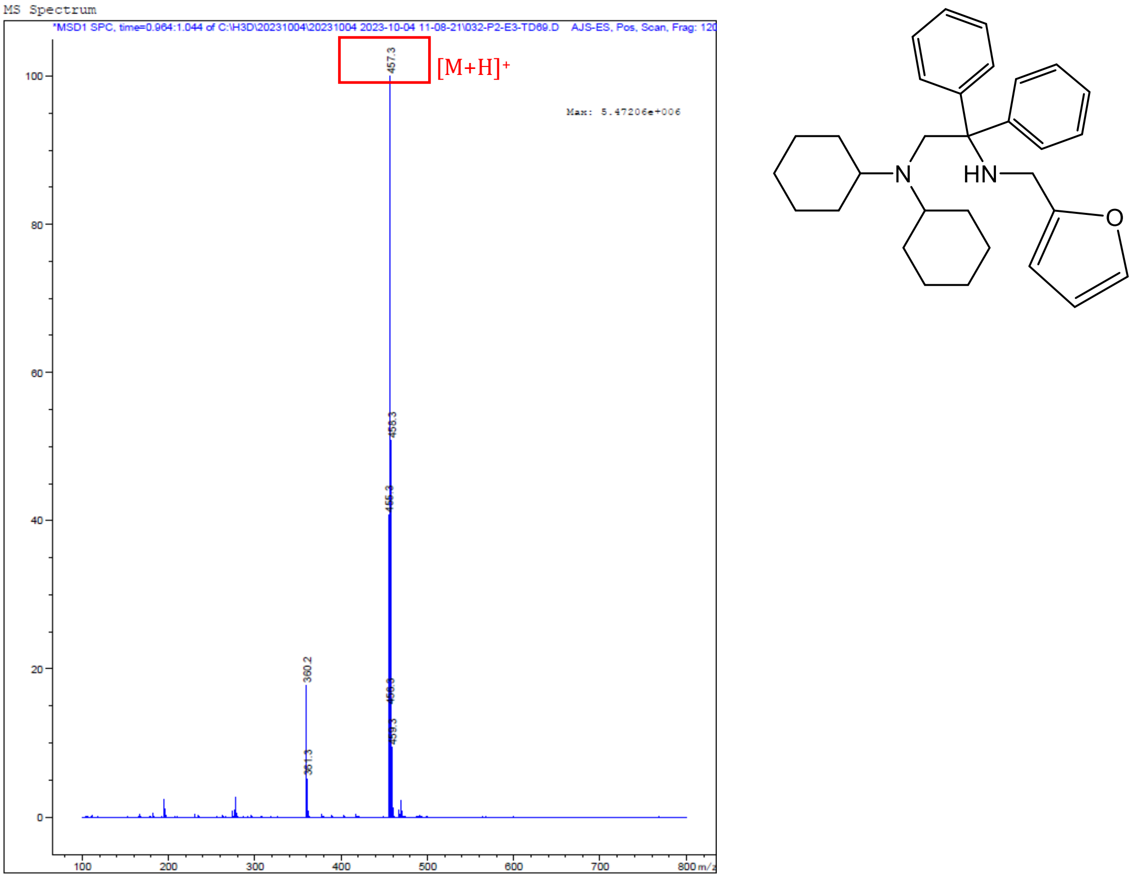

Figure A57. LC-MS trace of the furfuryl substituted additional product.

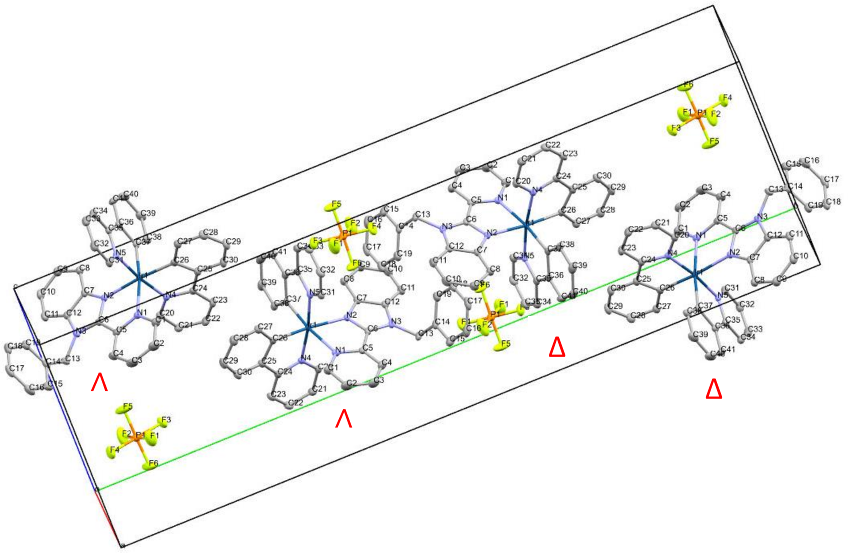

Figure A58. Unit cell displaying the two pairs of enantiomers (Δ, ∧) of complex **C2**.